A Search for Charm and Beauty in a Very Strange World

A Dissertation Presented

by

Jason Adrian Kamin

to

The Graduate School

in Partial Fulfillment of the

Requirements

for the Degree of

Doctor of Philosophy

in

Physics

Stony Brook University

August 2012

Stony Brook University

The Graduate School

Jason Adrian Kamin

We, the dissertation committee for the above candidate for the **Doctor of Philosophy** degree, hereby recommend acceptance of this dissertation.

Professor Thomas K Hemmick, Thesis Advisor
Department of Physics and Astronomy

Professor Ismail Zahed, Chairman of the Defense Committee
Department of Physics

Professor Thomas Weinacht
Department of Physics and Astronomy

Professor Axel Drees
Department of Physics and Astronomy

Dr. Craig Woody
Physics Department, Brookhaven National Laboratory

This dissertation is accepted by the Graduate School.

Charles Taber
Interim Dean of the Graduate School

Abstract of the Dissertation

A Search for Charm and Beauty in a Very Strange World

by

Jason Adrian Kamin

Doctor of Philosophy

in

Physics

Stony Brook University

2012

The Relativistic Heavy Ion Collider (RHIC) was built to produce and study the extremely hot and dense phase of matter called Quark Gluon Plasma (QGP) in which the degrees of freedom are individual partons rather than composite hadrons. Since 2000, RHIC has collided various species of particles in order to disentangle and isolate the properties of the strongly interacting QGP: p+p to set a baseline, d+Au to establish a control experiment, Au+Au to definitively create the QGP, and Cu+Cu to bridge the gap between d+Au and Au+Au .

Electron-positron pairs are a particularly effective probe of the QGP because they carry no color charge. Therefore, once created, these leptons do not interact strongly with the medium. As a result, they retain characteristics of the full time evolution and dynamics of the system. There are many features of interest in the dielectron invariant mass spectrum. The low mass region ($<$ 1 GeV/c^2) consists primarily of pairs from Dalitz decays of light

hadrons and direct decays of vector mesons that can be modified by the medium, while the intermediate ($1 < m < 3$ GeV/c^2) and high ($4 < m < 8$ GeV/c^2) mass regions are dominated by pairs from mesons containing charm and beauty respectively.

Of the multitude of measurements that PHENIX has produced over the last decade, one of the more mysterious and intriguing is a large enhancement of pairs in the low mass region in central Au+Au collisions compared to the p+p reference. Current theories are unable to explain the origin of this excess and a lingering question within the field is whether the presence of "cold" nuclear matter in the initial state of the collision, independent of the formation of a QGP, could possibly account for this increased yield.

To answer this question, this thesis explores the dielectron spectra in d+Au collisions at $\sqrt{s_{NN}} = 200\ GeV$. The d+Au system contains the cold nuclear matter in question but cannot create the required energy density to form a QGP, making it an ideal place to explore these effects. In addition, the 2008 d+Au dataset contains the necessary luminosity to also dissect the high mass region of the spectrum, thereby illuminating the characteristics of heavy flavor production. These include measuring the production cross sections for charm and beauty ($\sigma_{c\bar{c}}$, $\sigma_{b\bar{b}}$) as well as testing the validity of next-to-leading order perturbative Quantum Chromodynamics (NLO pQCD).

"So it goes..."
-Kurt Vonnegut

Contents

List of Figures

List of Tables

Acknowledgements

This thesis is a piece of work that would not have been possible without the help, love, and support of many, many people.

First, and most importantly, I'd like to express sincere gratitude for the love and support of my family. None of this would have ever been possible without my parents and brother. Since the day I was born, they've carried me through good times and bad and I love them deeply.

While at Stony Brook, I've been fortunate to work in the Relativistic Heavy Ion Group as well as with the PHENIX Collaboration. My advisor, Tom Hemmick, gave me my first PHENIX physics project in the summer of 2003 and has been a great advisor and mentor ever since (even though he *does* root for the wrong football team). Axel Drees, in addition to being a fantastic guide through the muddy waters of graduate school, has become a close friend (and climbing partner!) whom I admire and respect.

Thank you to my good friend Torsten for laying the dielectron framework for me to build upon. The cadre of postdocs and researchers at Stony Brook has been invaluable in teaching, helping, and guiding me through analysis details and physics problems. In particular, Deepali, Alan, and Ermias have become good friends as well as being great colleagues.

I'd also like to acknowledge Piotr Decowski, who first introduced me to upper level physics at Smith College and became a powerful force in shaping my career afterwards. I'm also appreciative of Fred Wirth and Suzan Edwards being instrumental in guiding me toward graduate school. Additional thanks go out to Zvi Citron who has been a good friend extending back to our time at Hampshire College as well as an indispensible colleague. Also, without Socoro's constant vigilence and help, I wouldn't have survived my first day at

Stony Brook.

A big thanks to all my roommates who've put up with me over the years. Katy, Elli, Baldo, Burton, Zvi, Regina, Luca and Barbara have all helped to provide a foundation for me here in Stony Brook without which things would have been significantly tougher (and less fun!).

Finally, I'd like to thank Katy whose presence, companionship, and support has taught me more than I could ever learn from any doctoral program.

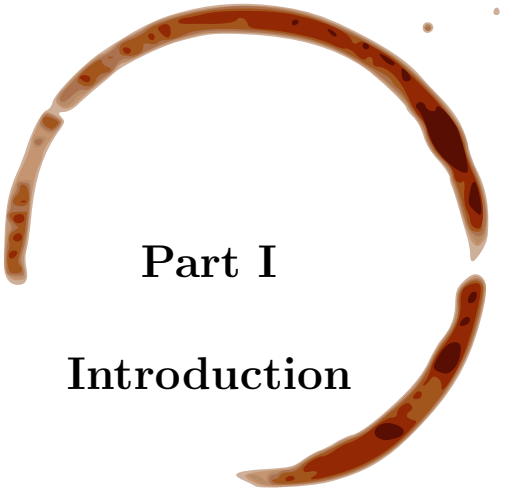

Part I

Introduction

CHAPTER 1

Physics Introduction and Motivation

> Why oh why didn't I take the blue pill??
>
> Cypher, The Matrix

1.1 Motivation

Since the dawn of civilization, humankind has been searching for some meaning in life, some beacon of purpose in the ever-expanding sphere that is the edge of the firelight. While very little progress has been made via metaphysics, the study of hard science has brought us a powerful mechanistic understanding of the world around us. In modern times, the Greek concept of "$\alpha\tau o\mu o\varsigma$", or the atom, has persisted and been a driving force in the study of particle physics.

What began as motes were eventually formalized to molecules; molecules whittled to atoms; atoms deconstructed to protons, neutrons, and electrons. Yet even the proton was not beyond dissection. Next came quarks and gluons, the hidden constituents of the nucleus. Refusing to concede their anonymity, these shadowy figures cowardly manifest as colorless ensembles, seducing scientists to delve even deeper to understand their individual characteristics.

Surely, the journey down the rabbit hole is not yet complete. However, our current understanding leaves us with two sets of 6 fundamental particles along

with 4 fundamental forces. They are summarized in Tables 1.1 and 1.2.

Quarks				Leptons			
Name	Sym	Charge	Mass (MeV/c^2)	Name	Sym	Charge	Mass (MeV/c^2)
up	u	$+^2/_3$	1.5-3.3	e-neutrino	ν_e	0	<0.003
down	d	$-^1/_3$	3.5-6.0	electron	e	-1	0.511
strange	s	$-^1/_3$	104^{+26}_{-34}	μ-neutrino	ν_μ	0	<0.19
charm	c	$+^2/_3$	1270^{+70}_{-110}	muon	μ	-1	105.6
beauty	b	$-^1/_3$	4200^{+170}_{-70}	τ-neutrino	ν_τ	0	<18.2
top	t	$+^2/_3$	171200±2100	tau	τ	-1	1776.8

Table 1.1: Quarks and Leptons along with their physical properties [37].

Name	Relative strength	Range	Exchange particle
gravity	10^{-38}	∞	graviton
weak	10^{-13}	$< 10^{-18}$ m	Z^0, W^+, W^-
electromagnetic	10^{-2}	∞	photon
strong	1	∞	gluon

Table 1.2: Forces and their strength relative to the strong force.

1.2 Introduction

> It would be so nice if something made sense for a change.
>
> Alice in Wonderland

It is the subject of quarks and gluons that brings us to the conception of the Relativistic Heavy Ion Collider (RHIC). RHIC, along with its accompanying experiments, was designed and built to create and study a new phase of matter called the Quark Gluon Plasma (QGP). The QGP is the state of matter in which the degrees of freedom are quarks and gluons instead of the color-neutral hadrons [77]. The strategy to achieve such a high energy-density involves colliding Au nuclei at a center of momentum energy per nucleon $\sqrt{s_{NN}}$ = 200 GeV (ie. on average, each nucleon has an incoming energy of ∼100 GeV). In a fully head-on Au+Au collision, there are roughly 950 binary parton-parton collisions. Since the size of the QGP is ∼1000 fm^3, the energy density of the medium is naively ∼60 GeV/fm^3.

After the initial collision, it is believed that the leftover medium undergoes rapid thermalization < 5 fm/c during which the properties of the QGP are established. The thermalized medium then begins to expand into the vacuum for some time (15-100 fm/c) until it cools and "freezes out" in a final hadronic state, which in turn fragments into the vacuum (and eventually into our detectors!).

1.2.1 Deconfinement

> Cause you could melt all... da.. stuff!
>
> Vinnie to Shaldeen on why it's dangerous for her to be in the frozen food section.
> *My Blue Heaven*

Within the Quantum Chromodynamics (QCD) framework, lattice calculations of both the energy density and pressure of the system indicate a phase transition around a critical temperature, T_C [79]. The left panel of Figure 1.1 shows a steep rise in the energy density divided by T^4 at the critical temperature. The right panel shows a similar rise in the pressure divided by T^4 near $T_C = 173 \pm 8$ MeV [80]. This characteristic jump in density and pressure are indicative of a phase transition. In this case, the transition represents the quarks and gluons being liberated from the cage of color-neutral hadrons and being free to traverse the QGP at will.

A schematic phase diagram of QCD matter is shown in Figure 1.2 where the temperature, T, is plotted as a function of the baryon chemical potential, μ_B. Below the phase boundary, marked by the black line and the experimental blue points, nuclear matter takes the form of a hadron gas where all the partons are locked up in colorless hadrons. Above this line, however, the partons are able to move freely about the medium; this is the realm of the QGP.

The conditions necessary to create a QGP are indeed rare in the universe. However, neutron stars are an example of a (possible) QGP as their densities are high enough for the neutrons to be overlapping yet still have a low temperature[78]. In Figure 1.2 they would lie in the high μ_B and low temperature regime. Alternatively, QGP is also thought to be the state of matter that existed just fleeting microseconds after the Big Bang. This is the other extreme pole on the diagram as it lives at low μ_B and high temperature. Studying the properties of such a medium clearly has implications for not only how

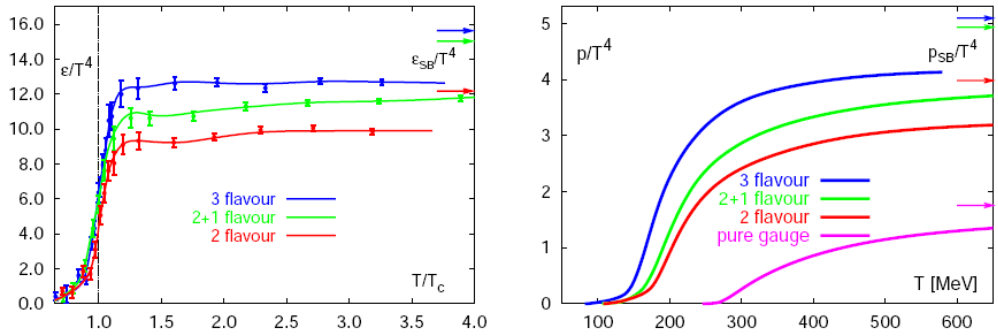

Figure 1.1: Lattice QCD calculations for the energy density vs T/T_C (left) and the pressure vs temperature (right). Both are scaled by $1/T^4$. The colored lines shown are for different quark flavor combinations.

the universe evolved but also what things might be like in some very extreme environments.

1.2.2 Direct Probes

> The way to get started is to quit talking and begin doing.
>
> Walt Disney

Since the QGP dissolves the color cage of a hadron which finds itself immersed in it, the constituents of the medium are partonic. Finding an effective probe of a medium which has a tendency to dissolve any hadron which passes through it is challenging. While many observables are available to the RHIC experiments (and are outlined in the experimental white papers [1], [2], [3], [4]), one of the more effective classes are referred to as penetrating probes. There are two main types of penetrating probes:

Hard probes

These consist of particles that are created in an initial hard scattering of the collision. Since they are produced at $t \approx 0$, hard probes must traverse the QGP before they can be detected thereby allowing them the opportunity to be modified by the medium. Typical examples are high p_T particles from jets and particles containing heavy quarks.

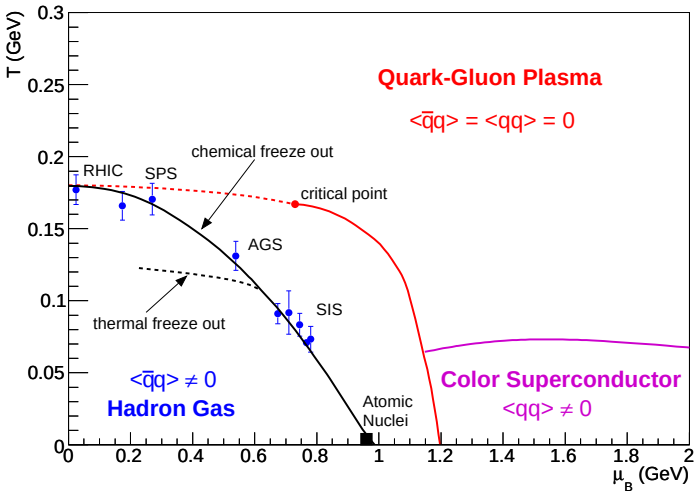

Figure 1.2: Schematic phase diagram of QCD matter as function of temperature T and baryonic chemical potential μ_B. The measured chemical freeze out points for various experiments (hence collision energies), including RHIC, are shown as points [81]. The *dashed* line denotes the thermal freeze out. The existence and exact location of a critical point are unknown.

Electromagnetic probes

Leptons and photons are effective probes of a strongly coupled medium since, being inherently color-neutral, they do not interact via the strong force. Therefore, they have the ability to escape the medium relatively unscathed retaining information about their production mechanism. Typical examples are dilepton pairs and direct photons.

The dielectron spectrum is a rich source of information which allows this thesis to have a dual focus incorporating both categories. Dilepton pairs are obviously EM probes and reveal information about how hadronic sources are modified by the medium (π^0, η, η', ρ, ω, ϕ, J/ψ, ψ', and Υ all contain dilepton channels). However, in addition, they can bridge the gap to hard probes by looking at pairs that originate from semi-leptonic B and D meson decays. These charm and beauty based mesons are typically created in the initial hard scattering, thereby putting them in the category of hard probes as well. Since the semi-leptonic open heavy flavor decays occur well after the QGP has dispersed, the decay kinematics are unaffected by the medium. Any modification to the final spectral shape would indicate some modification of the heavy flavor particles in response to the medium.

1.2.3 Cold Nuclear Matter Effects

> Revenge is a dish that is best served cold. It is very cold in space...
>
> Khan, Star Trek

As far back as the early 1980's deep inelastic scattering experiments have shown that the distribution of quarks inside a proton (or neutron) is modified when the nucleon is packed inside a heavy nucleus. The quarks inside one nucleon seem to feel the presence of the quarks in a neighboring nucleon. This has traditionally been measured by comparing the cross sections or structure functions of deuterons to those of heavier nuclei. In 1983, the European Muon Collaboration (EMC) published the ratio of iron to deuteron cross sections measured through muon deep inelastic scattering [84]. The results, plotted as a function of Bjorken x, are shown in the inset of Figure 1.3. Since 1983, additional experiments have flushed out this result in other heavy nuclei [85] (as well as lighter nuclei [86]) and the results are summarized in the main panel of Figure 1.3.

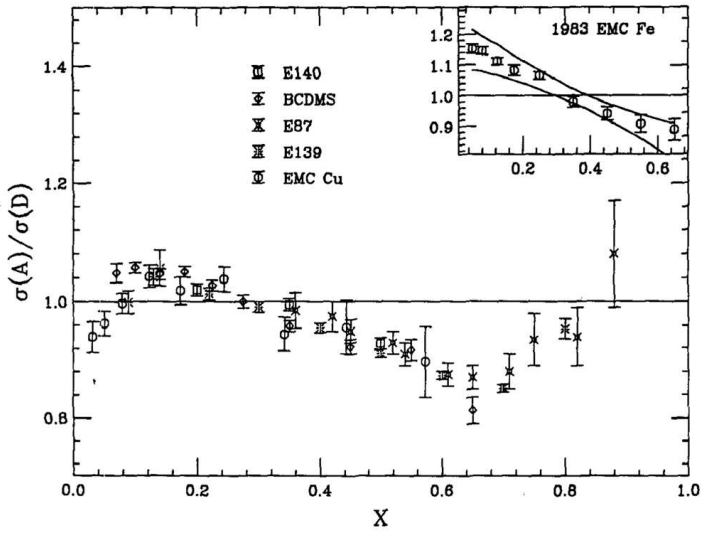

Figure 1.3: Ratios of the DIS cross sections of iron and copper targets to deuterium. The inset shows the original EMC result from 1983.

None of the structures in Figure 1.3 are particularly well understood. The four main regions of interest are highlighted below:

Shadowing

Below $x \approx 0.1$ the ratio is less than unity. This is typically attributed to multiple soft scattering and/or coherence effects due to overlapping nuclear wave functions. As the nucleons get squeezed together inside a dense nucleus, the nucleon separation can become smaller than the spatial extent of the gluon wave function. Since lower x partons are overwhelmingly gluons (see Figure 1.4) the overlapping of the gluons can cause them to fuse together. This effect would deplete the heavy nucleus of low x partons.

Anti-Shadowing

Between approximately $0.1 < x < 0.3$ the nuclear cross section is enhanced. The aforementioned gluonic fusion in the shadowing region merges two low x gluons and into a single higher x gluon, which then populates the anti-shadowing region and results in an excess.

EMC Effect

From $0.3 < x < 0.7$ there is a steady decline. This region is named after the experiment that first observed the effect and there is generally no consensus on the explanation in the community.

Fermi Motion

Above $x \approx 0.7$ the ratio again rises above unity due to Fermi motion of the nucleons.

The robustness and longevity that these results have maintained over the past 30 years, along with the lack of a comprehensive fundamental understanding of their origins, often tempt the nuclear community to use them as explanations for other various observations (even though they are nothing more than *phenomenological* observations!).

A major challenge in interpreting observables in heavy ion collisions is determining which modifications are *initial state effects*, simply due to the presence of additional nucleons changing the incoming parton distribution functions (PDFs), rather than the creation of a QGP. To disentangle initial state effects from final state effects, it is necessary to create experimental conditions in which there are extra relativistic nucleons hanging around while keeping the energy density low enough so as not to create a QGP. At RHIC, this is accomplished through d+Au collisions (motivating the subject of this thesis!).

However, this is not the only reason to collide deuterium with Au nuclei. There are cold nuclear matter effects that are interesting (and perplexing) in

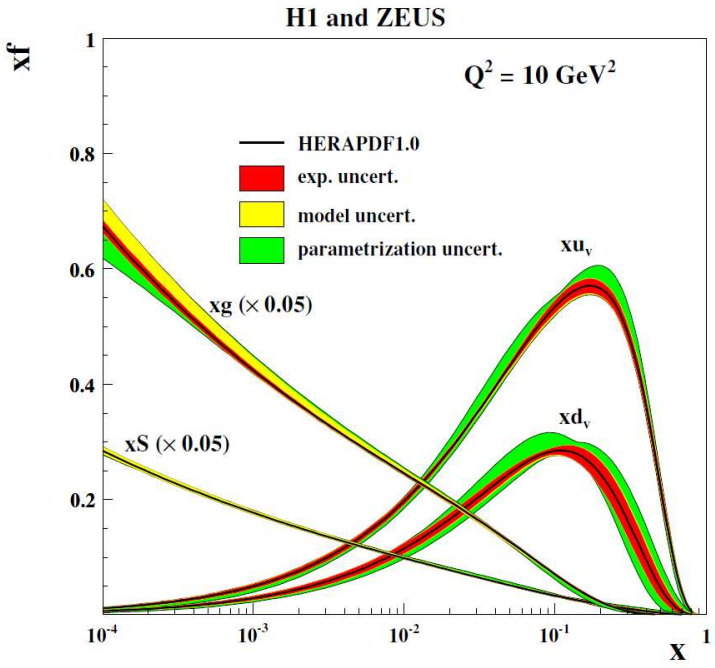

Figure 1.4: The x evolution of the parton distributions as measured by HERA [87].

their own right. For example, Figure 1.5 shows the *nuclear modification factor* for d+Au collisions measured at PHENIX [82], defined as

$$R_{dA}(p_T) = \frac{d^2N^{dA}/dp_T dy}{(\langle N_{coll}\rangle/d^2N^{pp})/dp_T dy}. \tag{1.1}$$

The characteristic enhancement of high momentum particles is not well understood and is referred to as the Cronin Effect, as it was first observed by Cronin *et.al.* in 1974 when firing protons at beryllium, titanium, and tungsten targets [14]. The effect is generally considered to be a result of multiple soft scattering of the incoming partons as they propagate through the target nucleus [88].

In d+Au collisions at PHENIX the Cronin Effect is observed to have a mass dependence and this is a phenomenon that begs for further investigation. While noble attempts were made in 2003 by this author [89] which used simple relativistic kinematics to explain the mass dependence, no definitive conclusion was reached. However, as recently as 2012, PHENIX has submitted for publication results which contain R_{dA} for single electrons originating from heavy flavor decays [83]. These electrons are primarily the decay daugh-

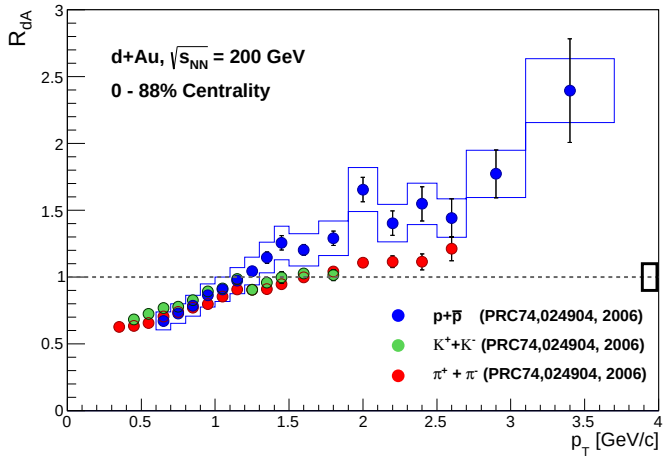

Figure 1.5: R_{dA} for pions, kaons, and protons. The mass dependent Cronin Effect is apparent.

ters of D and B mesons in events which contain open heavy flavor. Figure 1.6 shows a compilation of the charged pion, kaon, and proton R_{dA} along with the single electrons from D and B mesons.

It is vital to keep in mind that the single electron data is *not* the actual R_{dA} of the D and B mesons themselves, instead only their decay products. For this reason, one must be very careful in interpreting the data in Figure 1.6 as it isn't actually an apples-to-apples comparison. Typically, the electron's p_T loosely corresponds to $\sim$1 GeV/c higher momentum for a D meson. In the meantime, a promising study is currently underway to disentangle the electron p_T from the heavy flavor meson p_T. Therefore, it remains speculative whether or not Figure 1.6 is actually evidence of the Cronin effect in D and B mesons. [1]

[1]In addition, PHENIX recently installed a Silicon Vertex Detector capable of pinpointing the decay vertex of the daughter electron, thereby enabling a separation of charm and beauty in the single electron decay channel.

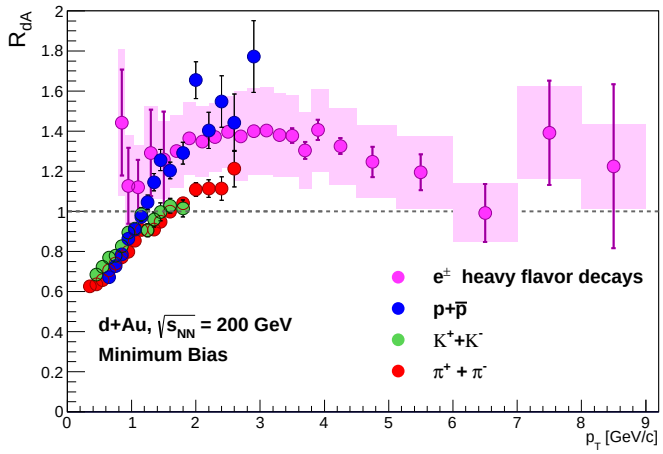

Figure 1.6: The nuclear modification factor R_{dA} for various sources.

CHAPTER 2

Past Dielectron Results

> Who controls the past controls the future; who controls the present controls the past.
>
> George Orwell, *1984*

While PHENIX has produced an extensive collection of dielectron results in p+p , Cu+Cu , and Au+Au over the past 10 years, dilepton measurements have been a hot topic in nuclear physics for quite some time. Many interesting results have been recorded at other facilities around the world. A few highlights are listed below.

The High Acceptance DiElectron Spectrometer (HADES) is a fixed target experiment at the SIS accelerator at GSI which has measured the dielectron continuum up to $m_{ee} = 1$ GeV/c^2 in low energy collisions of light ions, such as C+C at 1 and 2 GeV [90] [91]. The ChErenkov Ring Electron Spectrometer (CERES) was a fixed target experiment at the Super Proton Synchrotron (SPS) at CERN located at NA45[1]. It measured the dielectron continuum in heavy ion collisions (S+Au and Pb+Au) at beam energies ranging from 40 to 200 GeV [92] [93] [94]. Another CERN experiment, NA60[2], measured dimuon pairs in In+In and Pb+Pb collisions from open charm decays by having a

[1] NA45 stands for 45^{th} experimental proposal for the North Access point of the ring.

[2] Again, named after the 60^{th} proposal at the North Access point.

precise vertex tracker, thereby isolating the muons based on their parent's decay position from the interaction point [95] [96].

2.1 Run5 p+p

To establish a baseline expectation for the dielectron program at RHIC, PHENIX has measured e^+e^- pairs in p+p collisions at $\sqrt{s}$ =200 GeV. Figure 2.1 shows the invariant mass spectrum along with the expectation from hadronic sources and open heavy flavor decays (called the *cocktail*[3]). The spectrum is dominated at low mass, below ∼150 GeV/c^2, by π^0 Dalitz decays. The low mass region (LMR) ($150 < m_{ee} < 750$ MeV/c^2) is an olio of sources including η, η', ω, and ϕ Dalitz decays as well as pairs from open charm decays. The vector meson peaks of the ω and ϕ rise above the continuum between $0.750 < m_{ee} < 1.1$ GeV/c^2 (with some additional pollution from the ρ underneath the ω). Filling the hadronic void in the intermediate mass range (IMR) above the ϕ meson ($1.1 < m_{ee} < 2.8$ GeV/c^2), pairs from $c\bar{c}$ hard scatterings are most prevalent with some contribution from $b\bar{b}$ events. Above the J/ψ and ψ' peaks, the continuum of the high mass range (HMR) open beauty is the biggest player (with some help from the open charm). Finally above the Υ peak, Drell Yan production, ($q\bar{q} \to \gamma^* \to \ell^+\ell^-$, see Section 8.2.3), is believed to become influential in the mass spectrum.

The lower panel of Figure 2.1 shows the ratio of the data to the expected cocktail. Within the systematic uncertainties, there is outstanding agreement between the two; the data are fully represented by the cocktail, indicating a comprehensive understanding of the spectral makeup of the mass spectrum. With this mass spectrum in hand, PHENIX has established a robust baseline for the heavy ion collisions.

Moreover, having demonstrated full control over the cocktail ingredients, the hadronic components are then subtracted and the mass spectrum from heavy flavor decays is shown in the left panel of Figure 2.2. This mass spectrum is fit with the PYTHIA line shapes for charm and beauty to obtain cross sections for $c\bar{c}$ and $b\bar{b}$ events. The resulting cross sections are

$$\sigma_{c\bar{c}} = 518 \pm 47(\text{stat.}) \pm 135(\text{syst.}) \pm 190(\text{model})\ \mu\text{b}$$
$$\sigma_{b\bar{b}} = 3.9 \pm 2.4(\text{stat.})^{+3}_{-2}(\text{syst.})\ \mu\text{b}$$

[3]this is referred to as the *cocktail* because it consists of an involved mixture of various ingredients. See Part IV for details on how a cocktail is constructed.

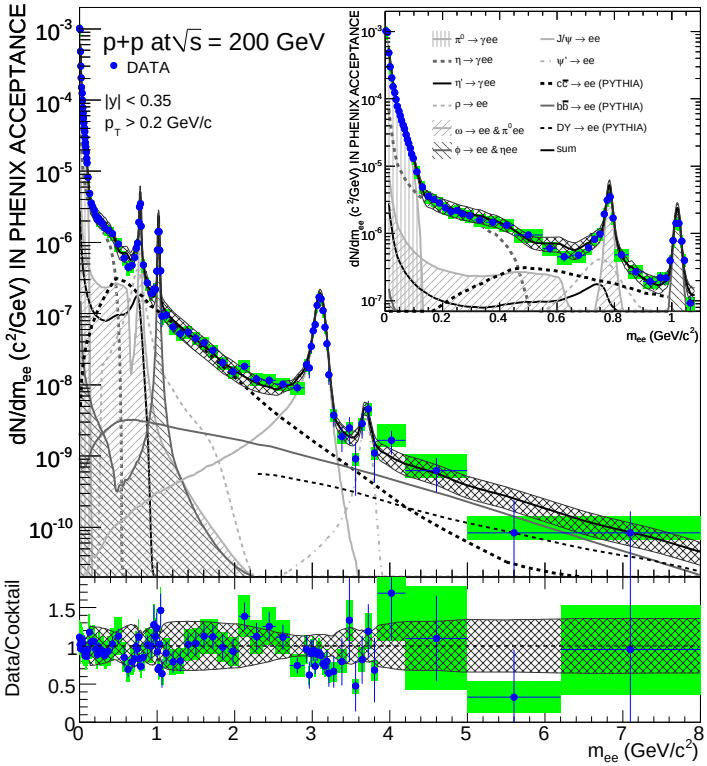

Figure 2.1: e^+e^- pair yield as a function of pair mass p+p collisions at $\sqrt{s_{NN}} = 200GeV$. The expectation from hadronic sources is also shown along with the contribution from open heavy flavor (referred to as the *cocktail*). The ratio of data to cocktail is shown in the lower panel.

While the agreement in the p_T integrated mass spectra between PYTHIA and the data is quite good, the mass integrated IMR p_T spectra are not as concordant. The right panel of Figure 2.2 reveals that, while the low p_T (below $\sim$1.5 GeV/c) spectra agree reasonably well, above 1.5 GeV/c the PYTHIA fails to represent the data. Since the bulk of the yield sits at low p_T, it isn't surprising that the p_T integrated spectra agree quite well. In the original publication [70] this is justified by the fact that the PYTHIA calculation only incorporates leading order (LO) diagrams resulting in every heavy quark pair being produced back-to-back, inherently pushing the subsequent pair p_T lower than reality. It is additionally pointed out that a next-to-leading order (NLO) calculation is probably required to reproduce the p_T dependence. However, it should be noted that in the PYTHIA p_T spectrum in Figure 2.2, the contribution from beauty is neglected. Stay tuned for more details on this point

(Section 10).

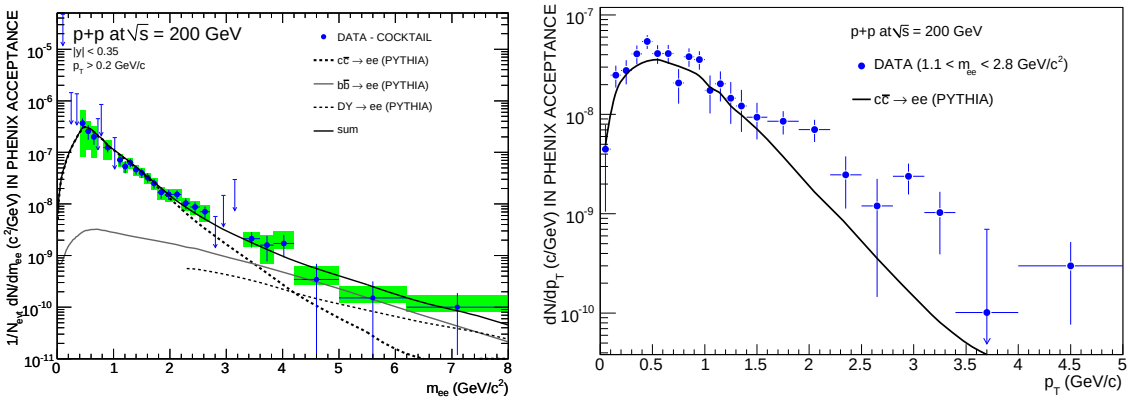

Figure 2.2: Left: e^+e^- mass spectrum from open heavy flavor. The hadronic contributions have been subtracted. Right: e^+e^- p_T spectrum in the mass range $1.1 < m_{ee} < 2.8$ GeV/c^2. The yield is compared to the PYTHIA calculation filtered into the PHENIX acceptance.

2.2 Run4 Au+Au

In 2004, PHENIX took a large dataset of Au+Au collisions at $\sqrt{s_{NN}} = 200$ GeV. The results are shown in Figure 2.3. The unexpected (and now famous) result [69] is a large enhancement of pairs in the LMR (up to a factor of ∼4) with respect to the cocktail highlighted in the left panel of Figure 2.3. Current theory has been unable to explain this discrepancy. Moreover, the right panel of Figure 2.3 shows the centrality dependence of this excess. Clearly, it is an effect that turns on as the centrality increases. This is a strong indication that it is related to the formation of a QGP.

In contrast, the data in the IMR shows good agreement in the most central collisions. However, as the system evolves toward more peripheral events, a slight excess is observed over the cocktail. While it has been hypothesized that the presence of an abundance of nuclear matter (like a Au nucleus) might smear the angular correlations of the open heavy flavor $q\bar{q}$ pairs, a simulation of this effect only serves to *reduce* the yield. A more likely explanation for this excess is opposite arm *jet pairs* (see Section 6.2). This source of, so called, *correlated background* is not subtracted from the Au+Au spectrum. The justification for ignoring this uninteresting component in the Au+Au analysis is that the

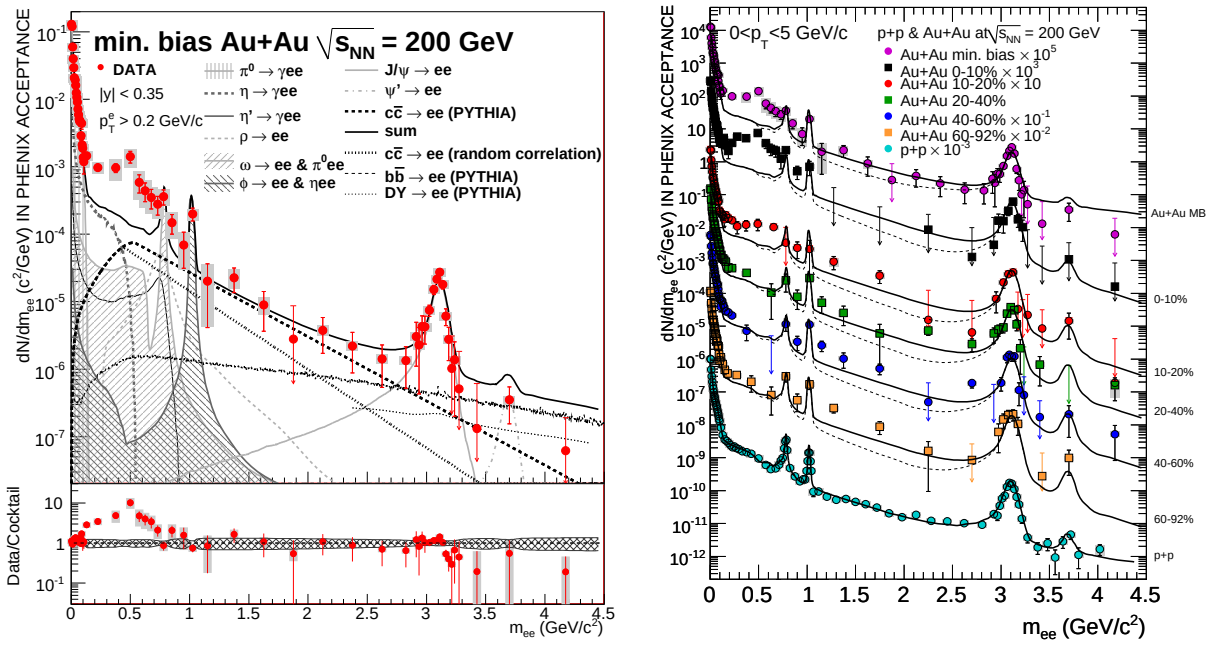

Figure 2.3: Left: e^+e^- pair yield as a function of pair mass in Au+Au collisions at $\sqrt{s_{NN}}$ = 200 GeV. The expectation from hadronic sources is also shown along with the contribution from open heavy flavor (referred to as the *cocktail*). The ratio of data to cocktail is shown in the lower panel. Right: Centrality dependence of mass spectra.

signal-to-background ratio is so low that PHENIX is unable to resolve them in the Au+Au dataset. It's possible, however, that the S/B improves in more peripheral collisions (in the IMR) to the extent that the jet pairs begin to emerge above the signal. This would result in an excess similar to what is observed in Au+Au collisions.

To further corral the low mass excess in Au+Au collisions, Figure 2.4 shows mass spectra in increasing p_T slices. The majority of the excess is located at low p_T (below $\sim$1 GeV/c). This is interesting since, while extreme care was taken to not only fully control the background subtraction in this region but also assign appropriate systematic uncertainty, the excess is inversely correlated to the S/B. This obviously does not imply cause-and-effect; it is simply a duly noted observation.

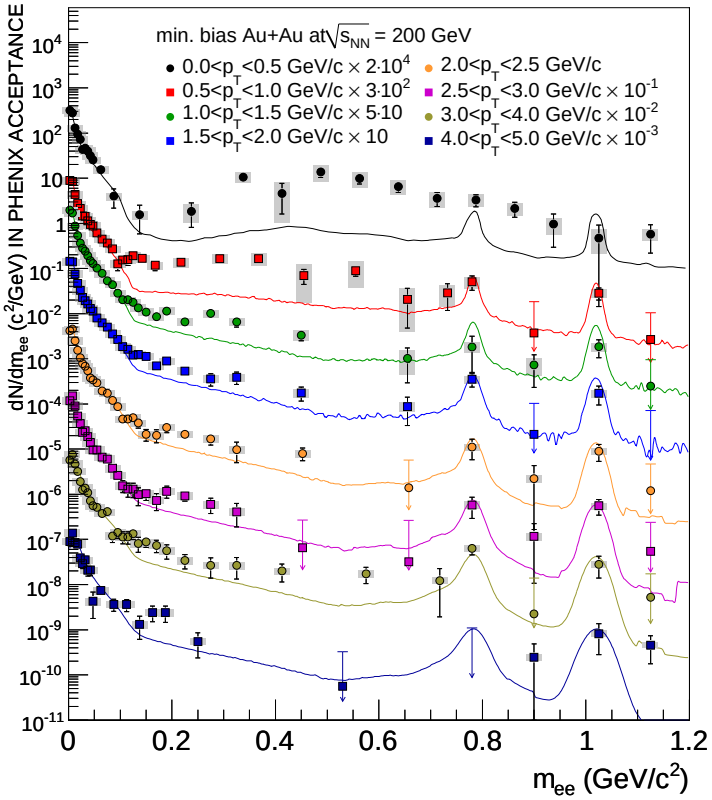

Figure 2.4: The e^+e^- pair invariant mass distributions in Au+Au collisions. The p_T ranges are shown in the legend. The solid curves represent an estimate of hadronic sources.

2.3 Run5 Cu+Cu

To round out the nucleus-nucleus dielectron measurements, the Cu+Cu system has also been reported (not yet published but granted preliminary status). This system is convenient since the range of the number of binary collisions, $<N_{Coll}>$, that the Au+Au system spans is roughly $20-800$ with the higher particle multiplicity per event (and hence statistical precision) weighted towards higher $<N_{Coll}>$). Cu+Cu collisions allow the measurements to extend from $\sim$10 to $\sim$200 in $<N_{Coll}>$.

Figure 2.5 shows the Minimum Bias Cu+Cu dielectron mass spectrum along with the accompanying cocktail; the lower panel illustrates the ratio of the two. Minimum Bias collisions show a hint of an excess in the LMR, although the specific shape seems to differ from that of Au+Au . One inter-

esting feature, however, is the seemingly observed excess in the IMR. This is reminiscent of the (potential) excess in peripheral Au+Au collisions, although the correlated background of jet and cross pairs (see Section 6.2 for full details) has been subtracted in the Cu+Cu dataset.

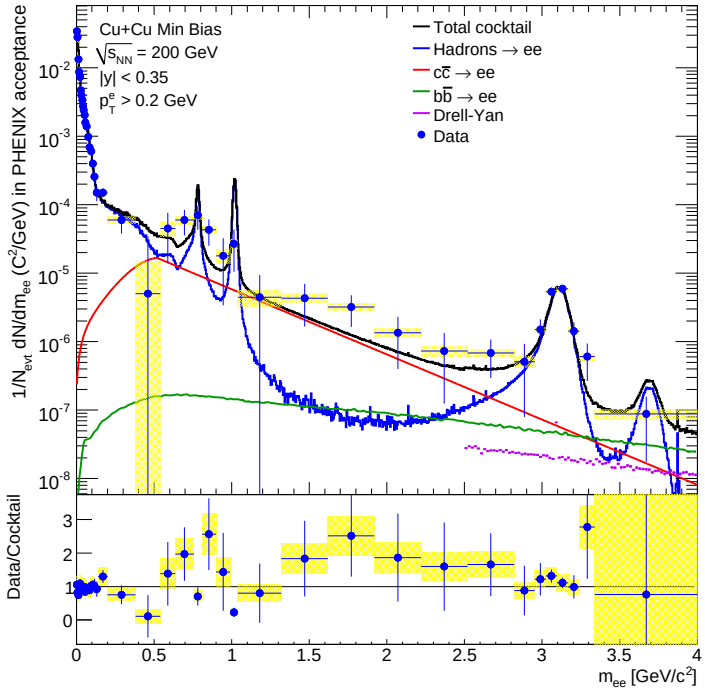

Figure 2.5: e^+e^- pair yield as a function of pair mass for Minimum Bias Cu+Cu collisions at $\sqrt{s_{NN}} = 200GeV$. The expectation from hadronic sources is also shown along with the contribution from open heavy flavor (referred to as the *cocktail*). The ratio of data to cocktail is shown in the lower panel.

To further explore these two regions, the four-paneled Figure 2.6 shows the Cu+Cu mass spectra split into centrality bins. The most central collisions do indeed show an excess in the LMR! However, this should come as a bit of a surprise to the careful reader in light of the Au+Au results; the $<N_{Coll}>$in Cu+Cu collisions that the excess corresponds to ($\sim$150) maps to a centrality in Au+Au collisions (roughly 40% centrality) where no excess is observed. Musing on this incongruent fact, we quote the indelible Roy Lacey: *"interesting, indeed"*.

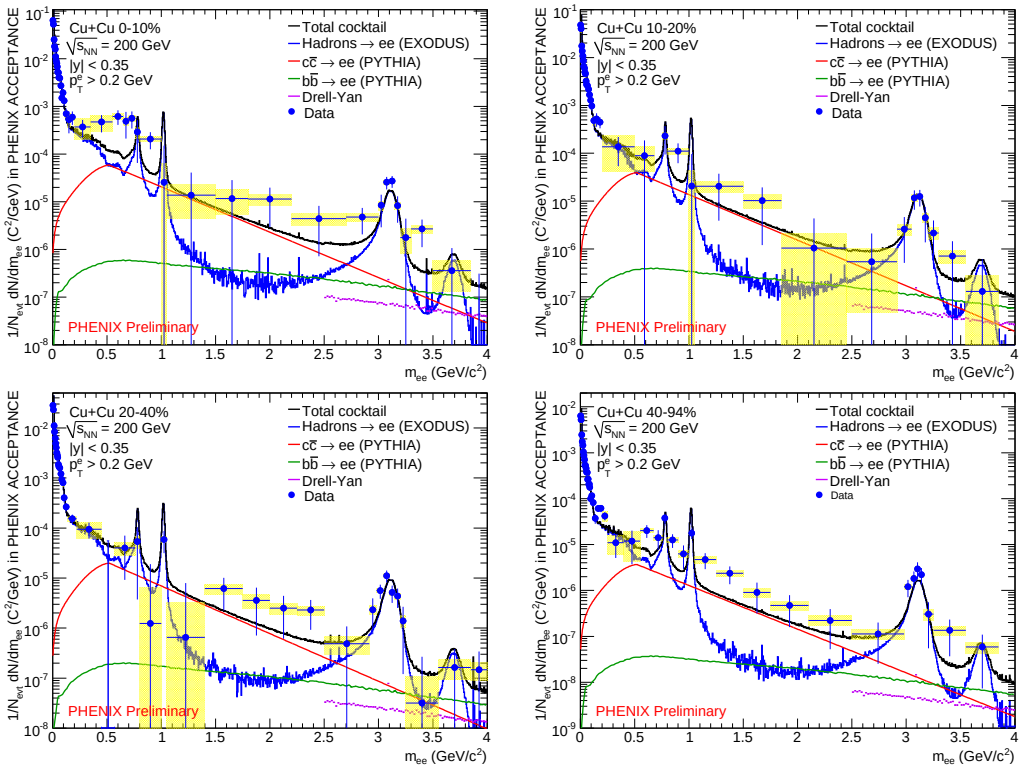

Figure 2.6: e^+e^- pair yield as a function of pair mass in Cu+Cu collisions at $\sqrt{s_{NN}} = 200GeV$. The expectation from hadronic sources is also shown along with the contribution from open heavy flavor. The various panels show different centrality ranges.

2.4 STAR Dielectrons

Recently, the STAR collaboration has begun to report dielectron measurements (facilitated by a time-of-flight upgrade in 2009). The p+p results were submitted in April 2012 for publication in Phys. Rev. C. [97]. The left panel of Figure 2.7 shows STAR's p+p mass spectrum along with their generated cocktail. While the ratio (lower panel) illustrates a probable systematic shape difference between the data and cocktail, most of the points' uncertainty bars/bands do agree.

An interesting side note is that the input $c\bar{c}$ cross section used in the cocktail generated by STAR is $\sigma_{c\bar{c}} = 0.92 \pm 0.10 \pm 0.26mb$. Since this is nearly a factor of two higher than the published charm cross section from PHENIX, we can look at what difference using PHENIX's $\sigma_{c\bar{c}}$ would make to

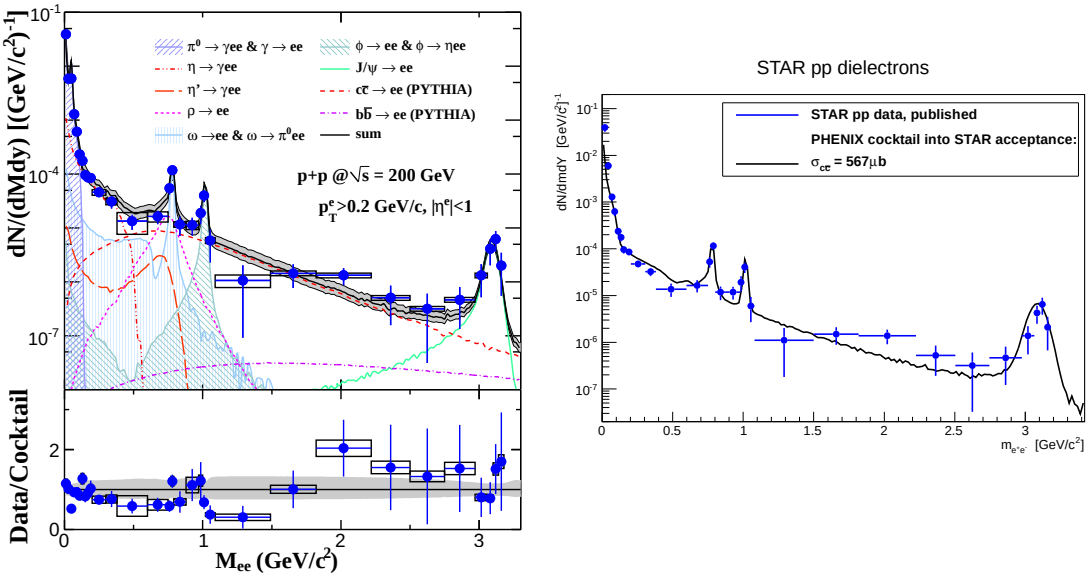

Figure 2.7: Left: The comparison of the dielectron mass spectrum between data and simulation after efficiency correction within the STAR acceptance in $\sqrt{s}$ = 200 GeV p+p collisions (submitted for publication). Right: STAR dielectron data overlaid with a cocktail generated by PHENIX into the STAR acceptance.

the comparison. The right panel of Figure 2.7 shows the STAR data (without systematic uncertainties) plotted with a cocktail generated, by PHENIX, into the STAR acceptance. An obvious (unresolved) inconsistency is that using a cross section nearly twice as low for the charm seems to give a very similar answer. One potential reason for this is that PHENIX uses an NLO calculation (MC@NLO , see Part IV) instead of PYTHIA which is LO.

Additionally, STAR has released a preliminary result for the Au+Au dataset from the 2010 RHIC run. The left panel of Figure 2.8 shows the results along with the STAR-generated cocktail. Here an input cross section for charm of $\sigma_{c\bar{c}} = 960\mu b$ is used. The hint of a shape dependence seen in the STAR p+p data is fully realized in the Au+Au data to cocktail ratio. Even so, STAR observes an excess in the low mass region. While it is not as dramatic as the observed PHENIX excess, the community is eagerly awaiting STAR's final result in the Au+Au system. It will be interesting to see if resolving the systematic shape distortion that currently exists in the data drives the LMR excess up to agree with PHENIX (or if the discrepancy will remain).

Again, to investigate the difference in $\sigma_{c\bar{c}}$ used by STAR and PHENIX,

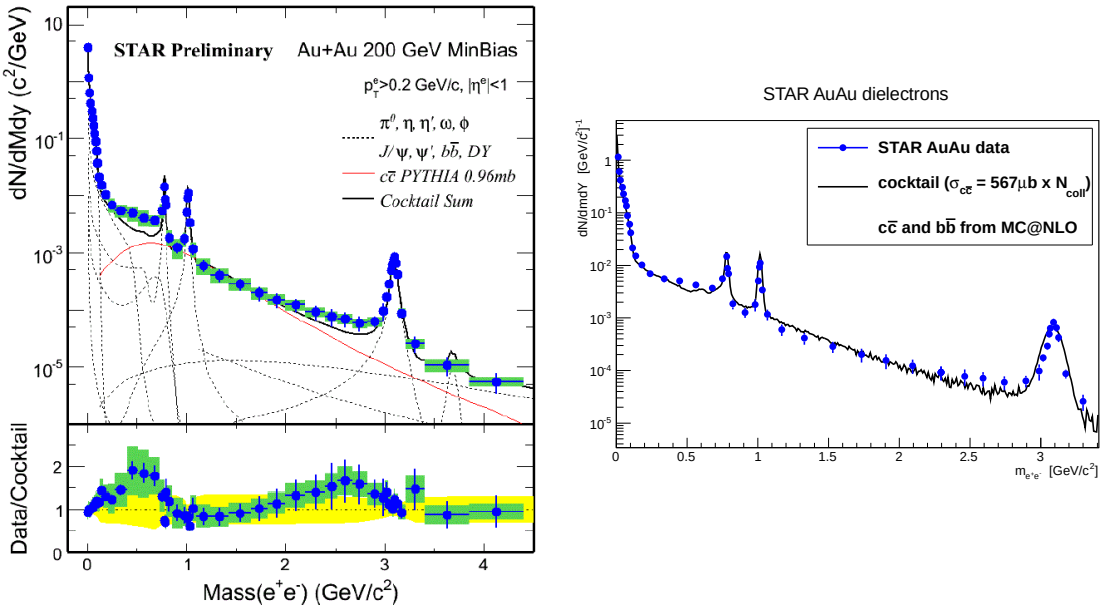

Figure 2.8: Left: The comparison of the dielectron mass spectrum between data and simulation after efficiency correction within the STAR acceptance in $\sqrt{s}$ = 200 GeV Au+Au collisions (released as preliminary result). Right: STAR dielectron data overlaid with a cocktail generated by PHENIX into the STAR acceptance.

PHENIX has prepared a Au+Au cocktail and fed it into the STAR acceptance using the measured PHENIX $\sigma_{c\bar{c}} = 567\mu b$. Similar to the p+p in Figure 2.7, the PHENIX cross section used with the MC@NLO calculation seems to agree with the STAR data reasonably well (at least seemingly as well as the STAR cocktail does). This begs for future investigations, however, and is not the primary focus of this thesis.

CHAPTER 3

d+Au Motivation

> It's easier to predict the past
> than to remember the future.
>
> The Edgemir Group,
> *A Long Island Based Think Tank*

While the motivations for studying d+Au collisions are vast and numerous, this thesis focuses on primarily two topics. They are briefly outlined in the following sections.

3.1 Low Mass Region

The number of binary collisions probed by d+Au collisions can definitively bridge the gap between Au+Au and Cu+Cu collisions and the much simpler $N_{Coll} = 1$ p+p system. $<N_{Coll}>$for d+Au collisions spans from $\sim$3 to $\sim$15. Moreover, the typical separation of the proton and neutron inside the deuteron is $\sim$4 fm, larger than the average radius of the Au nucleus. Therefore, d+Au collisions are generally very "p+p like", the difference being the presence of additional nuclear matter from the Au nucleus.

For these reasons, d+Au is an extremely natural environment to use as a control experiment for the Au+Au collisions. Data from d+Au collisions can immediately determine whether the excess seen in Au+Au (and potentially

Cu+Cu) is due to initial state effects, namely the presence of cold nuclear matter, or the Quark Gluon Plasma.

3.2 Intermediate and High Mass Regions

The 2008 d+Au dataset has the statistical precision to pin down the cross sections for charm and beauty. This will not only yield results with smaller uncertainties than previously measured (particularly for beauty) but also help to resolve the outstanding discrepancies between the STAR and PHENIX charm cross sections.

This analysis will also benefit from the use of NLO calculations performed for the open heavy flavor components of the spectrum. Utilizing a more realistic simulation will increase the accuracy of the cross section measurements while the improved 2D fitting techniques which are implemented significantly increase the precision.

Part II

Experimental Apparatus

CHAPTER 4

The PHENIX Experiment

This chapter describes the Pioneering High Energy Nuclear Interaction eXperiment (PHENIX). The acronym PHENIX is apropos since this particular RHIC experiment was "born of the ashes" of four rejected detector proposals: TALES, SPARC, OASIS, and DIMUON.

4.1 The Relativistic Heavy Ion Collider

> That's no moon. It's a space station.
>
> Obi-Wan Kenobi

The Relativistic Heavy Ion Collider (RHIC) is a particle accelerator and collider at Brookhaven National Laboratory located on Long Island, New York. It produces heavy ion collisions of several different species at varying energies. Beginning operation in 2000, RHIC has produced collisions of p+p , d+Au , Cu+Cu , Au+Au , U+U , and Cu+Au with energies ranging from $\sqrt{s_{NN}}$ of 9 GeV up to 200 GeV in heavy ion collisions (as well as up to 500 GeV in p+p collisions). The designed luminosity is $2 \times 10^{26} cm^{-2} s^{-2}$ for Au ions and $2 \times 10^{26} cm^{-2} s^{-2}$ for protons.

The collider consists of two concentric beams with independent ion sources. Arbitrarily named, the *blue ring* circulates clockwise and the *yellow ring* circulates counter-clockwise. There are six interaction points where the beams can

be brought to collide, four of which have been used for experiments. An aerial view of the RHIC facility is shown in Figure 4.1. RHIC's ability to produce asymmetric collisions (with the center-of-mass frame equal to the lab frame) as well as having spin polarized proton beams maintaining a $\sim 50\%$ average polarization make it a unique and versatile facility in the world of high energy and nuclear particle physics. The information for the first ten years of RHIC operations is summarized in Table 4.1.

During the first five years of running, RHIC had 4 experiments recording data from collisions: BRAHMS [44], PHOBOS [45], STAR [47], and PHENIX [46]. PHOBOS and BRAHMS were smaller experiments designed primarily for low p_T physics (looking at particles at high rapidity) and were decommissioned in 2005 and 2006, respectively. PHENIX and STAR are larger experiments (physically, they're both approximately the size a small house) and are still currently in operation. The analysis and results presented herein are based on data taken at PHENIX during the 2008 d+Au run.

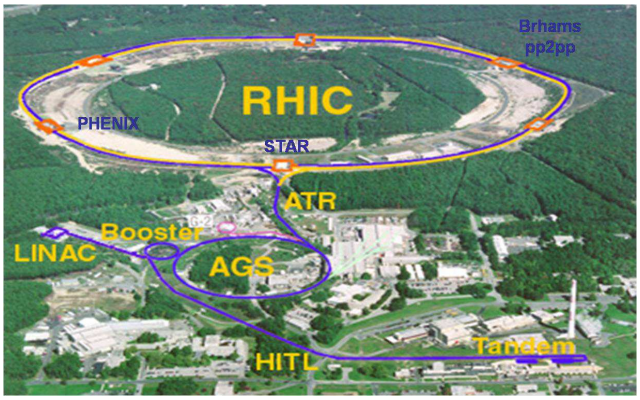

Figure 4.1: The RHIC facility as seen from the air. The circumference of the main RHIC ring is 2.4 miles (3.8 km).

4.2 PHENIX Overview

> Cyclops are kings amongst the blind.
>
> Elli Pomoni

PHENIX is a sophisticated experiment that consists of several independent

Run	Year	Species	$\sqrt{s_{NN}}$ (GeV)	$\int Ldt$	$N_{Tot}(sampled)$
1	2000	$Au+Au$	130	1 μb^{-1}	10M
2	2001/2002	$Au+Au$	200	24 μb^{-1}	170M
		$p+p$	200	0.15 pb^{-1}	3.7G
3	2002/2003	$d+Au$	200	2.74 nb^{-1}	5.5G
		$p+p$	200	0.35 pb^{-1}	6.6G
4	2003/2004	$Au+Au$	200	241μb^{-1}	1.5G
		$Au+Au$	62.4	9 μb^{-1}	58M
5	2004/2005	$Cu+Cu$	200	3 nb^{-1}	8.6G
		$Cu+Cu$	62.4	0.19 pb^{-1}	0.4G
		$Cu+Cu$	22.5	2.7 μb^{-1}	9M
		$p+p$	200	3.8 pb^{-1}	85G
6	2006	$p+p$	200	10.7 pb^{-1}	230G
		$p+p$	62.4	0.1 pb^{-1}	28G
7	2007	$Au+Au$	200	0.813 nb^{-1}	5.1G
8	2008	$d+Au$	200	80 nb^{-1}	160G
		$p+p$	200	5.2 pb^{-1}	115G
9	2009	$p+p$	500	14 pb^{-1}	308G
		$p+p$	200	16 pb^{-1}	936G
10	2010	$Au+Au$	200	1.3 nb^{-1}	8.2G
		$Au+Au$	62.4	0.11 nb^{-1}	700M
		$Au+Au$	39	40 μb^{-1}	250M
		$Au+Au$	7.7	0.26 μb^{-1}	1.6M
11	2011	$p+p$	500	89.9 pb^{-1}	???G
		$Au+Au$	19.6	15.7 μb^{-1}	???G
		$Au+Au$	200	4.97 nb^{-1}	???G
		$Au+Au$	27	32.7 μb^{-1}	???G
12	2012	$p+p$	200	74? pb^{-1}	???G
		$p+p$	500	ongoing	???G
		$U+U$	193	ongoing	???G
		$Cu+Au$	200	ongoing	???G

Table 4.1: The 12 RHIC runs and the integrated luminosity delivered to the PHENIX experiment. N_{Tot} corresponds to the total number of sampled events.

detector subsystems designed to explore the complex environment generated by relativistic heavy ion collisions. In order to investigate this hot, dense nuclear medium, PHENIX specializes in measuring direct probes such as electrons, muons, photons and hadrons.

The PHENIX coordinate system is defined with the z-axis along the beam line, pointing north, the x-axis pointing west and the y-axis perpendicular to both of them, aimed at the sky. The experiment broadly consists of 2 central arm spectrometers for charged particle tracking at mid rapidity, two muons arms at forward rapidity, as well as global detectors built around the beam pipe at very high rapidity.

The central arms are located at pseudorapidity $|\eta|$ <0.35, and each arm covers $\pi/2$ in the azimuthal angle. They are symmetrically offset such that there is a 68° gap centered around the positive y-axis leaving a 112° hole below. Rapidity, Y is defined as

$$Y = \frac{1}{2} \ln \frac{1 + \beta \cos \theta_{cm}}{1 - \beta \cos \theta_{cm}} = \frac{1}{2} \ln \frac{E + p_z c}{E - p_z c} \tag{4.1}$$

where β is the angle from the beam axis in the center of mass frame. When a particle is traveling close very close to the speed of light (c), the rapidity can be approximated by the pseudo-rapidity, η,

$$\eta = -\ln \tan \frac{\theta_{cm}}{2} = \frac{1}{2} \ln \frac{|\vec{p}| + p_L}{|\vec{p}| - p_L} \tag{4.2}$$

where p_L is the component of momentum along the beam axis.

The charged particle tracking, is performed in the central arms by the Drift Chamber (DC) and three layers of Pad Chambers (PC1, PC2, and PC3). The DC and PCs also supply the primary momentum determination for charged particles in coordination with the Central Magnet, which provides an axial magnetic field parallel to the beam. Sandwiched between the PC layers are several particle identification detectors: two time of flight detectors,TOF and Aerogel, a Time Expansion Chamber (TEC), and a Ring Imaging Cherenkov detector (RICH). The RICH is the primary electron identification device in PHENIX. The outer layer of the central arms is and electromagnetic calorimeter (EMCal). Six of eight EMCal sectors are lead scintillator (PbSc) while the lower two sectors in the east arm are lead glass (PbGl). It should be noted that the azimuthal angle coordinate, ϕ, is rotated by $\pi/2$ so that ϕ=0 points straight down into the largest hole in the acceptance to avoid track reconstruction complexity when ϕ=0. The PHENIX acceptance is shown in ϕ and η space in Figure 4.2.

The muon arms cover a full 2π in azimuth with -1.2> η >-2.2 in the south arm and 1.2< η <2.4 in the north arm. Recently, PHENIX has added additional calorimetry at even higher η called the Muon Piston Calorimeters (MPCs), named for their location in the Muon Arm Magnet Pistons. They cover 3.1< η <3.9 and -3.1> η >-3.7, in the north and south arms respectively.

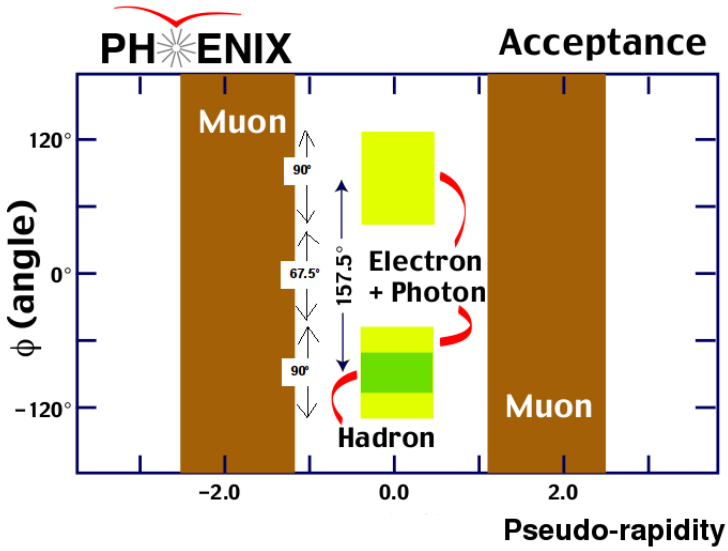

Figure 4.2: PHENIX acceptance for identified electrons, muons, photons and hadrons. The east arm is depicted above the west arm.

Finally, there are global detectors that provide the event trigger as well as event level information such as collision time, vertex position, and centrality. This information is obtained primarily with Beam Beam Counters (BBCs). Supplementary event level information is provided by a Zero Degree Calorimeter (ZDC) and Forward Calorimeter (FCAL). Figure 4.3 shows a schematic of the PHENIX detectors as they were in Run 8 (2008).

The following sections discuss the detector systems used in the present analyses.

Subsystem	$\Delta\eta$	$\Delta\phi$	Specifications
Magnets			
Central (CM)	± 0.35	2π	Up to 1.15 Tm
Muon (MMS)	-1.1 to -2.2	2π	0.72 Tm for $\eta = 2$
Muon (MMN)	1.1 to 2.4	2π	0.72 Tm for $\eta = 2$
Global Detectors			
Beam-beam Counters (BBC)	$\pm$ (3.1 to 3.9)	2π	Start timing, fast vertex
Zero-degree Calorimeter (ZDC)	3 mrad	2π	Minimum bias trigger
Central Arms			
Drift Chambers (DC)	± 0.35	$2 \times \pi/2$	Good momentum and mass resolution $\sigma_m/m = 1\%$ at $m = 1$ GeV
Pad Chambers (PC)	± 0.35	$2 \times \pi/2$	Pattern recognition, tracking for non-bend direction
Ring Imaging Cherenkov Counter (RICH)	± 0.35	$2 \times \pi/2$	Electron ID
Time of Flight (ToF)	± 0.35	$\pi/4$	Hadron ID, $\sigma < 100$ ps
EMCal (PbSc)	± 0.35	$\pi/2+\pi/4$	Electron and photon ID and energy measurement
EMCal (PbGl)	± 0.35	$\pi/4$	$e^{\pm}/\pi^{\pm}$ separation at $p >$ 1 GeV/c by EM shower and $p < 0.35$ GeV/c by ToF $K^{\pm}/\pi^{\pm}$ separation up to 1 GeV/c by ToF
Muon Arms			
MuTr South	-1.15 to -2.25	2π	
MuTr North	1.15 to 2.44	2π	
MuID South	-1.15 to -2.25	2π	Steel absorber and Iarocci tubes for
MuID North	1.15 to 2.44	2π	μ/had separation

Table 4.2: Summary of the PHENIX detector subsystems.

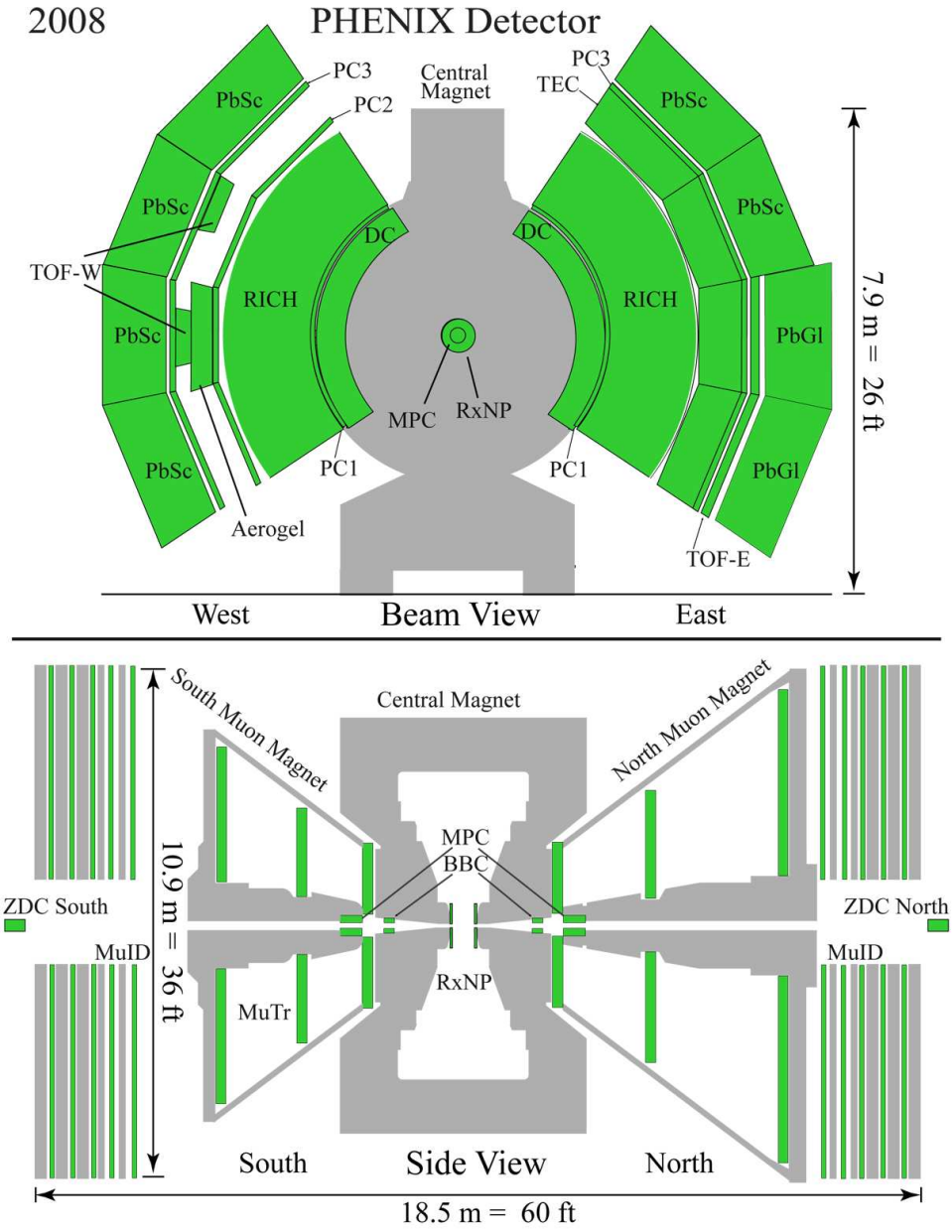

Figure 4.3: A schematic view of PHENIX in Run 8 (2008). The upper panel shows the beamline perpendicular to the page. The lower panel shows a side view with the beam axis parallel to the page.

4.3 PHENIX Global Detectors

The first order of business when measuring a heavy ion collision (or $p+p$ collision) is to determine where the collision happened, when the collision happened, the orientation of the impact parameter, and the centrality of the collision. This kind of event topology is handled by three sets of detectors, the Beam-Beam Counters (BBC), the Zero Degree Calorimeter (ZDC) and the Forward Calorimeter (FCAL).

4.3.1 Beam Beam Counters

The BBCs consist of [49] two arrays of 64 hexagonal shaped PMTs mounted on quartz Cherenkov radiators. When the shrapnel from a collision flies along close to the beam line, the minimum ionizing particles (MIPs) are detected when they deposit Cherenkov light in the quartz crystals. This light is subsequently captured in the PMTs which are layered concentrically around the beampipe. The BBC has a dynamic range spanning 1 to 30 minimally ionizing particles. This broad sensitivity allows the BBC to operate in the full range of RHIC collisions. They are located 1.44 m away from the interaction point corresponding to $3.1 < |\eta| < 3.9$. Each BBC surrounds the beampipe and has an outer radius of 30 cm and inner radius of 5 cm. A picture of a single PMT and radiator element as well as a full BBC array is shown in Figure 4.4.

Figure 4.4: Left: photograph of the BBC array. Right: a single PMT and radiator element.

The BBCs primary purpose is to serve as a serve as a "minimum bias" (MB) trigger, informing the PHENIX electronics that there was a collision.

In addition, they also record the time and position along the z-axis of the event. By averaging the arrival time of charged particles in the north and south BBCs, the collision time, t_0, is calculated as

$$t_0 = \frac{t_{BBC_S} + t_{BBC_N}}{2} - \frac{L}{c} \tag{4.3}$$

where L is the distance from $z = 0$ to the BBC, while the collision vertex along the z-axis, z_{vertex}, is determined by

$$z_{vertex} = \frac{t_{BBC_S} - t_{BBC_N}}{2}\, c \tag{4.4}$$

The event is considered acceptable and the PHENIX Level-1 trigger fires if $|z_{vertex}| \leq 38\ cm$. The time resolution of a single BBC element is 52 ps. Assuming that BBC PMTs fire with an independent probability from one another, then the z_{vertex} position resolution is then

$$\sigma_{z_{vertex}} = 52\ ps \times \sqrt{N_{PMTs}^{BBC_N} + N_{PMTs}^{BBC_S}}\, c \tag{4.5}$$

where $N_{PMTs}^{BBC_{N/S}}$ are the number of PMTs that fired in the either the north or south BBC.

Since the MB trigger at PHENIX requires at least one PMT hit per BBC to announce a collision, this leads to a z_{vertex} position resolution of $\sim 1.1\ cm$ for $p+p$ collisions. Due to the higher multiplicity in heavy ion collisions, more PMTs tend to fire and the overall time resolution improves to $\sim 14\ ps$ for a typical Au+Au collision leading to a z_{vertex} resolution of 3 mm. $d + Au$ collisions fall in between these extremes typically around 0.5 cm.

The BBC is also used in the centrality determination (in coordination with the ZDC and FCAL). 5.3.2.

4.3.2 Zero Degree Calorimeter

PHENIX, along with the other three RHIC experiments, is equipped with a pair of ZDC detectors [22]. These are hadronic calorimeters positioned 18 m north and south of the interaction point. They are positioned on the far sides of the accelerator's first "DX" dipole magnets after the beams are split, allowing them to be between the two beamlines, hence at "zero degrees." Each ZDC consists of three Cherenkov sampling tungsten plate modules which are read out by a PMT. The depth of the plates corresponds to two hadronic interaction lengths. The ZDCs cover $\theta < 3\ mrad$ ($y \gtrsim 6.5$) and have a single arm time resolution of $\sim 150\ ps$.

Figure 4.5 shows a schematic view of the PHENIX global detectors. The ZDCs are a common feature of all four RHIC experiments.

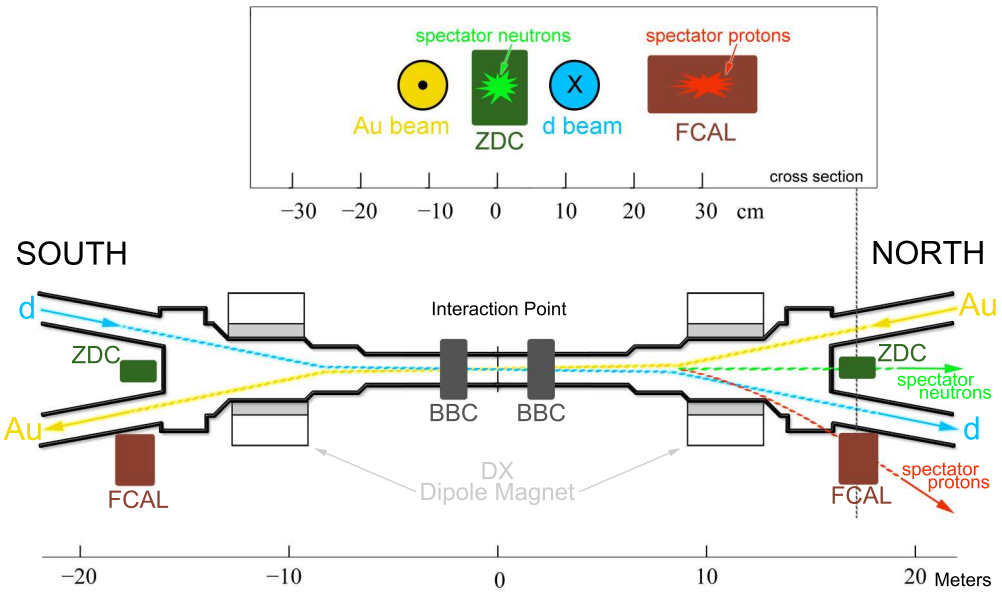

Figure 4.5: FCAL, ZDC and BBC positions relative to the vertex. The vertical scale in the figure is arbitrary. The insert at the top shows the position of primary beam, spectator neutron and proton spots at the FCAL and ZDC locations; deuteron beam, spectator neutrons and protons go into the plane, and the Au beam is coming out of the plane.

The primary purpose of the ZDC is to measure spectator neutrons which are evaporated from the colliding ions. By placing the ZDCs at x=y=0 behind the DX magnets, the rest of the beam, as well as other charged fragments, have been swept away while the neutrons are left free to enter the ZDC. In Au+Au collisions, the ZDC is used in coordination with the BBC to determine the centrality. However, this is not the case for d+Au (or p+p , obviously) collisions; only the BBC is used.

The ZDC serves another purpose in d+Au collisions: it is used to tag events in which only the proton interacted with the Au nucleus. A deuteron has a relatively small binding energy of $\sim 2.22\ MeV$ and, therefore, a charge radius of 2.14 fm. This means that the typical separation between the proton

and the neutron is $\sim 4\ fm$. For reference, the radius of a Au nucleus is $\sim 7.5\ fm$ while for a proton it's $\sim 0.878\ fm$. Consequently, it is reasonably likely that only the proton *or* the neutron from the deuteron will strike the Au nucleus. By observing the spectator neutron in the d-going side (north) ZDC, $p + Au$ events can be tagged (see Figure 4.6). The energy resolution of a single 100 GeV neutron is σ =19 GeV.[22]

4.3.3 Forward Calorimeter

The FCAL [23] is a hadronic calorimeter consisting of lead scintillating fiber modules. Each module is 10 cm × 10 cm × 117cm and the average tower density is 9.6 g/cm3. The FCAL's total depth corresponds to 60 nuclear interaction lengths. The two arrays are located 18m from the interaction point along the beam pipes downstream of the first beam-line deflecting magnet (DX) (see Figure 4.5).

In d+Au collisions the north FCAL is used to detect $n+Au$ events similarly to the ZDC for $p + Au$. When the DX magnets steer the $d + Au$ beam down the beamline, they *oversteer* any spectator protons *out* of the beampipe... and straight into the waiting FCAL! By tagging events that have a 100 GeV proton in the north FCAL (d-going side), $n + Au$ collisions can be identified (see Figure 4.6). The FCAL has an energy resolution of $\sigma = 40\ GeV$ for a 100 GeV proton from the deuteron fragmentation.

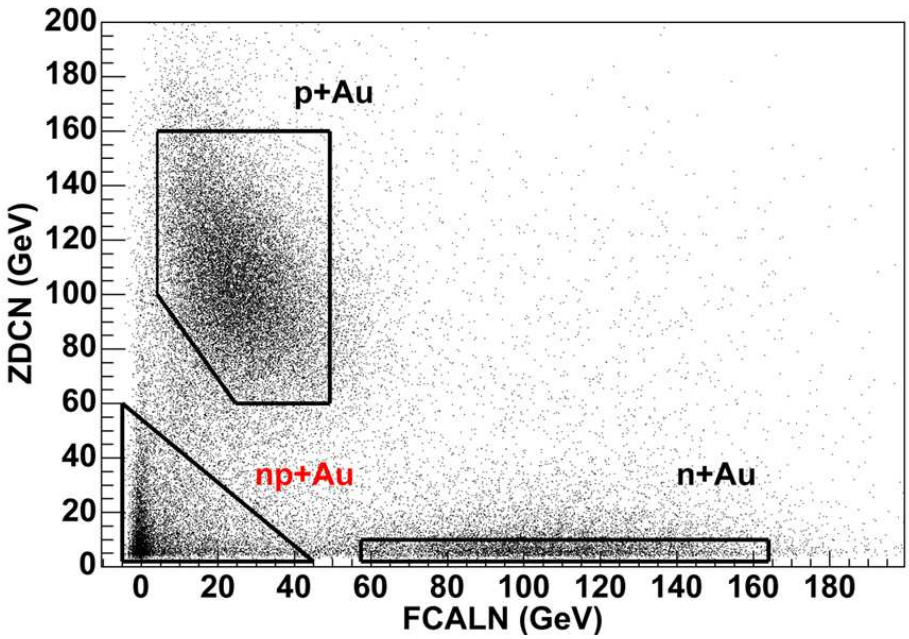

Figure 4.6: Scatter plot of the energy deposited in the ZDC North vs the FCAL North (d-going side). Solid lines indicate the cuts that define $p + Au$ and $n + Au$ collisions.[26]

4.4 PHENIX Central Arm Detectors

Obviously you're not a golfer.

The Dude

This analysis (along with many others in PHENIX) is performed primarily in the Central Arms. The west arm covers $-\frac{3}{16}\pi < \phi < \frac{5}{16}\pi$ and the east arm $\frac{11}{16}\pi < \phi < \frac{19}{16}\pi$. The detectors used in the present analyses and discussed below are instrumented symmetrically in the two arms.

4.4.1 Central Magnet

In order to track the momentum of charged particles it is useful to immerse them in a magnetic field. The resulting deflection angle can be measured and the particle's momentum inferred from it. A stable magnetic field is maintained in PHENIX by the Central Magnet (CM) [48]. The CM consists of two pairs of Helmholtz coils inside a steel yoke. The inner coils have 144 turns and the outer coils have 120 turns each. The generated magnetic field is axially symmetric around the beamline and parallel to the z-axis generating charged particle bend in the x-y plane. Figure 4.7 shows the resulting field lines in the y-z plane.

The PHENIX CM can be run in "adding" mode, where the inner and outer coils are fed current in the same direction (++, –), or "bucking" mode, where they're energized opposite to one another (+-, -+). Adding mode results in a higher strength field and a larger deflection angle for charged particles (see Section 4.4.2) thus improving the momentum resolution. However, the Hadron Blind Detector (see Section 11.1) upgrade used in Runs 9 and 10, requires a field-free region within 50 cm of the beampipe. Figure 4.8 shows that this can be accomplished in bucking mode. In addition, no matter the mode, the B-field dies off after $r >\sim 2\ m$. This allows the software tracking model to assume that tracks which pass through the Central Arms are straight, vastly simplifying the offline reconstruction. In adding mode, a charged particle passes through a field integral of $\int \mathbf{B} \cdot d\mathbf{l} = 1.15$ T·m at $z \approx 0$. In bucking mode, the field integral is ~ 0.43 T·m.

4.4.2 Drift Chambers

Tracking in the PHENIX Central Arms begins with the two Drift Chambers [20]. Each arm is a multiwire gas chamber built of a cylindrical titanium frame

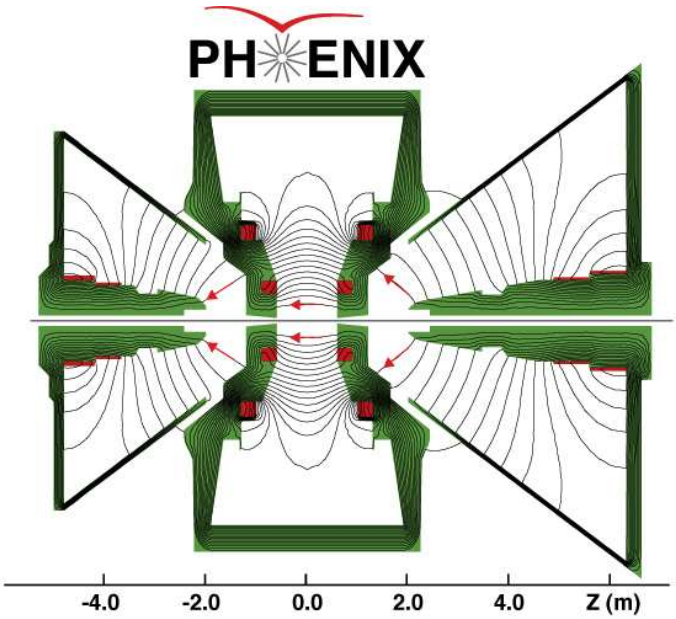

Figure 4.7: Magnetic field lines created by the PHENIX central arm and muon arm magnets.

with 5 *mil* (0.127 *mm*) Al-mylar entrance and exit windows. The entrance window sits at a radius of 2.02 *m* from the beamline and, with a chamber depth of 44 *cm*, the exit window sits at a $r = 2.46$ *m*. For a schematic view of the DC proportions, see Figure 4.9. In each arm, the frame supports over 20,000 wires in total. Each arm is divided into 20 sectors, called keystones, and each keystone has 6 types of wire modules: X1, U1, V1, X2, U2, and V2. One keystone covers 4.5° in the azimuth and has 6400 anode wires.

A 50/50 Argon-Ethane gas mixture is flowed through the DCs, ensuring stability of the ionization drift velocity and a low diffusion coefficient while still allowing high gain. When a charged particle traverses the chamber, it ionizes the gas molecules leaving a path of ionization electrons in its wake. The liberated electrons then drift towards an anode wire with a reasonably constant drift velocity, thereby making their drift time proportional to the electron's starting distance from the wire. During the design phase of the DC, the following requirements were imposed:

- Single wire resolution better than 150 μm in r-ϕ.
- Single wire two track separation better than 1.5 *mm*.

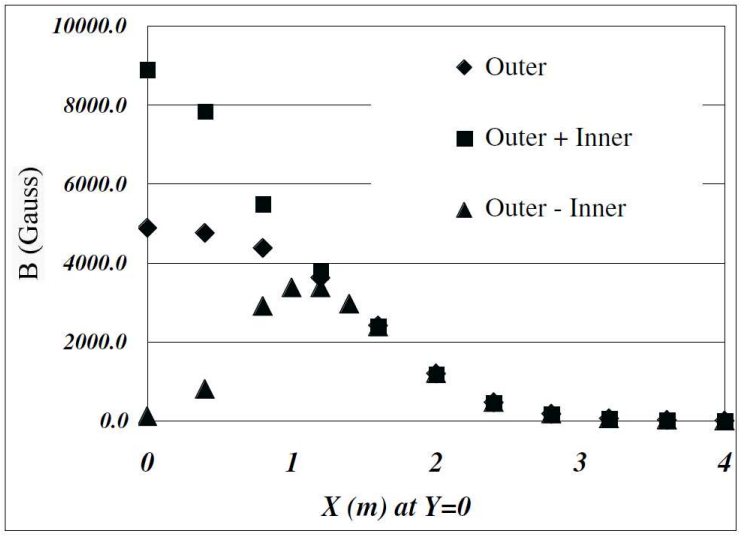

Figure 4.8: Total central magnetic field strength as a function of radius from the beamline.

- Single wire efficiency better than 99%.
- Spatial resolution in the z direction better than 2 mm.

In order to accommodate the high multiplicity environment of a heavy ion collision (up to 500 tracks), each wire is divided in half by a 100 μm thick strip of non-conductive kapton thereby defining two discrete sides of every wire, effectively doubling the available bits for pattern recognition in the tracking. Moreover, to eliminate ambiguities in reconstruction, more than just the anode wires are necessary. Figure 4.10 shows the conglomerate of wires used in the DC. The potential wires help maintain the electric field that terminates at the cathode. The gate wires restrict the ionization collection region to increase the precision of the drift time while the back wires are held at low voltage to block signal from one side of the anode. By reducing the amount of ionization that reaches the anode, the location of each track coordinate can be very localized thereby significantly reducing the strain on the reconstruction algorithm. The typical maximum drift time, corresponding to a drift path of ~ 2 cm, is around 500 ns resulting in a typical drift velocity of ~ 4 $cm/\mu s$ (see Figure 4.11.

The DC hit information is processed through a combinatorial Hough transformation [50] in coordinates ϕ and α. ϕ is defined as the angle where the track bisects the DC at a reference radius of $r = 2.24$ m and α is the track's deflection angle from an infinite momentum track at the reference radius (see Figure

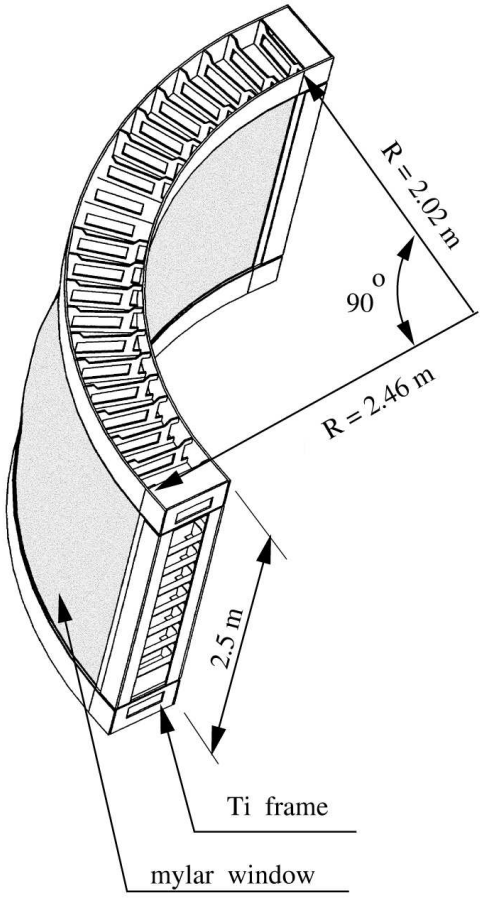

Figure 4.9: A side view of a single keystone on the left, and a top view of the wire orientations on the right.

4.12). The Hough transformation assumes zero magnetic field inside the DC volume (straight line track). Due to the individual wire efficiencies being less than optimal (between 90% and 95%), only 4 hits are required in each of the X layers (instead of the perfect 6). This results in a single track efficiency of greater than 99%.

The combinatorial Hough transformation is extremely powerful! Every combinatorial pair of hits is mapped to the Hough Space as a point, the x and y value of which define the "track" made by the two points in question. Figure 4.13 shows a Toy Hough Transform example (in the coordinate space of slope vs y-intercept). Every peak in the Hough space corresponds to a track. The efficacy of this modeling is apparent by how high the peaks rise above the

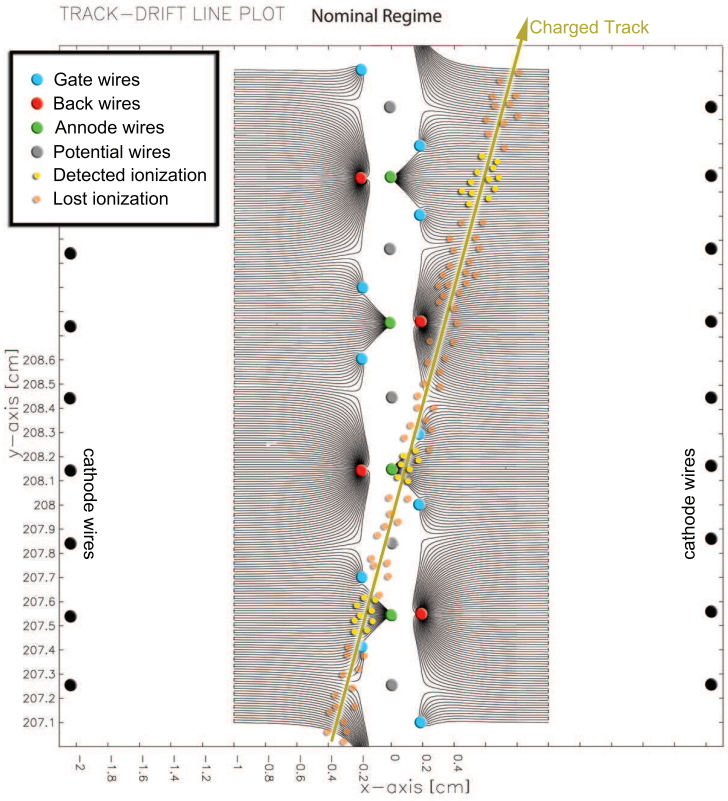

Figure 4.10: A calculation of drift lines as well as a schematic view of ionization collection from a charged track. This particular track, for example, would yield three signal points at approximately (-0.2, 207.5), (0.1, 208.2), and (0.6, 209.3).

grass in the Hough Space. A similar procedure is used in PHENIX for the DC track reconstruction (where (α, ϕ) from Figure 4.12 are used instead of (slope, y-intercept)) and results in $> 99\%$ efficiency for a given track. The resolution in the DC is very close to the design specification: $\sim 165\ \mu m$.

Additional refinement is performed by removing any background or "ghost" tracks in a two-step process. Once the Hough Transform seeds track candidates, each hit is individually evaluated to determine which track it belongs to by calculating a weight based on its closeness to the straight track line. Each hit is then associated to the closest track and subsequently removed from consideration of all other tracks. A track must have a minimum of 8 total hits (from layers X1 and X2) to be considered. The procedure is first preformed for X layers and then for the U and V layers before the reconstruction continues

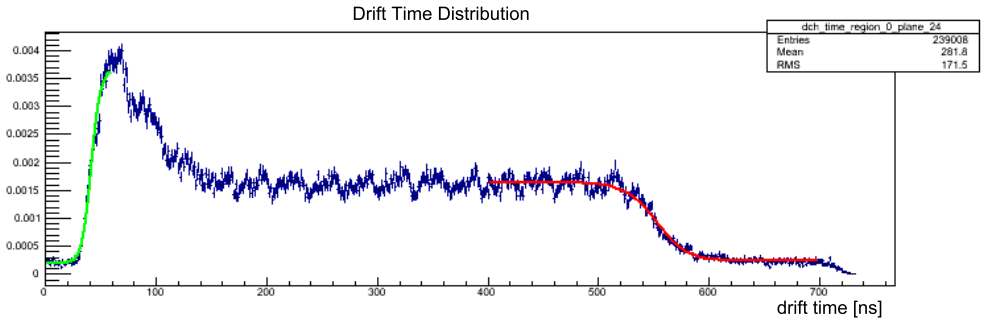

Figure 4.11: A typical drift time spectrum from the DC. The green fit marks the t_0 and the red fit marks the t_{max}.

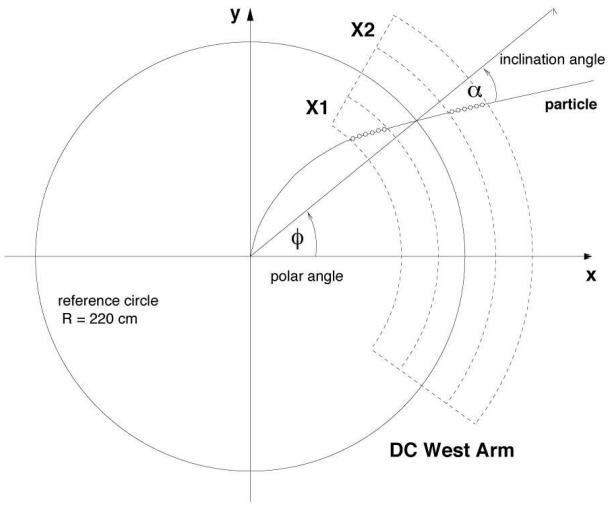

Figure 4.12: Definition of the ϕ and α coordinates outputted by the Hough transformation of the DC wire hit information.

by utilizing information from the Pad Chambers.

4.4.3 Pad Chambers

The Pad Chambers [20] (PC1, PC2, PC3) consist of 3 independent layers of multiwire proportional chambers. Each layer consists of a single wire plane bounded on both sides by a cathode plane; the inner cathode is solid while the outer is finely segmented into an array of pixels (Figure 4.14). Three pixels

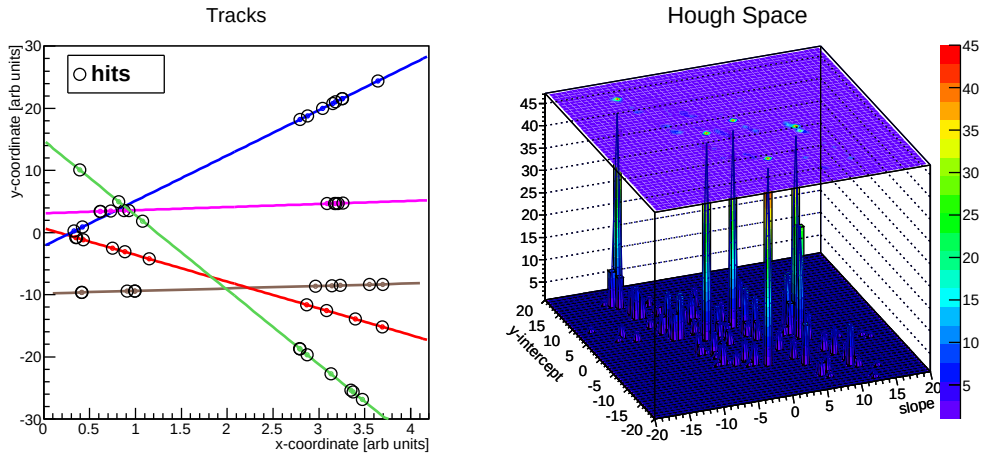

Figure 4.13: A toy monte carlo of a combinatorial Hough Transform. Every combinatorial pair of points in the left panel corresponds to an entry in the right panel. This method converges on all tracks with better than 99% efficiency.

define a *cell* in the PC and, to avoid false positive signals, all three pixels in a cell must fire to constitute a hit. The pad geometry is shown in Figure 4.15.

The locations of the three layers is shown in Figure 4.3; The PC1 layer sits immediately on the back side of the Drift Chamber, PC3 sits immediately in front of the Electromagnetic Calorimeter, and the PC2 is located behind the Ring Imaging Cherenkov Detector (although PC2 is only in the west arm).

In order to reduce the the number of (costly) readout channels, the interleaved pixels are chained together in 9x9 blocks and read out in one channel. However, the three pixels that constitute a particular cell are always in separate (but neighboring) channels, thereby making each cell has its own unique channel triplet. This reduces the readout channels by a factor of 9 while still maintaining position resolution of 1.7 mm in $\hat{z}$ and 2.5 mm in $\hat{x}$ and $\hat{y}$.

The Pad Chambers are the only non-projective detectors in the central arms. The PC1 layer (when matched to the DC track) is crucial in pinning down the track's $\hat{z}$ coordinate at the exit window of the Drift Chamber. Meanwhile, matching a track to the PC3 (in both ϕ and z) helps to suppress background in the Electromagnetic Calorimeter (EMCal). Approximately 30% of the particles in the EMCal are secondary particles produced by multiple scattering or decay products and low momentum tracks that miss the DC but still get bent into the EMCal. Matching the PC3 to a central

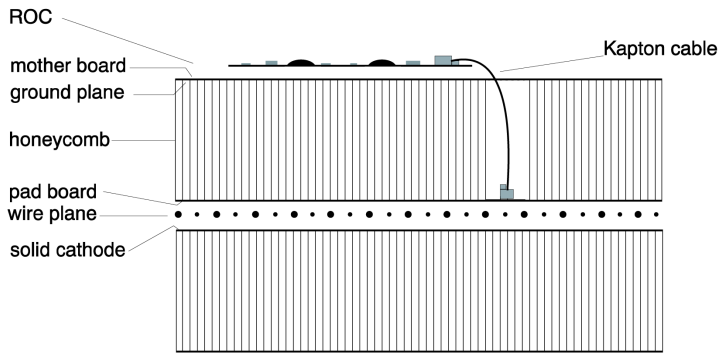

Figure 4.14: A vertical cut through a chamber view of the PC.

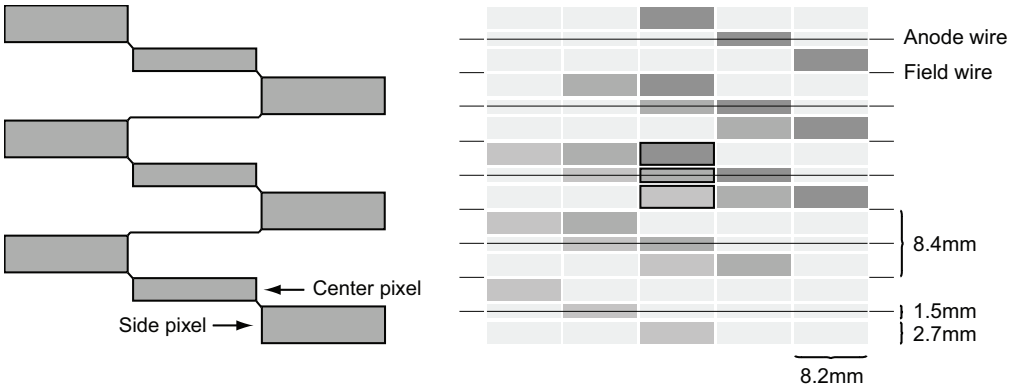

Figure 4.15: Left: The pad and pixel geometry for the PC. Right: Interleaved pad layout; a 3 pixel cell is at the center.

arm track (in the DC and PC1) results in a tracking efficiency of $\sim 98\%$, independant of p_T. The overall momentum resolution for the 2008 d+Au run is $\delta p/p = 0.011 \oplus 0.0116p$, where p is in GeV/c.

4.4.4 Ring Imaging Cherenkov Detectors

There is a Ring Imaging Cherenkov Counter (RICH) [21] in each of the central arms located immediately behind the PC1 (see Figure 4.3). The RICH is primarily a particle ID detector that distinguishes electrons from hadrons. It operates by measuring the Cherenkov radiation that is emitted by a particle traveling faster than the speed of light inside some medium. This optical boom (analog to a sonic boom) is an conical shaped electromagnetic shock

wave emitted at θ_C with respect to the trajectory of the particle:

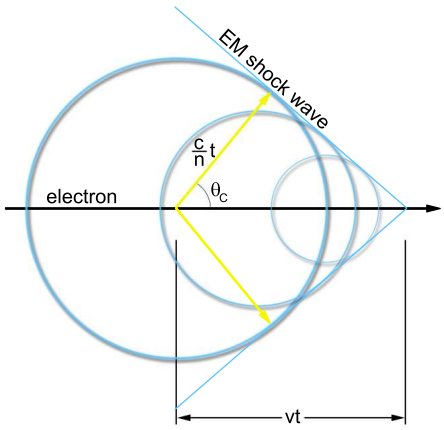

$$\cos\theta_C = \frac{1}{\beta\, n} = \frac{\sqrt{\frac{m^2}{\vec{p}^2} + 1}}{n} \quad (4.6)$$

Figure 4.16: Cherenkov radiation.

where n is the index of refraction of the medium being traversed. When $\cos\theta_C \leq 1$, θ_C becomes real and the particle emits Cherenkov radiation. Since $\cos\theta_C$ is a strong function of mass, the Cherenkov momentum threshold is much lower for electrons than other heavier particles. Figure 4.17 shows the thresholds for the lightest particles. Electrons begin to radiate at $p = 18\ MeV/c$ while pions don't start to emit Cherenkov light until $p = 4.65\ GeV/c$. The RICH has a hadron rejection of $\sim 10^4$ when the particles momentum is below the pion threshold.

Each detector has an 8.9 m^2 entrance window, a 21.6 m^2 exit window, and a volume of 40 m^3. Inside the detector are 48 mirror panels composing a 20 m^2 reflecting area in two intersecting spherical surfaces. A schematic view of the detector is shown in Figure 4.18.

The RICH uses CO_2 as the radiator gas, which has a refractive index of $n = 1.00045$. This corresponds to a velocity threshold of $\beta = 0.99590168$. Cherenkov radiation produced in the detector volume is focused by the mirrors onto an array of PMTs located on either side of the entrance window. Assuming a velocity of $\beta \approx 1$, a radiating charged particle emits photons which are focused into a ring with an asymptotic diameter of approximately 11.8 cm. A typical relativistic electron produces an average of 11 photo-electrons. Figure 4.19 shows the approximate size of the expected RICH ring, search radius, and PMT size.

There are various variables that are reconstructed by the RICH the most useful of which being n_0 (defined in Section 5.4.1). For reference, the additional "n" variables are shown in Figure 4.20.

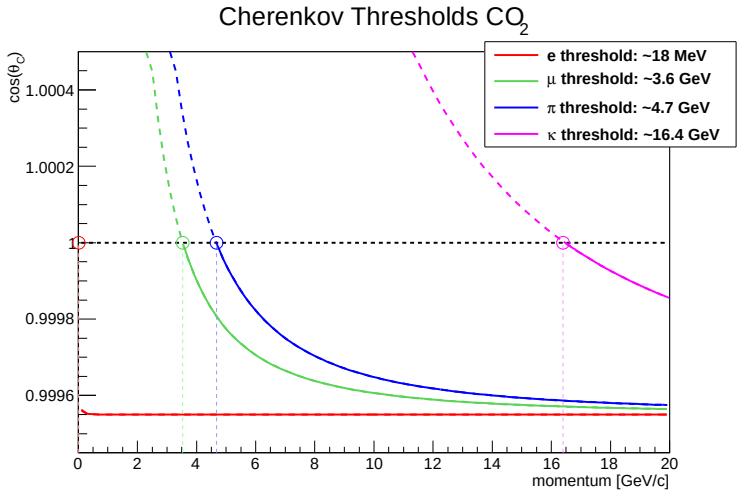

Figure 4.17: Cherenkov thresholds for various particles in the RICH. When $\cos\theta_C \leq 1$ the particle emits radiation.

4.4.5 Electromagnetic Calorimeter

PHENIX has a high resolution electromagnetic calorimeter (EMCal) which was designed to measure the energies and spacial positions of photons and electrons. The EMCal is the outermost detector in the central arms and consists of 8 sectors (4 in each arm) segmented in ϕ. Six of the sectors are made of lead scintillator (PbSc) while the two lowermost sectors in the east arm are lead glass (PbGl), with an energy resolution of $\sigma_E/E = 8.1\%/\sqrt{E} \oplus 2.1\%$ and $5.9\%/\sqrt{E} \oplus 0.8\%$ respectively.

The PbSc is a shashlik type sampling calorimeter comprised of alternating tiles of Pb and scintillator. Each of the 6 sectors consists of 18 supermodules; each supermodule contains 36 modules; each module is made of 4 5x5 cm^2 towers; each tower has 66 sampling tiles (yes, that is over 1M tiles in the PbSc!). Within a tower the sampling cells are optically ganged together by 36 longitudinally penetrating wavelength shifting fibers which collect the light for detection by a phototube, resulting in a single readout for each tower. See Figure 4.21 for the schematic layout of a PbSc module. A cell is 5.6 mm thick (0.277 X_0) and the active depth of a tower is 37.5 cm leading to an overall radiation length of 18 X_0. The timing resolution for the PbSc is ~150 ps for electromagnetic showers and ~400 ps for hadronic showers. The time of flight capabilities allow PHENIX to also identify low momentum pions and protons using the PbSc. The nuclear interaction length of the PbSc is 0.85 X_0.

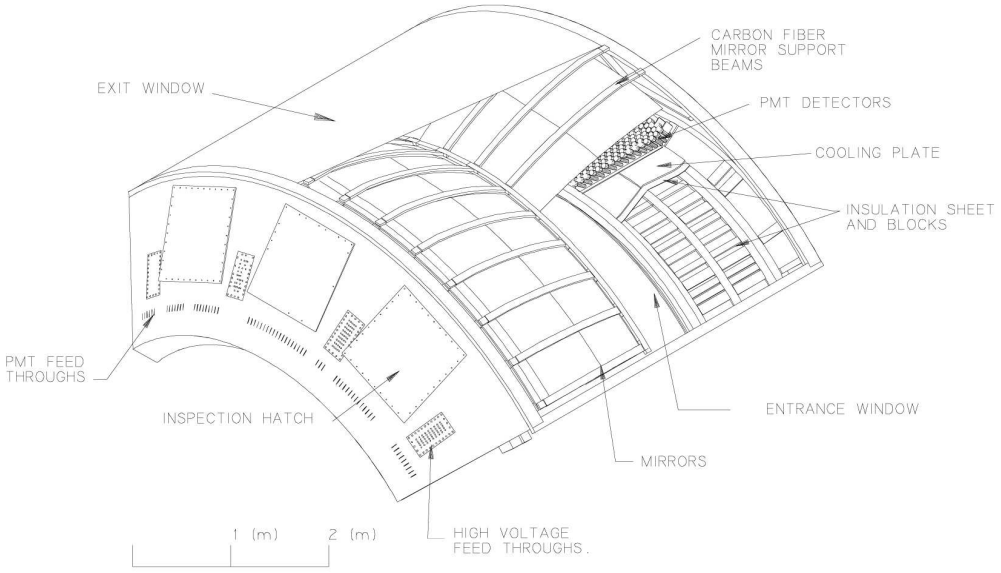

Figure 4.18: A cutaway view of a RICH chamber.

The PbGl is a Cerenkov detector and, therefore, not used for hadron identification. While the timing resolution is worse than the PbSc ($\sim$300 ps) the granularity and energy resolution are better. Each PbGl sector is consists of 192 supermodules and each supermodule contains 24 4x4 cm^2 modules in a 6x4 array, as illustrated in Fig. 4.22. The modules are held together by carbon fiber and epoxy resin and the signal is read out by photo-multipliers at the base of each module, housed behind 0.5 mm steel panes. There is a built in LED calibration and gain monitoring system at the front end of each supermodule. The modules are 40 cm deep (14.4 X_0).

PHENIX uses two different type of calorimeters on purpose. The PbSc and PbGl have different advantages/disadvantages and the systematic uncertainty associated with each is different. By using each calorimeter as a cross-check for the other, PHENIX has the ability to reduce the overall systematic uncertainty in the calorimetry measurements.

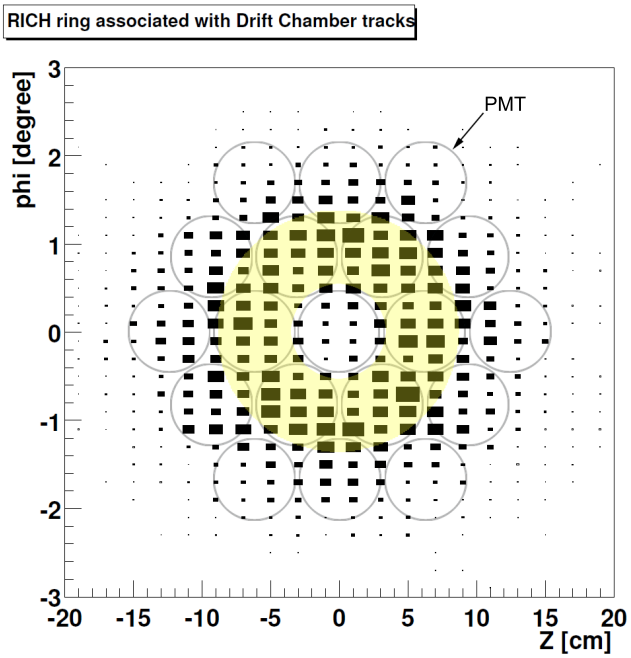

Figure 4.19: Contour plot of RICH hits relative to the projected ring centroid from tracking, summed over many tracks. PMTs are superimposed in gray as well as the search region that is used for the reconstructed RICH variable, $n0$ (See Section 5.4.1) in yellow.

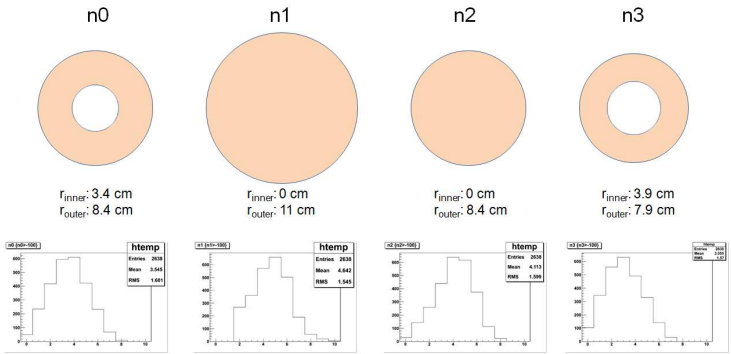

Figure 4.20: The "n" variables from the RICH subsystem. The shaded area corresponds to the search region for PMT hits for the various variables.

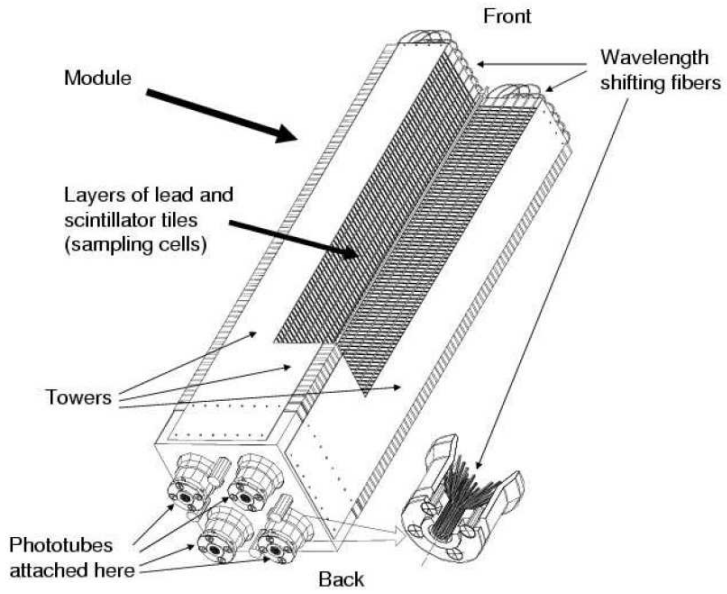

Figure 4.21: PbSc module.

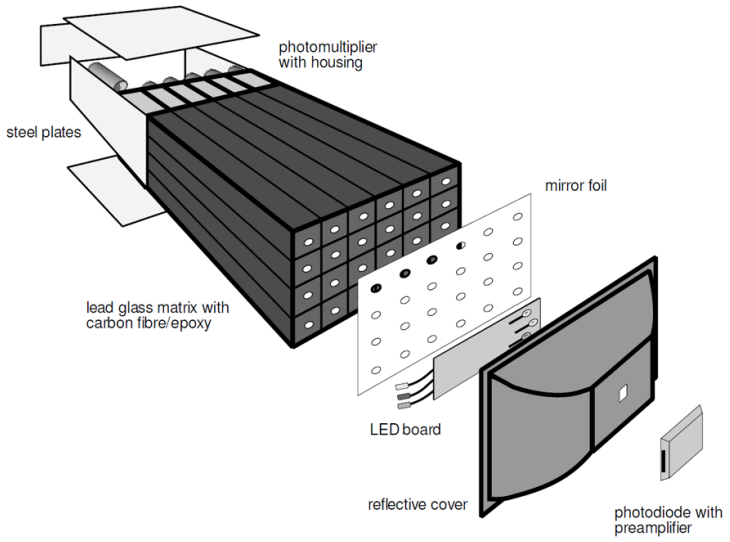

Figure 4.22: PbGl supermodule.

Part III

Data Analysis

CHAPTER 5

Analysis Fundamentals

When you have a hammer,
everything looks like a nail.

Abraham Maslow

5.1 Towards Mass Spectra...

The ultimate goal of this analysis is to study the invariant mass and p_T spectra of e^+e^- pairs in $d + Au$ collisions calculated as

$$\begin{aligned} m_{ee}^2 &= (\mathbf{P}_+ + \mathbf{P}_-)^{\mathbf{2}} \\ &= (E_+ + E_-)^2 - (\vec{p}_+ + \vec{p}_-)^2 \qquad (5.1) \\ p_T^2 &= (p_{x,+} + p_{x,-})^2 + (p_{y,+} + p_{y,-})^2 \qquad (5.2) \end{aligned}$$

where $E_\pm = \sqrt{\vec{p}_\pm^2 + m_e^2}$, $m_e = 511$ keV$/c^2$, and the 3-momentum vector $\vec{p}_\pm$ and measured with the drift chamber.

This is a challenging task since, within an event, the source of any electron or positron is unknown. Therefore, the strategy employed is to create all combinations of e^+e^- pairs in an event to create a *foreground* invariant mass spectrum, which contains all of the "signal" pairs as well as an abundance of combinatorial background pairs. The combinatorial background is then estimated and statistically subtracted from the foreground. There are additional

sources of correlated pairs that are uninteresting and must also be removed from the spectrum via a combination of cuts (both at the single electron level and at the pair level) and statistical subtraction.

Described in Part II, PHENIX's limited acceptance compounds the difficulty of the measurement by reducing the acceptance for e^+e^- pairs even further than for single particles. Frequently, one of the daughters escapes the detector acceptance leaving its mate alone to be mis-paired with other electrons thereby only contributing to the combinatorial background but not to the signal! The signal-to-background (S/B) ratio is worse in higher multiplicity environments and is shown as a function of mass for $p + p$, $d + Au$, and peripheral $Au + Au$ in Figure 5.1.

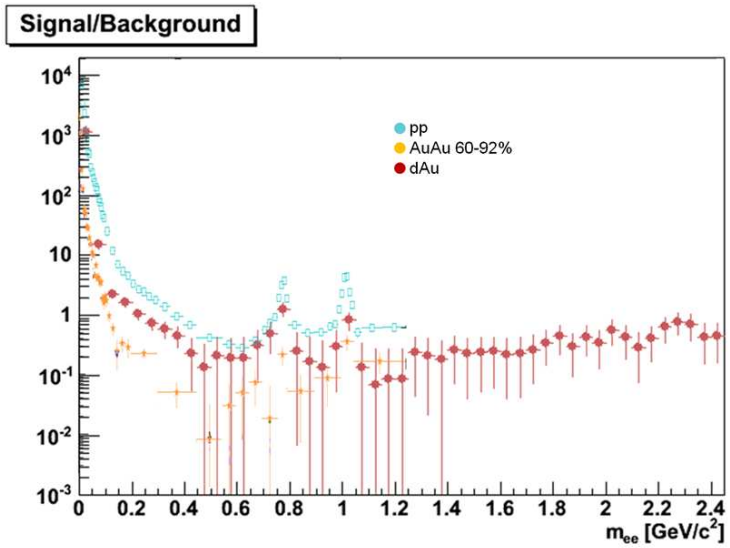

Figure 5.1: The estimated signal-to-background ratio for p+p, d+Au, and peripheral Au+Au.

When considering dielectron pair spectra, we have more at our disposal than simply e^+e^- pairs. There are also like-sign pairs (e^+e^+, e^-e^-) as well as mixed event pairs (Sections 6.3, 6.1). All of these distributions contribute to estimating the background that must be subtracted from the foreground.

The analysis roughly consists of the following steps:

- **Quality Assurance (QA)** - Sections 5.2, 5.2.1, 5.2.2
  Determine which events are acceptable for use in the analysis.
  Determine fiducial detector acceptance.

- **Single Electron Selection** - Section 5.4
  Select tracks for electron candidates.
- **Dielectron Pair Selection** - Section 5.5
  Select pairs for signal candidates.
- **Background Estimation/Subtraction** - Chapter 6
  Estimate combinatorial background and statistically subtract it.
  Estimate correlated background and statistically subtract it.
- **Efficiency Corrections** - Chapter 7
  Calculate efficiency of detector dead area and reconstruction algorithm.
  Measure high energy electron trigger efficiency.
- **Systematic Uncertainty** - Section 7.4
  Estimate all systematic uncertainty.
- **EXODUS Cocktail** - Chapter 8
  Use Monte Carlo techniques to predict spectrum of known sources to compare to data.

In this thesis, the following nomenclature is used:

FG12	**F**ore**G**round Type**1**Type**2**	same event e^+e^-
FG11	**F**ore**G**round Type**1**Type**1**	same event e^-e^-
FG22	**F**ore**G**round Type**2**Type**2**	same event e^+e^+
BG12	**B**ack**G**round Type**1**Type**2**	mixed event e^+e^-
BG11	**B**ack**G**round Type**1**Type**1**	mixed event e^-e^-
BG22	**B**ack**G**round Type**2**Type**2**	mixed event e^+e^+

Table 5.1: Shorthand nomenclature for like-sign/unlike-sign and real/mixed events.

5.2 Run Selection

> It is not down on any map; true places never are.
>
> Herman Melville
> *Moby Dick*

In this analysis, data from the 2008 RHIC run (Run8) d+Au $\sqrt{s_{NN}} = 200\ GeV$ were analyzed. The data were recorded with both a Minimum Bias (MinBias) trigger and with an electron (ERT_E) trigger (see Section 7.2). There were two different ERT_E energy thresholds used, nominally 600 MeV and 800 MeV. In total, 3.1B triggered events were analyzed corresponding to 116.6B MinBias-equivalent events. The breakdown of events in this analysis are shown in Table 5.2.

RunGroup	analyzed ERT evts	eq. sampled MB evts	ERT_E threshold	B-Field
A1	267M , 431M	6.6B , 9.7B	600 MeV	++
A2	448M , 658M	11.1B , 16.3B	600 MeV	++
B	564M , 814M	12.4B , 17.9B	600 MeV	++
C1	523M , 757M	31.5B , 45.6B	800 MeV	- -
C2	304M , 444M	18.3B , 26.7B	800 MeV	- -
MinBias	NA	1.17B , 1.67B	NA	both

Table 5.2: Number of events in each run group after QA. The first listing is for $|z_{vtx}| < 17$ and the second is for $|z_{vtx}| < 30$.

5.2.1 Quality Assurance

It is vitally important to control the detector acceptance, dead areas, and instabilities as tightly as possible to reduce systematic uncertainties due to detector edge effects and "gray" areas in the acceptance. To this end, 2D maps of the DC readout board number vs α (as defined in Figure 4.12) are scanned for dead areas and regions where the detector may not be operating at full efficiency (gray areas). These problematic regions are then cut out by geometric cuts in this space. These are called *fiducial cuts* and are applied *a priori* to the dataset before any other analysis is performed. There is a set of fiducial cuts for every run group (see Section 5.2.2).

The DC board number is related derived from the azimuthal angle of the track and creates a more orthogonal space reflecting the hardware coordinates to examine detector inefficiencies, dead areas, and noisy regions. An example of these maps before and after fiducial cuts is shown in Figure 5.2.

In addition, a fiducial cut is applied which corresponds to the convolution of the acceptance of the DC, RICH, and EMCal as a function of particle charge, transverse momentum, and the azimuthal trajectory of the particle at the collision vertex. This space (shown in Figure 5.3) is a convenient way to visualize the central arm acceptance since charged particles are deflected azimuthally by the magnetic field. For this reason, a single track's acceptance (represented by diagonal boundaries in this space) is defined by a given detector's edge in ϕ as well as its radius from the interaction point.

The acceptance for a track with charge q, transverse momentum p_T and azimuthal emission angle ϕ_0 can be described by the logical AND of these conditions:

$$\begin{aligned} \phi_{\min} \leq \phi + q\frac{k_{\mathrm{DC}}}{p_T} \leq \phi_{\max} \\ \phi_{\min} \leq \phi + q\frac{k_{\mathrm{RICH}}}{p_T} \leq \phi_{\max} \end{aligned} \tag{5.3}$$

where k_{DC} and k_{RICH} represent the effective azimuthal bend to DC and RICH ($k_{\mathrm{DC}} = 0.206$ rad $\cdot$ GeV/c and $k_{\mathrm{RICH}} = 0.309$ rad $\cdot$ GeV/c). One arm covers the region from $\phi_{\min} = \frac{-3}{16}\pi$ to $\phi_{\max} = \frac{5}{16}\pi$, the other arm from $\phi_{\min} = \frac{11}{16}\pi$ to $\phi_{\max} = \frac{19}{16}\pi$. This is also the definition used in the both the reconstruction efficiency (Section 7.1) and in the hadronic cocktail Monte Carlo (Section 8.1).

5.2.2 Run Groups

To identify and evaluate which runs had similar conditions (in both detector dead area and trigger live area), the figure of merit used was number of electrons per event. This was examined in both MinBias triggered events and for ERT_E triggered events. Specifically, for MinBias events, tracks were counted that passed both the eID and quality cuts listed in Table 5.4 in a given run and then divided by the number of events (Equation 5.4).

$$\frac{N_e}{N_{evt}^{MB}} \tag{5.4}$$

$$\frac{N_e^{trig}(1 < p_T < 4\ GeV/c)}{N_{evt}^{MB}} \tag{5.5}$$

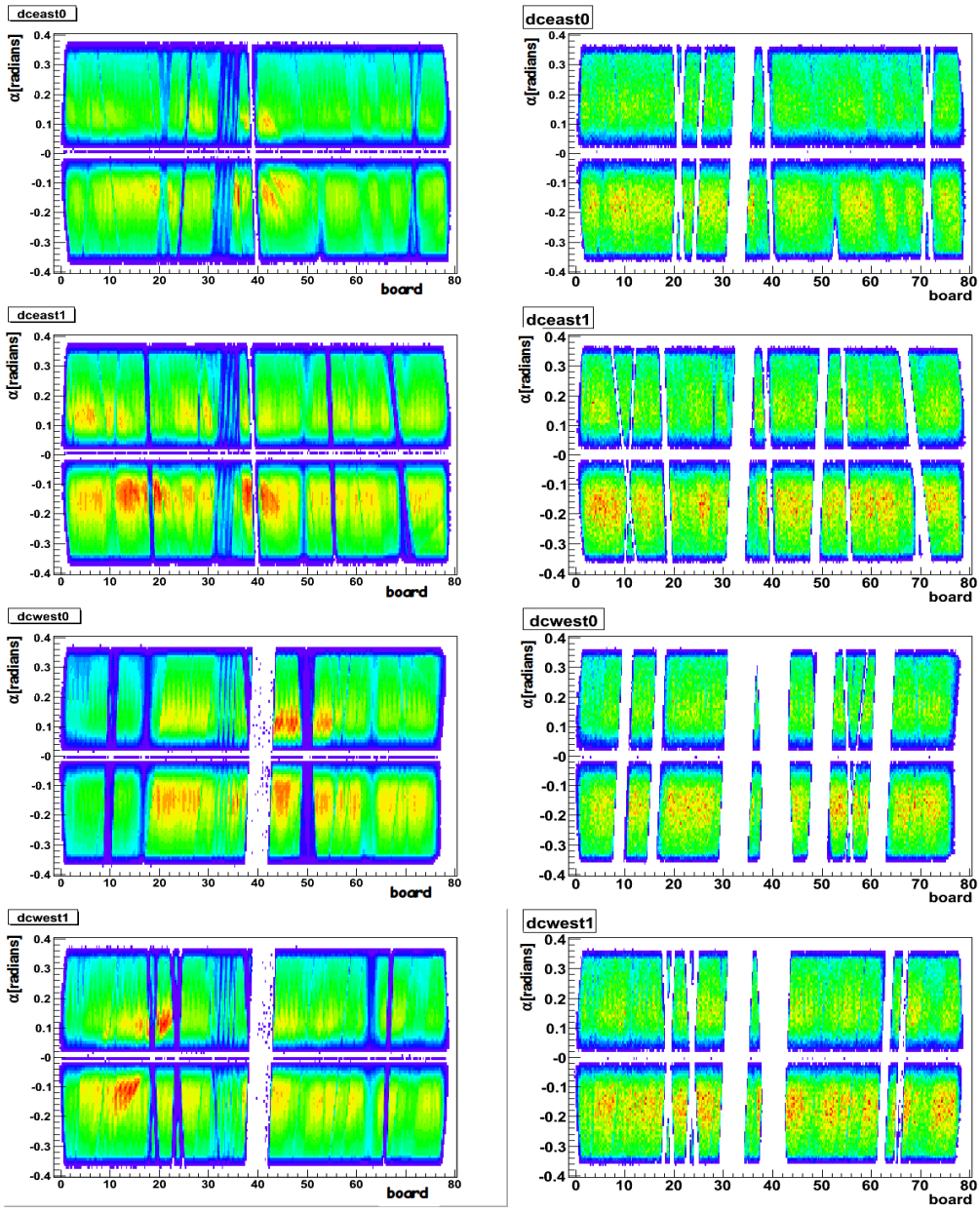

Figure 5.2: Alpha vs board distribution for DC/PC1 quality assurance studies before (left) and after (right) fiducial cuts. The south (0) and north (1) sectors of the east and west DC are shown separately.

This quantity (for MinBias electrons) highlights any dead areas in the detector and is plotted as a function of run number in Figure 5.4. There are

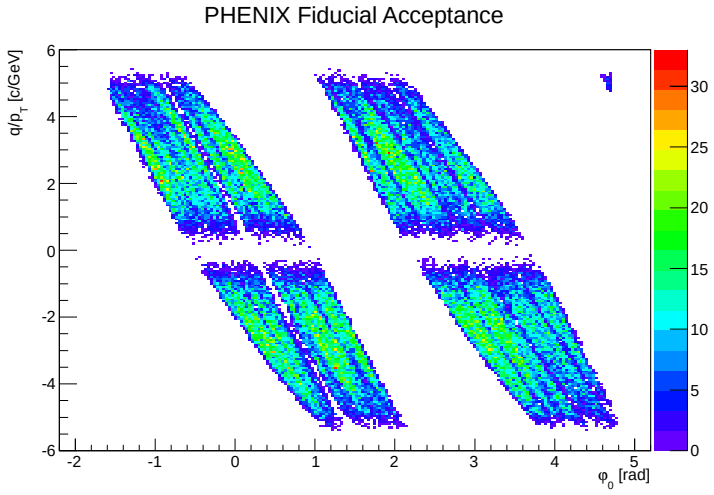

Figure 5.3: The central arm acceptance for electrons at PHENIX.

two distinct drops in N_e/N_{evt}^{MB} forming three regions in this diagnostic. The first drop corresponds to a large portion of the PC1 failing near run number 248800. The track hit-maps for run groups A1 and A2 are plotted in Figure 5.5, showing the region of the PC1 that failed midway through Run8.

Additionally, starting with run 252969, there was a stripe in the EMCal sector 6 (East arm sector 2, depending on the numbering scheme) that failed for the remainder of the Run8. This trouble area is shown in Figure 5.6. To account for these detector degradations, the data must be treated independently for each duration and separate reconstruction efficiencies must be calculated and applied to each.

To explore the continuity of the ERT_E trigger live area over the course of Run8, N_e^{trig}/N_{evt}^{MB} (Figure 5.4) is also studied as a function of run number (the ERT_E trigger is discussed in detail in Section 7.2). This quantity is a convolution of the aforementioned detector dead areas (PC1, EMCal E2) and the trigger live area. The trigger threshold was increased from 600 MeV to 800 MeV near run number 250500, creating a natural run division there. In addition, during the first half of the run (600 MeV threshold), the trigger electronics were unreliable in the west arm of the RICH for half of the supermodules mapping to EMCal sector 1. Figure 5.7 shows the trigger efficiency in the RICH as a function of p_T for half of these supermodules (the rest of W1 looks similar). This created a bimodal behavior in N_e^{trig}/N_{evt}^{MB} which is illustrated in the y-axis projection of this region (Figure 5.4). Therefore, run group A is additionally split according to whether the RICH was reliable or

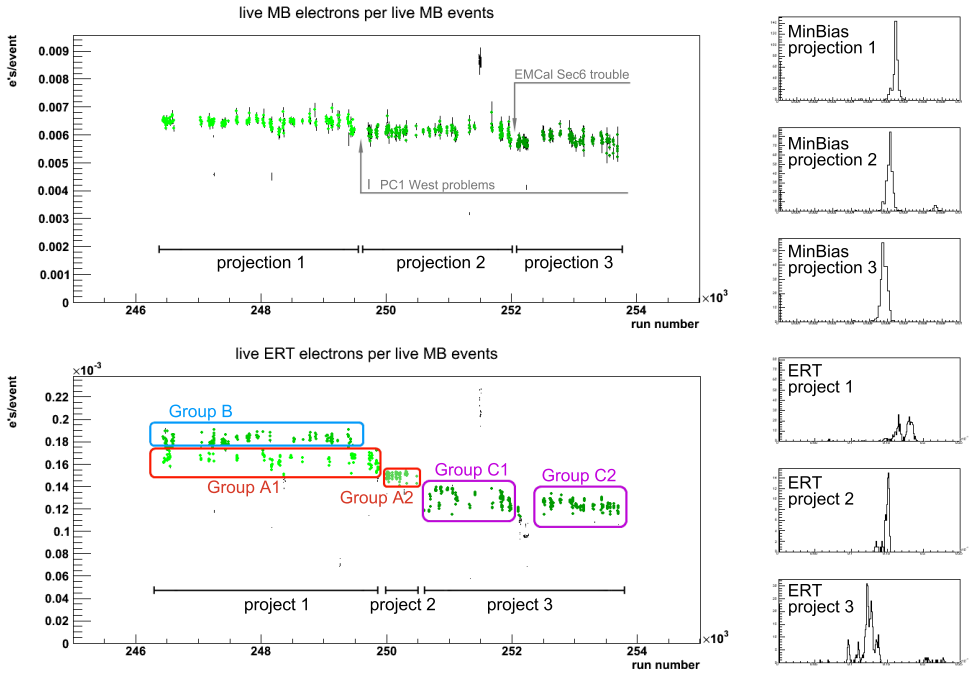

Figure 5.4: Upper panel: MinBias electrons per MinBias event. Lower panel: ERT triggered electrons per MinBias event. Final run groups are denoted in the lower panel. Y-axis projections for different sets of run numbers are in the right-hand panels.

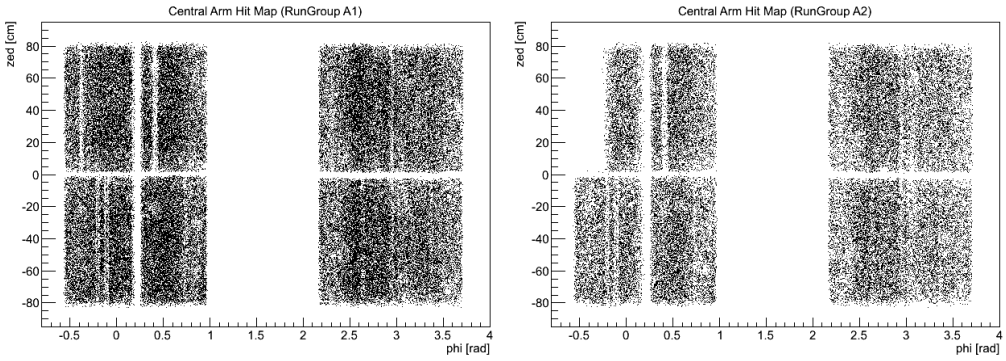

Figure 5.5: zed vs ϕ distributions highlighting the degradation of the PC1 between run groups A1 (left) and A2 (right). The chunk around $\phi \approx -0.25$ and positive zed can be seen to disappear in group A2.

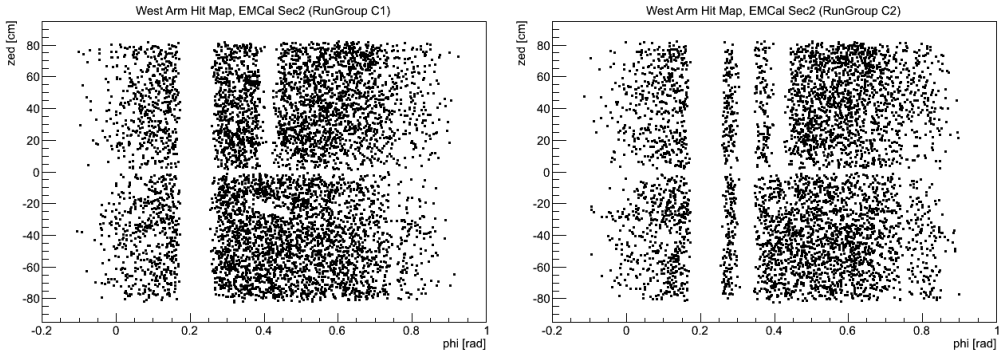

Figure 5.6: zed vs ϕ distributions highlighting the degradation of the EMCal between run groups C1 (left) and C2 (right). The stripe at $\phi \approx 0.325$ highlights the difference between group C2 and the rest of the run.

not for a given run. The final run groups are shown in Figure 5.4.

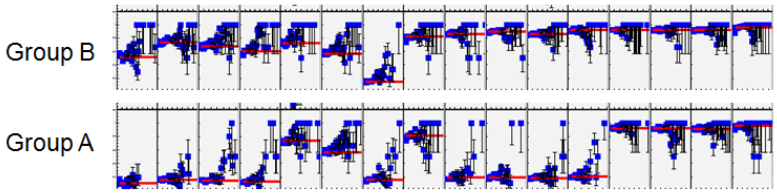

Figure 5.7: The trigger efficiency of the RICH as a function of p_T for supermodules in sector W1 during the 600 MeV threshold Run Groups. This highlights the difference between Groups A1&A2 and Group B.

5.3 Event Topology

> Look here, friend, if you have anything important to tell us, out with it; but if you are only trying to bamboozle us, you are mistaken in your game; that is all I have to say.
>
> Ishmael
> *Moby Dick*

5.3.1 Minimum Bias Trigger

The Minimum Bias (MinBias) trigger in PHENIX is based on at least 1 phototube firing in the BBC as well as the collision vertex being within ± 38 cm:

$$MB \equiv (BBC \geq 1) \cap (|z_{vertex}| < 38\ cm) \tag{5.6}$$

Unfortunately, this condition introduces a bias that depends on the multiplicity of the event. For p+p collisions, the BBC cross section was measured to be $\sigma_{BBC}^{p+p} = 23.0 \pm 2.2$ mb via the Van Der Meer scan technique [55]. This corresponds to 54.5 ± 6% of the total inelastic p+p cross-section at $\sqrt{s_{NN}} = 200\ GeV$ ($\sigma_{inel}^{p+p} = 42 \pm 3$ mb).

In $d+Au$ collisions, using photodissociation of the deuteron as a reference [56], the measured cross-section is $\sigma_{BBC}^{d+Au} = 1.99 \pm 0.10$ b [57] corresponding to 88.5 ± 4% of the total $d+Au$ inelastic cross-section, $\sigma_{inel}^{d+Au} = 2.26 \pm 0.1$ b.

The MinBias trigger is more likely to fire on events that contain a hard scattering due to the higher multiplicity in such events. Similarly, soft partonic scattering or single/double diffractive scattering have a lower probability to generate a trigger in the BBC. Therefore, the BBC MinBias trigger will bias the recorded sample to have a higher fraction of hard scattering events than would be recorded from the inclusive BBC trigger cross section. This bias was measured by using a random clock trigger, supplied by RHIC, which fires every time there is a bunch crossing. Upon the clock trigger firing, PHENIX looks in the central arms for any charged hadrons and can thereby determine the BBC trigger bias.

In $p+p$ events, the BBC fires on 79 ± 2 % of the events and for $d+Au$, it fires on 99 ± 2 % (independent of p_T). When calculating the invariant yield of particles, the measured yield must be corrected for the fraction of events missed by the MinBias trigger as well as the trigger bias. This correction factor is 0.545/0.79 for $p+p$ collisions and 0.88/0.99 for minimum bias $d+Au$ collisions.

5.3.2 Centrality

One of the most important global parameters used to classify the initial collision geometry in a nuclear collision is the *centrality*. The centrality is a measure of the impact parameter, b, which is the distance between the centers of the colliding nuclei. Centrality is reported as a percentile from 0 - 100%, with 0% unintuitively being the most central (think *"0% of all collisions are*

more central than this one"). Figure 5.8 shows a schematic picture of colliding nuclei illustrating different centralities.

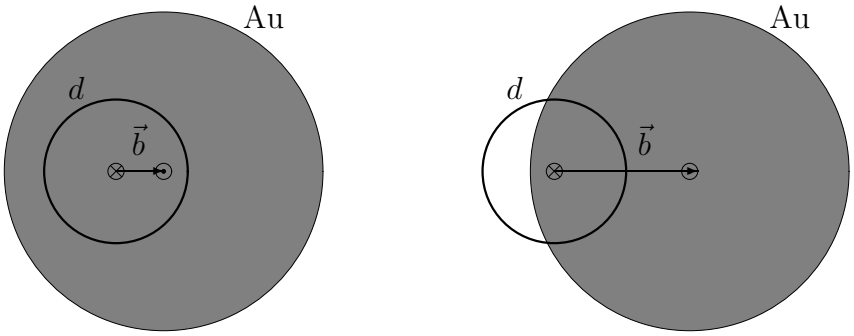

Figure 5.8: Overlap of two gold nuclei for different impact parameters $\vec{b}$.

Since nuclei at 100 GeV/nucleon are relativistically compressed by a factor of ∼100 in the direction of the beamline, they are akin to two pancakes colliding head-on. The centrality determines (with some probability) the impact parameter and consequently the geometric nuclear overlap of the collision. The typical "size" of the deuteron can be inferred from Figure 5.9 which shows the probability of the distance between the proton and neutron.

PHENIX determines the centrality of the collision by measuring the charge collected in the BBCs (see Figure 5.10. For d+Au collisions, only the BBC south (Au-going side) detector is considered. This method assumes that the BBC signal is proportional to the number of participating nucleons in the Au nucleus, N_{part}^{Au}, and that the hits in the BBC are uncorrelated from one another. The distribution of the mean number of binary collisions, N_{coll}, as well as N_{part} are calculated through a Monte Carlo simulation of the Glauber model [28].

The Glauber model, based on a geometric picture of a heavy ion collision, assumes that the nucleons travel with straight-line trajectories. A binary nucleon-nucleon collision is predicted if the transverse distance between two nucleons is less than $\sqrt{\sigma_{NN}/\pi}$ where the inelastic nucleon-nucleon cross-section is $\sigma_{NN} = 42mb$ measured in p+p collisions at $\sqrt{s_{NN}} = 200GeV$. Figure 5.11 shows the impact parameter distributions for different centralities determined by Glauber simulations.

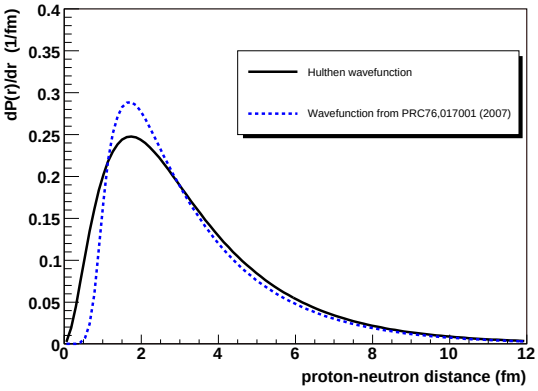

Figure 5.9: Probability distribution for the proton – neutron distance in the deuteron from the Hulthén wavefunction and the dispersion approach from [51].

Traditionally in PHENIX simulations, the deuteron nucleus is modeled using the wave function derived by Hulthen [27]

$$\phi_d(\mathbf{r}_{pn}) = \left(\frac{\alpha\beta(\alpha+\beta)}{2\pi(\alpha-\beta)^2}\right)^{\frac{1}{2}} \frac{(e^{-\alpha\mathbf{r}_{pn}} - e^{-\beta\mathbf{r}_{pn}})}{\mathbf{r}_{pn}}, \tag{5.7}$$

where $\alpha = 0.228\ fm^{-1}$; $\beta = 1.18\ fm^{-1}$; and $\mathbf{r}_{pn}$ refers to the separation between the proton and the neutron. The Au nucleus is modeled using a Woods-Saxon density distribution

$$\rho(r) = \frac{1}{1 + e^{\left(\frac{r-c}{a}\right)}}, \tag{5.8}$$

where the diffuseness parameter a = 0.54 fm, c is the nuclear radius = $1.12A^{1/3}$ - $0.86A^{-1/3} = 6.38\ fm$.

However for the 2008 PHENIX dataset, instead of using the Hulthén description, the Glauber Monte Carlo calculations were updated with a deuteron description based on a dispersion potential-less inverse scattering approach [51]. The S state wave function (the D state probability is only 6.2%) is:

$$u(r_{pn}) = \sum_{j=1}^{16} C_j e^{-m_j r_{pn}},\ m_j = \alpha + m_0(j-1)^1 \tag{5.9}$$

[1]Coefficients C_j and parameters α and m_0 are in [51]

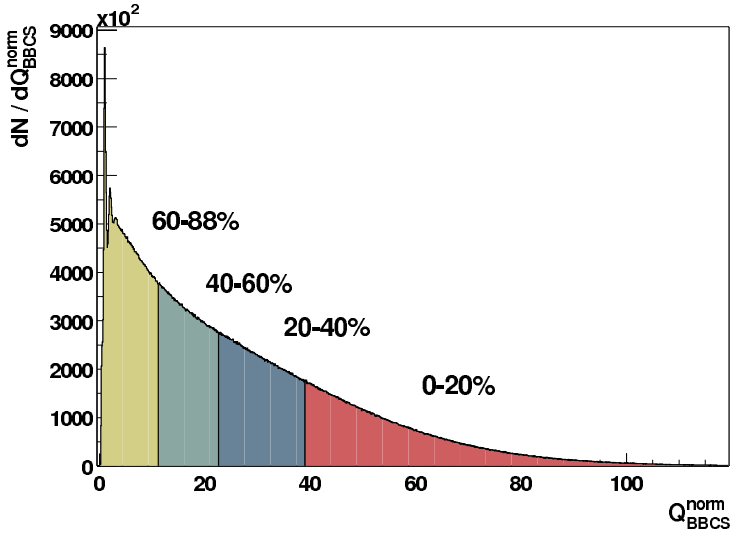

Figure 5.10: Distribution of the "normalized" charge deposited in the BBC south. The normalization is done such that Q^{norm}_{BBCS} corresponds to the number of hits in the detector.

Figure 5.9 shows the comparison of the probability distribution for the proton – neutron distance calculated via the traditional Hulthén wave function compared the dispersion approach of Equation 5.9 taken from [52]. The use of the more modern description in the Glauber Monte Carlo calculations has little effect on the extracted collision parameters. These parameters, N_{coll}, N_{part} (the number of participating nucleons), and C_{BBC} (the correction factor to the yield) are shown for both the Hulthén description and the dispersion approach in Table 5.3.[2]

C_{BBC} corrects the yield for two competing effects: the BBC trigger bias and the centrality bin shift.

The distributions of the number of binary nucleon-nucleon collisions, N_{coll} from the Glauber simulations are shown for different centrality classes in Figure 5.11. The average N_{coll} is labeled in the legend as well as summarized in Table 5.3.

[2] C^{Run3}_{BBC} is incorrect in [54], a mistake that is acknowledged in [53]. It is listed *correctly* in Table 5.3.

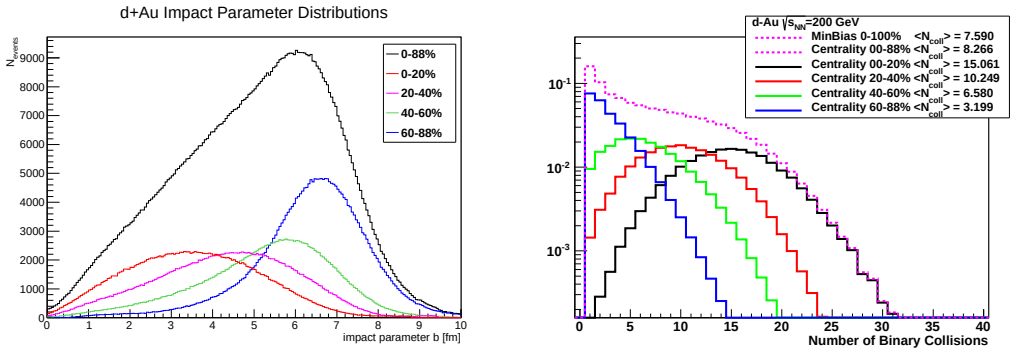

Figure 5.11: Impact parameter distributions for different centrality classes.[29]

Centrality	$\langle N_{coll} \rangle^{Run3}$	$\langle N_{coll} \rangle^{Run8}$	C_{BBC}^{Run3}	C_{BBC}^{Run8}	$\langle N_{part} \rangle^{Run8}$
00-20%	15.37 ± 1.0	15.1 ± 1.0	0.95 ± 0.029	0.941 ± 0.010	15.6 ± 0.9
20-40%	10.63 ± 0.7	10.3 ± 0.7	0.99 ± 0.007	1.000 ± 0.006	11.1 ± 0.6
40-60%	6.95 ± 0.6	6.6 ± 0.4	1.03 ± 0.009	1.034 ± 0.017	7.7 ± 0.4
60-88%	3.07 ± 0.3	3.2 ± 0.2	1.04 ± 0.027	1.031 ± 0.055	4.2 ± 0.3
00-88%	8.47 ± 0.7	8.29 ± 0.6	1.00 ± 0.02	1.00 ± 0.055	9.2 ± 0.5
0-100%	7.45 ± 0.6	7.30 ± 0.5	0.885 ± 0.02	0.883 ± 0.055	8.1 ± 0.4

Table 5.3: Comparison of the Run3 and Run 8 Glauber Monte Carlo derived quantities.

5.3.3 Collision Vertex

The collision vertex, the z coordinate of the event, is another global property of an interaction. It dictates the detector acceptance for tracks in the (conventional coordinate of) polar angle, θ. However, generally in particle physics, the preferred coordinate to represent this axis is the pseudorapidity, η, defined as

$$\eta = -\ln\left[\tan\frac{\theta}{2}\right] = \frac{1}{2}\ln\left[\frac{|\vec{p}| + p_L}{|\vec{p}| - p_L}\right], \tag{5.10}$$

which is a specialized representation of the rapidity, Y, when the particle's mass equals zero.

$$Y = \frac{1}{2}\ln\left[\frac{E + p_L}{E - p_L}\right] \tag{5.11}$$

The pseudorapidity (or rapidity) is used primarily because it is invariant under Lorentz transformations (actually, the distribution is offset by a con-

stant, however, the *shape* doesn't change). Another advantage to pseudorapidity is that most particle distributions are constant with respect to it (at mid-rapidity). The relationship between rapidity and polar angle θ is shown in Figure 5.12 for different masses. At mass equal to zero, the rapidity *is* the pseudorapidity.

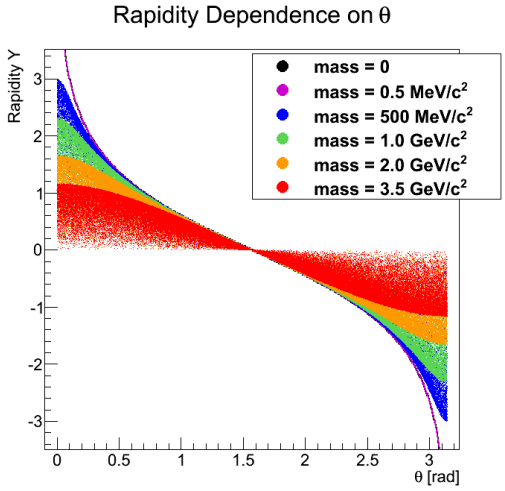

Figure 5.12: Rapidity as a function of polar angle θ for various mass values. The black line, mass=0, is identically the pseudorapidity line and electrons, represented by the purple distribution, are well approximated by the pseudorapidity.

PHENIX's acceptance in pseudorapidity changes depending on the z_{vertex} of the collision. The right panel of Figure 5.13 shows how a particle's phase space in η changes with the collisions vertex. The left panel shows the central arm acceptance in z_{vertex} vs η.

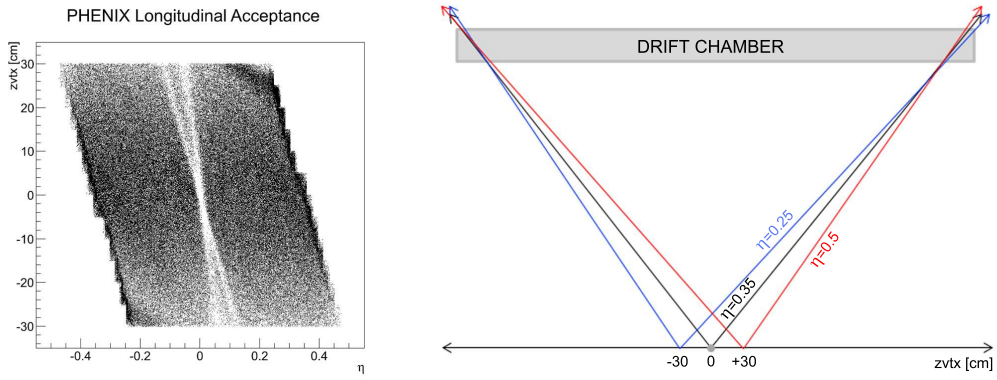

Figure 5.13: The longitudinal acceptance of the PHENIX central arms. Left panel: schematic diagram of a track's pseudorapidity originating from different z_{vertex}. Right panel: PHENIX's acceptance in z_{vertex} vs η.

5.4 Electron Cuts

5.4.1 Electron Identification

> Aren't you a little short for a Storm Trooper?
>
> Princess Leia

Table 5.4 summarizes the cuts relevant to this analysis. A description of each variable follows the table.

category	cut	purpose
event		
	$\lvert\mathbf{z_{vertex}}\rvert < 17.0$	control event geometry
single track		
	$\mathbf{ecore} > 150\ MeV$ $200\ MeV < \mathbf{p_T} < 20\ GeV$ $\mathbf{quality} = 63 \,\vert\vert\, 31 \vert\vert\, 51$ $\sqrt{\sigma^2_{\mathbf{\Delta}\phi} + \sigma^2_{\mathbf{\Delta z}}} < 5.0\sigma$	track quality
	$\mathbf{n0} \geq 2$ $\mathbf{chi2/npe0} < 10.0$ $\frac{\mathbf{E}}{\mathbf{p}} > 0.5$	electron ID
	$!\left(\phi > 0.75\ \&\&\ \phi < 2.4\ \&\&\ \frac{\mathbf{E}}{\mathbf{p}} < 0.85\right)$	γ conversions from HBD strut
pair		
	$[\phi_{\mathbf{V}} < 0.1]\ \vert\vert\ [\mathbf{mass} < 30\ MeV\ \&\&\ \phi_{\mathbf{V}} < 0.25]$	γ conversions
	$\mathbf{dcent} \geq 10.0\sigma$	RICH ghosts

Table 5.4: Summary of electron ID cuts.

track quality

A bit pattern representing the reconstruction quality of the track. If the track is reconstructed by both of the X1 and X2 sections of the DC and is uniquely associated with hits in U or V stereo wires, the value of `quality` is 63 (in case a unique PC1 hit is found too) or 31 (in case the

PC1 hit is found but ambiguous). If there are no UV hits found, but a PC1 hit is, `quality` is 51.

ecore

Energy deposited in EMCal cluster.

EMCal match ($\sigma_{\Delta\phi}$)

Displacement in ϕ between the position of the associated EMCal cluster and the projection of the track onto the EMCal. The quantity is measured in units of momentum-dependent resolution. For example, $\Delta\phi < 2$ means that the position of the associated EMCal cluster in ϕ is within 2σ of the projected track position. The particle hit position of an EMCal cluster is particle-species dependent due to different shower shapes. Here the parametrization has been optimized for electrons.

EMCal match ($\sigma_{\Delta z}$)

Analogous to the previous variable, for the z coordinate.

n0

Number of hit RICH PMTs in an annular region with an inner radius of 3.4 cm and outer radius of 8.4 cm around the track projection on the RICH. The expected radius of a Čerenkov ring emitted by an electron is 5.9 cm.

chi2/npe0

A χ^2-like shape variable of the RICH ring associated with the track divided by the number of photo-electrons measured in a given ring (npe0).

dcent

The displacement of any two track projections in the RICH. Reported in a sigmalized quadrature sum of $\Delta\phi$ and Δz where $\Delta\phi$ is the ϕ difference between the DC projection on the RICH and the associated RICH ring (same for Δz). Note that 10σ is approximately 2 RICH ring diameters.

E/p

A variable quantifying energy-momentum matching, where E is the energy measured by EMCal and p is the momentum of the track. For electrons, this quantity is approximately a Gaussian distribution around 1.0.

The primary electron identifying cut is the RICH variable, n_0, the efficacy of which can be seen in Figure 5.14. This is a highly discriminating cut that provides good hadron rejection while maintaining high eID efficiency.

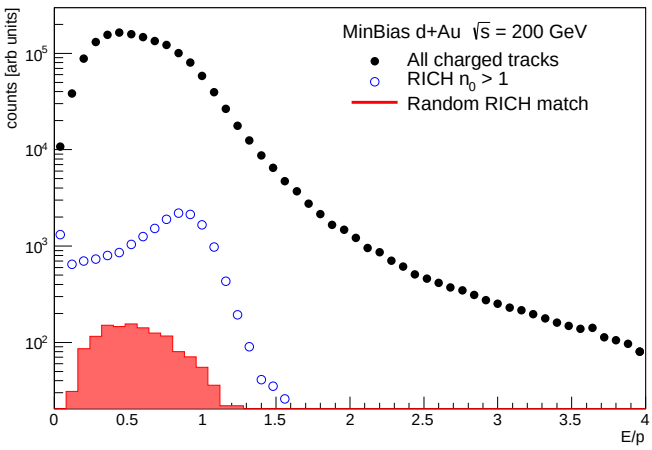

Figure 5.14: E/p distribution for all charged tracks (black), after applying the RICH n_0 cut, and contribution of randomly associated hadrons (red) for good quality tracks.

The rest of the single track cuts are shown in Figure 5.15.

5.4.2 HBD Strut Conversions

Even though the Hadron Blind Detector was not installed for Run8, the support structures *were* in place above the beamline at about $\pm$ 30° from vertical and a radius of $\sim$ 1 m (see Figure 5.16). This is inside the radius of the DC but out of the acceptance for an infinite momentum track. The problem arises when a photon hits one of these struts and converts to an e^+e^- pair. The magnetic field is capable of bending the electron (or positron) back into PHENIX's acceptance. Since these electrons do not originate at the vertex, they have less magnetic field to traverse than the reconstruction assumes and therefore are assigned a momentum that is too high. However, they still deposit all of their energy in the EMCal making the measured energy of the track correct.

With a momentum *higher* than its energy, the measured E/p of such a track is too *low*. This creates a peak in the E/p distribution around 0.5 – 0.6 in the EMCal sectors that are at the top of the detector (3 in the east arm, 7 in the west arm). Figure 5.17 shows the E/p distributions independently for each charge. Predictably, the magnetic field bends all positive α tracks into the west arm and negative α tracks into the east arm (α is defined in Section

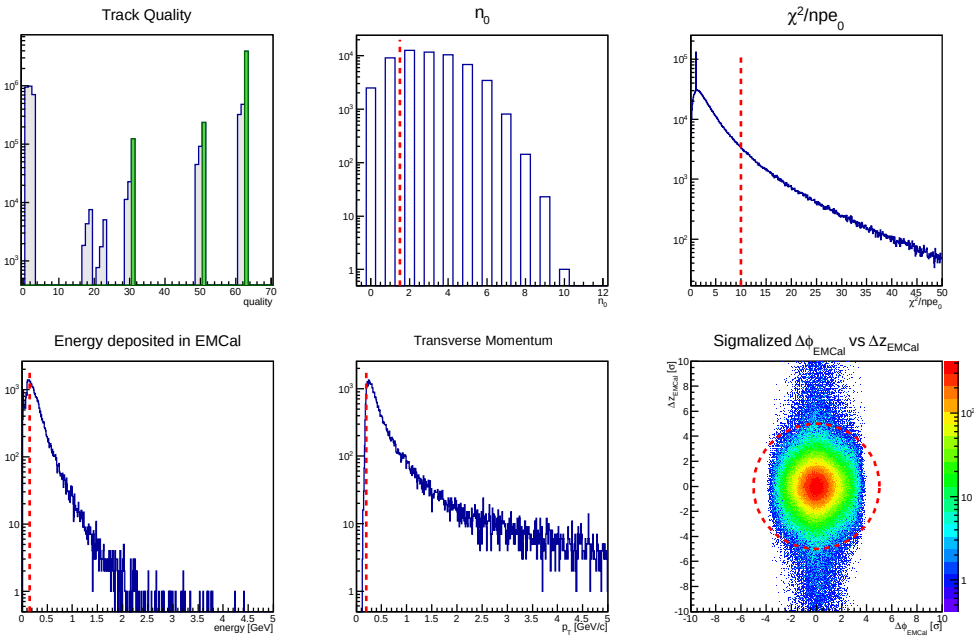

Figure 5.15: Summary of single electron cuts.

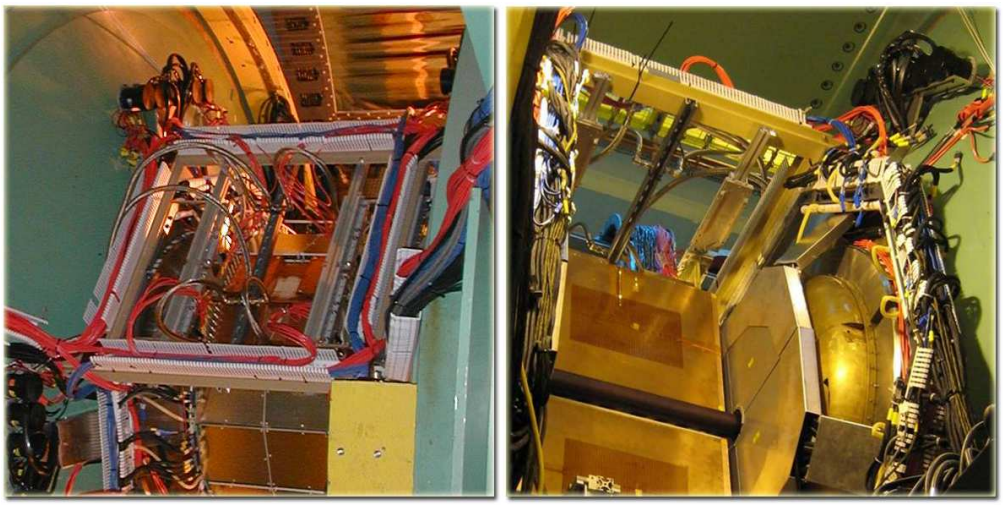

Figure 5.16: Left: birds-eye view of the HBD support struts. Right: View of the HBD struts from below.

4.4.2).

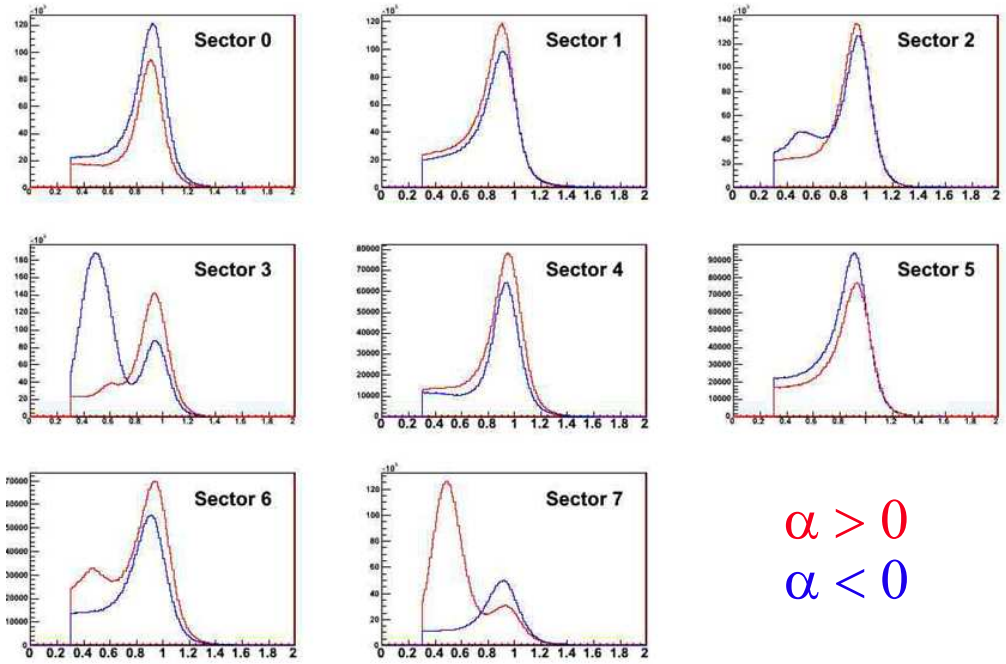

Figure 5.17: Sector-by-sector E/p distributions separated by α (translatable to charge).

Since these γ-conversion electrons are located at ϕ near the top of the detector and peak in E/p around 0.6, they are best identified in the 2D plane of ϕ_{DC} vs E/p. Figure 5.18 shows the ϕ_{DC} distribution as well the ϕ_{DC} vs E/p plane. A two-dimensional cut in this plane (shown as the red dotted line) proved to be the most efficient way to remove these electrons. For a full discussion on γ-conversions and how they are more generally dealt with, see Section 5.5.1

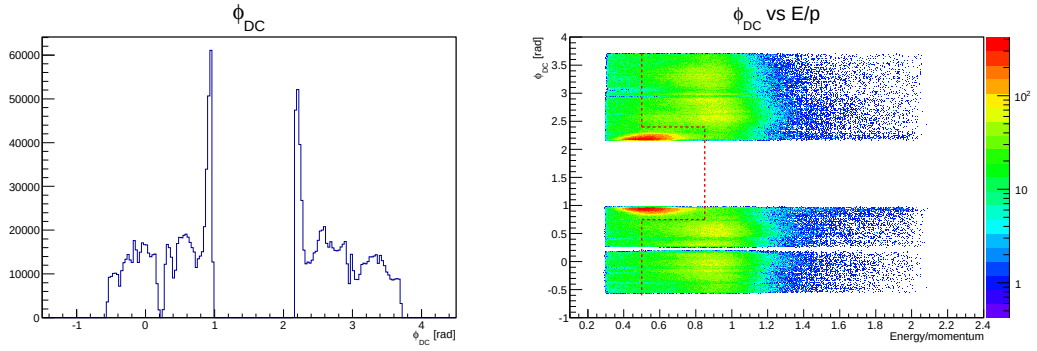

Figure 5.18: Right panel: ϕ measured at the DC reference radius. The peaks between 0.75 and 2.4 radians are primarily γ-conversion electrons from the HBD support strut. Left panel: ϕ_{DC} vs E/p. The red-dotted line shows the cut used in this analysis to eliminate these electrons.

5.5 Pair Cuts

> Let the wookie win.
>
> C-3P0

5.5.1 Photon Conversions

As mentioned in Section 5.4.2, photons that convert in material between the interaction point and the Drift Chamber characteristically distort the measured momenta of their e^+ and e^- daughters by *over*estimating the B-Field integral that the track has passed through. For this reason, these electrons from γ-conversions have a smaller α than they should and therefore higher p_T as measured by the Drift Chamber. Figure 5.19 illustrates a γ-converting in the beampipe and the resulting e^+e^- pair whose momenta are misreconstructed by the tracking algorithm.

Aside from the aforementioned HBD strut conversions, photons primarily convert in the beampipe and in the air between the beampipe and the Drift Chamber (as well as other various support structures). The invariant mass of these misreconstructed e^+e^- pairs (should be zero but instead) is monotonically proportional to the conversion radius. The results of a fast toy Monte Carlo are shown in Figure 5.20. This simulation is only valid for when the conversion radius is small compared to the distance to the drift chamber. For

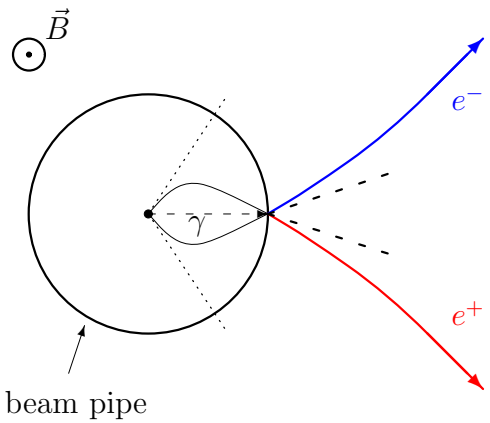

Figure 5.19: Misreconstruction of the opening of a conversion pair. Shown are the photon and the conversion pair which is created in the beam pipe. The real opening angle between the original trajectories (dashed lines) is much smaller than the reconstructed opening angle, artificially created by tracking the particles back to the collision vertex (dotted lines).

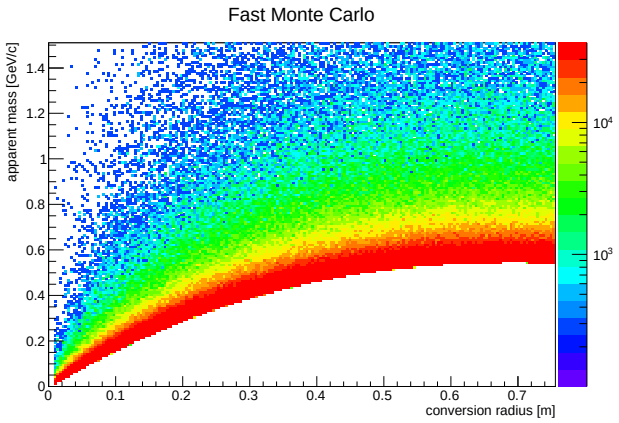

Figure 5.20: Apparent mass of photon conversion dielectron pair as a function of its conversion radius.

low conversion radii, the relationship is approximately linear. For reference, the beampipe sits at $r = 3\ cm$ ($\sim 20\ \mathrm{MeV}/c^2$) and there is a volume of air between the beampipe and the DC. Photon conversions in the air wind up sitting as a wide peak around $\sim 300\ \mathrm{MeV}/c^2$. The mass spectrum from conversion e^+e^- pairs is shown in Figure 5.21 (as well as like-sign and mixed events for both).

Since these e^+e^- pairs from γ-conversions are not a dielectron physics signal but instead a detector artifact leftover from stray photons, they should be removed from the analysis. This is accomplished by a cut on a pair-wise variable, ϕ_V, defined as

$$\vec{u} = \frac{\vec{p}_1 + \vec{p}_2}{|\vec{p}_1 + \vec{p}_2|} \tag{5.12a}$$

$$\vec{v} = \vec{p}_1 \times \vec{p}_2 \tag{5.12b}$$

$$\vec{w} = \vec{u} \times \vec{v} \tag{5.12c}$$

$$\vec{u}_a = \frac{\vec{u} \times \hat{z}}{|\vec{u} \times \hat{z}|} \tag{5.12d}$$

$$\phi_V = \arccos\left(\frac{\vec{w} \cdot \vec{u}_a}{|\vec{w}||\vec{u}_a|}\right). \tag{5.13}$$

Here $\vec{p}_1$ is the 3-momentum vector of the electron and $\vec{p}_2$ the 3-momentum vector of the positron.

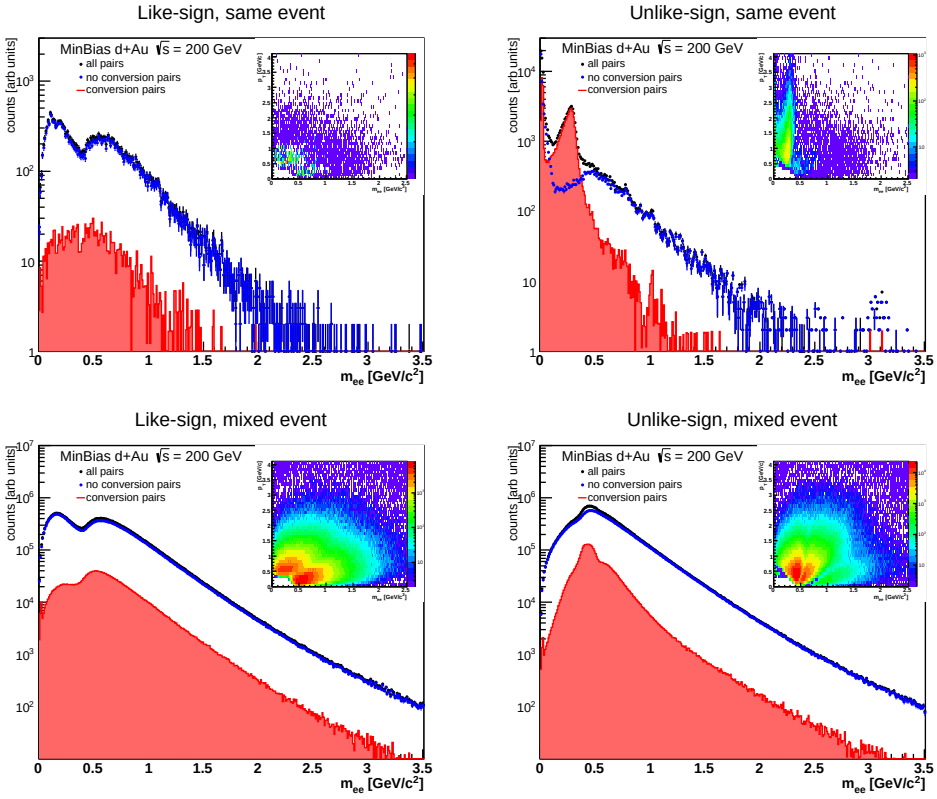

Figure 5.21: Invariant mass distributions of likesign (left panels) and unlikesign (right panels) pairs in real events (top panels) and mixed events (bottom panels). All pairs are shown in black, pairs failing the conversion cut in red and the difference in blue.

This is a cut on the orientation of the plane defined by the opening angle of the pair with respect to the magnetic field. e^+e^- pairs from photon conversions have no intrinsic opening angle. Therefore, the only way they can be separated from each other is by the magnetic field pulling them apart. In this case, the opening angle will be aligned perpendicular to the magnetic field. However, any pair that decays from a source with mass must have an opening angle that is randomly oriented with respect to the magnetic field. Figure 5.22 illustrates this concept.

Figure 5.23 shows where the conversion pairs exist. The pair cut that is used is defined in Table 5.4 and is drawn in the right-hand panel of Figure 5.23. The ϕ_V of the cut is loosened at lower mass for two reasons. First,

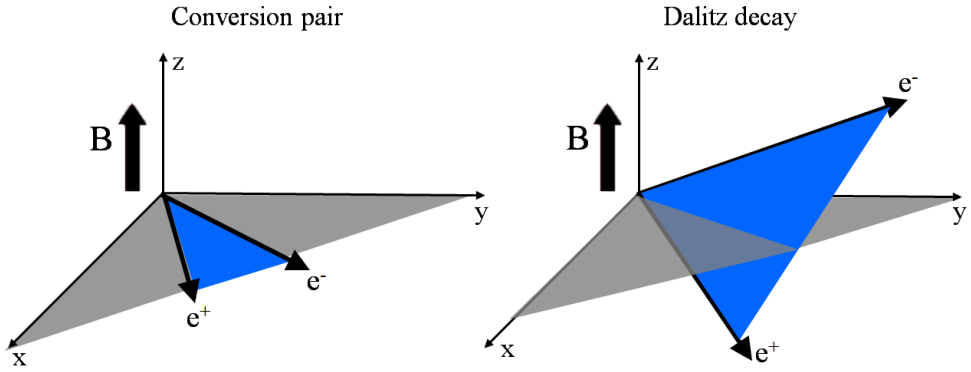

Figure 5.22: Left panel: the plane defined by the opening angle of a conversion pair (blue) is parallel to the plane defined by the magnetic field (gray). Right panel: However, the opening angle of, for example, a Dalitz decay (blue) is randomly oriented with respect to the magnetic field (gray).

as the opening angle of the pair becomes very small the ϕ_V resolution gets worse. Secondly, the multiple scattering in the Beryllium beampipe additionally smears the orientation of the opening angle making it necessary to cut at higher ϕ_V at low mass.

Since mass is approximately proportional to conversion radius at low mass (Figure 5.20), the left panel of Figure 5.23 proxies an x-y representation of where conversions originate. In total, the conversions cut removes $\sim 98\%$ of γ-conversions.

5.5.2 RICH Ghost Cut

An additional source of contamination in the dielectron spectrum are hadron tracks (mostly pions) that share a RICH ring with an electron. These are referred to as *RICH ghosts* and they occur when two tracks are parallel in the RICH. As seen in Figure 5.24, the spherical RICH mirrors focus a track's Cherenkov emission into a ring on the PMT plane. This is convenient as it ensures that the light has a definite shape as well as reduces the phase space in which the light is distributed resulting in a more precise hit on the RICH PMT plane. The downside is that parallel tracks will point to the same place on the PMT plane leaving the RICH hit to DC track association ambiguous.

Since these RICH ghosts are purely a detector artifact, they are not reproduced by mixed events and must be removed before background subtraction.

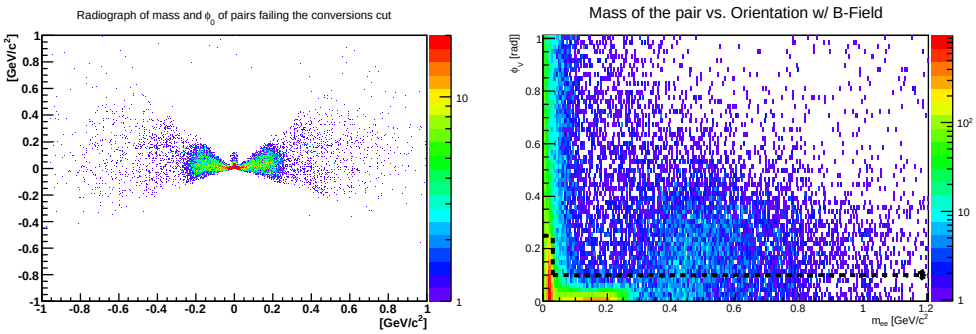

Figure 5.23: Left panel: A radiograph plot where mass $\rightarrow$ radius and $\phi_0 \rightarrow \phi$. This is approximately an x–y representation of where conversions originate in PHENIX. Right panel: The mass vs ϕ_V space in which the conversion cut is made (the cut is shown by the dotted black line).

In addition, the like-sign ghost pairs populate a different region in mass and p_T space than unlike-sign pairs. The ghost pairs are shown in Figure 5.25.

In order to remove these RICH ghosts from the data sample, a cut is placed on the distance between any two track's projections on the RICH PMT plane. If the track projections are within 10 σ of each other in $\Delta\phi_{RICH} \oplus \Delta z_{RICH}$ then the entire event is rejected. The variable Δ_{center} between tracks i and j is defined as

$$\Delta_{\rm center} = \sqrt{(z^i_{\rm center} - z^j_{\rm center})^2/\sigma^2_{z_{\rm center}} + (\phi^i_{\rm center} - \phi^j_{\rm center})^2/\sigma^2_{\phi_{\rm center}}} \qquad (5.14)$$

with $\sigma_{z_{\rm center}} = 3.6$ cm and $\sigma_{\phi_{\rm center}} = 10$ mrad being the rms of the distributions of ring distances (without any pair cut) in $\hat{z}$ and $\hat{\phi}$ directions, respectively. A cut of $\Delta_{\rm center} > 10$ (equivalent to 36 cm) corresponds to approximately twice the expected ring diameter of an electron ($\sim$16.8 cm) ensuring that no two tracks have overlapping rings in the RICH. A two ring diameter track projection separation is necessary to completely isolate the Cherenkov light between two tracks. When the light can bleed from one ring to another, the ring shapes get distorted and a variable like χ^2/npe_0 starts to lose discriminatory power. Cutting at two ring diameters results in a more reliable reconstruction efficiency calculation, thereby reducing the systematic uncertainty of the RICH cuts.

It should also be noted that this pair cut is actually performed at the event level rather than the pair level. If *any* dielectron pair candidate in an

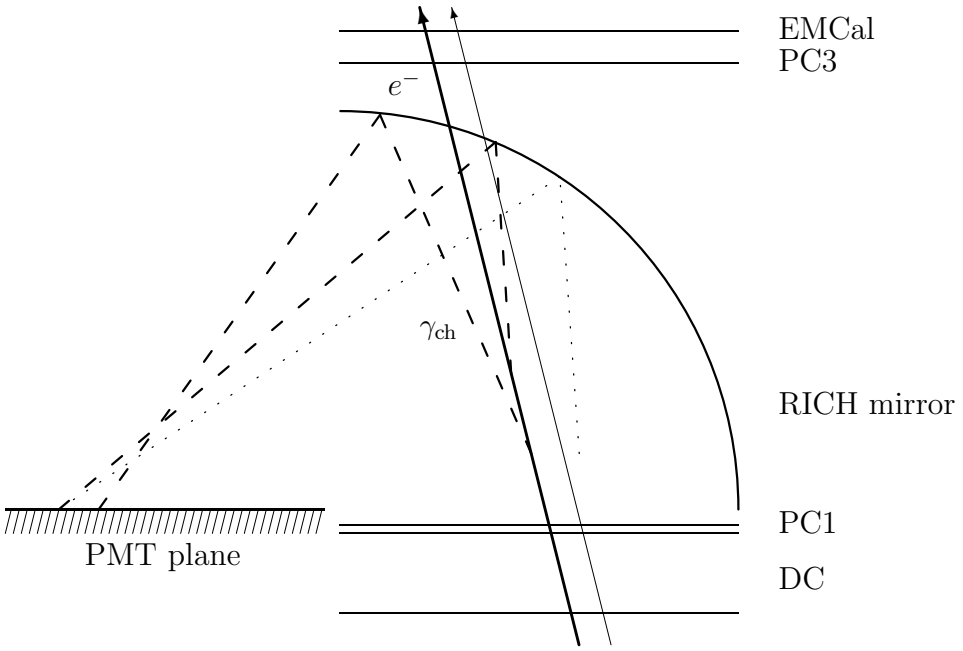

Figure 5.24: Overlapping rings in the RICH PMT plane due to two parallel tracks.

event fails this cut, the entire event is thrown away. While this may seem like a drastic strategy, its purpose is to preserve the counting statistics between like-sign/unlike-sign and mixed/real events. The $\Delta\phi_{center}$ and Δz_{center} distributions are show in Figure 5.26 for both real and mixed events.

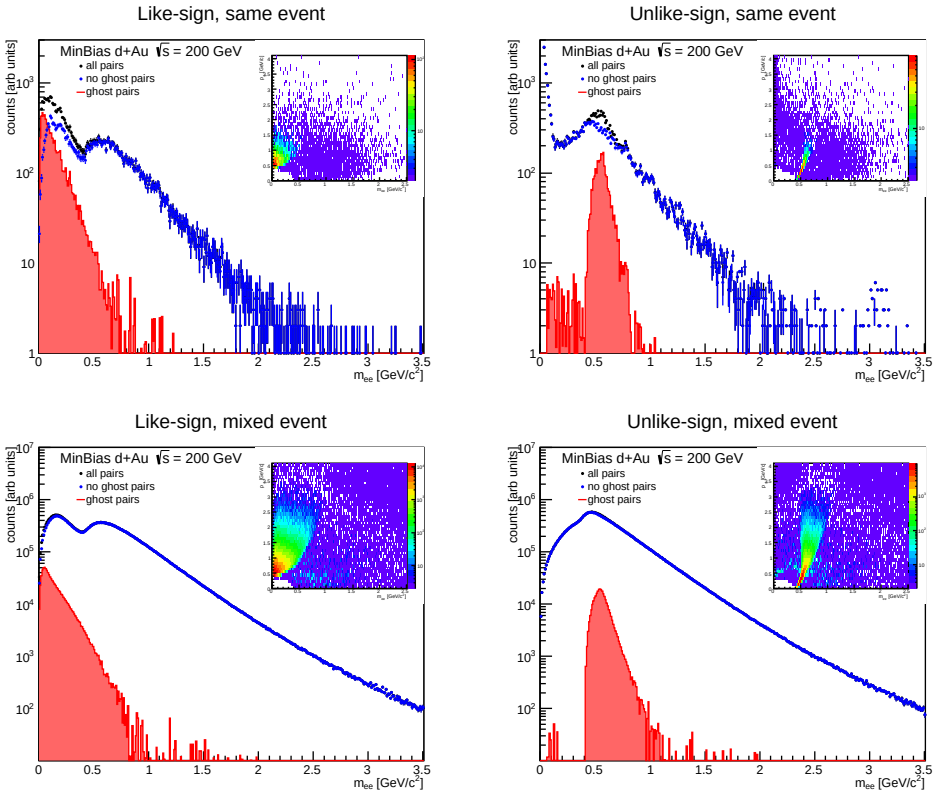

Figure 5.25: RICH ghosts for unlike-sign and like-sign as well as mixed events and same events.

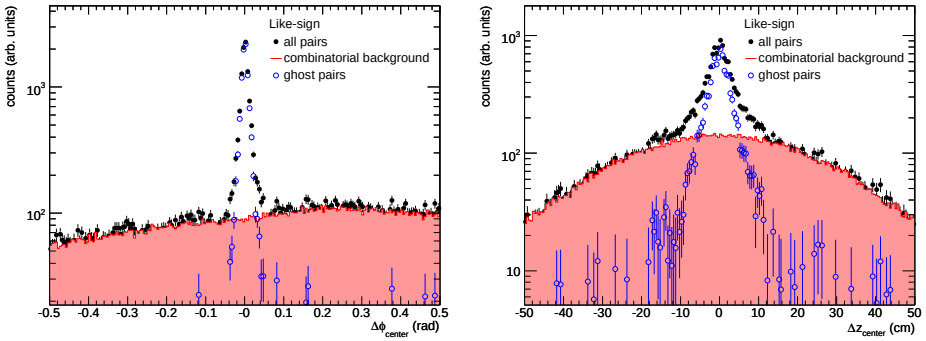

Figure 5.26: Distance of the ring centers associated to two tracks in $\Delta\phi_{\text{center}}$ (left) and Δz_{center} (right).

CHAPTER 6

Background Estimation

6.1 Event Mixing

The "traditional" method of estimating the combinatorial background is to use a technique called *event mixing*. This essentially means taking an electron from event i and pairing it with a positron from event j. To ensure that events i and j have similar event topology (described in Section 5.3) this is performed in pools of centrality and z_{vertex}. For the d+Au analysis, events were categorized into 9 z_{vertex} pools and 5 centrality pools. By creating a pair from two separate (but similar) events, it is assured that the pair is not correlated and, therefore, by definition, combinatorial in nature.

When performed properly, event mixing can produce a combinatorial spectrum with extremely high statistics. However, the downside is that the resulting spectrum must be normalized to the appropriate level to be subtracted from the foreground. This normalization is delicate and necessitates extremely fine control in its handling, particularly in regions of low signal-to-background.

6.1.1 Signal-to-Background

The bull always wins.

Dan Kuhar

While Figure 5.1 illustrated the p_T integrated S/B only dropping to the 10% level, in the mass vs p_T plane it can drop as low as single digits percent in some regions (see Figure 6.1). This results in a precarious situation. Since the p_T distribution is a steeply falling spectrum, the majority of the yield sits at the lowest pair momentum, indeed in exactly the region where the S/B is lowest in the LMR. For this reason, an explicit pair cut has been implemented in the d+Au dataset of $mc^2 \oplus p_T c < 450$ MeV. This is different from the *implicit* pair cut that exists in previous PHENIX dielectron analyses, imposed by the PHENIX aperture, of ∼400 MeV. [1]

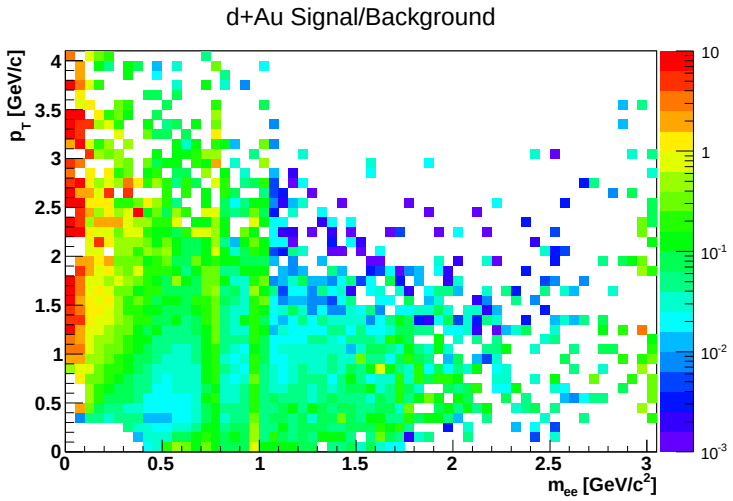

Figure 6.1: The estimated signal-to-background ratio for d+Au.

6.1.2 Normalization Mathematics

Beginning with the assumption that e^+ and e^- are always produced in pairs and that these pairs are produced statistically independent of each other, it

[1] Note that when comparisons between datasets are made, care is taken to ensure that the same cut is made on both datasets thus making an "apples-to-apples" comparison.

has been shown [69] that

$$\langle BG_{+-}\rangle = 2\sqrt{\langle BG_{++}\rangle\langle BG_{--}\rangle}. \tag{6.1}$$

Using this relation as a bedrock for the normalization, the likesign spectra can be used to calculate the proper factor by which the mixed event distributions need to be scaled to mimic the uncorrelated background which exists in the same event spectra.

Assuming that the likesign spectra contain no correlated pairs, the normalization is quite simple. Under this premise, the full integral of likesign pairs in the mixed event spectra should be made to match the total number in the same event spectrum and then transformed via equation 6.1 to reveal the proper normalization for the unlike-sign mixed event distribution.

However, the assumption of no correlated pairs in the same event likesign distributions is wrong! There are indeed correlations that need to be excluded when taking the ratio of (same event)/(mixed event) in the likesign. These are explained in detail in the following Section 6.2 (and their existence is even used to our advantage as described in Section 6.3). For the moment though, suffice it to say that the normalization is performed in a region of the likesign spectra where the correlated pairs are negligible. This region is defined by:

$$m_{ee} > 300 \text{ MeV}/c^2 \quad \&\& \tag{6.2a}$$
$$m_T < 1.2 \text{ MeV}/c^2 \quad \&\& \tag{6.2b}$$
$$p_T/c - 1.5m_{ee} \leq 200 \text{ MeV}/c^2 \quad \&\& \tag{6.2c}$$
$$p_T/c - 0.75m_{ee} \geq 0 \text{ MeV}/c^2. \tag{6.2d}$$

and illustrated in Figure 6.2.

6.2 Correlated Background

> When the eagles are silent, the parrots begin to jabber.
>
> Winston Churchill

While the mixed event background describes the shape of the combinatorial background quite well, there are additional sources of correlated pairs. These pairs are uninteresting as they are essentially correlated through the pion mass and decay kinematics and, therefore, must be removed from the

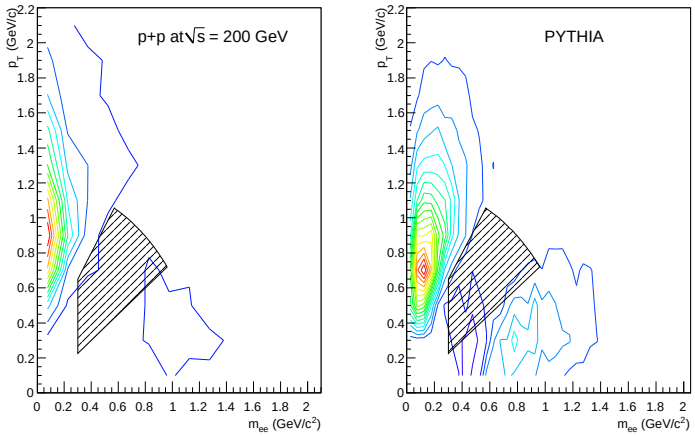

Figure 6.2: Mixed event subtracted like-sign spectrum in data (left) and as calculated with PYTHIA (right) as function of invariant mass and p_T. The dashed region outlines the normalization area as defined in equation 6.2.

spectrum. Dubbed *cross pairs* and *jet pairs*, these correlations exist both in the unlike-sign spectrum and the like-sign spectrum. Moreover, they are the only source of correlations in the like-sign spectrum making them directly accessible through the like-sign channel. This correlated background originates from hadronic decays in jets, primarily from pions. Figure 6.3 schematically illustrates the origin of cross pairs and jet pairs.

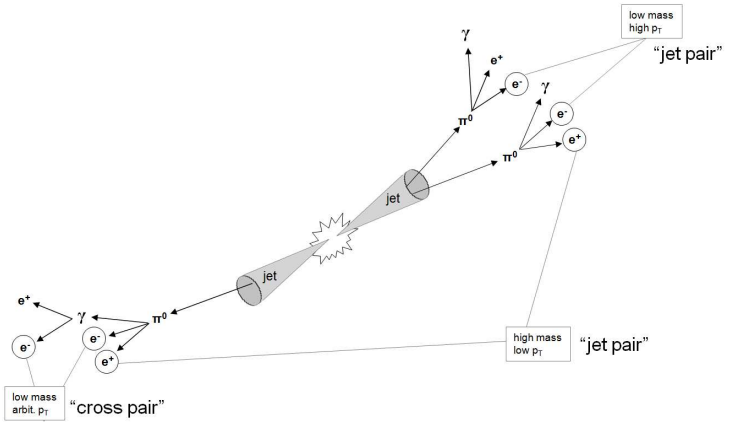

Figure 6.3: An illustration of how cross pairs and jet pairs are formed.

Figure 6.4 shows the mass distributions for unlike-sign and like-sign pairs. As the like-sign mixed events do not reproduce the shape of the real events, the correlated background can be estimated via the like-sign pairs.

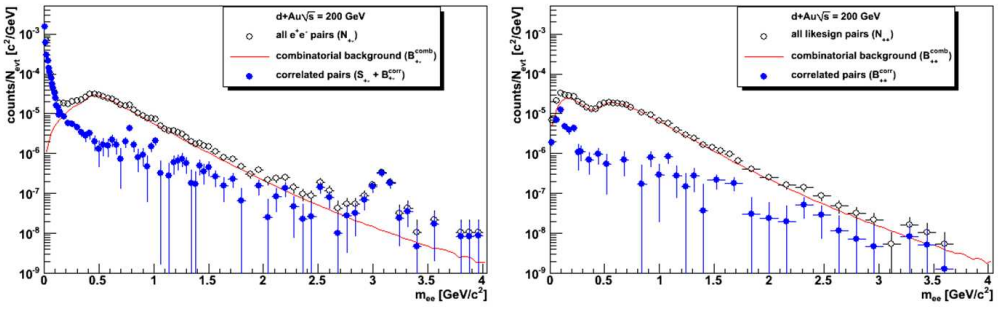

Figure 6.4: Left: Correlated pairs in the unlike-sign mass spectrum found by subtracting the normalized mixed event spectrum from the unlike-sign same event spectrum. Right: Correlated background in the like-sign mass spectrum.

6.2.1 Cross Pairs

Cross pairs originate from hadronic decays that result in two e^+e^- pairs. The primary culprits are π^0 that double Dalitz decay ($\pi^0 \to \gamma^*\gamma^* \to e^+e^-e^+e^-$). This produces like-sign and unlike-sign combinatorial pairs at the same rate. Since the leptons are all produced from the same π^0, they typically have small opening angles. Under the approximation that the electron mass is nearly zero, the invariant mass of the parent can be approximated by

$$m_{ee} = 2|p_+p_-|(1 - \cos\theta) \tag{6.3}$$

and these pairs subsequently manifest at low mass with arbitrary p_T.

Similar to the double Dalitz decays are the $\pi^0 \to \gamma^*\gamma$ followed by $\gamma^* \to e^+e^-$ and the real photon converting in detector material. While the pair that comes directly from the γ^* is considered signal and the photon conversions are removed with a ϕ_V cut on the pair (Section 5.5), any of the remaining *cross* pairs are correlated pairs which do not exist in the mixed events. This is correlated background which must be removed. The cross pairs can be seen as a peak near ≈ 100 MeV in the like-sign spectrum in Figure 6.4.

6.2.2 Jet Pairs

The other source of correlated background are pairs which do not come from the same parent but are correlated via jets that are formed in the initial hard scattering. When the electron and positron come from opposite (back-to-back) jets, the resulting pair typically has a low p_T and high mass; when they come from two separate hadrons in the same jet, the pair typically has a high p_T and low mass.

6.3 Like-sign Subtraction

> Life is simpler when you plow around the stumps.
>
> country wisdom

To avoid the complication of determining the absolute mixed event normalization as well as having to calculate the correlated background this analysis employs a like-sign subtraction method. The like-sign distribution is absolutely normalized and produces combinatorial pairs at the same rate as the unlike-sign foreground. As can be seen in Figure 6.3, it also produces cross pairs and jet pairs as the same rate as the unlike-sign.

However, Figure 6.5 shows raw mass distributions for the ERT triggered dataset (a triggered dataset is shown to illustrate this issue out to reasonably high mass; the MinBias data sample suffers from poor statistical precision above 2 GeV/c). The raw like-sign distribution does *not* reproduce the mixed events (even beyond the excess due to the correlated background). This is due to the acceptance difference between unlike-sign pairs and like-sign pairs in PHENIX (Section 6.3.1).

6.3.1 Relative Acceptance Correction

> You threw out a ringer for a ringer!
>
> The Dude

The two-arm configuration of the PHENIX central arms results in a different acceptance for like-sign pairs and unlike-sign pairs (Figure 6.6). Unfortunately, this makes the raw like-sign spectrum unusable as a background

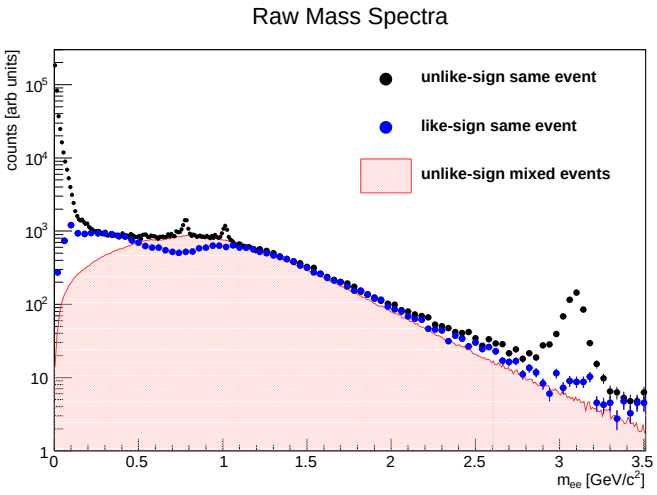

Figure 6.5: Raw invariant mass spectra for ERT (600 MeV) triggered events. The mixed event normalization is described in Section 6.1.2.

estimator. Therefore, before the like-sign foreground can be subtracted from the unlike-sign, a correction must be applied to account for this different acceptance.

On the bright side, however, this relative acceptance difference between like-sign and unlike-sign pairs can be measured by looking at the mixed event spectra. The *relative acceptance correction* is thus defined as

$$\alpha = \frac{BG12}{BG1122} \tag{6.4}$$

where $BG1122$ could naively be defined as

$$BG1122 = BG11 + BG22. \tag{6.5}$$

However, note that this definition of $BG1122$ is modified in equation 6.10b

This is a purely geometric correction and must be calculated for each run group individually since the geometric acceptance changes slightly for each group. For MinBias datasets, this is straightforward; the MinBias events are simply mixed. However, for the ERT triggered datasets, the MinBias sample must be mixed with the additional requirement that at least one of the electrons fired the ERT trigger. If the ERT sample is used for event mixing then the the distribution becomes distorted.

The cause of this distortion can be understood in terms of statistically mixing two (potentially different) single electron distributions. When the ERT

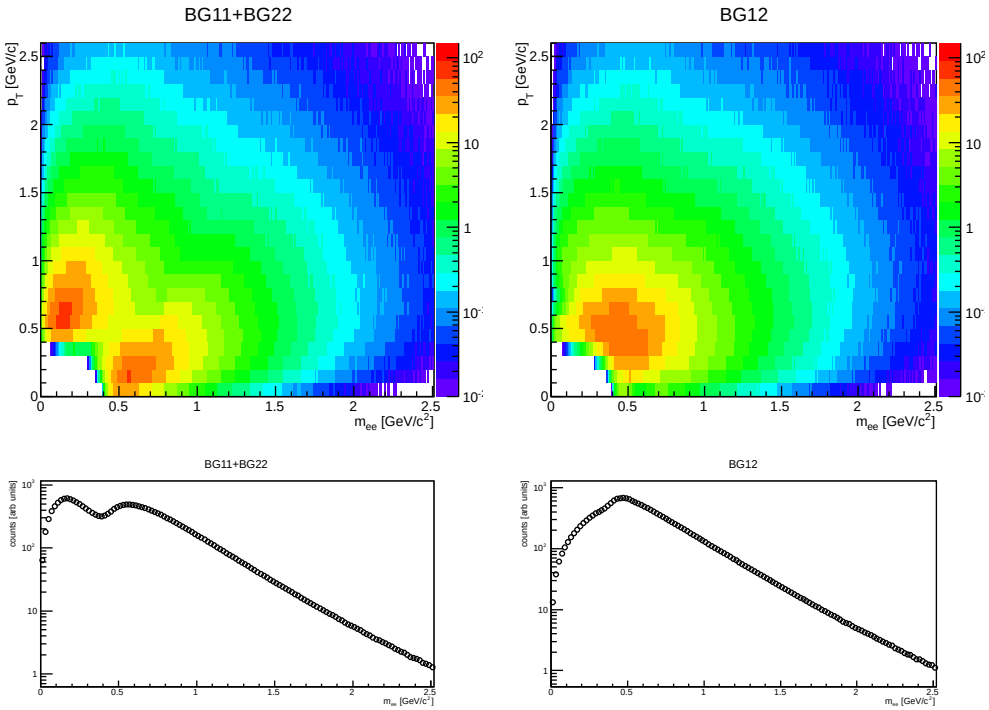

Figure 6.6: Due to the two-arm acceptance of PHENIX, like-sign (left) and unlike-sign (right) pairs occupy different regions in phase space.

combinatorial background is produced in the foreground, it is made by pairing one electron which comes from a triggered p_T distribution with another which comes from a non-triggered distribution. However, if event mixing were to be performed on an ERT sample, then *both* electrons would be sampled from a triggered distribution thereby *not* correctly reproducing the combinatorial pairs that exist in the foreground.

The relative acceptance correction for MinBias events is shown in Figure 6.7 as well as its effect on the like-sign spectrum. Since α is a function of both mass and p_T, the correction must be calculated and subsequently applied differentially in mass and p_T.

Hence, the following calculation would naively be used to determine the

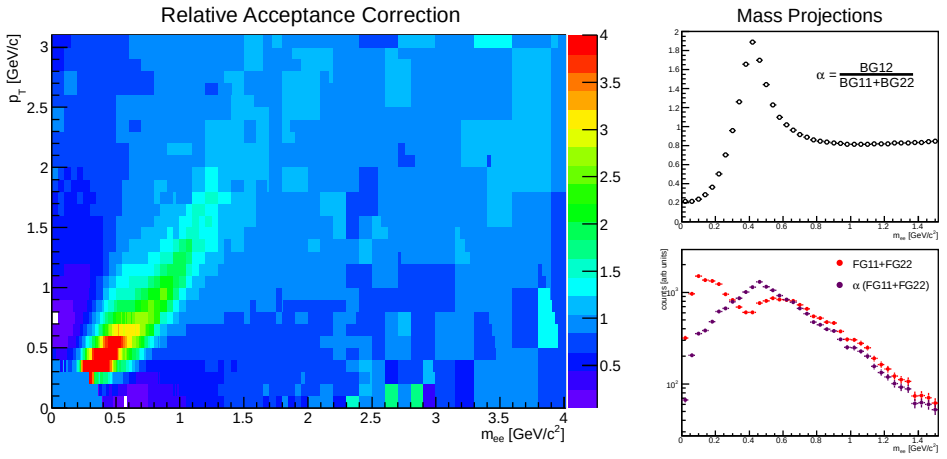

Figure 6.7: Left: The relative acceptance correction (α) in mass vs p_T space. Right: The mass projection of α (upper) and its effect on the like-sign spectrum (lower).

raw signal, S, (differentially in mass and p_T):

$$S = FG12 - \alpha \cdot FG1122 \tag{6.6a}$$

$$S = FG12 - \frac{BG12}{BG1122} \cdot FG1122 \tag{6.6b}$$

where

$$FG1122 = FG11 + FG22. \tag{6.7}$$

However, note that this definition of $FG1122$ is modified in equation 6.10a

6.3.2 Damage Control

> The villain laughs in every movie.
>
> Jamil Edgemir

Using the like-sign subtraction method, a large uncertainty develops around mass ≈ 0.5 GeV/c and $p_T \approx 0.5$ GeV/c stemming from the following issues:

- The calculation is performed differentially in mass *and* p_T thereby significantly reducing the statistics in any given bin.
- The S/B is lowest around in this region (Figure 6.1).
- The like-sign spectrum suffers from a reduction in statistical precision in this region due to the PHENIX two-arm acceptance (6.6)
- The relative acceptance correction (α) and it's associated systematic uncertainty (Section 7.4) are largest in this region.

Therefore, to minimize the overall uncertainties in the measured spectra, Equation 6.6a is modified and the signal is calculated as

$$S = FG12 - N \cdot BG12 - \alpha \left[FG1122 - N \cdot BG1122 \right] \tag{6.8}$$

Equation 6.8 is equivalent to Equation 6.6a in the limit that the binning in mass and p_T doesn't change in any of the distributions. However, a smoothing of the data is applied to α before it is used in the calculation. This is accomplished by strategically rebinning α with increasing strength as mass and p_T increase. This is appropriate since α must approach a constant, unity, at high mass and high p_T.

The mixed events ($BG12$, $BG11$, and $BG22$) have very small statistical uncertainty while the foregrounds, on the other hand, suffer from large statistical uncertainty. Therefore, subtracting the mixed events doesn't appreciably change the statistical uncertainty of the measurement. Figure 6.4 shows that, while the ratio of correlated background to signal is non-negligible, the fraction of correlated background in the combinatorial background *is* small. Moreover, it is unnecessary to apply the relative acceptance correction to the entire combinatorial background. Since the largest contributor to the systematic uncertainty (in the region where the S/B is lowest, Figure 6.1) is α, this strategy minimizes the number of non-combinatorial pairs that feel the effect of α.

In addition, because the "twice square root" relationship is only valid in the *integral*, not differentially in mass and p_T, a further modification must be made to the calculation. It should be noted that this modification is unnecessary in the case where the e^+e^+ and e^-e^- distributions are identical along the axes on which the calculation is performed (here, mass and p_T). Since there are slight asymmetries between the single e^+ and e^- p_T distributions due to the track reconstruction algorithm as well as detector dead areas, the asymmetries in the like-sign pair distributions are amplified and thus non-negligible.

By taking the derivative of Equation 6.1 it is assured that the *integral* of the likesign will still be correct.

$$\frac{d^2}{\mathrm{d}m\,\mathrm{d}p_T}\left[2\sqrt{\iint_{m\,p_T} BG11(m,p_T)\,\mathrm{d}m\mathrm{d}p_T}\cdot\sqrt{\iint_{m\,p_T} BG22(m,p_T)\,\mathrm{d}m\mathrm{d}p_T}\right]$$
$$=\sqrt{\frac{\iint BG22(m,p_T)}{\iint BG11(m,p_T)}}\cdot BG11(m,p_T)+\sqrt{\frac{\iint BG11(m,p_T)}{\iint BG22(m,p_T)}}\cdot BG22(m,p_T) \tag{6.9}$$

and, therefore, the likesign distribution, $FG1122$ and $BG1122$, are redefined as

$$FG1122(m,p_T)=\sqrt{\frac{\iint FG22(m,p_T)}{\iint FG11(m,p_T)}}\cdot FG11(m,p_T)+\sqrt{\frac{\iint FG11(m,p_T)}{\iint FG22(m,p_T)}}\cdot FG22(m,p_T) \tag{6.10a}$$

$$BG1122(m,p_T)=\sqrt{\frac{\iint BG22(m,p_T)}{\iint BG11(m,p_T)}}\cdot BG11(m,p_T)+\sqrt{\frac{\iint BG11(m,p_T)}{\iint BG22(m,p_T)}}\cdot BG22(m,p_T) \tag{6.10b}$$

and the relative acceptance bin-by-bin in mass and p_T becomes

$$\alpha(m,p_T)=\frac{BG12(m,p_T)}{\sqrt{\frac{\iint BG22(m,p_T)}{\iint BG11(m,p_T)}}\cdot BG11(m,p_T)+\sqrt{\frac{\iint BG11(m,p_T)}{\iint BG22(m,p_T)}}\cdot BG22(m,p_T)}. \tag{6.11}$$

The final raw signal is calculated as Equation 6.8 with the likesign definitions from Equation 6.10a and Equation 6.10b. Appendix A describes a toy Monte Carlo that was used to validate that Equation 6.9 is the correct formulation of the likesign spectra.

CHAPTER 7

Efficiency Corrections

Any experimental setup and apparatus suffers from inefficiencies and PHENIX is no exception. However, detailed Monte Carlo simulations provide the ability to correct for these detector deficiencies and measure final particle yields (with some degree of uncertainty). Both the reconstruction and ERT trigger efficiencies are calculated and applied differentially in the mass vs p_T space.

7.1 Reconstruction Efficiency

> Haste is toil to the living and nothing to the dead.
>
> Alan Dion

The reconstruction efficiency, ϵ_{rec}, is the product of all the efficiencies due to the detector setup and reconstruction algorithms. This includes

- Detector dead areas
- PHENIX track reconstruction software
- electron identification
- single electron track cuts
- e^+e^- pair cuts.

To correct for these inefficiencies a full scale Monte Carlo simulation was run using the GEANT3 [73] framework developed at CERN. The PHENIX collaboration has a fully implemented description of its detector called PISA (PHENIX Integrated Simulation Application). PISA takes any primordial distribution of particles as input and then simulates PHENIX's response to them. The output from PISA is then run through the reconstruction software which generates output in a similar format to the actual data (although the final output files also contain the "input particle" information as well). With the simulated knowledge of what a given input to the detector/reconstruction software should render as output, an overall efficiency for the effects listed above can be constructed.

7.1.1 PISA Input

A fast Monte Carlo was used to generate 40 million e^+e^- pairs. 20 million were generated from $0 < mass < 16$ GeV and $0 < p_T < 9$ GeV and to increase the statistics at low $[m, p_T]$, an additional 20 million were generated in $0 < mass < 2$ GeV and $0 < p_T < 2$ GeV. The parent particles (which are decayed to e^+e^-) are generated with distributions following Table 7.1.

parent info		
variable	distribution	range
mass	flat	0−14, 0−2 GeV
p_T	flat	0−9, 0−2 GeV
ϕ	flat	0−2π
pseudorapidity (η)	flat	-1 − 1
(x, y) origin	none	(0,0)
z_{vertex}	taken from data (Figure 7.1)	-30 − 30
decay info		
variable	distribution	range
ϕ^* (z-axis rotation)	flat	0−2π
$\cos\theta^*$ (x-axis rotation)	flat	0−1
single electron cuts		
	cut	
	$p_T > 180\ MeV$	
	$\|\eta\| < 0.5$	
	Eq 5.3 protracted by 0.2 radians	shown in Figure 7.1

Table 7.1: The generated input spectra parameters for PISA .

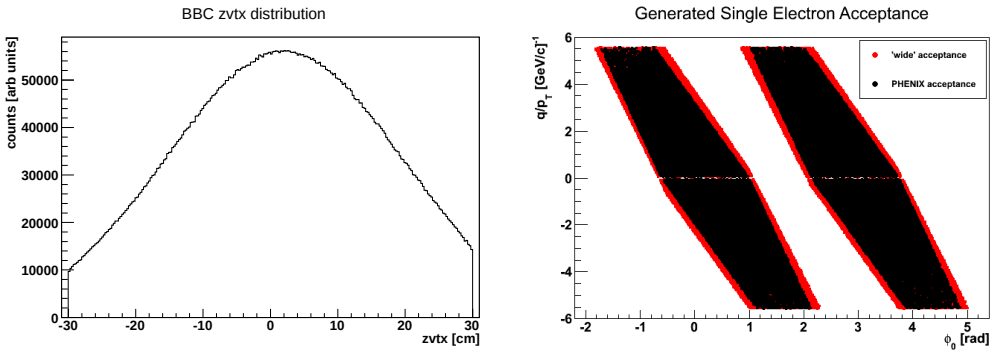

Figure 7.1: Left: The collision z_{vertex} distribution sampled from MinBias events at PHENIX. Right: The central arm acceptance for electrons at PHENIX. The red area shows the geometry into which particles were thrown into PISA and the black area is the actual PHENIX acceptance.

To save computing time, before the pair is run through PISA the decay electrons are checked to verify that they even fell *near* the PHENIX acceptance. If the electrons are nowhere near the detector it is an inefficient use of computing resources to run them through a full detector simulation. Therefore, the nominal PHENIX acceptance (parametrized by Eq 5.3) was extended by 0.2 radians and only those pairs which fall into the red area in Figure 7.1 are used for the efficiency calculation.

7.1.2 Weighting Function

In order to account for the inevitable bin-shift that results from any steeply falling spectrum, a weighting must be applied to both the input to PISA as well as the pairs from the simulated analysis of the PISA output. The weighting function is constructed from the cocktail shape along the mass axis and then uses generic m_T scaling (described in Section 8.1) to construct the p_T dependence.

There is one adaptation to the weighting function that must be made with respect to the mass dependence of the cocktail before it can be used. The resonance peaks create huge gradients in the spectrum making the calculated efficiency extremely sensitive to the difference between the simulated momentum resolution and the actual momentum resolution. Rather than have the reconstruction efficiency attempt to correct for the inherent momentum resolution, a nearly impossible task, the peaks are removed from the weighting function.

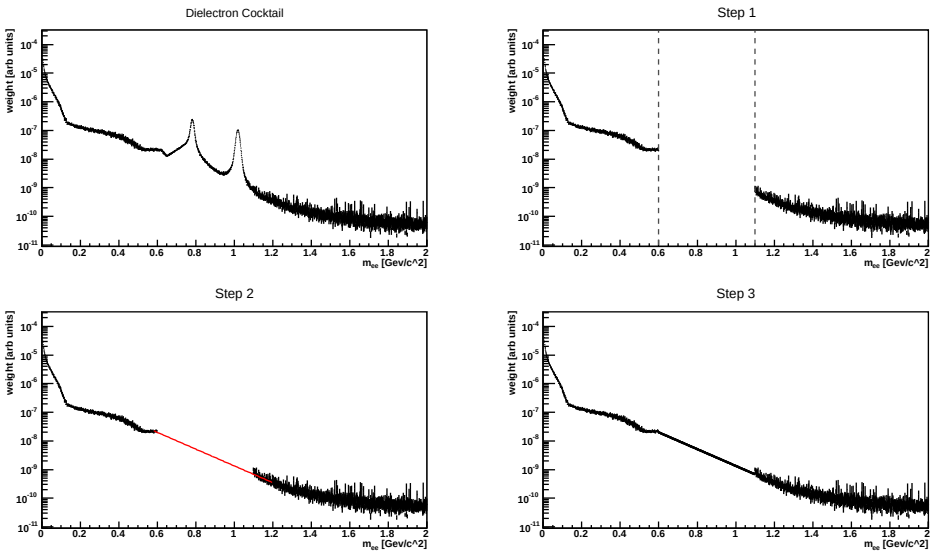

Figure 7.2: The 3 step process to remove the mass peaks from the efficiency weighting function.

This peak removal is accomplished via a 3 step process illustrated in Figure 7.2. First, in the region where a resonance resides, the points are removed from the spectrum. Next, a falling exponential function is fit across the newly created hole in the spectrum. Finally, the hole is filled back in by generating points from the fitted exponential. This creates a smoothly falling weighting function along the mass axis shown in Figure 7.3.

It is important to retain a map of which pair is which with respect to the PISA input and reconstructed output. The same weight must be applied to the pair on both ends of the simulation. Moreover, the weight that is used must be the weight of the original *input* pair mass and p_T.

Since the reconstruction process can shift a pair with a particular mass and p_T into a neighboring bin. Even if there is equal probability to shift the particle one way or another, a steeply falling exponential spectrum will result in more bins falling from higher in the spectrum to lower in the spectrum simply because there are more particles capable of moving in that direction. This weighting procedure ensures that any systematic bin-shifting of pairs that happens in the data is accounted for in the efficiency correction.

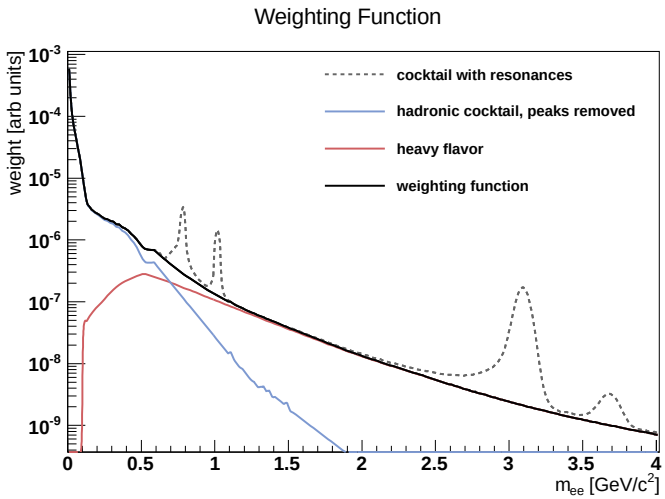

Figure 7.3: The mass dependence of the efficiency weighting function.

7.1.3 Efficiency Calculation

The PISA output is run through an imitation analysis which replicates all of the cuts and algorithms that the actual data encounters. The beauty of using GEANT3 based simulation software is that it replicates all of the known processes that occur inside the detector and allows access to the simulation output in the same format as actual data enabling a realistic analysis to be performed on it.

Finally, the nominal PHENIX acceptance (the black area in Figure 7.1 parametrized by Eq 5.3) is applied to both the simulated output as well as the input. It should be noted that this corrects the data to the phase space of what an idealized PHENIX detector would return. It does *not* correct the data to a 4π acceptance (nor even 2π). To fully acceptance correct the data to 4π one would need to know the polarization (and resulting kinematics) of the open heavy flavor decays. Currently, these are not known. Therefore, all dielectron measurements at PHENIX are reported with the caveat that the yield is what an ideal PHENIX detector would see.

A separate efficiency is calculated for every individual run group (see Section 5.2.2). Since the data is analyzed differentially in mass and p_T the efficiencies must be calculated and applied in the same space. One example of these is shown in Figure 7.4.

Over the course of the 2008, the detector live area (the primary determinant of the run groups) systematically degraded. Therefore, the reconstruction

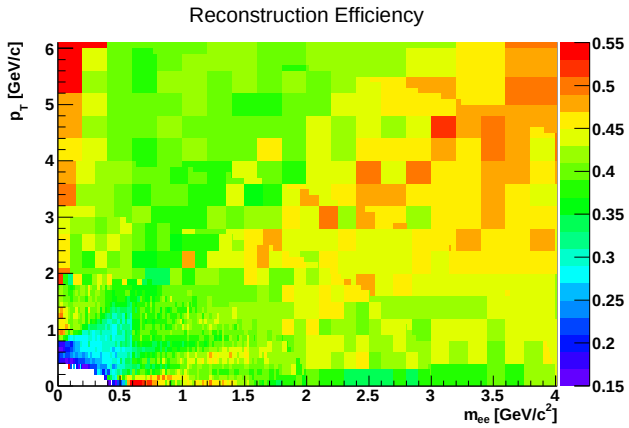

Figure 7.4: The 2D representation of the reconstruction efficiency.

efficiency only got lower as time passed. Moreover, most of the ERT triggered statistics were taken during the second half of the run (ie. more ERT triggered events and less MinBias events were recorded). In conjunction, the ERT energy threshold was raised (see Section 7.2.1) for the later half of the run. This led to there being a somewhat natural division between when the low mass (and p_T) statistics were taken and the higher mass (and p_T) statistics were collected.

To increase the high mass statistics, some cuts were also relaxed on the spectrum above the J/ψ ($m > 3.2\ GeV/c^2$). Specifically, the z_{vertex} requirement was released from $|z_{vertex}| \leq 17\ cm$ to $|z_{vertex}| \leq 30\ cm$ in addition to the ϕ_V cut being removed. Figure 7.5 shows the reconstruction efficiency as a function of mass for two analysis conditions:

- *low mass*: The reconstruction efficiency calculated for conditions early in the d+Au run with $|z_{vertex}| \leq 17\ cm$ and the regular ϕ_V cut (described in Table 5.4) (more representative of the spectrum below the J/ψ).

- *high mass*: The reconstruction efficiency calculated for conditions late in the d+Au run with $|z_{vertex}| \leq 30\ cm$ and the ϕ_V cut removed above 600 MeV/c^2 (more representative of the spectrum above the J/ψ).

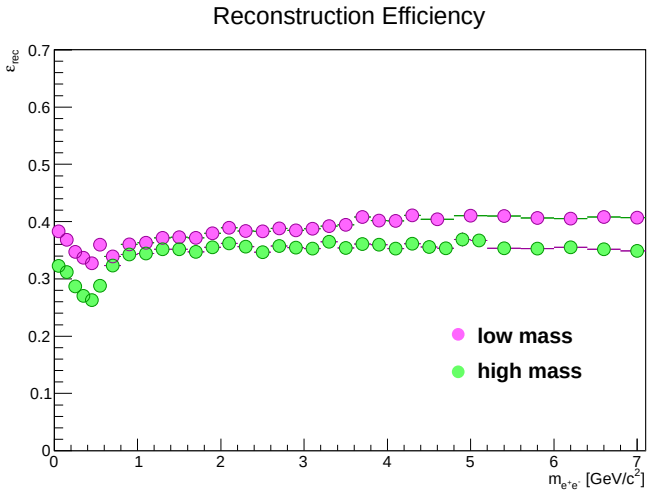

Figure 7.5: The mass projection of the reconstruction efficiency. The *low mass* (taken earlier in the run) and *high mass* (taken later in the run) designations are roughly representative of those regions of the spectrum (explained in the text).

7.2 Trigger Efficiency

> Democracy is the art and science of running the circus from the monkey cage.
>
> H. L. Mencken

7.2.1 ERT Overview

Collisions which produce a dielectron pair are extremely rare. Less than 1% of MinBias events contain a single electron (see Figure 5.4) resulting in less than $(1\%)^2$ events containing a pair. Moreover, to explore the high mass (and high p_T regime where the yield falls off by many orders of magnitude (for example, there is roughly a 5 order of magnitude difference between the pion and ψ' yield) it is necessary to implement an electron trigger which fires when an event is likely to contain a high p_T electron. This is called the ERT trigger (**E**MCal-**R**ICH **T**rigger) because it requires that there is a Cherenkov

ring deposited in the RICH that aligns spatially with an energy shower in the EMCal. A schematic diagram of the ERT trigger is shown in Figure 7.6.

The EMCal-RICH coincidence is determined in real-time and informs the data acquisition system (DAQ) whether to record the event. This is accomplished by using a look-up table to determine if the fired RICH trigger tile matches to a EMCal supermodule containing some minimum amount of deposited energy (set by the number of ADC counts). Since the algorithm checks the ADC counts (as opposed to the actual energy deposited), the energy threshold can only be approximately dialed in. During the 2008 d+Au run the energy threshold was nominally set to 600 MeV for roughly the first half the run and to 800 MeV for the second half.

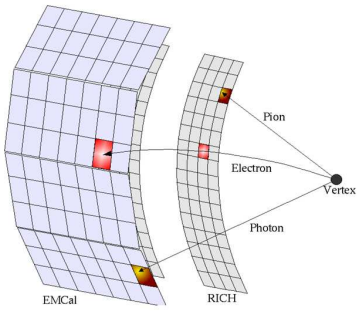

Figure 7.6: The principle scheme of the electron trigger.

7.2.2 Fitting Single Electrons

Requiring the ERT trigger to have fired in an event clearly biases the sample towards events with higher momentum electrons (obviously, since this is the point of the trigger!). This bias in the final e^+e^- mass and p_T spectra must be corrected for and determining the pair's trigger efficiency starts at the single electron level.

The efficiency of the ERT triggering electronics to fire on an electron was calculated as a function of p_T for each EMCal supermodule and for each RICH trigger tile for each run group separately. The trigger efficiency is calculated as

$$\varepsilon_{ERT} = \frac{N^e_{MB\&\&ERT}}{N^e_{MB}} \tag{7.1}$$

Though the calculation is performed with much finer granularity, for illustrative purposes the MinBias and ERT electron p_T spectra are shown in Figure 7.7 for each EMCal sector. In this figure, trigger dead areas have not been masked, which is evidenced by some of the spectra not converging at high p_T. The ratio of ERT to MinBias electrons (red to black in Figure 7.7) is the ERT trigger efficiency. An example of a typical trigger efficiency is shown in

Figure 7.8. The errors are calculated using Bayesian statistics since the ERT electrons are a sub-sample of the MinBias electrons.

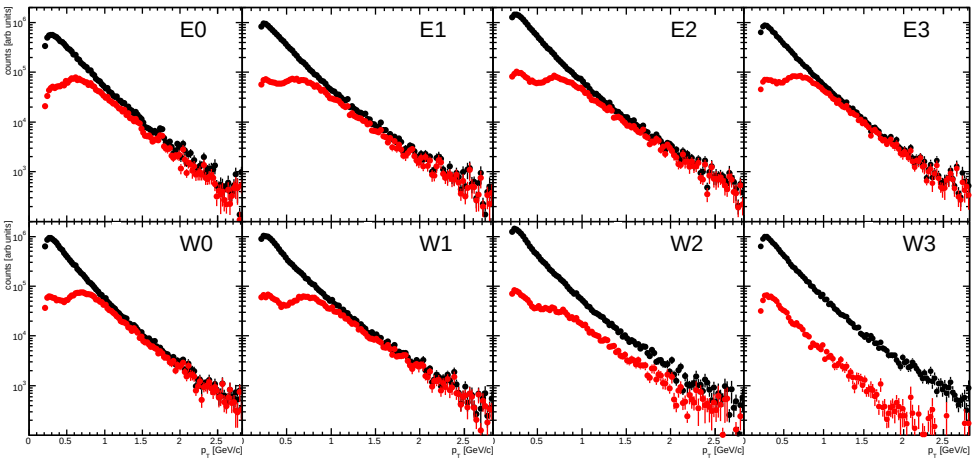

Figure 7.7: Single electron p_T distributions for MinBias (black) and ERT (red) events. Trigger dead areas have not been masked in these plots.

In order to parametrize ε_{ERT} as a function of p_T, a single Fermi function is insufficient. Therefore, the efficiency curves were fit using a combination of three Fermi functions:

$$\varepsilon_{ERT}(p_T) = F_{transition} \times F_{lowmom} + (1 - F_{transition}) \times F_{highmom} \tag{7.2}$$

where

$$F(p_T) = \frac{p_0}{\mathrm{e}^{-(p_T - p_1)/p_2} + 1}. \tag{7.3}$$

The parameters of F_{lowmom} are fixed by fitting in a momentum window from 300 - 700 MeV/c for the 600 MeV threshold (600 - 900 MeV/c for the 800 MeV threshold) and $F_{highmom}$ in a momentum window 0.6 - 3.5 GeV/c (0.8 - 3.5 GeV/c). The third Fermi function is used to transition between the two regions. The final fit using equation 7.2 is performed where the only free parameters are the p_1 and p_2 from $F_{transition}$ (p_0 is set to 1) and is shown in Figure 7.8. The single electron trigger efficiency spectra are well described by the resulting fits.

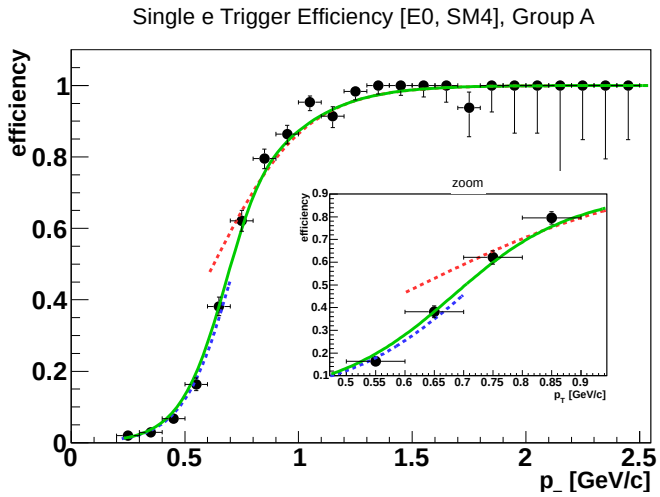

Figure 7.8: ERT trigger efficiency as a function of p_T for one supermodule. Inset shows a zoom of the region where the two Fermi functions are merged.

7.2.3 Pair Trigger Efficiency

There is a remaining issue which did not exist in previous dielectron analyses. During the 2005 Run, the trigger threshold was only ∼400 MeV and, even at low p_T, the single electron trigger efficiencies never got too close to zero. However, in 2008 the EMCal energy thresholds were high enough (600 and 800 MeV) that the single electron efficiencies were essentially zero at low momentum. Thus, while the fits describe the data extremely well, they suffer from a low p_T pedestal of false triggers from random overlaps with photons in the EMCal. This effect is illustrated in Figure 7.9. The problem is exacerbated in the *pair* trigger efficiency and can creep to as high as $m_T \approx 1.5$ GeV in the 600 MeV threshold data and $m_T \approx 2.0$ GeV for the 800 MeV dataset.

The upper panel in Figure 7.10 highlights the under correction of the data in the low m_T region. The p_T spectra of the pairs are plotted in a mass slice between $10 < m < 200$ MeV/c^2 for the MinBias dataset along with the two different trigger threshold ERT datasets. That the corrected ERT data does not match the MinBias is a clear indication that the pair trigger efficiency is not capable of correcting the triggered data fully to the MinBias. The solution is to simply not use the triggered data in any region where the correction is insufficient. However, rather than throw away so many statistics, a compromise was devised. If a post-production *software* requirement is enforced on the trigger particle (on the *single* electron), then we're able to recover the proper

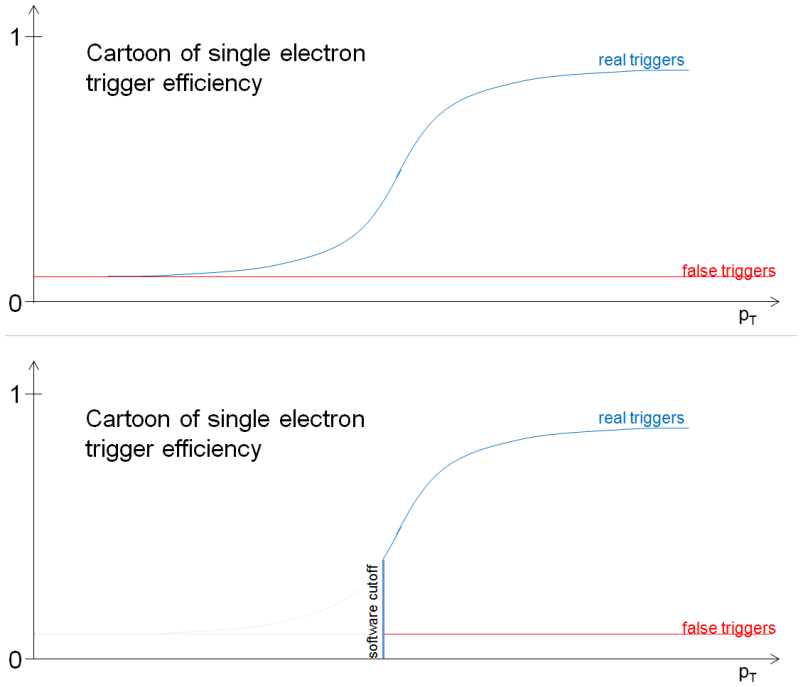

Figure 7.9: A cartoon of the single electron trigger efficiency.

pair trigger efficiency down to lower m_T. This sacrifices the very low m_T data in the triggered datasets – which is perfectly acceptable since those data were already uncorrectable using a traditional trigger requirement anyway! To satisfy the "new" trigger requirement the single trigger electron must additionally satisfy:

- *for 600 MeV threshold:* $p_T > 700\ MeV/c$
- *for 800 MeV threshold:* $p_T > 1\ GeV/c$

This requirement is depicted in the lower panel of the cartoon of Figure 7.9 and the result of its application is shown in the lower panel of Figure 7.10. Using this technique, the pairs highlighted in the upper panel of Figure 7.10 by shaded blue (600 MeV) and red (800 MeV) are recovered. However, all pairs below where the triggered spectra match the MinBias spectrum must be chucked. By looking at the p_T spectra in different mass slices, the range where the trigger is valid can be mapped out in mass vs p_T. This mass vs p_T trigger validity range is different for the two different trigger thresholds. However, it turns out that for both thresholds, when the trigger efficiency is above 25%, the correction is valid. Therefore, anywhere the trigger correction was $< 25\%$,

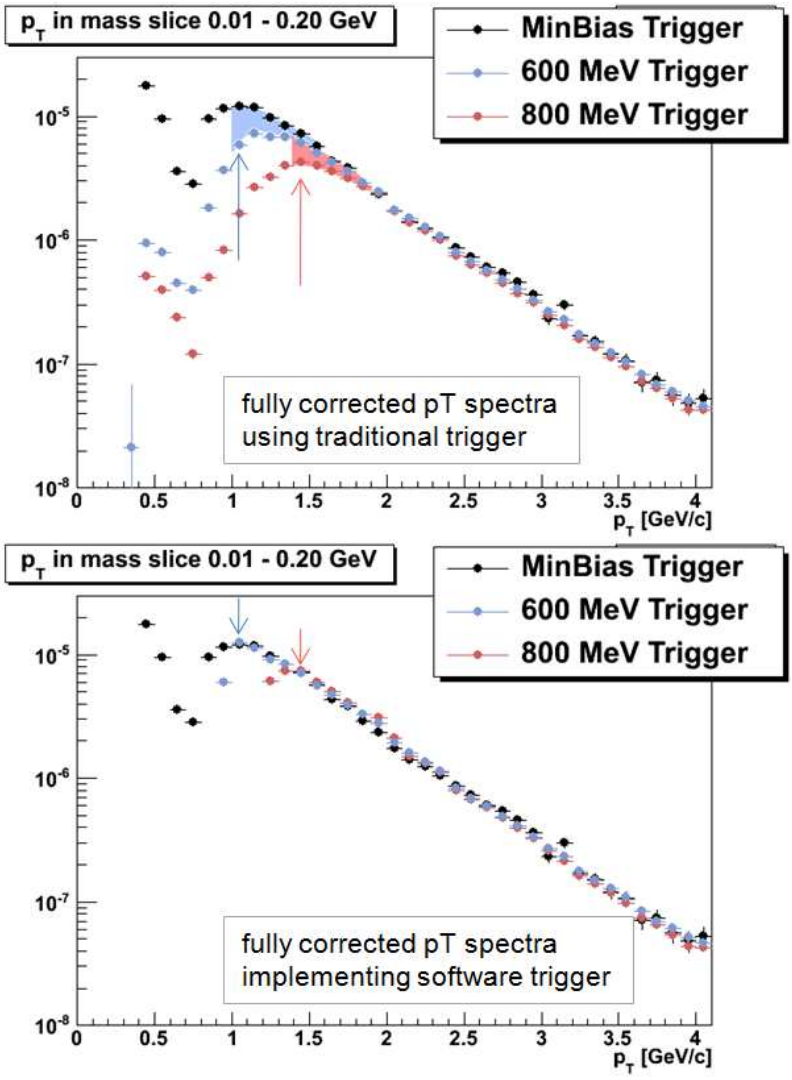

Figure 7.10: Pair p_T spectra at low mass. Upper panel: using traditional ERT trigger. Lower panel: using traditional trigger with additional software cutoff.

the e^+e^- pair trigger efficiency was set to zero. Figure 7.11 shows the final pair trigger efficiency for each trigger threshold.

For every Monte Carlo e^+e^- pair, the pair's trigger efficiency is calculated by the convolution of the two single electron trigger efficiencies:

$$\varepsilon^{ERT}_{e^+e^-}(m_{_{e^+e^-}}, p_{T_{e^+e^-}}) = 1 - [1 - \varepsilon_{e_1}(p_{T_{single}})][1 - \varepsilon_{e_2}(p_{T_{single}})] \tag{7.4}$$

While the efficiencies are applied to the data two dimensionally (mass and

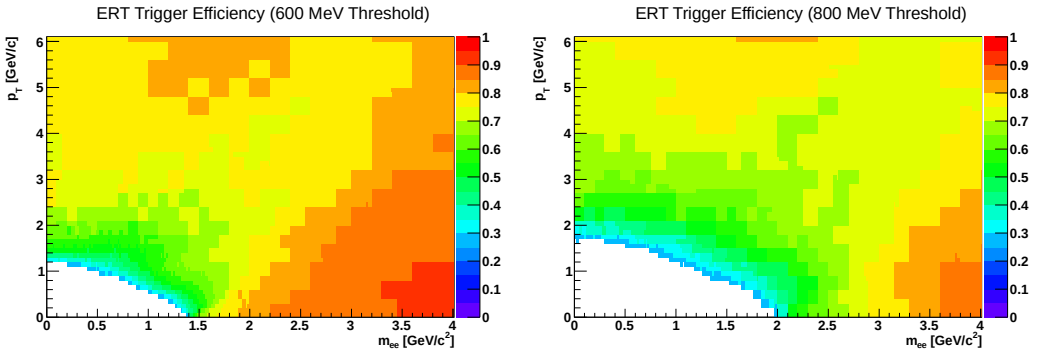

Figure 7.11: ERT trigger efficiencies including software cutoffs (for singles) and 25% hard edge for pairs.

p_T), it's easier to visualize the effect of the trigger when projected onto one axis or the other. The pT integrated ERT trigger efficiencies are shown as a function of pair mass in Figure 7.12. The two arm acceptance can be seen in the 600 MeV ε_{ERT} as a dip near 500 MeV/c^2. However, in the 800 MeV threshold efficiency the pairs that comprise the single arm acceptance are nearly completely washed out by the stringent trigger requirements.

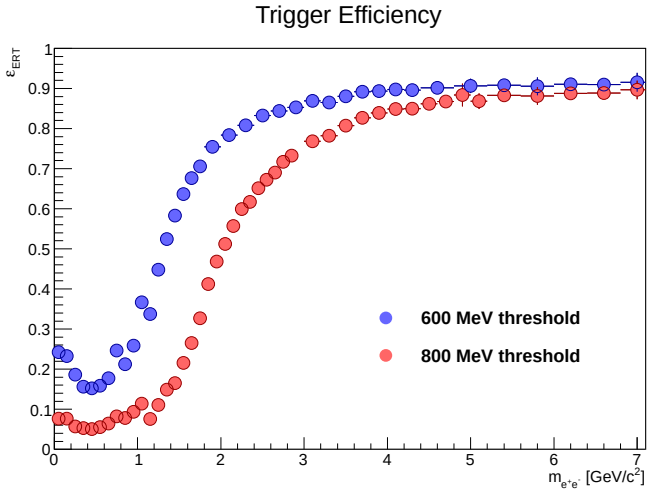

Figure 7.12: ERT trigger efficiencies including software cutoffs (for singles) and 25% hard edge for pairs projected onto the mass axis.

7.3 Summary of Efficiencies

> Patience is hangin' on through the bad times; stamina is hangin' on through the good.
>
> Katy Tschann-Grimm

7.3.1 Mass Summary

To summarize the mass dependence of the efficiency corrections, Figure 7.13 shows the effect of the reconstruction efficiency plotted simultaneously with the ERT trigger efficiency. The left panel shows ε_{rec} for run group B taken early in the 2008 Run with the standard analysis cuts as well as ε_{ERT} for the 600 MeV trigger threshold. These efficiencies are representative of what is applied at low mass and low p_T. The right panel shows ε_{rec} from run group C1 with the cuts optimized for high mass and p_T discussed in Section 7.1.3. The trigger efficiency shown is for the 800 MeV threshold. These efficiencies are more representative of what was used for the higher mass and p_T regions of the spectrum.

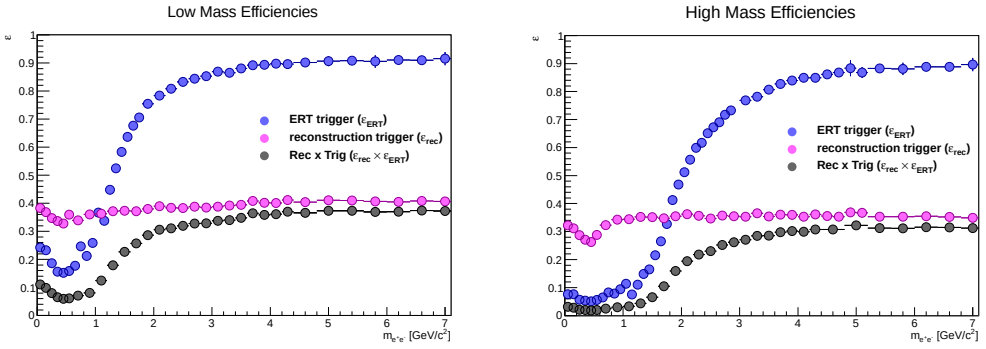

Figure 7.13: p_T integrated ε_{rec}, ε_{ERT} and $\varepsilon_{rec} \times \varepsilon_{rec}$ as a function of mass.

7.3.2 p_T Summary

To visualize the p_T dependence of the efficiencies, Figure 7.14 shows both ε_{rec} and ε_{ERT} for various mass ranges. The color code is given in the lower

right panel. The effect of the ERT trigger can be seen to decrease as higher mass. Below the J/ψ the trigger removes a substantial amount of low p_T pairs whereas above $\sim$4 GeV/c^2 the efficiency is nearly flat.

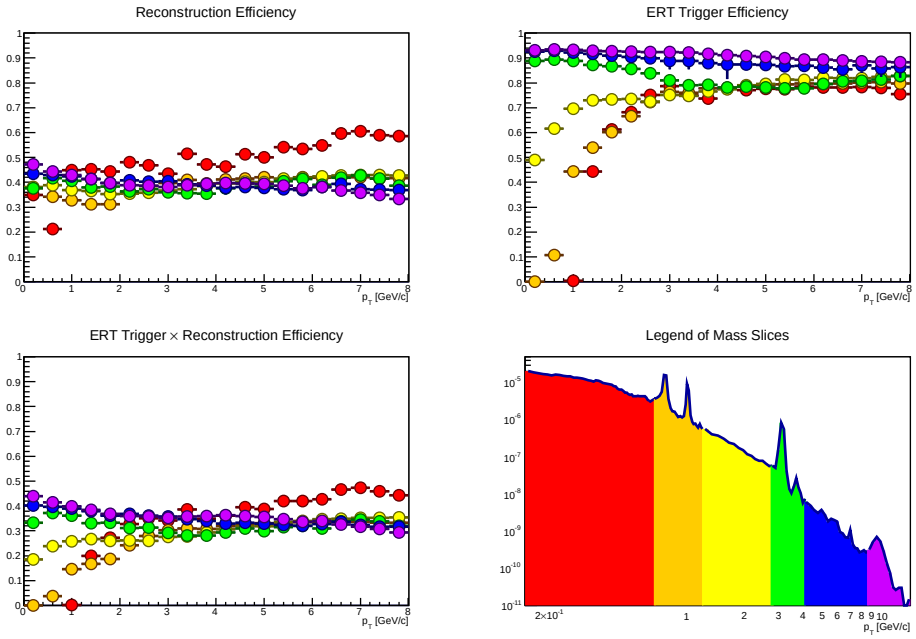

Figure 7.14: ε_{rec}, ε_{ERT} and $\varepsilon_{rec} \times \varepsilon_{rec}$ as a function of p_T for various mass slices.

7.3.3 Consistency Checks

> If I tell you a rooster dips snuff, you better lift his wing and look for a tin.
>
> Terry Bradshaw

As an internal consistency check, Run Groups A1, A2 and B can be fully corrected, both for reconstruction and trigger efficiency, and checked against one another as they are all within the 600 MeV threshold triggered data sample. They differ in the following respects:

- Group B: "normal" trigger efficiency, "normal" acceptance in PC1.

- Group A1: low ε_{trig} in 1 EMCal sec, "normal" acceptance in PC1.
- Group A2: low ε_{trig} in 1 EMCal sec, dead area in PC1 west.

Therefore, these groups provide a convenient cross check for the efficiency corrections. Specifically, without any efficiency corrections applied the spectra from the different Run Groups should be ordered, from highest to lowest yield, B, A1, A2. The left panel of Figure 7.15 shows the raw spectra for these three groups.

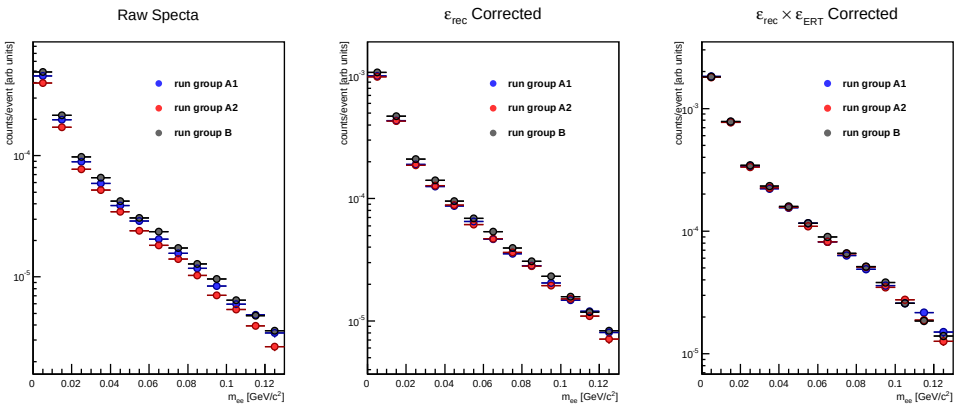

Figure 7.15: Mass spectra for run groups A1, A2 and B. Left: Raw spectra, the groups are ordered as expected. Center: Corrected for ε_{rec}, A1 and A2 merge. Right: Corrected for ε_{rec} and ε_{ERT}, all spectra match.

When the reconstruction efficiency is applied (but *not* the trigger efficiency) Groups A1 and A2 come together (Figure 7.15, center panel) but not up to Group B. This is exactly as expected since A1 and A2 only differ by their dead area in the PC1. Furthermore, after the trigger efficiency correction is applied (in addition to the reconstruction efficiency), Groups A1 and A2 are brought up to match Group B. This exercise illustrates that the analysis machinery for calculating and applying the efficiencies is self-consistent.

Another useful cross check is to look at all the different dataset (with all of their different efficiencies applied) to verify their consistency. Unfortunately, because of the different validity ranges for the trigger efficiencies, this check cannot be done below $\sim$2 GeV/c^2 (refer to Figure 7.11). Therefore, the region where the MinBias statistics are sufficient for a legitimate comparison is around the J/ψ peak. The comparison between the all of the 2008 datasets is shown in Figure 7.16. The good agreement confirms the internal consistency of the analysis.

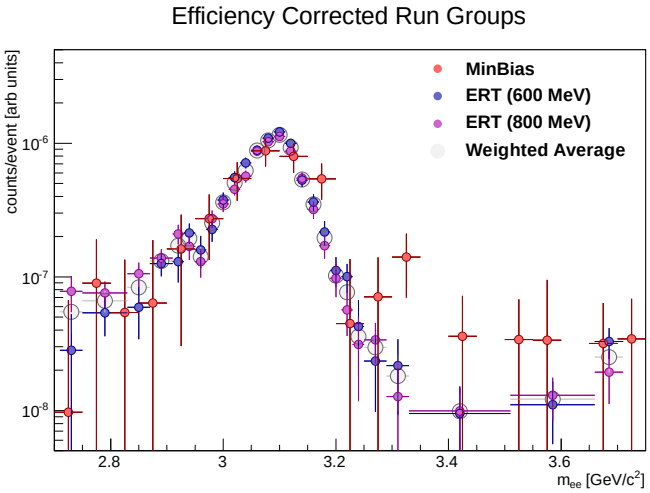

Figure 7.16: Fully efficiency corrected spectra compared at the J/ψ peak. In this region all datasets should agree.

For the final spectra, the weighted average is taken of all 10 datasets (5 run groups in both MinBias and ERT triggers) differentially in mass and p_T. The weight is determined by the number of Minimum Bias events in each dataset. It should be noted that the ERT data is ignored in the region where it is set to zero; the zeros do *not* contribute to the weighted average.

Figure 7.17 shows the effect of applying the final efficiencies to the raw data. While the efficiencies affect the overall yield, they do not appreciably distort the underlying shape of the dielectron spectrum.

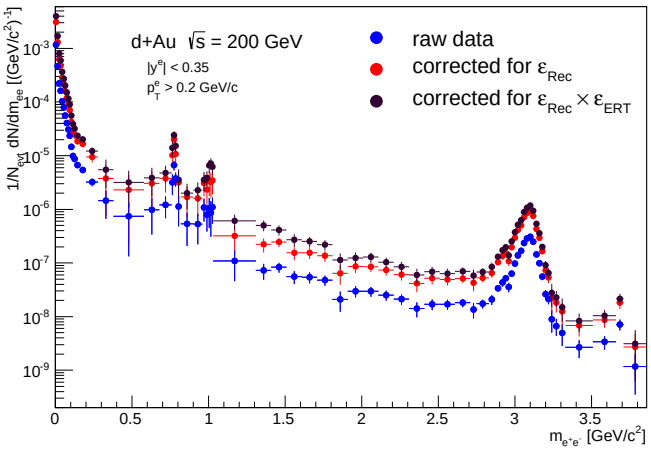

Figure 7.17: The effect of applying the reconstruction and trigger efficiencies to the raw data.

7.4 Systematic Uncertainty

> Irrationally held truths may be more harmful than reasoned errors.
>
> Thomas Henry Huxley

An important step in any credible measurement is determining what one does *not* know and estimating how much of an uncertainty that introduces to the result. There are a number of procedures in the analysis that lead to uncertainties and they are outlined in Table 7.2.

The uncertainty on the e^+e^- pair reconstruction is twice the uncertainty of the single electron efficiency [71] [60]. It includes the corrections due to ε_{Rec}, electron ID efficiency and geometric acceptance correction and is determined by varying the eID cuts, different acceptance corrections and incorporating known track reconstruction efficiencies [20]. Determining the systematic uncertainty on the conversion rejection cut as well as other pairs cuts is achieved by varying those cuts and running the analysis chain to see how the result is affected. The uncertainty due to the implementation of the electron trigger (ERT) is deduced by comparing the fully corrected triggered dataset to the Minimum Bias dataset and recording the variations. Uncertainties related to detector dead areas and run group variations are determined by the observed variations in the run QA (Sections 5.2.1 and 5.2.2).

By far, the largest contributor to the systematic uncertainty is the accuracy with which the relative acceptance correction is known. It is a function of the S/B since it's a correction to the background which gets subtracted from the sum of signal plus background. For this reason, an in depth Monte Carlo based study was performed to determine the extent to which this correction is controlled. In a Toy Monte Carlo[1] simulation of e^+e^- pairs was run into the nominal (refer to Section 7.1.3) PHENIX acceptance with different pieces of the detector removed. The area of the regions removed was chosen to be realistic both with regard to the typical size (of things like electronic boards failing, eg.) as well as what is on the edge-of-identifiable in the QA run group analysis. After removing random regions for many (hundreds of) regions, the variations in the calculable relative acceptance correction, α, as a function of mass is

[1]The vernacular use of the word "Toy" here simply refers to the fact that a full GEANT [73] simulation was not performed. It is *not* meant to imply that it shouldn't be taken seriously.

summarized in Figure 7.18. The variations are less than ±5% (shown by the gray bands) and a 5% uncertainty is assigned to the background determination. This leads to a signal-to-background dependent uncertainty of $5\% \cdot B/S$.

Table 7.2: Systematic uncertainties of the dilepton yield due to different sources with an indication of the applicable mass range.

Syst. Uncert. component	d+Au	Mass Range (GeV/c^2)
pair reconstruction	14%	0–14
conversion rejection	6%	0–0.6
pair cuts	5%	0.4–0.6
ERT efficiency	5%	$m_T \geq 1.5$
combinatorial background	$3\% \cdot B/S$	0–14
dead area cor, run groups	15%	0–2.5
	10%	2.5–14
relative acceptance cor	$5\% \cdot B/S$	0–2.5
	$2\% \cdot B/S$	2.5–5
	$1\% \cdot B/S$	>5

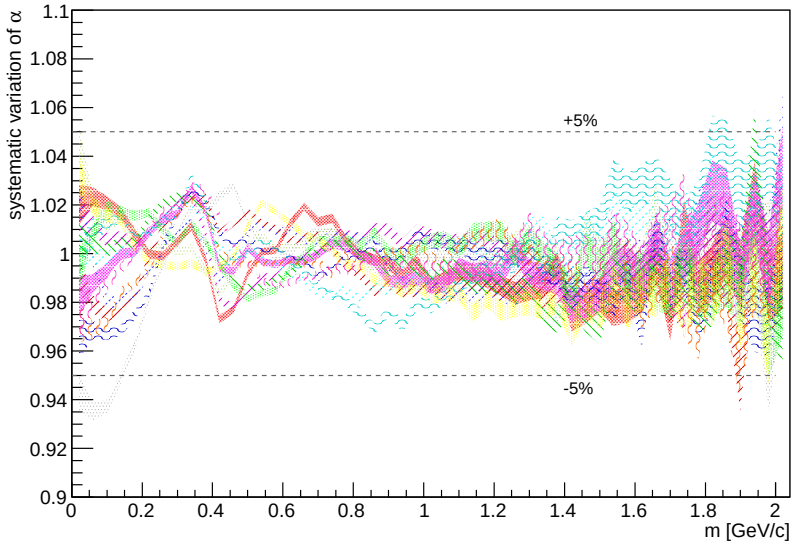

Figure 7.18: The systematic variation of the relative acceptance correction when small random pieces of the detector are removed.

Part IV

Expected Sources

CHAPTER 8

Monte Carlo Simulations

The mass vs p_T dielectron landscape is sufficiently complex that a full understanding of its shape must be constructed through the decomposition of all the leptonic sources in a collision. Therefore, a realistic simulation of the expected sources is crucial to interpret the data. The benefit of constructing a full component-by-component simulation is two-fold. Firstly, it serves as a benchmark for the dilepton analysis while yielding insight as to where excesses or suppressions might be found in the spectra. In addition, it allows for a detailed, simultaneous evaluation of each dilepton ingredient while providing a mechanism to extract specific physics quantities.

Within the PHENIX collaboration a detailed fast Monte Carlo software package called EXODUS has been developed for hadronic decays. EXODUS is fundamentally based on the rapidity density, dN/dy, of neutral and charged pions as well as the relative yield of other various hadrons. The open heavy flavor simulation is performed with the MC@NLO package [58], which performs next-to-leading-order calculations for open charm and beauty semi-leptonic decays.

8.1 Hadronic Cocktail

> Everybody has to believe in something. I believe I'll have another drink.
>
> W. C. Fields

EXODUS takes a parametrization of the p_T dependence of the invariant cross section of neutral and charged pions as primary input. The pion p_T distributions, as reported by PHENIX [59] [17], were fit to a modified Hagedorn function:

$$E\frac{d^3\sigma}{dp^3} = A\left(\mathrm{e}^{-\left(ap_T+bp_T^2\right)} + p_T/p_0\right)^{-n} \tag{8.1}$$

Table 8.1 shows the fit values and uncertainties. In addition to the pions, the other hadrons were parametrized utilizing the observed phenomenon of m_T *scaling*. The modified Hagedorn function (Equation 8.1) can be used to fit the p_T spectra of the other hadrons by fixing all free parameters except the amplitude, A, and replacing

$$p_T \rightarrow \sqrt{p_T^2 - m_{\pi^0}^2 + m_h^2} \tag{8.2}$$

where m_h is the mass of the hadron. The fit of the overall normalization then relates the total dN/dy of a given hadron to the dN/dy of the pions. This ratio is then used as input to the EXODUS simulation. The successful description of m_T scaling is apparent in Figure 8.1 which shows the p_T spectra for the π^0, $\pi^{\pm}$, η, ω, ϕ, and J/ψ. For the mesons that have not yet been measured in PHENIX, namely η', ρ, and ψ', the yield is assumed to scale the same as in p+p collisions with respect to the nearest meson in mass. For example, the ω is the closest meson in mass to the ρ, so the ρ/π ratio is found by

$$\frac{(\rho/\pi)^{dAu}}{(\omega/\pi)^{dAu}} = \frac{(\rho/\pi)^{pp}}{(\omega/\pi)^{pp}} \tag{8.3}$$

Table 8.2 is a compilation of the meson/π ratios used as input to EXODUS in the d+Au analysis (as well as p+p and Au+Au).

EXODUS applies the branching ratios [37] and implements the decay kinematics according to [60]. The electrons undergo both internal and external bremsstrahlung. External bremsstrahlung is approximated by placing all detector material to be traversed by the electron at the radius of the

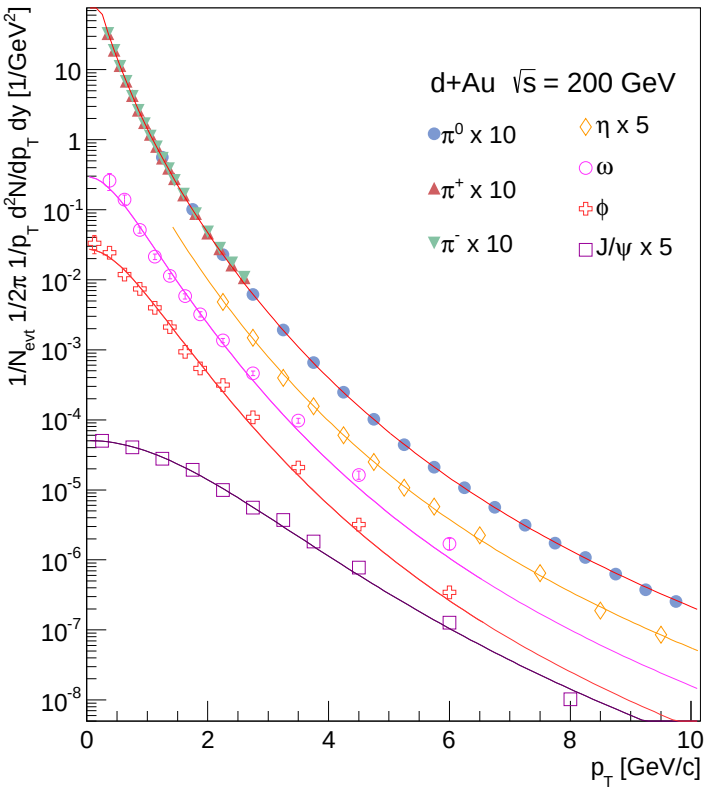

Figure 8.1: Compilation of meson invariant yields in d+Au collisions. The data are compared to the parametrization based on m_T scaling.

beampipe. The Dalitz decays ($\pi^0, \eta, \eta' \rightarrow \gamma e^+e^-$) as well as $\omega \rightarrow \pi^0 e^+e^-$ are treated with the Kroll-Wada expression [61] and the electromagnetic form factors measured by the Lepton-G collaboration [62, 63]. The vector mesons ($\rho, \omega, \phi, J/\psi, \psi' \rightarrow e^+e^-$) are assumed to be unpolarized and for their decay the Gounaris/Sakurai expression is used [64]. For Dalitz decays in which the third body is a photon, the angular distribution is sampled according to $1+\lambda \cos^2 \theta_{CS}$ distribution. θ_{CS} is the polar angle of the electrons in the Collins-Soper frame. Finally, EXODUS filters the e^+e^- pairs into the PHENIX acceptance (Section 5.2.1) while applying the measured momentum resolution from the 2008 RHIC run (Section 4.4.3).

Figure 8.2 shows the resulting expected invariant mass spectrum, referred to as the *cocktail*, (including open heavy flavor, to be discussed in Section 8.2).

Parameter	$p+p$	d+Au	Au+Au
$\frac{dN}{dy}\Big\|_{y=0}$	1.06 ± 0.11	5.42 ± 0.79	95.7 ± 6.9
A [mb GeV$^{-2}c^3$]	377 ± 60	37.099 ± 0.370	504.5 ± 10
a [(GeV/c)$^{-1}$]	0.356 ± 0.014	0.3275 ± 0.0016	0.52 ± 0.007
b [(GeV/c)$^{-2}$]	0.068 ± 0.019	0.0909 ± 0.0007	0.16 ± 0.010
p_0 [GeV/c]	0.7 ± 0.02	0.7748 ± 0.0011	0.7 ± 0.005
n	8.25 ± 0.04	8.3176 ± 0.0017	8.27 ± 0.02

Table 8.1: Fit parameters from the modified Hagedorn function (Equation 8.1) for $p+p$, d+Au , and Au+Au pion spectra (π^0 and $\pi^{\pm}$) and the corresponding rapidity density dN/dy.

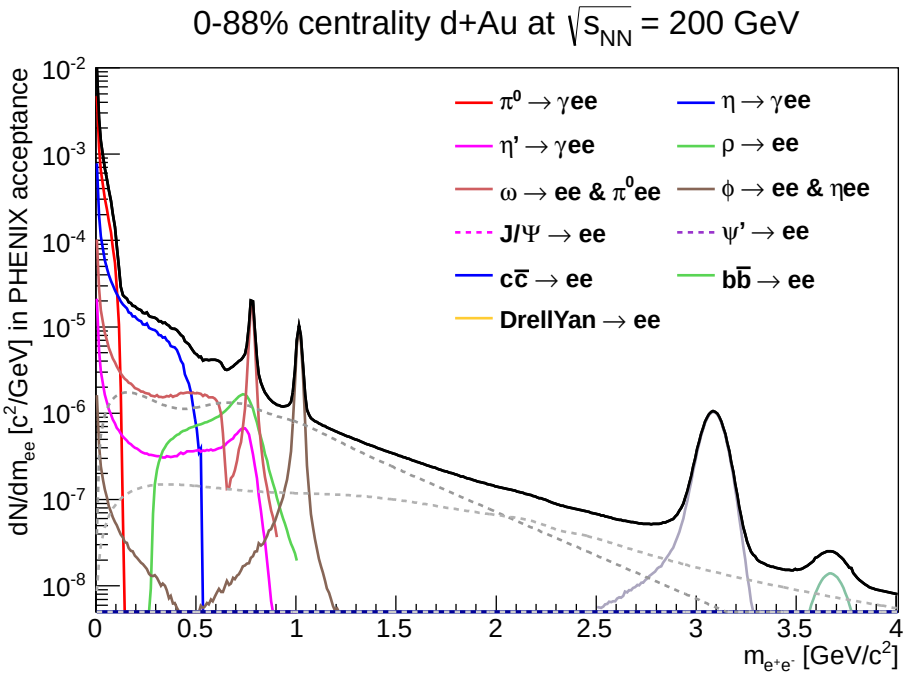

Figure 8.2: Expected invariant mass spectrum of e^+e^- pairs from hadronic decays in d+Au collisions at $\sqrt{s_{NN}} = 200$ GeV from Exodus .

	d+Au	p+p	Au+Au	d+Au data source
π^0	1.0	1.0	1.0	PPG044
η	0.1237	0.1032	0.112	PPG044
η'	0.0152	0.0127	0.02146	rel to $p+p$ PPG088
ρ	0.1106	0.0834	0.0898	rel to $p+p$ PPG088
ω	0.0971	0.0732	0.1032	AN840/PPG118
ϕ	0.0126	0.0084	0.0214	AN840/PPG096
J/ψ	2.23×10^{-5}	1.66×10^{-5}	1.82×10^{-5}	PPG125(PPG038,PPG078)
ψ'	3.15×10^{-6}	2.3×10^{-6}	2.7×10^{-6}	rel to $p+p$ PPG088
$\Upsilon(1S)$	2.09×10^{-7}	not used	not used	PPG142
$\Upsilon(2S)$	4.88×10^{-8}	not used	not used	PPG142
$\Upsilon(3S)$	2.87×10^{-8}	not used	not used	PPG142

Table 8.2: Input parameters for EXODUS . The uncertainties for the d+Au ratios are dominated by the dN/dy of the pions ($\sim$15%) for all except the Υ states, which are $\sim$90%.

8.2 Heavy Flavor Simulations

> If you hang around the barber shop long enough, sooner or later you're gonna get a haircut.
>
> Lynne Washington

Other than the hadronic contributions previously discussed, the remaining e^+e^- pairs come from open heavy flavor decays and Drell-Yan. Open heavy flavor decays are ones that come from the semi-leptonic decays of D and B mesons, which are correlated through flavor conservation. Past dielectron analyses in PHENIX have used PYTHIA (vers. 6.205 with the CTEQ5L parton distribution function), which is based on leading order pQCD calculations, to simulate both the open heavy flavor and Drell-Yan contributions to the spectrum.

However, for the d+Au analysis the MC@NLO (vers. 4.06 with the Les Houches Accord PDF [66]) [58] is used to calculate the initial hard scattering at the next-to-leading-order. Hard scattering events are generated with three bodies in the final state: $QQ \to c\bar{c}+X$ for open charm and $QQ \to b\bar{b}+X$ for open beauty. These events are subsequently fed to HERWIG (vers. 6.520) [65] for fragmentation into the vacuum. Additionally, MC@NLO calculates from first principle the total cross sections for open charm and beauty, $\sigma_{c\bar{c}} = 364\mu b$

and $\sigma_{b\bar{b}} = 1.96\mu b$. While this is lower than previously measured PHENIX dielectron results [70], it is within a factor of 2 and provides a reasonable anchor for measuring these cross sections in the d+Au data.

A large number of events are necessary for the simulation to be useful. This is primarily because MC@NLO generates the events in 4π and the PHENIX detector acceptance cuts out the vast majority of them. The rapidity distribution of single electrons from $c\bar{c}$ and $b\bar{b}$ events is shown in Figure 8.3. PHENIX's rapidity acceptance is $Y \leq \pm 0.35$ which cuts out roughly 82% of all single electrons. The two arm acceptance approximately cuts another factor of 2x while the p_T cut of 200 MeV/c removes another ~40%. Accounting for the particle ratios $D^+/D^0 = 0.45 \pm 0.1$, $D_s/D^0 = 0.25 \pm 0.1$, and $\Lambda_c/D^0 = 0.1 \pm 0.05$ and their respective branching ratios [37], the total branching ratio of $c \to e$ is $9.5\% \pm 1\%$. Naively, the probability to accept the pair is the square of the probability for the single thereby leaving roughly 1.3×10^{-3} % of e^+e^- pairs from open heavy flavor. Though merely a rough estimate, this number is actually within ~10% of the actual answer ($\sim 1.4 \times 10^{-5}$ e^+e^- pairs per generated NLO $c\bar{c}$ event). The situation is slightly less grim for $b\bar{b}$ ($\sim 3.5 \times 10^{-4}$ e^+e^- pairs per generated NLO $b\bar{b}$ event). Therefore, 2 billion open charm events and 1 billion open beauty events were simulated with MC@NLO .

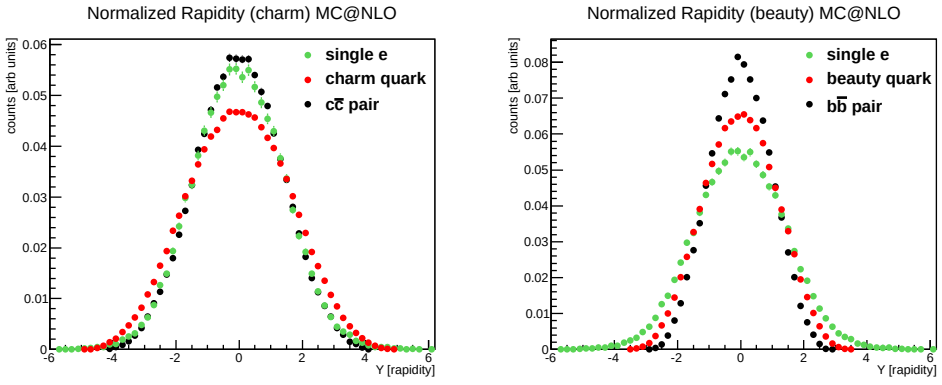

Figure 8.3: Rapidity distributions for $c\bar{c}$ and $b\bar{b}$ events.

Additionally, the Fixed-Order-Next-to-Leading-Log (FONLL) [67] calculation used for the PHENIX single electron heavy flavor publication [60] was extended to the dielectron channel. This is based on a leading order pQCD calculation augmented by the logarithmic terms at leading order and renormalized. All three calculations are compared in Section 8.2.4.

8.2.1 Open Charm

The following modifications have been made to the default MC@NLO configuration:

- ECM = 200 ($\sqrt{s_{NN}} = 200\ GeV$)
- CMASS = 1.29 (GeV/c^2, c mass fed to HERWIG)
- BMASS = 4.67 (GeV/c^2, b mass fed to HERWIG)
- HQUARK = 1.29 (GeV/c^2, heaviest quark mass)
- PROCESSID = -11704 ($QQ \rightarrow c\bar{c}+X$)
- PDFLIBRARY = LHAPDF (Les Houches Accord PDF)

In addition, being designed for LHC conditions, the default MC@NLO does not support the open charm processes (on the other hand, it does support the open beauty). Therefore, further modifications were made to the default code to enable this process.

Additionally, MC@NLO calculates the cross section for open charm $\sigma_{c\bar{c}} = 364\ \mu b$ corresponding to $d\sigma_{c\bar{c}}/dy = 103\ \mu b$. The measured value from the di-electron channel in p+p collisions at PHENIX is $\sigma_{c\bar{c}} = 544 \pm 39(\text{stat}) \pm 142(\text{syst}) \pm 200(\text{model})\ \mu b$ [70]. Meanwhile, the measured value from the single electron channel at PHENIX is $\sigma_{c\bar{c}} = 551 \pm 57(\text{stat}) \pm 195(\text{syst})\ \mu b$ [71] ($d\sigma_{c\bar{c}}/dy = 119\ \mu b$).

8.2.2 Open Beauty

For $b\bar{b}$, the following modifications have been made to the default MC@NLO configuration:

- ECM = 200 ($\sqrt{s_{NN}} = 200\ GeV$)
- CMASS = 1.29 (GeV/c^2, c mass fed to HERWIG)
- BMASS = 4.67 (GeV/c^2, b mass fed to HERWIG)
- HQUARK = 4.67 (GeV/c^2, heaviest quark mass)
- PROCESSID = -11705 ($QQ \rightarrow b\bar{b}+X$)
- PDFLIBRARY = LHAPDF (Les Houches Accord PDF)

Additionally, MC@NLO calculates the cross section for open beauty $\sigma_{b\bar{b}} = 1.96\ \mu b$ corresponding to $d\sigma_{b\bar{b}}/dy = 749\ nb$. The measured value from the dielectron channel in p+p collisions at PHENIX is $\sigma_{b\bar{b}} = 3.9 \pm 2.5(\text{stat})^{+3}_{-2}(\text{syst})\ \mu b$ [70].

8.2.3 Drell Yan

Drell-Yan production is the process when a quark from an incoming nucleus annihilates with an anti-quark from the other incoming nucleus to produce either a virtual photon or Z boson that decays to dileptons [30]. At the accessible masses in this analysis, Drell-Yan pairs always come from a virtual photon ($q\bar{q} \rightarrow \gamma^* \rightarrow \ell^+\ell^-$). The Drell-Yan contribution used is generated with PYTHIA [69] with an input cross section $\sigma_{DY} = 42 \pm 42nb$ [72].

8.2.4 Heavy Flavor Comparisons

While, in principle, the next-to-leading-order calculation from MC@NLO is the superior prediction for open heavy flavor, it's still instructive to compare it to the established calculations (PYTHIA , FONLL). In order to put every calculation on the same scale, the cross-sections were all set to the measured values in [70], $\sigma_{c\bar{c}} = 544\ \mu b$ and $\sigma_{b\bar{b}} = 1.96\ \mu b$. Figure 8.4 shows a comparison of the predicted dielectron spectra from open charm pairs. It should be noted that the MC@NLO spectrum includes the feed-down pairs from $D \rightarrow \kappa \rightarrow e$ while the PYTHIA and FONLL excludes these pairs. Figure 8.5 highlights the comparison of the open beauty continuum while Figure 8.6 compares the sum of charm and beauty. The MC@NLO beauty also includes feed down (and double feed down) pairs analogous to the charm via $B \rightarrow D \rightarrow e$.

An interesting observation is that, while the different calculations for the charm and beauty individually have quite different shapes from one another, their *sums* are actually reasonably similar above $\sim$2 GeV/c^2. Additionally, for the same input cross section, the yields appear quite different. This is simply a reflection of *where* the pairs fall in the mass vs p_T plane as the PHENIX acceptance tends to cut out many more pairs with $m \approx p_T$ (having an opening angle close to 90°) than pairs that lie close to either axis.

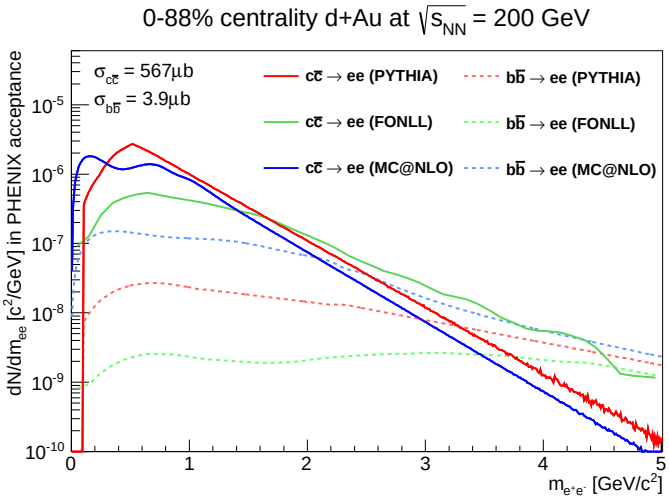

Figure 8.4: Comparisons of the open charm (and open beauty) dielectron spectra from PYTHIA , FONLL (Vogt), and MC@NLO .

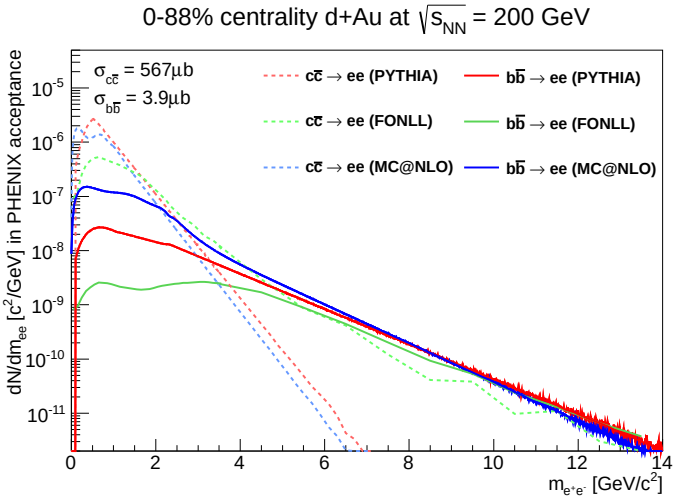

Figure 8.5: Comparisons of the open beauty (and open charm) dielectron spectra from PYTHIA , FONLL (Vogt), and MC@NLO .

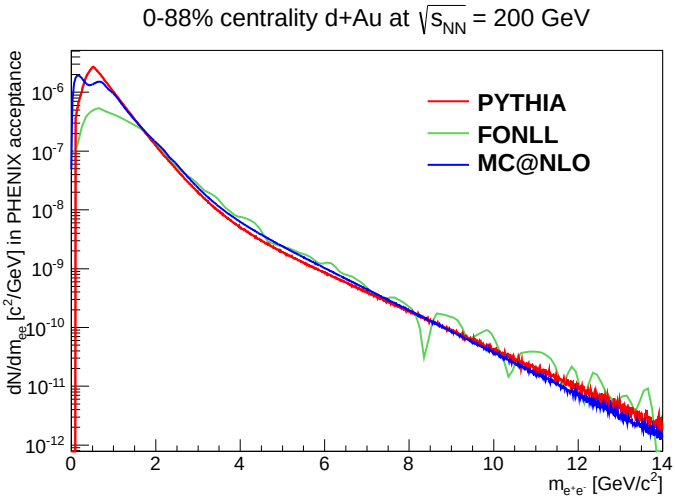

Figure 8.6: Comparisons of the sum of open charm and open beauty dielectron spectra from PYTHIA , FONLL (Vogt), and MC@NLO .

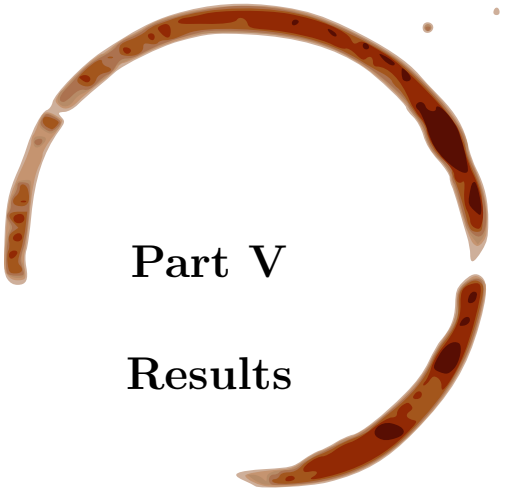

Part V

Results

Of the sweeping array of measurements that can be coaxed out of such a comprehensive dielectron dataset, this thesis primarily focuses on two categories; The low mass yields are used as a control experiment to bridge the gap between p+p and Au+Au by isolating any cold nuclear matter effects which exist in heavy ion collisions while the high mass yields illuminate the characteristics of heavy flavor production.

Additionally, utilizing the p_T axis to dissect the low mass region into its hadronic components allows for a detailed understanding of the spectral makeup of the continuum regions in between the vector meson peaks. The centrality dependence of the spectra test binary scaling of hard scattering as well as bridge the gap between the N_{Coll} probed by p+p collisions (simply 1) and heavy ions (both Cu+Cu and Au+Au).

Using the thorough understanding of the hadronic constituents gained in Section 9.3, the heavy flavor spectrum can be isolated and studied. The cross-sections for open charm ($\sigma_{c\bar{c}}$) and open beauty ($\sigma_{b\bar{b}}$) are extracted using MC@NLO as a theoretical reference. The $<N_{Coll}>$scaled d+Au p_T spectra of open charm and beauty are compared to both the p+p dielectron dataset as well as MC@NLO .

CHAPTER 9

d+Au as a Control Experiment

Back off man! I'm a scientist!!

Peter Venkman, Ph. D.
Ghostbusters

9.1 Comparison to p+p

The first measuring stick to lean against the d+Au data is the simple p+p system scaled by the expected increase in yield. Figure 9.1 shows the two collisional systems plotted together; the p+p has been scaled by the ratio of pion yields from measured PHENIX data:

$$\frac{\int_{0.38}^{8} \frac{dN^{\pi}_{dAu}}{dp_T}\,\mathrm{d}p_T}{\int_{0.38}^{8} \frac{dN^{\pi}_{pp}}{dp_T}\,\mathrm{d}p_T.} = 6.02 \tag{9.1}$$

in p_T units of GeV/c. The spectra agree reasonably well with the two mild exceptions. Due to the decreased signal-to-background in the d+Au system, the mass range between 300 and 600 MeV/c^2 has large statistical and systematic uncertainties leading to a visual discrepancy in that region. However,

within the uncertainties, the spectra are not inconsistent. Secondly, there was additional material in PHENIX during the 2008 RHIC Run with respect to the 2005 RHIC Run (the p+p dataset was taken in 2005) which decreased the momentum resolution via bremsstrahlung thereby smearing pairs to lower mass. This effect is seen on the low mass edge of the ϕ meson.

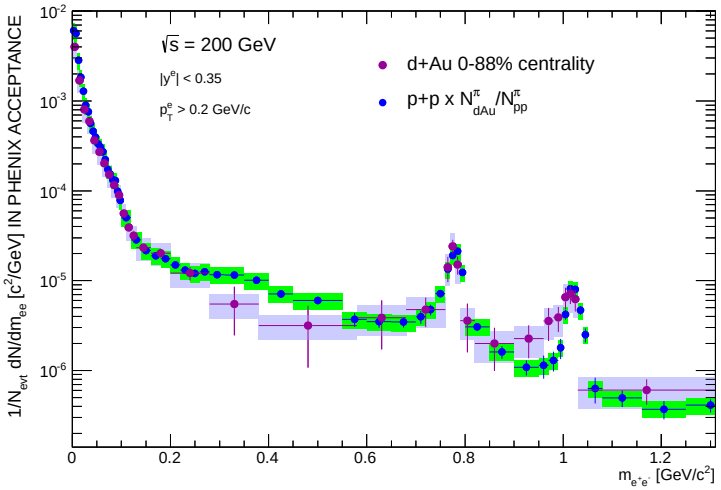

Figure 9.1: The overlay of dielectrons for d+Au collisions and p+p collisions scaled by the pion yield.

As there is clearly no enhancement in the low mass region (150 - 750 MeV/c^2) of the d+Au system, cold nuclear matter effects do not contribute to the enhancement that is observed in Au+Au collisions. It therefore follows that the Au+Au enhancement can most likely be attributed to final state effects, presumably the Quark Gluon Plasma.

Above mass ≈1 GeV/c^2 the yield is expected to scale with the number of binary collisions, $<N_{Coll}>$. Therefore, the p+p data is scaled by $<N_{Coll}>$and shows good agreement with the d+Au data in this intermediate mass range in Figure 9.2. The only notable exception is the previously published R_{dAu}[74] of the J/ψ of ~ 0.75 (p_T integrated). The ψ' also shows some suppression, which has yet to be quantified at PHENIX.

Overall, there is consistent agreement between the d+Au dielectrons and the appropriately scaled p+p data.

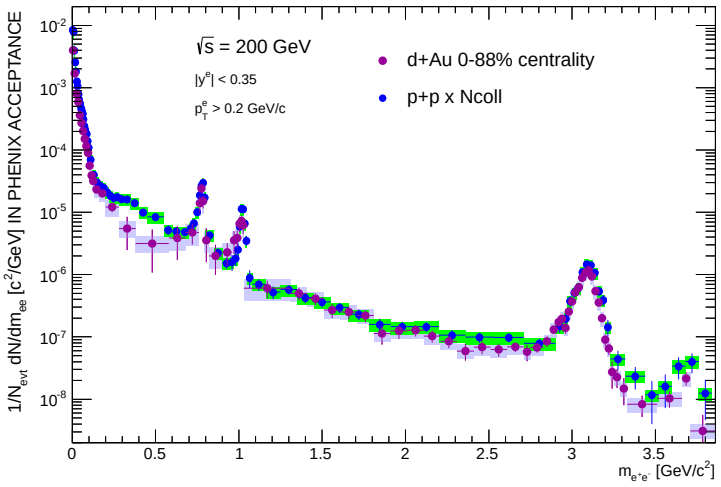

Figure 9.2: The overlay of dielectrons for d+Au collisions and p+p collisions scaled by the number of binary collisions (<N_{Coll} >).

9.2 Comparison to Cocktail

Part IV of this thesis outlined how a quantitative prediction for the d+Au dielectron spectrum was constructed by combining the hadronic components simulated with EXODUS with the heavy flavor calculated with MC@NLO and Drell-Yan simulated with PYTHIA . This full cocktail is shown in comparison to the data in Figure 9.3 across the entire mass range. The ratio is shown in the lower panel and is consistent with unity across an extremely large range in mass.

The vector meson resonance peaks of the ω, ϕ, J/ψ, ψ', and Υ are well described by the cocktail including the widths due to the intrinsic PHENIX detector resolution. In addition, the dielectron continua between the peaks are reproduced demonstrating full control over the various simulation components. Figure 9.4 shows the same spectra zoomed to highlight the lower mass region.

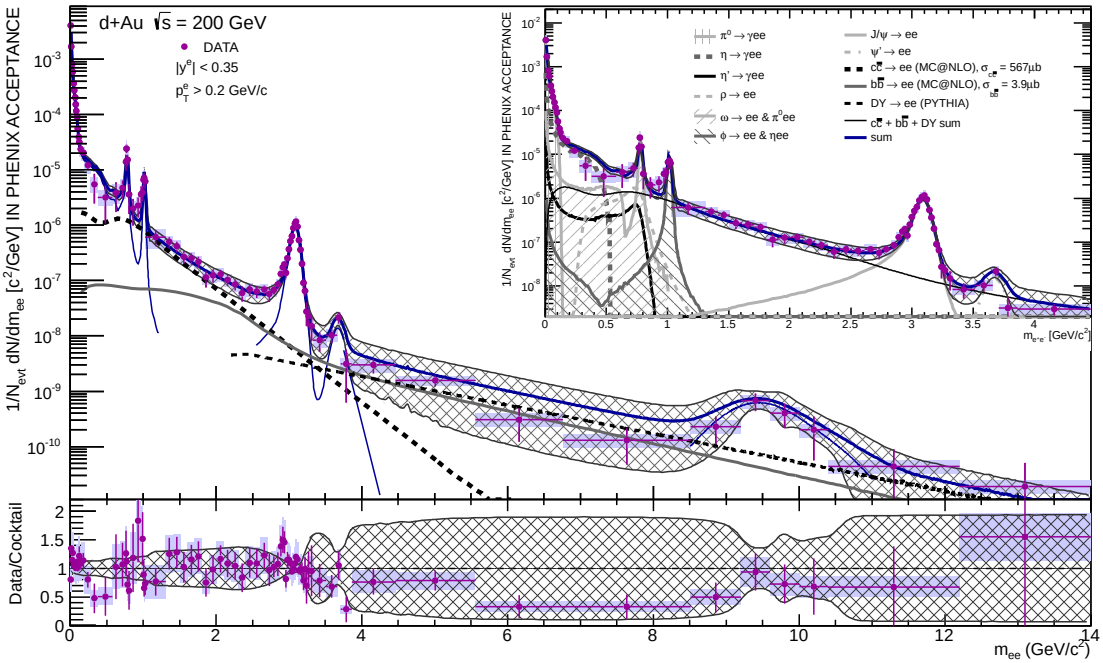

Figure 9.3: The e^+e^- pair yield per inelastic d+Au collision as a function of the invariant pair mass. The statistical uncertainty on the data is plotted as a bar while the systematic uncertainty is shown as shaded boxes. The expectation from known hadronic sources (the cocktail) is also plotted. The systematic uncertainty of the cocktail is plotted as a shaded region. Additionally, the various components are indicated in the legend. The inset is a zoom at lower mass while the lower panel is the ratio of the data to the cocktail.

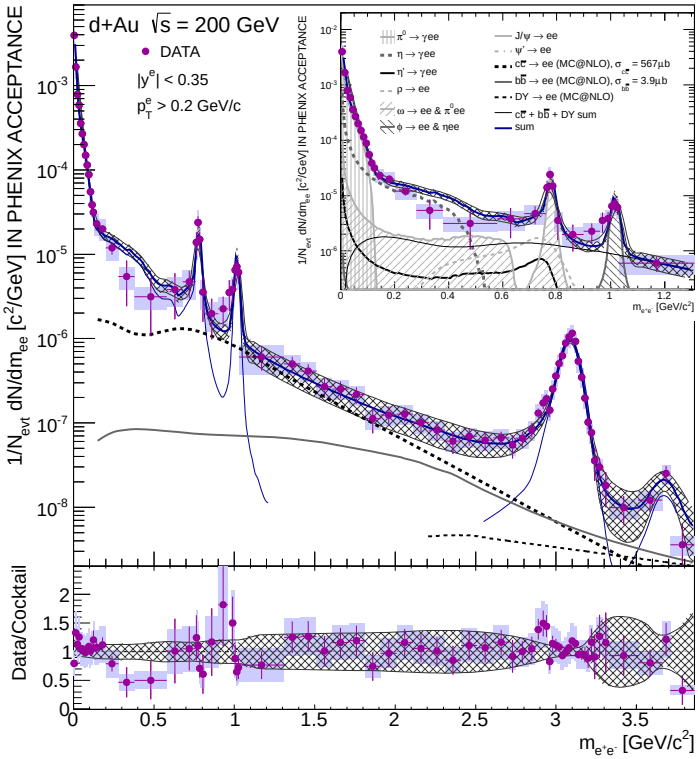

Figure 9.4: The e^+e^- pair yield per inelastic d+Au collision as a function of the invariant pair mass. The statistical uncertainty on the data is plotted as a bar while the systematic uncertainty is shown as shaded boxes. The expectation from known hadronic sources (the cocktail) is also plotted. The systematic uncertainty of the cocktail is plotted as a shaded region. Additionally, the various components are indicated in the legend. The inset zooms on the low mass region highlighting the lack of the excess seen in Au+Au collisions. The the lower panel is the ratio of the data to the cocktail.

9.3 Fine-Tuning the Cocktail

Aye - <clap> - dentical!!

Jim Trotter III
My Cousin Vinny

9.3.1 Transverse Momentum Dependence

Looking good Billy Ray!

Louis Winthorpe III
Trading Places

To test the transverse momentum dependence of the cocktail, the various components are fit to the data. For these fits, the shapes of each component are held fixed and the normalization (of each individual component) is left as a free parameter. The data are then fit two-dimensionally in mass and p_T simultaneously. The normalization fit values are shown in Table 9.1. The fit value is the additional normalization that each EXODUS cocktail component needs to best fit the data.

component	fit value	uncertainty (stat)
π^0	1.0391	0.0066
η	1.1936	0.0153
η'	1.2000	0.0694
ρ	1.2000	0.0195
ω	1.0061	0.0404
ϕ	1.0743	0.0459
J/ψ	1.0207	0.0188
ψ'	0.6804	0.0449
Υ (1S+2S+3S)	0.5625	0.0342
open charm	1.2448	0.0664
open beauty	1.0959	0.0903

Table 9.1: Fit parameters from a 2D fit of the normalizations of the cocktail components to the data.

In the fitting procedure (χ^2 minimization) the shapes of the η' and ρ are too similar for the fitting to stabilize and, therefore, the parameters are restricted to the systematic uncertainty on the cocktail inputs ($\sim$ 20%). The η' needs a slight adjustment of almost 20% also. The ψ' and Υ states show an additional suppression with respect to the J/ψ when compared to p+p collisions. As described in Sec 8.1, the ψ' and Υ are given the same initial suppression that is measured in the J/ψ ($\sim$0.75) [74]. The data-to-cocktail ratio of the rest of the vector mesons are consistent with unity. The results are quite stable, indicating that the cocktail describes the data well at all p_T.

Figure 9.5 shows the mass spectra in various p_T slices compared to the cocktail obtained through fitting. The agreement is striking across the entire p_T range indicating full control over the cocktail and its various components. In fact, the extent to which the cocktail matches the data differentially in mass and p_T is unprecedented in previous PHENIX dielectron analyses. This is a direct result of not only building (and improving) on existing analysis techniques but also incorporating an NLO calculation for the open heavy flavor. Moving forward, the cocktail changes from a metric of our understanding of the spectral makeup of the data to a tool that can be used to dissect the spectrum, allowing for a deeper analysis of the individual dielectron sources.

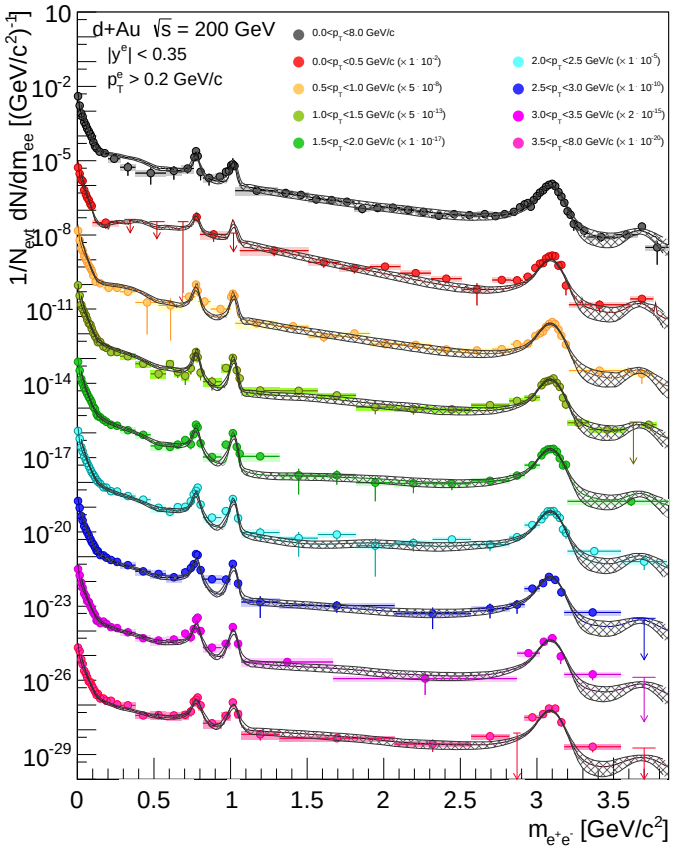

Figure 9.5: The dielectron mass distributions in d+Au collisions. The p_T ranges are indicated in the legend and the expectation of the hadronic sources is plotted for each. The arrows indicate upper limits (95% confidence level).

The p_T integrated results of the fine-tuned fit are shown in Figure 9.6.

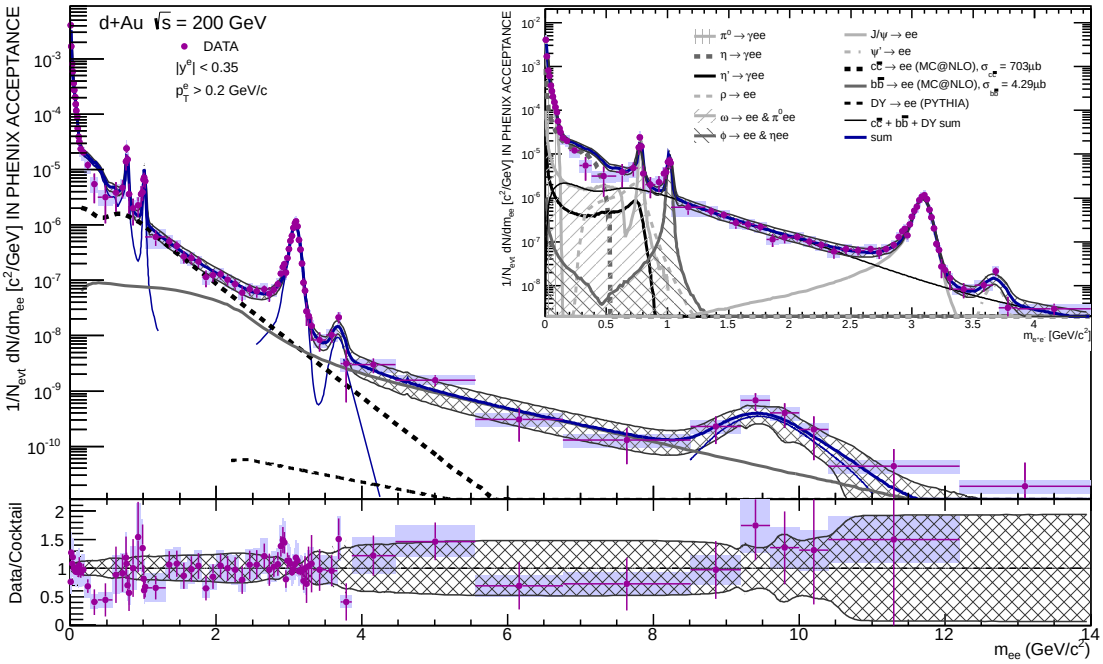

Figure 9.6: The e^+e^- pair yield per inelastic d+Au collision as a function of the invariant pair mass. The statistical uncertainty on the data is plotted as a bar while the systematic uncertainty is shown as shaded boxes. The expectation from known hadronic sources (the cocktail) is also plotted after being fine-tuned to the data. The systematic uncertainty of the cocktail is plotted as a shaded region. Additionally, the various components are indicated in the legend. The inset is a zoom at lower mass while the lower panel is the ratio of the data to the cocktail.

9.3.2 Centrality Dependence

Feeling good Lewis!!

Billy Ray Valentine
Trading Places

In addition to the slicing up the mass distributions into p_T ranges, the centrality of the collision can be used as another axis to view the data. Since the centrality dependence for most of the hadrons has not yet been measured by PHENIX, the cocktail for a particular centrality is constructed by a two component fit. The π^0, η, η', ρ, ω, and ϕ are locked to their *relative* amplitudes taken from the fitting described in Section 9.3.2 and then fit with one free normalization parameter while the same is done for the J/ψ, ψ', and Υ states. The open heavy flavor is simply scaled by the number of binary collisions ($<N_{Coll}>$).

Figure 9.7 shows the various centralities along with their individual cocktails. The centrality dependence is well described by this tuning. An important point is that the open heavy flavor (charm and beauty) scale with $<N_{Coll}>$as expected.

9.4 N_{Coll} and N_{Part} Scaling of Integral Yields

Even a blind man knows when
the sun is shining.

Jerry Garcia

Putting the $<N_{Coll}>$(or N_{Part}) scaling of the various regions of the dielectron spectrum in a global heavy ion picture is vital for disentangling cold nuclear effects from the consequences of forming a Quark Gluon Plasma. To this end, the lower panel of Figure 9.8 shows the integrated yield of the mass spectra for $m_{ee} < 100$ MeV/c^2. Since the π^0 multiplicity scales roughly with the number of participating nucleons, the yield in this range is expected to scale linearly with N_{Part}. This expected scaling is confirmed (within the systematic uncertainties) in the dielectron data in Figure 9.8 in all of the measured collisional systems at PHENIX: p+p , d+Au , Cu+Cu , and Au+Au .

However, the low mass region between $150 < m_{ee} < 750$ MeV/c^2 does not exhibit the same N_{Part} dependence in the more central Au+Au and most

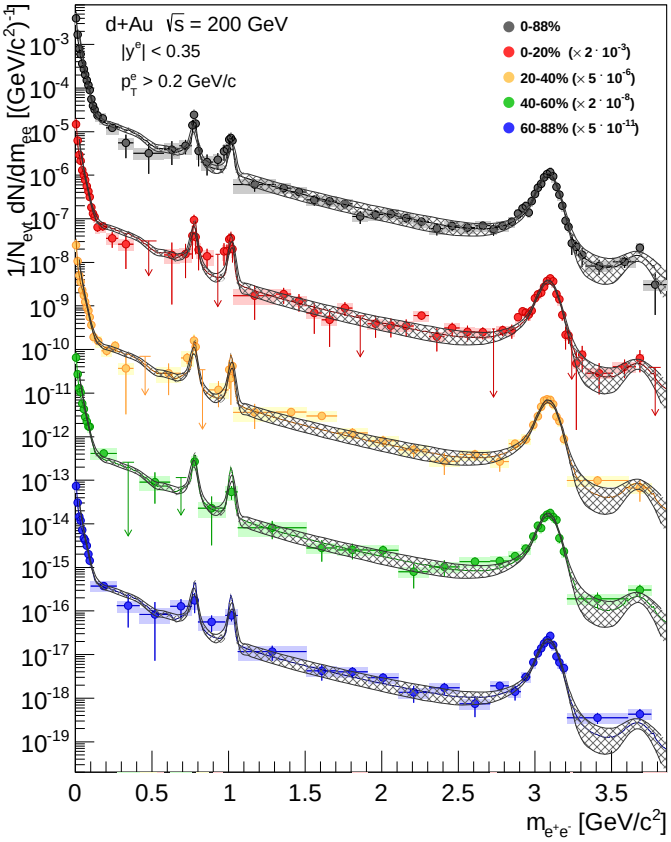

Figure 9.7: The dielectron mass distributions in d+Au collisions. The centrality ranges are indicated in the legend and the expectation of the hadronic sources is plotted for each.

central Cu+Cu collisions. The top panel in Figure 9.8 illustrates the low mass enhancement that is hypothesized to be attributed to the QGP. Since the d+Au data tracks the expected hadronic yield (as does the peripheral Cu+Cu and Au+Au), the excess cannot be reconciled as a consequence of cold nuclear matter effects. The presence of additional nuclear matter (relative to p+p) in the initial state of the collision does not contribute to the low mass enhancement seen in Au+Au .

An additional region of interest to this thesis is the intermediate mass region between the ϕ and J/ψ peaks ($1.2 < m_{ee} < 2.8$ GeV/c^2). The hadronic cocktail decomposition, illustrated in Figure 8.2, indicates that the domi-

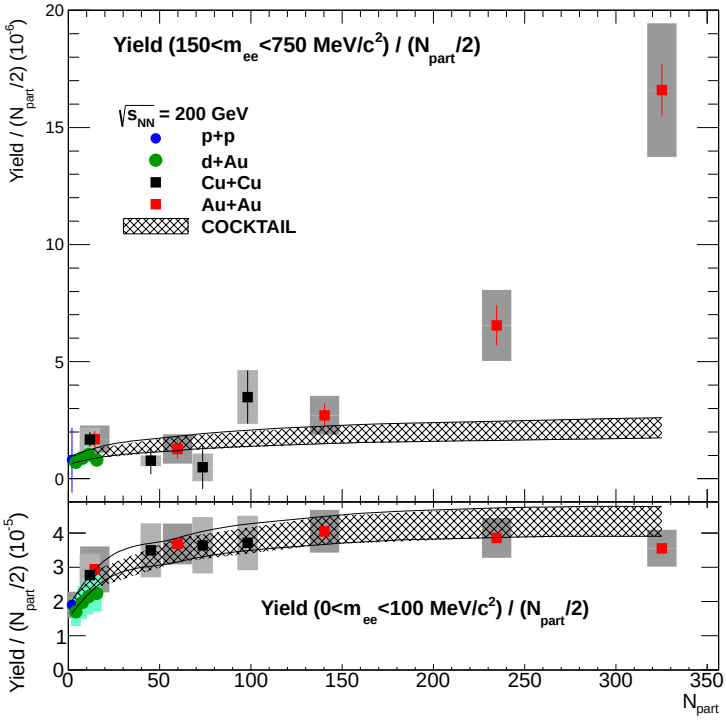

Figure 9.8: Dielectron yield per participating nucleon pair as function of N_{Part} for the mass range $150 < m_{ee} < 750$ MeV/c^2 (a) and $m_{ee} < 100$ MeV/c^2 (b). Statistical and systematic uncertainties are shown separately. Also shown are the expected cocktail yields with the band reflecting the systematic uncertainty on the cocktail.

nant contribution in this region comes directly from open heavy flavor decays. This mechanism is described in detail in Section 8.2. Since these pairs are thought to be correlated through the initial hard scattering (via a charm quark which forms a semi-leptonically decaying D meson), they *should* scale directly with the number of binary collisions, $<N_{Coll}>$. Figure 9.9 shows the yield/$<N_{Coll}>$in the intermediate mass region as a function of N_{Part} for p+p , d+Au , Cu+Cu , and Au+Au . Within the large systematic uncertainty of the Cu+Cu and Au+Au data, all of the systems and centralities are consistent with one another as well as with the expectation. This indicates that the production mechanism of open charm and beauty (as well as the resulting decay kinematics) are reasonably well understood and begs for a more quantitative investigation into measuring $\sigma_{c\bar{c}}$ and $\sigma_{b\bar{b}}$.

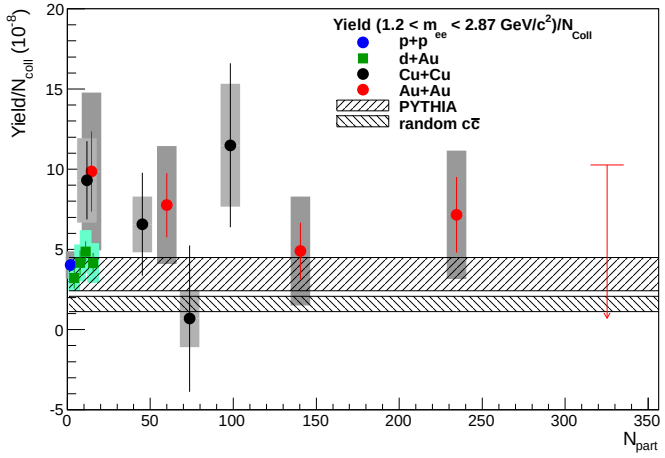

Figure 9.9: Dielectron yield per binary collision as function of N_{Part} for the mass range $1.2 < m_{ee} < 2.8$ GeV/c^2. Statistical and systematic uncertainties are shown separately. Also shown are two bands corresponding to two different estimates of the contribution from charmed meson decays. The width of the bands reflect the uncertainties on the charm cross section only.

CHAPTER 10

Heavy Flavor Extraction

10.1 Heavy Flavor Spectrum

> Be the flame, not the moth.
>
> Cassanova

Above a mass of $\sim$1.1 GeV/c^2 the dilepton continuum is dominated by semi-leptonic decays of D and B mesons that are correlated through flavor conservation. Therefore, to extract the cross sections for heavy flavor ($\sigma_{c\bar{c}}$ and $\sigma_{b\bar{b}}$), the vector meson peaks need to be subtracted and the remaining continuum can be fit with the shapes of the charm and beauty spectra obtained from MC@NLO . An important subtlety in the procedure is that the simulation must be manipulated in the same way that the data is handled.

It is well known that there are likesign correlations in the dilepton spectra from heavy flavor decays [75]. There are two sources of likesign correlated pairs in the heavy flavor continuum. The first originates from *feed down* leptons where a B meson first decays to a D meson and then the D meson to a lepton. An example of this decay chain, starting with a B^+B^- might look like:

$B^+ \to \bar{D}^0 e^+ \nu_e$, $\bar{D}^0 \to e^-$ anything.
$B^- \to \bar{D}^0 \pi^-$, $D^0 \to e^+$ anything.

which clearly creates both likesign and unlike-sign pairs.

The second source of correlated likesign pairs is from $B^0\bar{B}^0$ particle-antiparticle oscillations. A B^0_d oscillates with a probability of $\sim$17% while a B^0_s does so $\sim$49% of the time. Therefore, in the primary dilepton channel, the probability of the $B^0_d\bar{B}^0_d$ ($B^0_s\bar{B}^0_s$) system to produce an unlike-sign pair is $\sim$70% ($\sim$50%), whereas roughly 30%(50%) of the primary correlated pairs will manifest as likesign [76].

Fortunately, the MC@NLO package accounts for these effects and they can be quantified. Figure 10.1 shows the relative amount of correlated likesign pairs from these sources. The right panel of Figure 10.1 shows that the likesign pairs do represent an appreciable fraction of the unlike-sign signal in the open beauty continuum. In fact, the overall reduction in the unlike-sign signal of open beauty from subtracting the likesign correlations is $\sim$53% (slightly more than a factor of 2). However, after being filtered through the PHENIX acceptance, the reduction is closer to $\sim$40%.

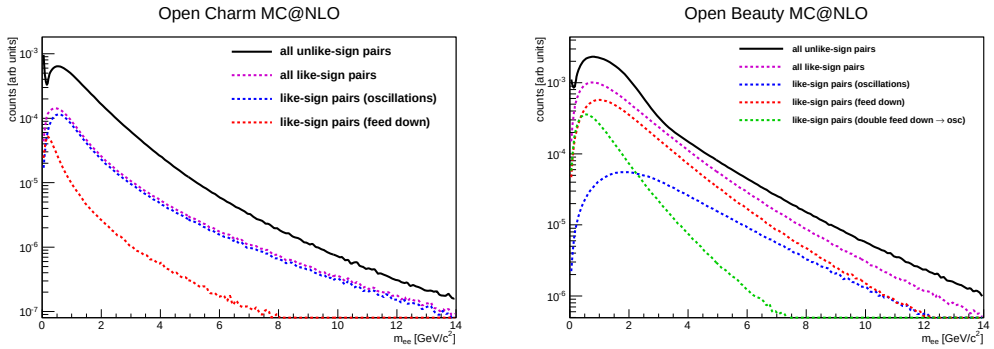

Figure 10.1: Relative abundances of correlated likesign pairs for open charm (left) and beauty (right).

The correlated likesign pairs from charm are shown in the left panel of Figure 10.1. In the open charm spectrum the effect is less severe. The reduction in the overall unlike-sign signal is $\sim$20% and, after being filtered into the PHENIX acceptance, results in a negligible $\sim$0.2% loss in measured signal. The overall difference in likesign signal is shown in Figure 10.2. The effect is only relevant for the open beauty.

Since the likesign is used in this analysis as an estimation of the uncorrelated background (plus cross pairs and jet pairs), there is indeed some correlated signal subtracted from the heavy flavor continuum. Therefore, this same contribution is subtracted in the MC@NLO simulation before comparing to the data. Figure 10.3 shows the dielectron spectrum after subtracting the π^0, η, η',

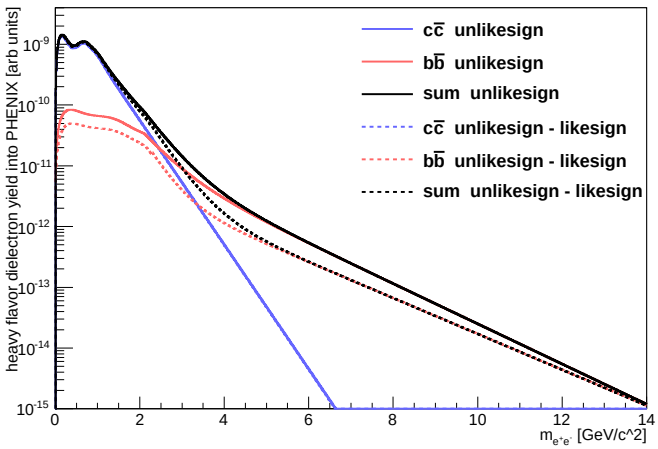

Figure 10.2: Simulated heavy flavor spectrum before (solid) and after (dashed) subtracting correlated likesign pairs.

ρ, ω, ϕ, J/ψ, ψ', and Υ components after having fit the relative contributions to the data (Section 9.3).

The remaining spectrum is fit with the shapes of the MC@NLO heavy flavor spectra leaving the overall normalization of both charm and beauty as free parameters. The data are fit 2-dimensionally, in mass and p_T. Along the mass axis, however, the fit is only performed in the ranges $1.16 < m_{ee} < 2.40$ and $4.1 < m_{ee} < 7.2$ GeV/c^2 so that any residual mismatch of the EXODUS cocktail shape does not affect the fit. The final normalization parameters to the MC@NLO curves reveal the measured cross sections for charm and beauty:

$$\sigma_{c\bar{c}} = 704 \pm 47(stat) \pm 183(syst) \pm 40(model)\mu b$$
$$\sigma_{b\bar{b}} = 4.29 \pm 0.39(stat) \pm 1.08(syst) \pm 0.11(model)\mu b$$

The final χ^2 per degree of freedom of this fit is

$$\chi^2/NDF = \frac{55.971}{53-2} = 1.097$$

indicating not only a convergent result but also that the actual uncertainties in the analysis are properly accounted for in the final quoted uncertainties.

Moreover, it should not be left unnoted that because the two dimensional fitting procedure utilizes information in the mass and p_T directions *simulta-*

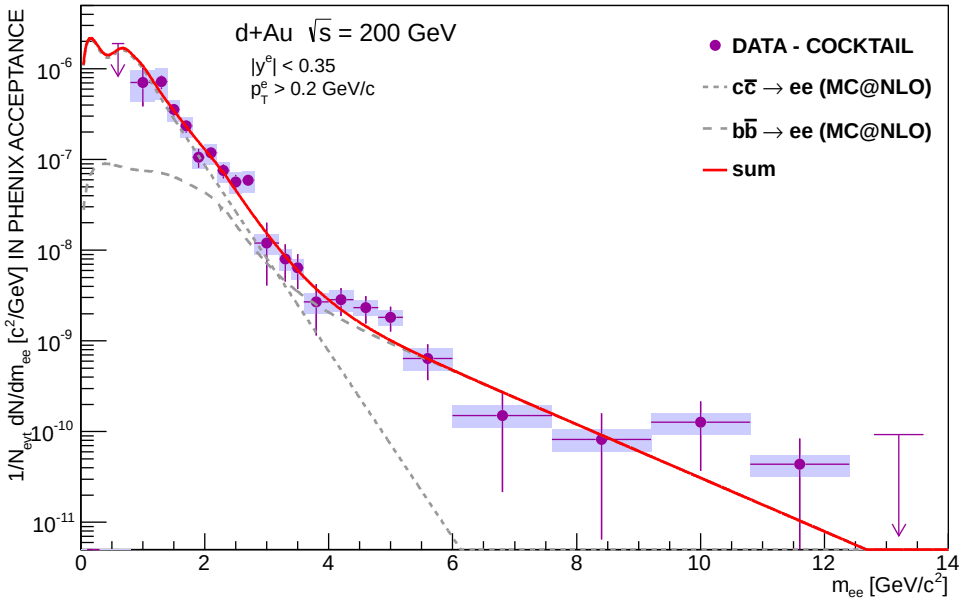

Figure 10.3: e^+e^- mass distribution from semi-leptonic open heavy flavor decays. The contribution from π^0, η, η', ρ, ω, ϕ, J/ψ, ψ', and Υ mesons is subtracted from the inclusive pair yield. The arrow indicate upper limits (95% CL). The individual charm and beauty components are also shown.

neously, this method leads to a very powerful result. The evolution of the complex interplay of the open charm and beauty pairs is shown in Figure 10.4. At low p_T the charm dominates the intermediate mass region while the beauty carries the lion's share of the yield in the high mass region. Between $1.5 < p_T < 2.5$ GeV/c they are roughly equal across all mass. Finally, above ~3 GeV/c, beauty takes over below the J/ψ while charm becomes influential at higher masses. This is primarily due to $b\bar{b}$ feed down pairs piling up in the intermediate mass region at high p_T while the charm spectral mass shape doesn't evolve as dramatically with momentum. Clearly, the ability of MC@NLO to describe the p_T dependence is more than simply a novelty! Exploiting the transverse momentum dependence as an additional lever arm for the χ^2 minimization helps to make the overall fit significantly more robust than using the mass projection alone.

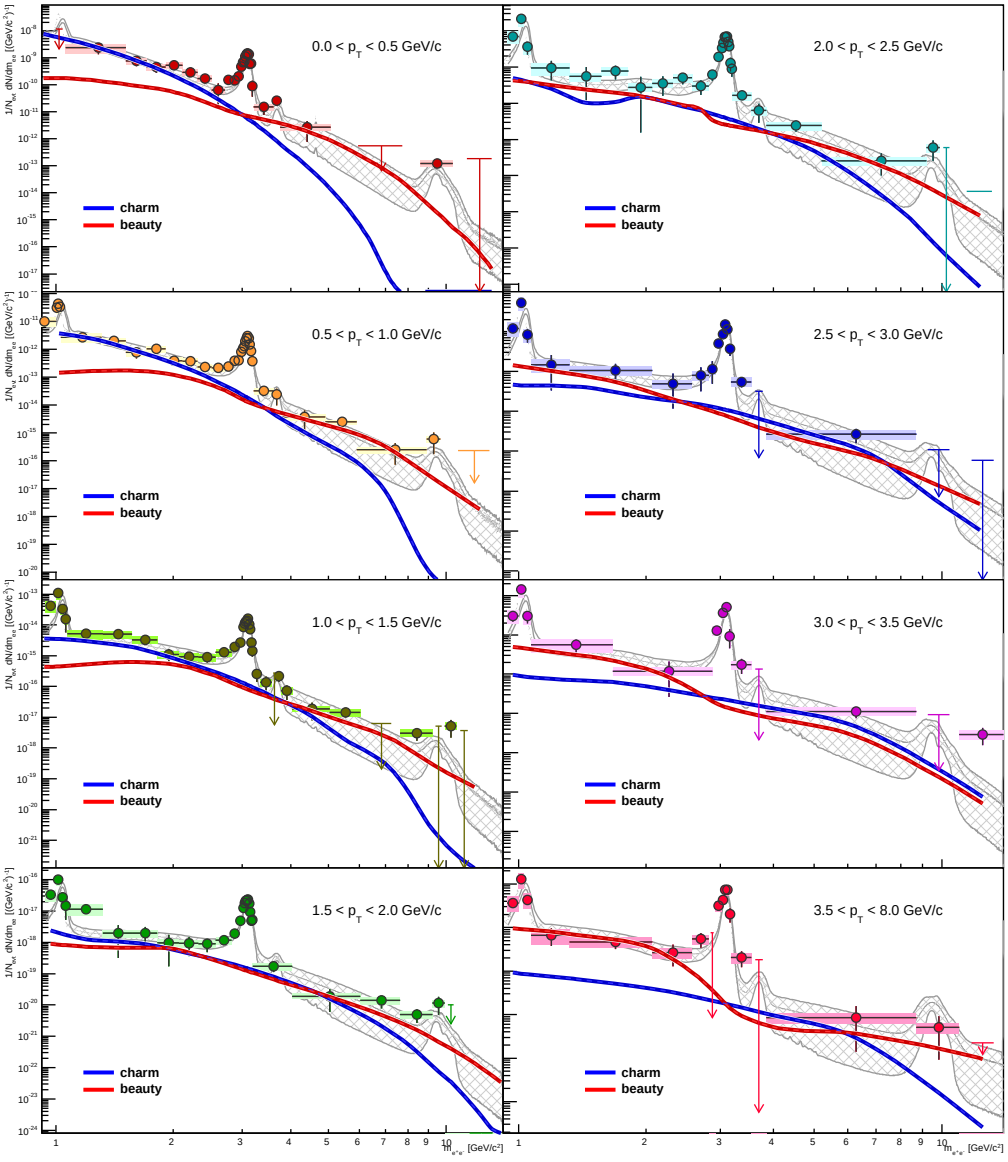

Figure 10.4: Invariant mass spectra of e^+e^- pairs in increasing p_T slices. The data are shown as points (along with shaded boxes for the systematic uncertainty), the cocktail as the hashed band, and the contribution of open charm and beauty based on MC@NLO calculations as the blue and red lines. The complex relationship between charm and beauty reinforces the credibility of the 2D fitting algorithm.

10.2 Heavy Flavor Momentum Dependence

> To get something you've never had you've got to do something you've never done.
>
> Pauletta Pearson Washington

It is well known that a major weakness in leading order open heavy flavor simulations (such as PYTHIA , which was used for previous dielectron analyses) is the inability to describe the data at high p_T. Above $\sim$2 GeV/c, leading order calculations fail because, without a third body in the final state of the initial hard scattering, every $c\bar{c}$ pair is back-to-back in the (incoming parton's) center-of-momentum frame. In the oversimplification that the electron preserves most of the D meson's p_T, which in turn preserves most of the c quark's p_T, the e^+e^- pair will also be back-to-back. This unnaturally restricts the phase space of the simulated e^+e^- pair to high mass and low p_T resulting in a spectrum that will fall off faster than a higher order calculation.

The top panel of Figure 10.5 shows the p_T spectra for p+p and ($<$N$_{Coll}>$scaled) d+Au dielectrons in the intermediate mass range ($1.15 < m_{ee} < 2.8$ GeV/c^2). Superimposed on the data are the calculations from both PYTHIA (leading order) and MC@NLO (next-to-leading order). The PYTHIA is normalized by fitting to the p+p data and the MC@NLO by fitting the d+Au dataset outlined in the previous section. The PYTHIA clearly under estimates the data above $\sim$2 GeV/c while the MC@NLO describes the momentum shape well out to 8 GeV/c (above 8 GeV/c the statistics run out in the data).

In addition to the comparing the p_T dependence of the d+Au data to various calculations, it's also interesting to compare it with the p+p dataset. This is traditionally accomplished through a quantity called the *nuclear modification factor*, which is defined generically for any collisional system, $A + B$, as

$$R_{AB}(p_T) = \frac{d^2N^{AB}/dp_Tdy}{(\langle N_{coll}\rangle/d^2N^{pp})/dp_Tdy} \tag{10.1}$$

In the absence of medium-induced effects, particle production in nucleus-nucleus collisions should scale with the number of binary collisions in the high-p_T region, resulting in $R_{AB} = 1$ at high-p_T. In the low p_T region, the yield is not expected to scale with N_{coll}, but with the number of participants, N_{part} and reflects the bulk properties of the system. This scaling can be modified

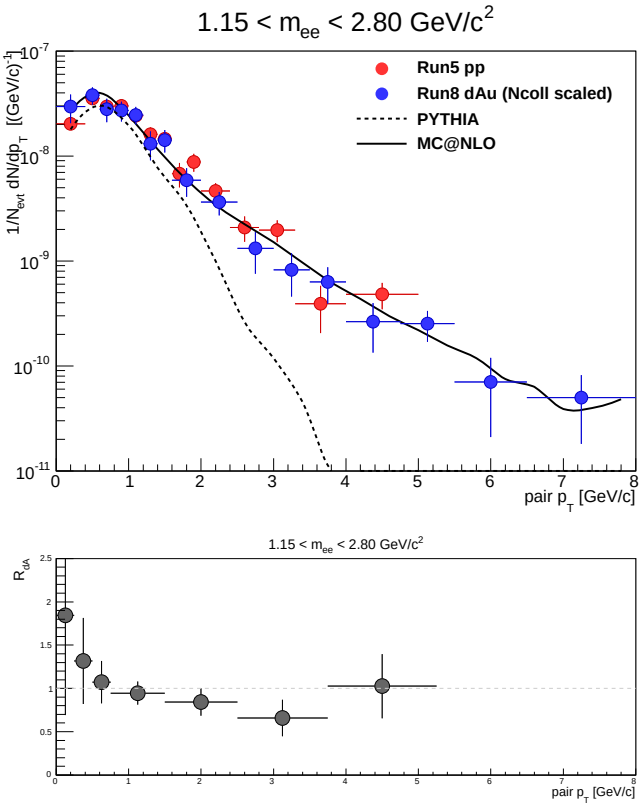

Figure 10.5: Upper: Measured p_T distributions of e^+e^- pairs in the intermediate mass range ($1.15 < m_{ee} < 2.8$ GeV/c^2) for p+p and d+Au (scaled by $<N_{Coll}>$) collisions. The data are corrected for ε_{Rec} and ε_{ERT} but not for the geometric acceptance of PHENIX. The yields are compared to calculations from PYTHIA and MC@NLO . Lower: R_{dA} of the IMR.

when the initial parton distribution is changed in the nuclear environment or when the partons lose energy in the medium prior to fragmentation resulting in $R_{AB} < 1$.

The nuclear modification factor for the intermediate mass region in d+Au collisions is plotted as a function of p_T in the lower panel of Figure 10.5. Although there is a suspicious monotonic falling trend below ~4 GeV/c, within the statistical precision, dielectrons in the intermediate mass region seem to be unmodified by the presence of cold nuclear matter in the initial state. It is yet unclear if the (potentially statistically insignificant) mild suppression at $p_T \approx 3$ GeV/c is consistent with the D meson Cronin Effect which is seen

in the single electron channel (Figure 1.6). Unfortunately, due to a lack of statistics in the p+p data sample, the R_{dA} for beauty is inaccessible.

10.3 Global Heavy Perspective

> That rug really tied the room together.
>
> The Dude

The $\sqrt{s_{NN}}$ dependence of the total charm cross section, $\sigma_{c\bar{c}}$, places the measurements of this thesis in a more global perspective. Figure 10.6 shows the NLO pQCD calculation [68] as a function of $\sqrt{s_{NN}}$ compared to experimental data. For the low energy ($\sqrt{s_{NN}} \approx 20$ GeV) points, data from SPS and FNAL are shown along with the high energy ($\sqrt{s_{NN}} = 630$ GeV) value from the UA2 Collaboration. PHENIX's two published measurements at $\sqrt{s_{NN}} = 200$ GeV are shown: the single electron channel from p+p collisions [60] and the dielectron channel [70]. The d+Au $\sigma_{c\bar{c}}$/<N$_{Coll}$ >is also shown. The measurements are in agreement with the large uncertainty of the NLO pQCD calculation thus reinforcing the validity of an NLO approach to pQCD.

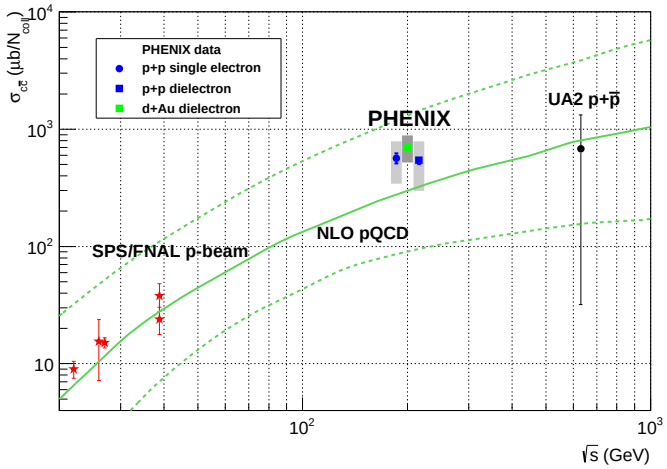

Figure 10.6: .

For the same NLO calculation, the beauty cross section is plotted in Figure 10.7 along with available data. Previous PHENIX p+p measurements are

plotted along with the d+Au result of this thesis. There are no unexpected cold nuclear matter effects which influence the $<N_{Coll}>$scaling of the cross section. Moreover, NLO pQCD seems to be a successful description of the data within its systematic uncertainty.

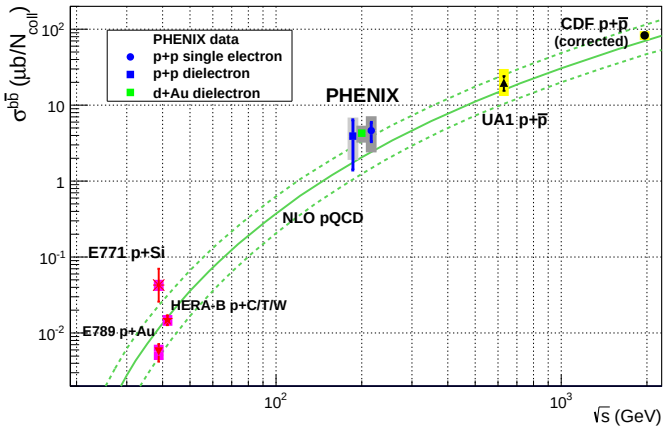

Figure 10.7: .

CHAPTER 11

Outlook

> The future's so bright, I gotta wear shades.
>
> Timbuk3

Moving forward, there is still much work to be done with the dielectron data. Higher precision measurements are ripe and waiting for future analyzers to extract additional information out of them. In particular,

- 2005 ERT triggered Cu+Cu $\sqrt{s_{NN}} = 200$ GeV dataset can bring additional statistics at higher mass and pair p_T;
- 2006 p+p $\sqrt{s} = 200$ GeV dataset with nearly 3 times the statistics of the 2005 data. ERT trigger was also turned up higher allowing access to higher mass and pair p_T;
- 2009 p+p $\sqrt{s} = 200$ GeV dataset taken with the Hadron Blind Detector (HBD) installed (see following section) to establish proof-of-principle of working upgrade;
- 2010 Au+Au $\sqrt{s_{NN}} = 200$ GeV dataset taken with the HBD to verify low mass enhancement result;
- 2010 Au+Au energy scan at $\sqrt{s_{NN}} = 200$, 62.4, 39, 7.7 GeV to explore onset of low mass enhancement;

- 2011 p+p $\sqrt{s}$ = 510 GeV dataset. First look at new energy regime for p+p ;
- 2012 U+U and Cu+Au datasets introduce exotic geometries to the story.

Rather than delve into each of the topics in full, details of the Hadron Blind Detector (HBD) upgrade as well as additional physics to be explored with the 2008 d+Au dataset are discussed below.

11.1 Hadron Blind Detector

> I should never have switched
> from scotch to martinis.
>
> Humphrey Bogart

The large systematic uncertainty in the Au+Au data in the low mass region stems from the S/B being less than half a percent in the phase space of $m \approx p_T \approx 500$ MeV/c^2. This is unfortunate since it is precisely where the large excess is observed. This dismally low S/B is primarily due to photon conversions and π^0 Dalitz decays in which one of the electron brethren escape the detector. In order to combat this, an upgrade to PHENIX was installed for the 2009 and 2010 RHIC runs. The Hadron Blind Detector (HBD) is a windowless and mirrorless Cherenkov detector which consists of triple Gas Electron Multiplier (GEM) stacks within a chamber filled with CF_4. The CF_4 is used both as the radiator gas as well as the GEM avalanche gas. The top-most GEM of the triple-stack is coated with CsI, which serves as a photocathode for the Cherenkov radiation. [98]

The HBD's purpose was to identify e^+e^- pairs with very small opening angle (< 200 mrad) within a magnetic field free region close to the beampipe. In the absence of a B-field to create an opening angle between the pair, the raw Cherenkov blobs deposited on the CsI-coated GEMs are typically either overlapping or (at most) $\sim$2 blob diameters apart ($\sim$3.4 cm). By cutting on a single "blob amplitude" signal versus a double signal, the HBD can reject these pesky Dalitz pairs and photon conversions *before* the B-field pulls them apart (being pulled apart is what allows one of the electrons to escape the acceptance while the other can hit the detector).

This reduction in the combinatorial background (while, presumably, not affecting the signal) will enable the 2010 Au+Au dataset to have significantly smaller systematic uncertainty due to the background estimation. This will

provide crucial verification of the low mass enhancement since the phenomenon currently resides in a region of mass and p_T where the S/B is $< 0.5\%$. The data are currently being analyzed and show promise of being able to deliver a more precise result. The preliminary p+p results using the HBD show an improvement in the S/B near $m = 500$ GeV/c^2 of about a factor of five.

11.2 Additional Physics

Swing when you're winning.

Torsten Dahms

Beyond the physics already extracted from the d+Au dataset there are further fruitful endeavors to be undertaken. The R_{dA} of the ψ' and Υ are certainly accessible, although the Υ will require analyzing the 2006 p+p dataset to obtain comparable statistics to the d+Au dataset. Currently, the p+p data only extend to 8 GeV/c^2 in mass.

Moreover, including the 2006 p+p data would allow the R_{dA} of both open charm and open beauty to be flushed out with higher precision while simultaneously verifying the reported $\sigma_{c\bar{c}}$ and $\sigma_{b\bar{b}}$. The only reason the R_{dA} of the beauty continuum is out of the scope of this thesis is because the statistics are currently unavailable in p+p . Additionally, future studies with MC@NLO also need to be performed to determine how to translate the p_T dependence of R_{dA} of the heavy flavor single electrons to the pair p_T.

The full control of the spectral makeup of the spectrum can be extended to strip the data down to investigate the more hidden components such as the ρ and η', even possibly allowing a disambiguation between them. An upper limit for the $\eta \to e^+e^-$ decay channel is also ripe for the picking. Particularly at $p_T > 1$ GeV/c, the S/B is very good in the data and the cocktail does an excellent job of describing that region. The current limit for the branching ratio of this decay is 5.6×10^{-6} [99]. This can certainly be improved upon!

Finally, the primary reason that dielectron spectra measured at PHENIX are not fully acceptance corrected (up to 2π and 1 unit of rapidity *at* midrapidity, as can be done for the vector mesons) is that the polarization of the open heavy flavor was never known. However, the inclusion of the MC@NLO simulation into the analysis can allow for a full acceptance correction of the entire spectrum, leading to a more generalized result which is independent of the PHENIX aperture, a feat not yet performed within the collaboration.

11.3 Concluding Remarks

> Silver has a place in heaven, gold a place in hell.

Among all measurements that are accessible within the scientific program at RHIC, dielectrons remain the most compelling and elusive. Their elusiveness is driven by both the rarity of these signals as well as their small signal-to-background ratio. Moving forward into the second phase of RHIC operations, it is expected that further intriguing physics will be within reach. Every observable at RHIC benefits from compiling a full suite of precision measurements in the baseline set of collisional systems: p+p , Au+Au , and d+Au . This thesis completes the trilogy by providing the d+Au results for the very first time and thereby represents a significant advancement in the field of relativistic heavy ion physics.

Bibliography

[1] K. Adcox *et al.*, Nucl. Phys. **A757**, 184 (2005). 5

[2] I. Arsene *et al.*, Nucl. Phys. **A757**, 1 (2005). 5

[3] B. B. Back *et al.*, Nucl. Phys. **A757**, 28 (2005). 5

[4] J. Adams *et al.*, Nucl. Phys. **A757**, 102 (2005). 5

[5] K. Adcox *et al.*, Phys. Rev. Lett. **88**, 022301 (2002).

[6] S. S. Adler *et al.*, Phys. Rev. Lett. **91**, 072301 (2003).

[7] S. S. Adler *et al.*, Phys. Rev. C **69**, 034910 (2004).

[8] M. Gyulassy and M. Plumer, Phys. Lett. **B243**, 432 (1990); X. N. Wang and M. Gyulassy, Phys. Rev. Lett. **68**, 1480 (1992).

[9] S. S. Adler *et al.*, Phys. Rev. Lett. **97**, 052301 (2006).

[10] S. S. Adler *et al.*, Phys. Rev. C **71**, 051902 (2005).

[11] S. S. Adler *et al.*, Phys. Rev. Lett. **91**, 172301 (2003)

[12] V. Greco, C. M. Ko and P. Lévai, Phys. Rev. Lett. **90**, 202302 (2003).

[13] D. Kharzeev, Yu. V. Kovchegov and K. Tuchin, Phys. Rev. D **68**, 094013 (2003).

[14] J. W. Cronin *et al.*, Phys. Rev. D **11**, 3105 (1975). 9

[15] P. B. Straub *et al.*, Phys. Rev. Lett. **68**, 452 (1992).

[16] S .S. Adler *et al.*, Phys. Rev. Lett. **91**, 072303 (2003).

[17] S .S. Adler *et al.*, Phys. Rev. Lett. **98**, 172302 (2007). 113

[18] M. Lev and B. Peterson, Z. Phys. **C21**, 155 (1983).

[19] K. Adcox *et al.*, NIM A **499**, 469-602 (2003).

[20] K. Adcox *et al.*, NIM A **499**, 489-507 (2003). 37, 42, 109

[21] M. Aizawa *et al.*, NIM A **499**, 508-520 (2003). 44

[22] C. Adler *et al.*, NIM A **499**, 433 (2003). 33, 35

[23] T. A. Armstrong *et al.*, NIM A **406**, 227 (1998). 35

[24] S. White, AIP Conf.Proc. **792**, 527 (2005).

[25] S .S. Adler *et al.*, Phys. Rev. Lett. **94**, 082302 (2005).

[26] Z. Citron, *Probing the Nucleus with d+Au Collisions at RHIC* Ph.D. thesis, Stony Brook University (2011); 36

[27] L. Hulthén and M. Sagawara, Handbuch der Physik **39**, (1957). 62

[28] R. J. Glauber and G. Matthiae, *High Energy Scattering of Protons by Nuclei* Nucl. Phys. **B21**, 135 (1970). 61

[29] J. L. Nagle *PHENIX Run-08 d+Au at 200 GeV Centrality Categorization (in support of PHENIX Final Results).* PHENIX Analysis Note AN900 (2010). 64

[30] Cheuk-Yin Wong, Introduction to high energy heavy-ion collisions. World Scientific, Singapore, (1994). 119

[31] T. Sjöstrand, L. Lönnbland and S. Mrenna, arXiv:hep-ph/0108264 (2001).

[32] V. Ryabov, [for PHENIX Collaboration], Nucl. Phys. **A774**, 735 (2006).

[33] S .S. Adler *et al.*, Phys. Rev. C **74**, 024904 (2006).

[34] J. Adams *et al.*, Phys. Lett. **B637**, 161 (2006).

[35] S .S. Adler *et al.*, Phys. Rev. C **74**, 0307022 (2004).

[36] H. G. Fischer, [for NA49 Collaboration], Nucl. Phys. **A715**, 118 (2003).

[37] Review of Particle Properties, W. M. Yao *et al.*, Jornal of Phys. **G33**, 1 (2006). 3, 113, 117

[38] S. S. Adler *et al.*, Phys. Rev. Lett. **95**, 202001 (2005)

[39] Y. Zhang *et al.*, Phys. Rev. C **65**, 034903 (2002).

[40] X. N. Wang, Phys. Rev. C **61**, 064910 (2000). Y. Zhang *et al.*, Phys. Rev. C **65**, 034903 (2002).

[41] B. Z Kopeliovich *et al.*, Phys. Phev. Lett. **88**, 232303 (2002). A. Accardi and D. Treleani, Phys. Rev. D **64**, 116004 (2001). I. Vitev and M. Gyulassy, Phys. Rev. Lett. **89**, 252301 (2002)

[42] A. Accardi, arXiv: hep-ph/0212148.

[43] B. Alper *et al.* [British-Scandinavian Collaboration], Nucl. Phys. **B100**, 237 (1975).

[44] M. Adamczyk *et al.*, *The BRAHMS experiment at RHIC.* Nucl. Instr. and Meth., **A499**, 437-468 (2003). 26

[45] B. B. Back *et al.*, *The PHOBOS detector at RHIC.* Nucl. Instr. and Meth., **A499**, 603-623 (2003). 26

[46] K. Adcox *et al.*, *PHENIX detector overview.* Nucl. Instr. and Meth., **A499**, 469-479 (2003). 26

[47] K. H. Ackerman *et al.*, *STAR detector overview.* Nucl. Instr. and Meth., **A499**, 624-632 (2003). 26

[48] S. H. Aronson *et al.*, *PHENIX Magnet System.* Nucl. Instr. and Meth. A, **A499**, 480-488 (2003). 37

[49] M. Allen *et al.*, *PHENIX inner detectors.* Nucl. Instr. and Meth. A, **A499**, 549-559 (2003). 32

[50] S. Johnson *et al.*, *Three-Dimensional Track Finding in the PHENIX Drift Chamber by a Combinatorial Hough Transform Method.* International Conference on Computing in High Energy Physics (CHEP '98), Chicago, USA, 1998. (1998). 39

[51] A.F. Krutov and V.E. Troitsky, *Parametrization Of The Deuteron Wave Function Obtained Within A Dispersion Approach.* Phys. Rev. C **76**, 117001 (2007). 62

[52] K. Reygers, *A New Parameterization of the Deuteron Wave Function for PHENIX Glauber Calculations.* PHENIX Analysis Note **633**. 63

[53] J. Nagle, *PHENIX Run8 d+Au at 200 GeV Centrality Categorization.* PHENIX Analysis Note **900**. 63

[54] J. Nagle and C. Zhang, *Centrality Determination in Deuteron-Gold Reactions Using the Beam-Beam Counter.* PHENIX Analysis Note **342**. 63

[55] A. Drees and X. Zhangbu, *Results from Luminosity Scans during the RHIC 2000.* In proceedings of the 2001 Particle Accelerator Conference, Chicago IL, 2001. 60

[56] S.R. Klein and R. Vogt, *Nuclear Shadowing and High p_T Hadron Spectra in Relativistic Heavy Ion Collisions.* Phys. Rev. C **67**, 047901 (2003). 60

[57] S.N. White, *Diffractive Dissociation - 50 years later.* In proceedings of the AIP Conference. 792, 527-531, 2005. 60

[58] S. Frixione and B.R. Webber, *Matching NLO QCD computations and parton shower simulations.* JHEP 0206:**029**, 2002. 112, 116

[59] S .S. Adler *et al.*, Phys. Rev. C **74**, 024904 (2006). 113

[60] A. Adare *et al.*, *Measurement of high-p_T Single Electrons from Heavy Flavor Decays in p+p Collisions at $\sqrt{s_{NN}} = 200$ GeV* Phys. Rev. Lett. **97**, 252002 (2006) 109, 113, 117, 143

[61] N. M. Kroll and W. Wada, *Internal Pair Production Associated with the Emission of High-Energy Gamma Rays*, Phys. Rev. **98**, 1355 (1955). 114

[62] L. G. Landsberg, *Electromagnetic decays of light mesons*, Phys. Rep. **128**, 301 (1985). 114

[63] R. I. Dzhelyadin, *Study of the electromagnetic transition form-factor in $\omega \to \pi^0 \mu^+ \mu^-$ decay*, Phys. Lett. **B102**, 296 (1981). 114

[64] G. J. Gounaris and J. J. Sakurai, *Finite-Width Corrections to the Vector-Meson-Dominance Prediction for $\rho \to e^+ e^-$*, Phys. Rev. Lett. **21**, 244 (1968). 114

[65] G. Corcella and B.R. Webber *et al.*, *HERWIG 6.5*, JHEP 0101:**010**, 2001. 116

[66] M.R. Whalley *et al.*, *The Les Houches Accord PDFs (LHAPDF) and LHAGLUE*, Contributed to HERA and the LHC: A Workshop on the Implicati Conference: C05-03-21.1, Aug 2005. 116

[67] M. Cacciari, P. Nason, and R. Vogt, *QCD Predictions for Charm and Bottom Quark Production at RHIC*, Phys. Rev. Lett. **95**, 122001 (2005). 117

[68] R. Vogt, *The total charm cross section*, Eur. Phys. J. ST **155**, 213 (2008). 143

[69] A. Adare *et al.*, *Detailed measurement of the e^+e^- pair continuum in p+p and Au+Au collisions at $\sqrt{s_{NN}}$=200 GeV and implications for direct photon production* Phys. Rev. C **81**, 034911 (2010). 15, 82, 119

[70] A. Adare *et al.*, *Dilepton mass spectra in p+p collisions at $\sqrt{s_{NN}}$ = 200 GeV and the contribution from open charm* Phys. Lett. B **670**, 313 (2009). 14, 117, 118, 119, 143

[71] A. Adare *et al.*, *Heavy Quark Production in p+p and Energy Loss and Flow of Heavy Quarks in Au+Au Collisions at $\sqrt{s_{NN}}$=200 GeV* Phys. Rev. C **84**, 044905 (2011). 109, 118

[72] S. Gavin *et al.*, *Production of Drell-Yan pairs in high-energy nucleon-nucleon collisions* Int. J. Mod. Phys. **A10**, 2691 (1995). 119

[73] GEANT. *manual, v.3.2.1, cern program library w5013*, 1994. 92, 109

[74] A. Adare *et al.*, *Transverse-Momentum Dependence of the J/ψ Nuclear Modification in d+Au Collisions at $\sqrt{s_{NN}}$=200 GeV* arXiv:1204.0777 [nucl-ex], 2012. 125, 129

[75] P. Crochet and P. Braun-Munzinger, *Investigation of background subtraction techniques for high mass dilepton physics.* NIM A **484**, 564-572 (2002). 136

[76] D.E. Groom, *et al.*, Euro. Phys. J. **C15** (2000) 1. 137

[77] E. V. Shuryak, *Quantum chromodynamics and the theory of superdense matter.* Physics Reports **61**, ISSN 0370-1573 (1980). 3

[78] J. C. Collins and M. J. Perry, *Superdense matter: Neutrons or asymptotically free quarks?* Phys. Rev. Lett. **34**, 1353-1356 (1975). 4

[79] L. D. McLerran and B. Svetitsky, *A Monte Carlo Study of SU(2) Yang-Mills Theory at Finite Temperature.* Phys. Lett. **B98**, 195-198 (1981). 4

[80] F. Karsch, *Lattice Results on QCD Thermodynamics.* Nucl. Phys. **A698**, 199-208 (2002). 4

[81] P. Braun-Munzinger, *Particle Production in Heavy Ion Collisions.* (2003), arXiv:nucl-th/0304013v1. 6

[82] S. S. Adler *et al.*, *Nuclear Effect on Hadron Production in d+Au and p+p Collisions at* $\sqrt{s_{NN}}$*=200 GeV.* Phys. Rev. **C74** 024904 (2006). 9

[83] A. Adare *et al.*, *Cold nuclear matter effcts on heavy quark production.* submitted to Phys. Rev. Lett. , (2012). 9

[84] J. J. Aubert *et al.*, *The ratio of the nucleon structure functions F2N for iron and deuterium.* Phys. Lett. B **123**, 275 (1983). 7

[85] D. Geesaman, K. Saito, and A. Thomas, *The Nuclear EMC Effect.* Annual Review of Nuclear and Particle Science **45**, 337 (1995). 7

[86] J. Seeley *et al.*, *New Measurements of the European Muon Collaboration Effect in Very Light Nuclei.* Phys. Rev. Lett. **103**, 202301 (2009). 7

[87] F. Aaron *et al.*, *Combined measurement and QCD analysis of the inclusive* $e^{\pm}p$ *scattering cross sections at HERA.* Journal of High Energy Physics, 1 (2010). 9

[88] A. Accardi. *Cronin efect in proton-nucleus collisions: A survey of theoretical models.* hep-ph/0212148, (2000). 9

[89] J. Kamin *et al.*, *Investigating the Cronin Cartoon.* available online, `http://jason.kamin.com`, (2003). 9

[90] G. Agakichiev *et al.*, *Study of dielectron production in C+C collisions at 1 AGeV.* Phys. Lett. **B663**, 43 (2008), Preprint arXiv:0711.4281. 12

[91] G. Agakichiev *et al.*, *Dielectron Production in* ^{12}C+^{12}C *Collisions at 2 AGeV with the HADES Spectrometer.* Phys. Rev. Lett. **98**, 052302 (2007), Preprint arXiv:nucl-ex/0608031. 12

[92] G. Agakichiev *et al.* (CERES/NA45 Collaboration), *Enhanced Production of Low-Mass Electron Pairs in 200 GeV/Nucleon S+Au Collisions at the CERN Super Proton Synchrotron.* Phys. Rev. Lett. **75**, 1272 (1995). 12

[93] D. Adamova *et al.* (CERES/NA45 Collaboration), *Enhanced production of low-mass electron-positron pairs in 40 AGeV Pb+Au collisions at the CERN SPS.* Phys. Rev. Lett. **91**, 042301 (2003), Preprint arXiv:nucl-ex/0209024. 12

[94] D. Adamova *et al.* (CERES/NA45 Collaboration), e^+e^-*-pair production in Pb+Au collisions at 158 GeV per nucleon.* Eur. Phys. J. **C41**, 475 (2005), Preprint arXiv:nucl-ex/0506002. 12

[95] R. Shahoyan (NA60 Collaboration), *NA60 results on charm and intermediate mass dimuons' production in In+In 158 GeV* A^{-1} *collisions.* Eur. Phys. J. **G34**, S1029 (2007). 13

[96] S. Damjanovic (NA60 Collaboration), *Thermal dileptons at SPS energies.* Eur. Phys. J. **G34**, S1029 (2008). Preprint arXiv:0805.4153. 13

[97] L. Adamczyk *et al.*, *Di-electron spectrum at mid-rapidity in p+p collisions at* $\sqrt{s} = 200$ *GeV.* submitted to Phys. Rev. C. (2012) Preprint arXiv:1204.1890v1. 19

[98] W. Anderson *et al.*, *Design, Construction, Operation and Performance of a Hadron Blind Detector for the PHENIX Experiment.* NIM A **646.1** (2011). 146

[99] M. Berlowski *et al.*, *Measurement of* η *meson decays into lepton-antilepton pairs.* Phys. Rev. D. **77**, 032004 (2008). 147

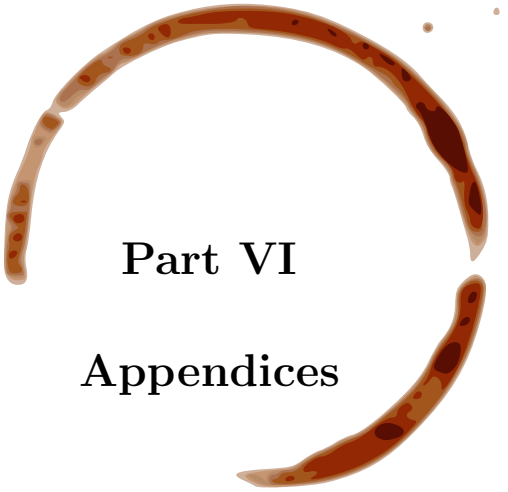

Part VI

Appendices

APPENDIX A

Toy Monte Carlo

A toy monte carlo was written to test the "twice square root" relationship (Equation 6.1) under the following circumstances:

- Single e^+ and single e^- p_T distributions have different shapes.
- Overall asymmetric multiplicities between e^+ and e^-.
- Calculating quantities differentially across mass and p_T.

To test the assumption of whether pure combinatorial pairs $BG12(m, p_T) = BG1122(m, p_T)$ and that the "twice square root" normalization relationship is valid with the conditions listed above, the following framework was used to create likesign and unlike-sign spectra:

- Generate N events of 2 (and *only* 2) leptons. Each single e^+ and e^- gets assigned the following:
  - randomly chosen charge (q) for each lepton
    - generated with relative amount of charge asymmetry as seen in data.
  - single e^+ and e^- p_T chosen from either:
    - realistic distribution seen in data
    - or any "cooked-up" distribution (to test assumptions).

  - random azimuthal angle, ϕ ($-\pi/2$ to $3\pi/2$)
  - random rapidity, Y (± 0.35)
  - *note: every pair is kept: 2π detector!*

- Creates 3 distributions:
  - BG12(m,p_T), BG11(m,p_T), BG22(m,p_T)
    *
  - *note: there are no signal pairs here!*

- Calculate 3 likesign distributions (BG1122(m,p_T))
  - *likesign arithmetic mean*

$$BG1122(m, p_T) = BG11(m, p_T) + BG22(m, p_T). \tag{A.1}$$

  - *likesign geometric mean*

$$BG1122(m, p_T) = 2 \cdot \sqrt{BG11(m, p_T) \cdot BG22(m, p_T)} \tag{A.2}$$

  - *likesign differential geometric mean*

$$BG1122(m, p_T) = \sqrt{\frac{\iint BG22(m, p_T)}{\iint BG11(m, p_T)}} \cdot BG11(m, p_T) + \sqrt{\frac{\iint BG11(m, p_T)}{\iint BG22(m, p_T)}} \cdot BG22(m, p_T) \tag{A.3}$$

- The assumption being tested is whether $BG12(m, p_T) = BG1122(m, p_T)$.

Since there was *no signal* injected into these pairs, the subtracted difference between the unlike-sign distribution (BG12) and the likesign distribution (BG1122) differentially in mass and p_T *should be* zero. Moreover, the situation is simplified by not needing a relative acceptance correction since the pairs are generated into 2π around the azimuth.

Starting with realistic p_T distributions taken by sampling real data for both positrons and electrons (Figure A.1), random pairs were generated and the BG12, BG11, and BG22 distributions were filled. The results shown here are using realistic shapes asymmetries (between e^+

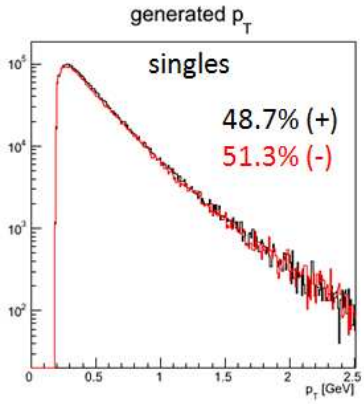

Figure A.1: e^+ (and e^-) input p_T distributions.

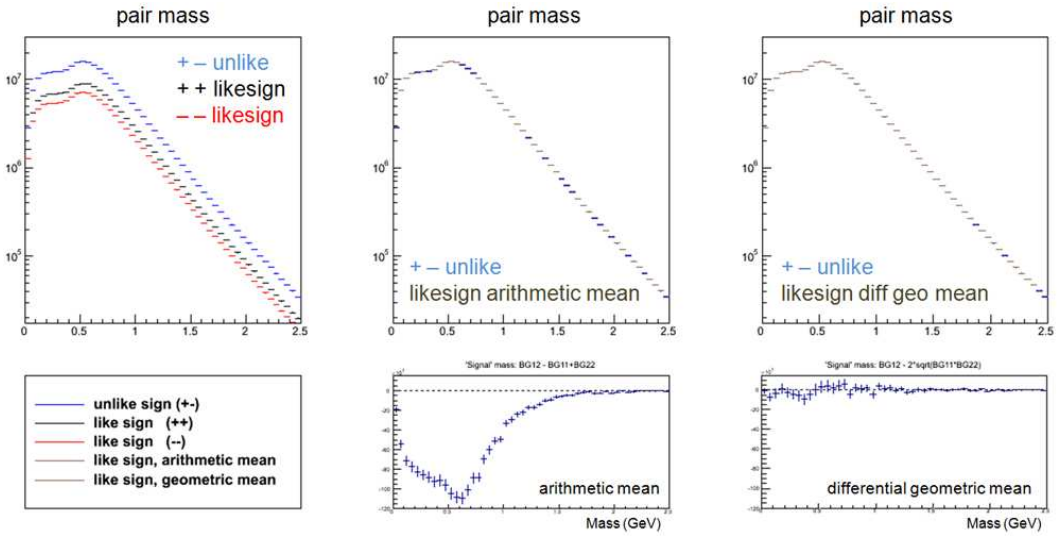

Figure A.2: The top left panel shows BG12, BG11, and BG22 as a function of mass. The middle top panel shows the BG12 and BG1122 calculated using the arithmetic mean. The top right panel shows the BG12 and BG1122 calculated using the differential geometric mean. The bottom left and right panels show the subtracted difference between the BG12 and BG1122 for the arithmetic and differential geometric mean, respectively.

and e^-) as well as overall multiplicity asymmetries of 48.7% positrons and 51.3% electrons.

The lower panels of Figure A.2 show the subtracted difference between the BG12 and BG1122 for the arithmetic mean (left) and differential geometric mean (right). The arithmetic mean distorts the shape of the "signal" (which should be zero in this simulation!) and oversubtracts dramatically. The differential geometric mean, on the other hand, does not suffer from such distortions.

In total, 5×10^8 pairs were generated and the "signal" from the three methods of calculating FG1122 with the above conditions is shown in Figure A.3). This scenario is the most realisitic since the single electron and positron distributions reflect what is seen in the 2008 d+Au dataset. Using the arithmetic mean clearly does not generate a likesign distribution that mirrors the unlike-sign. The geometric mean must be used! In addition, since the differential geometric mean is the correct representation to preserve the "twice square root" relationship when the calculations are done bin-by-bin in mass and p_T, this is the correct method to use. Moreover, when dealing with limited statistics, the non-differential geometric mean doesn't even make sense bin-by-bin.

This is because the method forces the resulting bin to zero if a bin in either the BG11 or BG22 is zero. This happens quite frequently in the real data when fine binning is used out to 8 GeV/c in p_T and 14 GeV/c^2 in mass.

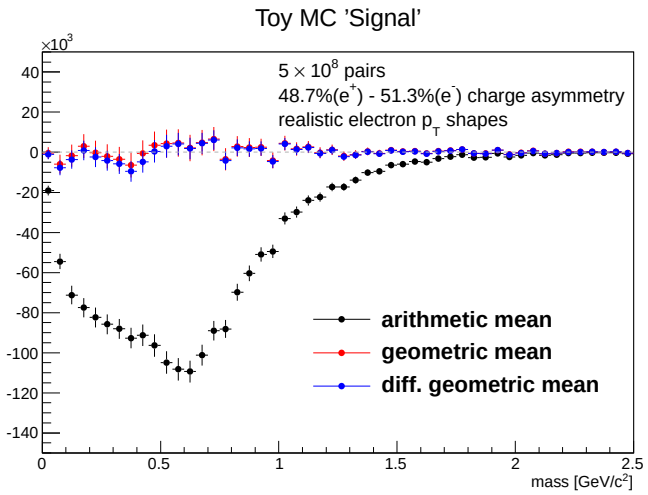

Figure A.3: The difference between BG12 – BG1122 for various calculations of the likesign distribution. The input parameters and distributions are representative of the 2008 d+Au running conditions.

In order to investigate the methodology, the toy Monte Carlo procedure was performed with various degrees of charge asymmetry as well as various degrees of initial p_T shape distortions. Figure A.4 illustrates an extreme (and unrealistic) case where 45% positrons and 55% electrons were generated. In addition, the positron's initial p_T was scaled by 0.9 resulting in highly asymmetric input distributions. These extreme input conditions lead to unacceptable distortions in the signal. However, even in this case, it is clear that the differential geometric mean results in the least distorted signal.

The geometric mean is the cleanest way to calculate the likesign distribution. In fact, in the scenario that the *shapes* of the single electron and positron are identical, the overall multiplicity asymmetry is handled exactly correctly by the differential geometric mean FG1122. This is illustrated in another case where the distributions are 35% positrons and 65% electrons. This type of asymmetry is completely unrealistic and results in a terrible oversubtraction when using the arithmetic mean. However, the geometric mean (both differentially and non-differentially) reveal exactly zero signal in the toy Monte Carlo. Figure A.5 shows the subtrated signal from each of the three methods.

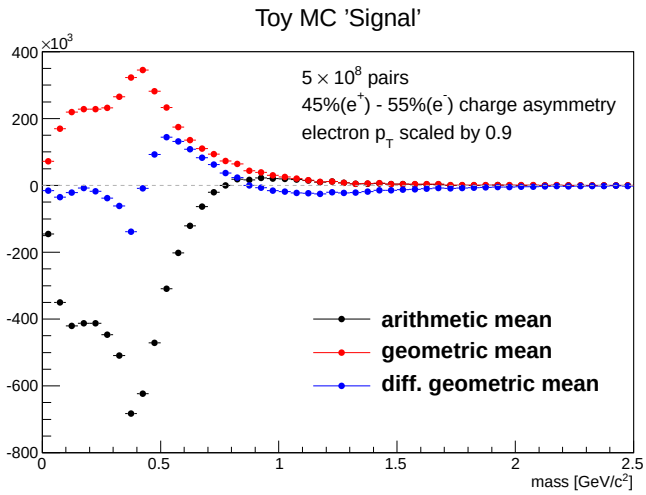

Figure A.4: The difference between BG12 – BG1122 for various calculations of the likesign distribution. The input parameters and distributions are unrealistically asymmetric.

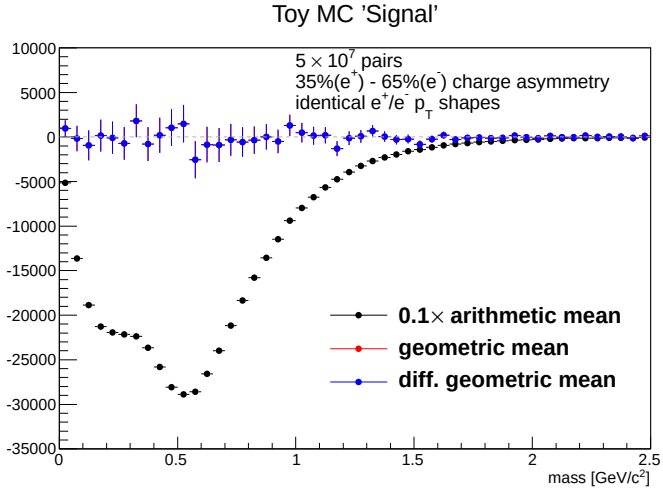

Figure A.5: The difference between BG12 – BG1122 for various calculations of the likesign distribution. The input parameters and distributions are highly asymmetric in e^+/e^- multiplicities.

In summary, of the three methods considered (arithmetic mean, geometric mean, and differential geometric mean), the arithmetic mean is only correct

if the single electron and positron distributions are completely symmetric. The geometric mean is correct in the full *integral*, however the calculation is performed differentially in mass and p_T, rendering this method insufficient. The differential geometric mean is the correct procedure under the requirement that the *shapes* of the electron and positron distributions are the same. This approximation is indeed legitimate (see Figure A.1) in the 2008 d+Au dataset. Moreover, the differential geometric mean is fully correct regardless of the e^+/e^- multiplicity asymmetry. Therefore, the differential geometric mean (equation A.3) is used in this analysis.

APPENDIX B

Data Tables

Table B.1 gives the data points for Figure 9.3.

mass (GeV/c^2)	$\frac{1}{N_{evt}}\frac{dN}{dm_{ee}}$ (c^2/ GeV)	Stat Uncert	Syst Uncert
0.005	4.003e-003	2.491e-005	1.121e-003
0.015	1.693e-003	1.675e-005	4.739e-004
0.025	8.010e-004	1.219e-005	2.243e-004
0.035	5.964e-004	1.135e-005	1.670e-004
0.045	3.628e-004	8.007e-006	1.016e-004
0.055	2.723e-004	7.169e-006	7.625e-005
0.065	2.021e-004	6.583e-006	5.657e-005
0.075	1.511e-004	6.029e-006	4.231e-005
0.085	1.160e-004	5.499e-006	3.249e-005
0.095	8.946e-005	5.164e-006	2.505e-005
0.105	5.588e-005	4.601e-006	1.565e-005
0.115	3.907e-005	4.351e-006	1.094e-005
0.125	3.179e-005	4.288e-006	8.900e-006
0.145	2.338e-005	2.343e-006	6.546e-006
0.180	2.020e-005	2.273e-006	5.656e-006
0.240	1.210e-005	2.068e-006	3.630e-006
0.330	5.491e-006	3.026e-006	1.647e-006
0.480	3.172e-006	2.093e-006	9.515e-007
0.630	3.860e-006	2.137e-006	1.467e-006
0.720	4.753e-006	1.715e-006	1.806e-006
0.765	1.405e-005	4.423e-006	5.340e-006

0.775	2.415e-005	4.323e-006	9.178e-006
0.785	1.514e-005	3.498e-006	5.753e-006
0.805	3.572e-006	1.976e-006	1.358e-006
0.860	1.990e-006	1.001e-006	7.562e-007
0.930	2.272e-006	9.033e-007	8.632e-007
0.970	3.559e-006	1.421e-006	1.352e-006
0.990	3.883e-006	1.197e-006	1.476e-006
1.005	6.557e-006	1.776e-006	2.492e-006
1.015	7.201e-006	1.711e-006	2.736e-006
1.025	6.217e-006	1.674e-006	2.363e-006
1.170	6.066e-007	1.909e-007	2.305e-007
1.360	5.017e-007	1.120e-007	1.304e-007
1.460	4.126e-007	8.815e-008	1.073e-007
1.560	2.703e-007	7.123e-008	7.029e-008
1.660	2.514e-007	5.716e-008	6.536e-008
1.760	2.191e-007	4.784e-008	5.697e-008
1.860	1.133e-007	3.770e-008	2.945e-008
1.960	1.243e-007	3.162e-008	3.233e-008
2.060	1.283e-007	2.614e-008	3.336e-008
2.160	1.032e-007	2.250e-008	2.683e-008
2.260	8.501e-008	1.938e-008	2.210e-008
2.360	5.952e-008	1.798e-008	1.548e-008
2.460	6.877e-008	1.625e-008	1.788e-008
2.560	6.305e-008	1.491e-008	1.639e-008
2.660	6.950e-008	1.236e-008	1.807e-008
2.730	5.764e-008	1.674e-008	1.499e-008
2.790	6.799e-008	1.205e-008	1.768e-008
2.850	8.496e-008	1.651e-008	2.209e-008
2.890	1.309e-007	1.686e-008	3.403e-008
2.920	1.720e-007	2.615e-008	4.472e-008
2.940	1.949e-007	2.570e-008	5.068e-008
2.960	1.387e-007	2.653e-008	3.607e-008
2.980	2.532e-007	3.048e-008	6.583e-008
3.000	3.707e-007	3.376e-008	9.638e-008
3.020	5.151e-007	3.750e-008	1.339e-007
3.040	6.295e-007	4.256e-008	1.637e-007
3.060	8.900e-007	5.029e-008	2.314e-007
3.080	1.066e-006	5.373e-008	2.771e-007
3.100	1.171e-006	5.462e-008	3.044e-007
3.120	9.368e-007	5.029e-008	2.436e-007

3.140	5.405e-007	4.049e-008	1.405e-007
3.160	3.585e-007	3.453e-008	9.320e-008
3.180	2.000e-007	2.767e-008	5.200e-008
3.200	9.030e-008	1.886e-008	2.348e-008
3.220	6.496e-008	1.352e-008	1.689e-008
3.240	2.751e-008	1.266e-008	7.153e-009
3.270	2.264e-008	7.560e-009	5.888e-009
3.310	1.486e-008	6.888e-009	3.863e-009
3.420	8.286e-009	3.098e-009	2.154e-009
3.585	1.033e-008	2.960e-009	2.686e-009
3.685	2.157e-008	5.073e-009	5.609e-009
3.785	3.099e-009	2.476e-009	8.057e-010
4.160	2.982e-009	8.655e-010	7.754e-010
5.010	1.579e-009	3.569e-010	3.000e-010
6.160	3.091e-010	1.865e-010	8.347e-011
7.635	1.312e-010	8.390e-011	3.543e-011
8.855	2.294e-010	1.197e-010	6.193e-011
9.400	6.728e-010	2.329e-010	1.817e-010
9.800	4.043e-010	1.901e-010	1.092e-010
10.200	2.018e-010	1.455e-010	5.447e-011
11.300	4.392e-011	4.593e-011	1.186e-011
13.100	1.911e-011	3.175e-011	5.160e-012

Table B.1: Data points for Figure 9.3 with statistical and systematic uncertainties.

Table B.2 gives the cocktail points for the regular "out-of-the-box" cocktail as well as the fine-tuned cocktail (fit in mass and p_T) with the associated systematic uncertainty for each. These cocktails are from Figures 9.3 and 9.6.

mass (GeV/c^2)	cocktail	Syst Uncert	fine-tuned	fine-tuned Syst
0.005	4.953e-003	1.987e-004	5.259e-003	2.109e-004
0.015	1.256e-003	1.987e-004	1.333e-003	2.109e-004
0.025	7.000e-004	3.501e-005	7.436e-004	3.720e-005
0.035	4.695e-004	3.501e-005	4.993e-004	3.720e-005
0.045	3.420e-004	1.967e-005	3.641e-004	2.095e-005
0.055	2.554e-004	1.967e-005	2.726e-004	2.095e-005
0.065	1.961e-004	9.943e-006	2.098e-004	1.065e-005
0.075	1.504e-004	9.943e-006	1.616e-004	1.065e-005
0.085	1.110e-004	6.250e-006	1.200e-004	6.783e-006
0.095	8.080e-005	6.250e-006	8.814e-005	6.783e-006
0.105	5.451e-005	3.132e-006	6.050e-005	3.496e-006
0.115	3.649e-005	3.132e-006	4.146e-005	3.496e-006
0.125	2.604e-005	1.937e-006	3.033e-005	2.266e-006
0.145	2.149e-005	1.969e-006	2.521e-005	2.310e-006
0.180	1.776e-005	1.660e-006	2.083e-005	1.948e-006
0.240	1.510e-005	1.454e-006	1.770e-005	1.705e-006
0.330	1.157e-005	9.691e-007	1.353e-005	1.133e-006
0.480	6.241e-006	7.516e-007	7.143e-006	8.583e-007
0.630	3.767e-006	4.536e-007	4.365e-006	5.254e-007
0.720	4.463e-006	4.666e-007	5.213e-006	5.529e-007
0.765	1.116e-005	2.150e-006	1.191e-005	2.239e-006
0.775	2.160e-005	2.150e-006	2.236e-005	2.239e-006
0.785	2.108e-005	2.060e-006	2.177e-005	2.136e-006
0.805	5.816e-006	4.452e-007	6.303e-006	4.975e-007
0.860	1.684e-006	2.318e-007	1.988e-006	2.739e-007
0.930	1.241e-006	1.871e-007	1.473e-006	2.224e-007
0.970	1.326e-006	1.836e-007	1.552e-006	2.147e-007
0.990	2.566e-006	3.132e-007	2.877e-006	3.503e-007
1.005	7.364e-006	1.069e-006	8.028e-006	1.161e-006
1.015	1.095e-005	1.069e-006	1.187e-005	1.161e-006
1.025	8.502e-006	7.652e-007	9.245e-006	8.339e-007
1.170	7.893e-007	1.283e-007	9.250e-007	1.074e-007
1.360	3.996e-007	8.821e-008	4.749e-007	7.343e-008
1.460	3.236e-007	7.294e-008	3.831e-007	6.048e-008
1.560	2.652e-007	5.835e-008	3.126e-007	4.813e-008

1.660	2.182e-007	4.865e-008	2.561e-007	3.995e-008
1.760	1.809e-007	4.244e-008	2.112e-007	3.470e-008
1.860	1.510e-007	3.572e-008	1.753e-007	2.904e-008
1.960	1.274e-007	3.096e-008	1.461e-007	2.489e-008
2.060	1.100e-007	2.771e-008	1.234e-007	2.179e-008
2.160	9.487e-008	2.469e-008	1.038e-007	1.896e-008
2.260	8.157e-008	2.157e-008	8.757e-008	1.623e-008
2.360	7.128e-008	1.832e-008	7.520e-008	1.350e-008
2.460	6.276e-008	1.578e-008	6.504e-008	1.142e-008
2.560	5.821e-008	1.400e-008	5.947e-008	1.002e-008
2.660	5.679e-008	1.228e-008	5.737e-008	8.694e-009
2.730	5.926e-008	1.137e-008	5.953e-008	7.992e-009
2.790	6.615e-008	1.094e-008	6.632e-008	9.452e-009
2.850	7.910e-008	1.111e-008	7.933e-008	1.114e-008
2.890	9.436e-008	1.121e-008	9.478e-008	1.126e-008
2.920	1.149e-007	1.195e-008	1.156e-007	1.204e-008
2.940	1.340e-007	1.258e-008	1.351e-007	1.270e-008
2.960	1.701e-007	1.320e-008	1.719e-007	1.336e-008
2.980	2.209e-007	1.750e-008	2.238e-007	1.774e-008
3.000	3.245e-007	2.207e-008	3.295e-007	2.243e-008
3.020	4.693e-007	2.207e-008	4.773e-007	2.243e-008
3.040	6.671e-007	3.080e-008	6.791e-007	3.133e-008
3.060	8.909e-007	4.368e-008	9.075e-007	4.449e-008
3.080	9.837e-007	5.060e-008	1.002e-006	5.155e-008
3.100	9.736e-007	5.489e-008	9.918e-007	5.592e-008
3.120	8.126e-007	3.744e-008	8.275e-007	3.811e-008
3.140	5.630e-007	2.557e-008	5.727e-007	2.599e-008
3.160	3.665e-007	1.672e-008	3.721e-007	1.695e-008
3.180	2.072e-007	1.117e-008	2.095e-007	9.150e-009
3.200	1.153e-007	1.073e-008	1.157e-007	5.086e-009
3.220	6.582e-008	9.794e-009	6.517e-008	4.554e-009
3.240	3.920e-008	9.474e-009	3.799e-008	4.313e-009
3.270	2.345e-008	7.971e-009	2.190e-008	3.523e-009
3.310	1.555e-008	6.256e-009	1.381e-008	2.630e-009
3.420	1.054e-008	4.468e-009	8.563e-009	1.726e-009
3.585	1.511e-008	4.529e-009	1.081e-008	2.607e-009
3.685	2.061e-008	3.721e-009	1.428e-008	2.578e-009
3.785	1.095e-008	3.494e-009	7.566e-009	1.942e-009
4.160	3.909e-009	2.140e-009	2.453e-009	7.194e-010
5.010	2.016e-009	1.161e-009	1.077e-009	3.276e-010

6.160	9.381e-010	5.728e-010	4.501e-010	1.471e-010
7.635	4.012e-010	2.371e-010	1.815e-010	5.706e-011
8.855	4.653e-010	2.562e-010	2.371e-010	6.966e-011
9.400	7.188e-010	1.859e-010	3.855e-010	9.997e-011
9.800	5.577e-010	2.337e-010	2.982e-010	1.249e-010
10.200	2.951e-010	1.091e-010	1.535e-010	5.659e-011
11.300	6.511e-011	2.902e-011	2.928e-011	1.161e-011
13.100	1.233e-011	7.764e-012	4.106e-012	2.618e-012

Table B.2: Cocktail points for regular cocktail and fine-tuned cocktail with associated systematic uncertainty.

Table B.3 gives the data points of the mass spectra in various p_T slices from Figure 9.5.

p_T (GeV/c)	mass (GeV/c^2)	$\frac{1}{N_{evt}}\frac{dN}{dm_{ee}}$ (c^2/GeV)	Stat Uncert	Syst Uncert
0.0 – 0.5	0.005	5.236e-004	1.457e-005	1.466e-004
0.0 – 0.5	0.015	2.973e-004	1.103e-005	8.324e-005
0.0 – 0.5	0.025	1.712e-004	8.761e-006	4.794e-005
0.0 – 0.5	0.035	1.543e-004	8.435e-006	4.319e-005
0.0 – 0.5	0.045	6.586e-005	5.260e-006	1.844e-005
0.0 – 0.5	0.055	4.451e-005	4.491e-006	1.246e-005
0.0 – 0.5	0.065	3.243e-005	4.339e-006	9.082e-006
0.0 – 0.5	0.075	2.573e-005	4.093e-006	7.205e-006
0.0 – 0.5	0.085	1.755e-005	3.664e-006	4.914e-006
0.0 – 0.5	0.095	1.487e-005	3.537e-006	4.164e-006
0.0 – 0.5	0.185	3.116e-006	8.933e-007	8.726e-007
0.0 – 0.5	0.345	-2.513e-007	2.226e-006	7.540e-008
0.0 – 0.5	0.520	1.848e-007	1.615e-006	7.023e-008
0.0 – 0.5	0.690	1.130e-006	1.134e-006	4.295e-007
0.0 – 0.5	0.780	5.191e-006	1.539e-006	1.973e-006
0.0 – 0.5	0.890	1.042e-006	5.238e-007	3.961e-007
0.0 – 0.5	1.020	1.071e-007	5.324e-007	4.071e-008
0.0 – 0.5	1.285	2.334e-007	9.696e-008	8.869e-008
0.0 – 0.5	1.610	7.752e-008	2.918e-008	2.016e-008
0.0 – 0.5	1.810	4.517e-008	1.770e-008	1.174e-008
0.0 – 0.5	2.010	5.191e-008	1.048e-008	1.350e-008
0.0 – 0.5	2.210	2.860e-008	6.507e-009	7.436e-009
0.0 – 0.5	2.410	1.720e-008	5.624e-009	4.473e-009
0.0 – 0.5	2.610	6.348e-009	4.925e-009	1.650e-009
0.0 – 0.5	2.770	1.529e-008	3.527e-009	3.975e-009
0.0 – 0.5	2.870	1.468e-008	4.281e-009	3.816e-009
0.0 – 0.5	2.940	2.034e-008	5.181e-009	5.288e-009
0.0 – 0.5	2.990	4.699e-008	7.926e-009	1.222e-008
0.0 – 0.5	3.020	6.905e-008	1.288e-008	1.795e-008
0.0 – 0.5	3.040	7.318e-008	1.392e-008	1.903e-008
0.0 – 0.5	3.060	1.114e-007	1.661e-008	2.896e-008
0.0 – 0.5	3.080	1.322e-007	2.017e-008	3.436e-008
0.0 – 0.5	3.100	1.467e-007	1.873e-008	3.813e-008
0.0 – 0.5	3.120	1.359e-007	1.794e-008	3.534e-008
0.0 – 0.5	3.140	5.791e-008	1.215e-008	1.506e-008
0.0 – 0.5	3.160	6.154e-008	1.253e-008	1.600e-008

0.0 – 0.5	3.190	8.880e-009	5.236e-009	2.309e-009
0.0 – 0.5	3.410	1.500e-009	7.413e-010	3.901e-010
0.0 – 0.5	3.685	2.598e-009	9.858e-010	6.754e-010
0.0 – 0.5	4.410	2.658e-010	1.873e-010	6.912e-011
0.0 – 0.5	6.830	9.393e-012	2.257e-011	2.536e-012
0.0 – 0.5	9.500	1.221e-011	0.000e+000	3.295e-012
0.0 – 0.5	12.200	6.044e-012	6.044e-012	1.632e-012
0.5 – 1.0	0.005	1.475e-003	2.023e-005	4.131e-004
0.5 – 1.0	0.015	6.064e-004	1.351e-005	1.698e-004
0.5 – 1.0	0.025	2.885e-004	9.342e-006	8.079e-005
0.5 – 1.0	0.035	2.336e-004	8.705e-006	6.541e-005
0.5 – 1.0	0.045	1.382e-004	6.423e-006	3.869e-005
0.5 – 1.0	0.055	1.051e-004	5.737e-006	2.942e-005
0.5 – 1.0	0.065	7.928e-005	5.194e-006	2.220e-005
0.5 – 1.0	0.075	5.639e-005	4.646e-006	1.579e-005
0.5 – 1.0	0.085	4.664e-005	4.499e-006	1.306e-005
0.5 – 1.0	0.095	3.660e-005	4.148e-006	1.025e-005
0.5 – 1.0	0.105	2.308e-005	3.840e-006	6.462e-006
0.5 – 1.0	0.120	1.285e-005	2.339e-006	3.597e-006
0.5 – 1.0	0.150	1.115e-005	1.643e-006	3.121e-006
0.5 – 1.0	0.205	7.388e-006	1.487e-006	2.069e-006
0.5 – 1.0	0.260	7.233e-006	2.270e-006	2.170e-006
0.5 – 1.0	0.330	5.078e-006	1.696e-006	1.523e-006
0.5 – 1.0	0.455	1.870e-006	1.774e-006	5.609e-007
0.5 – 1.0	0.610	1.416e-006	1.363e-006	5.381e-007
0.5 – 1.0	0.730	3.225e-006	1.311e-006	1.226e-006
0.5 – 1.0	0.775	9.940e-006	3.392e-006	3.777e-006
0.5 – 1.0	0.785	5.575e-006	2.305e-006	2.119e-006
0.5 – 1.0	0.830	2.031e-006	8.182e-007	7.720e-007
0.5 – 1.0	0.935	1.013e-006	3.572e-007	3.848e-007
0.5 – 1.0	1.005	3.094e-006	7.081e-007	1.176e-006
0.5 – 1.0	1.015	4.271e-006	7.212e-007	1.623e-006
0.5 – 1.0	1.025	3.268e-006	5.948e-007	1.242e-006
0.5 – 1.0	1.170	2.672e-007	7.417e-008	1.015e-007
0.5 – 1.0	1.410	2.022e-007	4.721e-008	5.256e-008
0.5 – 1.0	1.610	7.577e-008	2.975e-008	1.970e-008
0.5 – 1.0	1.810	1.044e-007	1.836e-008	2.716e-008
0.5 – 1.0	2.010	3.886e-008	1.196e-008	1.010e-008
0.5 – 1.0	2.210	3.653e-008	8.506e-009	9.497e-009
0.5 – 1.0	2.410	2.335e-008	6.614e-009	6.072e-009

0.5 – 1.0	2.610	2.156e-008	4.640e-009	5.605e-009
0.5 – 1.0	2.770	2.433e-008	4.778e-009	6.326e-009
0.5 – 1.0	2.870	3.831e-008	5.793e-009	9.961e-009
0.5 – 1.0	2.940	4.049e-008	7.023e-009	1.053e-008
0.5 – 1.0	2.990	8.110e-008	1.073e-008	2.109e-008
0.5 – 1.0	3.020	1.053e-007	1.616e-008	2.739e-008
0.5 – 1.0	3.040	1.269e-007	1.801e-008	3.299e-008
0.5 – 1.0	3.060	1.902e-007	2.198e-008	4.945e-008
0.5 – 1.0	3.080	2.490e-007	2.415e-008	6.473e-008
0.5 – 1.0	3.100	2.976e-007	2.631e-008	7.738e-008
0.5 – 1.0	3.120	2.486e-007	2.540e-008	6.464e-008
0.5 – 1.0	3.140	1.490e-007	1.913e-008	3.875e-008
0.5 – 1.0	3.160	8.559e-008	1.610e-008	2.225e-008
0.5 – 1.0	3.190	3.683e-008	7.057e-009	9.576e-009
0.5 – 1.0	3.410	3.260e-009	9.936e-010	8.477e-010
0.5 – 1.0	3.685	2.422e-009	1.460e-009	6.296e-010
0.5 – 1.0	4.335	3.768e-010	2.711e-010	9.797e-011
0.5 – 1.0	5.410	2.494e-010	7.727e-011	4.739e-011
0.5 – 1.0	7.410	2.477e-011	1.767e-011	6.688e-012
0.5 – 1.0	9.285	5.974e-011	4.225e-011	1.613e-011
0.5 – 1.0	11.830	5.677e-012	8.850e-012	1.533e-012
1.0 – 1.5	0.005	1.855e-003	1.369e-005	5.194e-004
1.0 – 1.5	0.015	7.051e-004	8.271e-006	1.974e-004
1.0 – 1.5	0.025	3.040e-004	5.273e-006	8.512e-005
1.0 – 1.5	0.035	2.053e-004	4.363e-006	5.749e-005
1.0 – 1.5	0.045	1.471e-004	3.784e-006	4.119e-005
1.0 – 1.5	0.055	1.107e-004	3.393e-006	3.100e-005
1.0 – 1.5	0.065	7.734e-005	2.756e-006	2.165e-005
1.0 – 1.5	0.075	5.399e-005	2.281e-006	1.512e-005
1.0 – 1.5	0.085	4.764e-005	2.422e-006	1.334e-005
1.0 – 1.5	0.095	3.288e-005	2.062e-006	9.207e-006
1.0 – 1.5	0.105	2.243e-005	1.851e-006	6.279e-006
1.0 – 1.5	0.115	1.651e-005	1.738e-006	4.622e-006
1.0 – 1.5	0.125	1.284e-005	1.491e-006	3.595e-006
1.0 – 1.5	0.135	9.170e-006	1.430e-006	2.568e-006
1.0 – 1.5	0.150	9.462e-006	9.566e-007	2.649e-006
1.0 – 1.5	0.170	6.261e-006	8.834e-007	1.753e-006
1.0 – 1.5	0.190	5.497e-006	8.791e-007	1.539e-006
1.0 – 1.5	0.220	3.752e-006	5.363e-007	1.126e-006
1.0 – 1.5	0.260	3.723e-006	5.402e-007	1.117e-006

1.0 – 1.5	0.330	2.499e-006	3.444e-007	7.497e-007
1.0 – 1.5	0.430	1.241e-006	2.390e-007	3.724e-007
1.0 – 1.5	0.530	4.896e-007	1.923e-007	1.860e-007
1.0 – 1.5	0.605	1.219e-006	2.714e-007	4.632e-007
1.0 – 1.5	0.655	5.827e-007	2.561e-007	2.214e-007
1.0 – 1.5	0.705	4.053e-007	2.308e-007	1.540e-007
1.0 – 1.5	0.740	8.104e-007	3.509e-007	3.080e-007
1.0 – 1.5	0.760	2.330e-006	3.674e-007	8.854e-007
1.0 – 1.5	0.775	3.758e-006	6.037e-007	1.428e-006
1.0 – 1.5	0.785	2.296e-006	5.033e-007	8.726e-007
1.0 – 1.5	0.805	5.409e-007	2.753e-007	2.056e-007
1.0 – 1.5	0.880	2.352e-007	1.309e-007	8.939e-008
1.0 – 1.5	0.970	8.371e-007	1.596e-007	3.181e-007
1.0 – 1.5	1.015	2.164e-006	2.059e-007	8.223e-007
1.0 – 1.5	1.040	6.763e-007	2.188e-007	2.570e-007
1.0 – 1.5	1.060	3.150e-007	1.981e-007	1.197e-007
1.0 – 1.5	1.195	1.031e-007	4.277e-008	3.917e-008
1.0 – 1.5	1.445	1.013e-007	2.535e-008	2.635e-008
1.0 – 1.5	1.695	6.637e-008	1.688e-008	1.726e-008
1.0 – 1.5	1.945	2.181e-008	1.067e-008	5.671e-009
1.0 – 1.5	2.195	1.839e-008	7.516e-009	4.782e-009
1.0 – 1.5	2.445	1.773e-008	5.588e-009	4.611e-009
1.0 – 1.5	2.695	2.625e-008	3.846e-009	6.825e-009
1.0 – 1.5	2.870	3.872e-008	5.800e-009	1.007e-008
1.0 – 1.5	2.970	5.388e-008	6.268e-009	1.401e-008
1.0 – 1.5	3.030	1.691e-007	2.253e-008	4.395e-008
1.0 – 1.5	3.050	2.246e-007	2.454e-008	5.839e-008
1.0 – 1.5	3.070	2.524e-007	2.626e-008	6.562e-008
1.0 – 1.5	3.090	2.769e-007	2.641e-008	7.198e-008
1.0 – 1.5	3.110	3.187e-007	2.882e-008	8.287e-008
1.0 – 1.5	3.130	2.067e-007	2.359e-008	5.374e-008
1.0 – 1.5	3.150	1.438e-007	2.114e-008	3.739e-008
1.0 – 1.5	3.170	5.374e-008	1.427e-008	1.397e-008
1.0 – 1.5	3.190	2.822e-008	9.722e-009	7.337e-009
1.0 – 1.5	3.270	5.171e-009	2.308e-009	1.345e-009
1.0 – 1.5	3.460	2.742e-009	1.445e-009	7.130e-010
1.0 – 1.5	3.630	1.657e-009	1.881e-009	4.307e-010
1.0 – 1.5	3.730	4.315e-009	1.514e-009	1.122e-009
1.0 – 1.5	3.905	1.437e-009	7.212e-010	3.736e-010
1.0 – 1.5	4.530	3.785e-010	2.210e-010	7.192e-011

1.0 – 1.5	5.530	2.909e-010	9.256e-011	7.855e-011
1.0 – 1.5	6.830	3.568e-011	4.389e-011	9.634e-012
1.0 – 1.5	8.430	6.136e-011	2.655e-011	1.657e-011
1.0 – 1.5	9.580	3.450e-011	3.450e-011	9.314e-012
1.0 – 1.5	10.280	1.038e-010	5.995e-011	2.803e-011
1.0 – 1.5	11.130	2.422e-011	2.422e-011	6.540e-012
1.0 – 1.5	12.130	0.000e+000	0.000e+000	0.000e+000
1.0 – 1.5	13.130	0.000e+000	0.000e+000	0.000e+000
1.0 – 1.5	13.815	0.000e+000	0.000e+000	0.000e+000
1.5 – 2.0	0.005	7.411e-004	2.756e-006	2.075e-004
1.5 – 2.0	0.015	3.268e-004	1.821e-006	9.150e-005
1.5 – 2.0	0.025	1.475e-004	1.146e-006	4.131e-005
1.5 – 2.0	0.035	9.891e-005	9.374e-007	2.769e-005
1.5 – 2.0	0.045	6.831e-005	8.552e-007	1.913e-005
1.5 – 2.0	0.055	5.019e-005	7.394e-007	1.405e-005
1.5 – 2.0	0.065	3.793e-005	6.512e-007	1.062e-005
1.5 – 2.0	0.075	2.856e-005	5.733e-007	7.998e-006
1.5 – 2.0	0.085	2.187e-005	5.068e-007	6.123e-006
1.5 – 2.0	0.095	1.688e-005	4.621e-007	4.726e-006
1.5 – 2.0	0.105	1.138e-005	4.149e-007	3.187e-006
1.5 – 2.0	0.115	9.252e-006	3.826e-007	2.591e-006
1.5 – 2.0	0.125	5.841e-006	3.030e-007	1.636e-006
1.5 – 2.0	0.135	4.772e-006	2.680e-007	1.336e-006
1.5 – 2.0	0.150	4.241e-006	1.843e-007	1.188e-006
1.5 – 2.0	0.170	3.375e-006	1.695e-007	9.449e-007
1.5 – 2.0	0.190	2.805e-006	1.624e-007	7.853e-007
1.5 – 2.0	0.220	2.126e-006	1.075e-007	6.377e-007
1.5 – 2.0	0.260	1.962e-006	1.051e-007	5.885e-007
1.5 – 2.0	0.330	1.296e-006	6.041e-008	3.889e-007
1.5 – 2.0	0.430	8.333e-007	5.886e-008	2.500e-007
1.5 – 2.0	0.530	2.983e-007	5.069e-008	1.134e-007
1.5 – 2.0	0.605	2.751e-007	7.298e-008	1.045e-007
1.5 – 2.0	0.655	3.353e-007	7.167e-008	1.274e-007
1.5 – 2.0	0.705	5.104e-007	7.642e-008	1.940e-007
1.5 – 2.0	0.740	3.424e-007	1.237e-007	1.301e-007
1.5 – 2.0	0.760	8.785e-007	1.321e-007	3.338e-007
1.5 – 2.0	0.775	2.157e-006	2.141e-007	8.198e-007
1.5 – 2.0	0.785	1.699e-006	2.089e-007	6.455e-007
1.5 – 2.0	0.805	3.758e-007	9.294e-008	1.428e-007
1.5 – 2.0	0.880	1.062e-007	4.106e-008	4.037e-008

1.5 – 2.0	0.970	3.327e-007	5.623e-008	1.264e-007
1.5 – 2.0	1.015	9.880e-007	9.546e-008	3.754e-007
1.5 – 2.0	1.040	2.714e-007	9.872e-008	1.031e-007
1.5 – 2.0	1.060	1.456e-007	9.356e-008	5.532e-008
1.5 – 2.0	1.195	1.132e-007	2.320e-008	4.301e-008
1.5 – 2.0	1.445	1.950e-008	1.627e-008	5.070e-009
1.5 – 2.0	1.695	1.960e-008	1.142e-008	5.096e-009
1.5 – 2.0	1.945	9.603e-009	7.889e-009	2.497e-009
1.5 – 2.0	2.195	9.246e-009	5.608e-009	2.404e-009
1.5 – 2.0	2.445	8.917e-009	4.101e-009	2.318e-009
1.5 – 2.0	2.695	1.151e-008	3.183e-009	2.992e-009
1.5 – 2.0	2.870	1.892e-008	4.971e-009	4.920e-009
1.5 – 2.0	2.970	4.954e-008	5.912e-009	1.288e-008
1.5 – 2.0	3.030	1.239e-007	1.854e-008	3.223e-008
1.5 – 2.0	3.050	1.773e-007	2.196e-008	4.611e-008
1.5 – 2.0	3.070	2.125e-007	2.385e-008	5.524e-008
1.5 – 2.0	3.090	2.225e-007	2.458e-008	5.784e-008
1.5 – 2.0	3.110	2.301e-007	2.467e-008	5.982e-008
1.5 – 2.0	3.130	1.723e-007	2.153e-008	4.481e-008
1.5 – 2.0	3.150	9.345e-008	1.759e-008	2.430e-008
1.5 – 2.0	3.170	4.841e-008	1.396e-008	1.259e-008
1.5 – 2.0	3.190	5.176e-008	1.395e-008	1.346e-008
1.5 – 2.0	3.615	1.738e-009	5.988e-010	4.518e-010
1.5 – 2.0	5.030	1.893e-010	1.281e-010	3.596e-011
1.5 – 2.0	6.830	1.400e-010	6.294e-011	3.780e-011
1.5 – 2.0	8.430	5.001e-011	2.344e-011	1.350e-011
1.5 – 2.0	9.580	1.144e-010	6.612e-011	3.090e-011
1.5 – 2.0	10.280	6.797e-013	5.000e-011	1.835e-013
1.5 – 2.0	12.315	0.000e+000	0.000e+000	0.000e+000
2.0 – 2.5	0.005	2.434e-004	1.114e-006	6.815e-005
2.0 – 2.5	0.015	1.178e-004	7.743e-007	3.298e-005
2.0 – 2.5	0.025	5.363e-005	5.235e-007	1.502e-005
2.0 – 2.5	0.035	3.541e-005	4.258e-007	9.916e-006
2.0 – 2.5	0.045	2.260e-005	3.420e-007	6.329e-006
2.0 – 2.5	0.055	1.612e-005	2.912e-007	4.515e-006
2.0 – 2.5	0.065	1.225e-005	2.548e-007	3.431e-006
2.0 – 2.5	0.075	9.142e-006	2.241e-007	2.560e-006
2.0 – 2.5	0.085	6.737e-006	1.965e-007	1.886e-006
2.0 – 2.5	0.095	5.101e-006	1.775e-007	1.428e-006
2.0 – 2.5	0.105	4.131e-006	1.790e-007	1.157e-006

2.0 – 2.5	0.115	3.229e-006	1.643e-007	9.042e-007
2.0 – 2.5	0.125	2.441e-006	1.452e-007	6.836e-007
2.0 – 2.5	0.135	2.095e-006	1.320e-007	5.865e-007
2.0 – 2.5	0.150	1.783e-006	8.650e-008	4.993e-007
2.0 – 2.5	0.170	1.273e-006	7.798e-008	3.565e-007
2.0 – 2.5	0.190	1.243e-006	7.904e-008	3.479e-007
2.0 – 2.5	0.220	8.689e-007	4.766e-008	2.607e-007
2.0 – 2.5	0.260	8.540e-007	4.747e-008	2.562e-007
2.0 – 2.5	0.330	5.511e-007	2.722e-008	1.653e-007
2.0 – 2.5	0.430	3.965e-007	2.600e-008	1.189e-007
2.0 – 2.5	0.530	1.882e-007	2.256e-008	7.150e-008
2.0 – 2.5	0.605	1.320e-007	3.060e-008	5.016e-008
2.0 – 2.5	0.655	1.994e-007	3.313e-008	7.576e-008
2.0 – 2.5	0.705	2.069e-007	3.612e-008	7.862e-008
2.0 – 2.5	0.740	3.466e-007	6.506e-008	1.317e-007
2.0 – 2.5	0.760	6.425e-007	6.987e-008	2.441e-007
2.0 – 2.5	0.775	9.217e-007	1.063e-007	3.503e-007
2.0 – 2.5	0.785	1.229e-006	1.141e-007	4.670e-007
2.0 – 2.5	0.805	2.505e-007	4.501e-008	9.520e-008
2.0 – 2.5	0.880	7.466e-008	1.780e-008	2.837e-008
2.0 – 2.5	0.970	1.364e-007	2.475e-008	5.184e-008
2.0 – 2.5	1.015	4.223e-007	4.485e-008	1.605e-007
2.0 – 2.5	1.050	7.175e-008	2.770e-008	2.726e-008
2.0 – 2.5	1.195	1.896e-008	1.044e-008	7.206e-009
2.0 – 2.5	1.445	1.101e-008	9.008e-009	2.863e-009
2.0 – 2.5	1.695	1.544e-008	6.413e-009	4.014e-009
2.0 – 2.5	1.945	5.522e-009	5.211e-009	1.436e-009
2.0 – 2.5	2.195	7.083e-009	3.865e-009	1.842e-009
2.0 – 2.5	2.445	1.001e-008	3.392e-009	2.604e-009
2.0 – 2.5	2.695	6.010e-009	2.653e-009	1.563e-009
2.0 – 2.5	2.870	1.227e-008	4.040e-009	3.191e-009
2.0 – 2.5	2.970	3.786e-008	5.092e-009	9.844e-009
2.0 – 2.5	3.030	6.571e-008	1.541e-008	1.709e-008
2.0 – 2.5	3.050	9.460e-008	1.643e-008	2.460e-008
2.0 – 2.5	3.070	1.353e-007	2.240e-008	3.519e-008
2.0 – 2.5	3.090	1.347e-007	2.038e-008	3.502e-008
2.0 – 2.5	3.110	1.375e-007	2.040e-008	3.574e-008
2.0 – 2.5	3.130	9.956e-008	1.660e-008	2.589e-008
2.0 – 2.5	3.150	7.374e-008	1.704e-008	1.917e-008
2.0 – 2.5	3.170	2.562e-008	1.063e-008	6.661e-009

2.0 – 2.5	3.190	1.794e-008	7.265e-009	4.664e-009
2.0 – 2.5	3.375	3.290e-009	8.534e-010	8.554e-010
2.0 – 2.5	3.700	1.250e-009	6.707e-010	3.249e-010
2.0 – 2.5	4.525	4.868e-010	1.599e-010	1.266e-010
2.0 – 2.5	7.200	5.102e-011	3.064e-011	1.378e-011
2.0 – 2.5	9.550	1.198e-010	6.919e-011	3.236e-011
2.0 – 2.5	10.250	3.970e-011	3.970e-011	1.072e-011
2.0 – 2.5	12.300	-7.407e-012	7.407e-012	2.000e-012
2.5 – 3.0	0.005	8.970e-005	6.299e-007	2.511e-005
2.5 – 3.0	0.015	4.749e-005	4.584e-007	1.330e-005
2.5 – 3.0	0.025	2.221e-005	3.137e-007	6.219e-006
2.5 – 3.0	0.035	1.441e-005	2.529e-007	4.034e-006
2.5 – 3.0	0.045	8.566e-006	1.959e-007	2.399e-006
2.5 – 3.0	0.055	6.275e-006	1.680e-007	1.757e-006
2.5 – 3.0	0.065	4.790e-006	1.482e-007	1.341e-006
2.5 – 3.0	0.075	3.613e-006	1.295e-007	1.012e-006
2.5 – 3.0	0.085	2.538e-006	1.119e-007	7.105e-007
2.5 – 3.0	0.095	1.941e-006	9.944e-008	5.436e-007
2.5 – 3.0	0.105	1.579e-006	9.886e-008	4.421e-007
2.5 – 3.0	0.115	1.191e-006	8.832e-008	3.335e-007
2.5 – 3.0	0.125	8.574e-007	7.589e-008	2.401e-007
2.5 – 3.0	0.135	8.268e-007	7.483e-008	2.315e-007
2.5 – 3.0	0.150	5.714e-007	4.488e-008	1.600e-007
2.5 – 3.0	0.170	5.673e-007	4.408e-008	1.588e-007
2.5 – 3.0	0.190	4.589e-007	4.073e-008	1.285e-007
2.5 – 3.0	0.220	3.630e-007	2.596e-008	1.089e-007
2.5 – 3.0	0.260	3.031e-007	2.451e-008	9.094e-008
2.5 – 3.0	0.330	2.245e-007	1.463e-008	6.734e-008
2.5 – 3.0	0.430	1.251e-007	1.336e-008	3.752e-008
2.5 – 3.0	0.530	1.009e-007	1.275e-008	3.833e-008
2.5 – 3.0	0.630	7.374e-008	1.267e-008	2.802e-008
2.5 – 3.0	0.705	1.152e-007	1.884e-008	4.379e-008
2.5 – 3.0	0.740	1.717e-007	3.352e-008	6.526e-008
2.5 – 3.0	0.760	2.481e-007	3.628e-008	9.427e-008
2.5 – 3.0	0.775	6.331e-007	6.474e-008	2.406e-007
2.5 – 3.0	0.785	5.764e-007	6.198e-008	2.190e-007
2.5 – 3.0	0.805	1.427e-007	2.457e-008	5.423e-008
2.5 – 3.0	0.880	6.186e-008	1.049e-008	2.351e-008
2.5 – 3.0	0.970	5.929e-008	1.445e-008	2.253e-008
2.5 – 3.0	1.015	2.577e-007	2.608e-008	9.792e-008

2.5 – 3.0	1.050	4.181e-008	1.588e-008	1.589e-008
2.5 – 3.0	1.195	7.237e-009	5.561e-009	2.750e-009
2.5 – 3.0	1.695	5.190e-009	2.520e-009	1.349e-009
2.5 – 3.0	2.320	2.467e-009	1.875e-009	6.414e-010
2.5 – 3.0	2.695	3.945e-009	2.358e-009	1.026e-009
2.5 – 3.0	2.870	5.687e-009	3.224e-009	1.479e-009
2.5 – 3.0	2.970	2.514e-008	4.249e-009	6.537e-009
2.5 – 3.0	3.040	4.256e-008	8.691e-009	1.107e-008
2.5 – 3.0	3.080	7.560e-008	1.079e-008	1.966e-008
2.5 – 3.0	3.120	5.687e-008	9.590e-009	1.479e-008
2.5 – 3.0	3.160	1.834e-008	6.043e-009	4.767e-009
2.5 – 3.0	3.365	2.739e-009	7.492e-010	7.122e-010
2.5 – 3.0	3.700	4.877e-010	5.567e-010	1.268e-010
2.5 – 3.0	6.275	1.314e-010	5.080e-011	3.416e-011
2.5 – 3.0	9.850	1.335e-011	2.058e-011	3.605e-012
2.5 – 3.0	12.500	9.783e-012	9.783e-012	2.641e-012
3.0 – 3.5	0.005	3.162e-005	3.518e-007	8.855e-006
3.0 – 3.5	0.015	1.780e-005	2.638e-007	4.983e-006
3.0 – 3.5	0.025	8.648e-006	1.839e-007	2.421e-006
3.0 – 3.5	0.035	5.481e-006	1.468e-007	1.535e-006
3.0 – 3.5	0.045	3.184e-006	1.120e-007	8.916e-007
3.0 – 3.5	0.055	2.430e-006	9.805e-008	6.805e-007
3.0 – 3.5	0.065	1.627e-006	8.103e-008	4.557e-007
3.0 – 3.5	0.075	1.450e-006	7.698e-008	4.059e-007
3.0 – 3.5	0.085	9.962e-007	6.472e-008	2.789e-007
3.0 – 3.5	0.095	7.698e-007	5.931e-008	2.156e-007
3.0 – 3.5	0.105	5.558e-007	5.097e-008	1.556e-007
3.0 – 3.5	0.115	4.391e-007	4.710e-008	1.229e-007
3.0 – 3.5	0.125	2.580e-007	4.078e-008	7.223e-008
3.0 – 3.5	0.135	2.646e-007	3.558e-008	7.410e-008
3.0 – 3.5	0.150	2.044e-007	2.488e-008	5.724e-008
3.0 – 3.5	0.170	2.387e-007	2.618e-008	6.684e-008
3.0 – 3.5	0.190	1.895e-007	2.564e-008	5.306e-008
3.0 – 3.5	0.220	1.404e-007	1.534e-008	4.212e-008
3.0 – 3.5	0.260	1.299e-007	1.558e-008	3.898e-008
3.0 – 3.5	0.330	8.814e-008	8.719e-009	2.644e-008
3.0 – 3.5	0.430	5.018e-008	7.831e-009	1.505e-008
3.0 – 3.5	0.530	4.093e-008	7.997e-009	1.555e-008
3.0 – 3.5	0.630	4.528e-008	7.576e-009	1.721e-008
3.0 – 3.5	0.705	7.726e-008	1.235e-008	2.936e-008

3.0 – 3.5	0.740	5.496e-008	1.812e-008	2.089e-008
3.0 – 3.5	0.760	1.198e-007	2.259e-008	4.553e-008
3.0 – 3.5	0.775	2.815e-007	4.115e-008	1.070e-007
3.0 – 3.5	0.785	3.366e-007	4.485e-008	1.279e-007
3.0 – 3.5	0.805	9.968e-008	1.661e-008	3.788e-008
3.0 – 3.5	0.880	2.104e-008	5.966e-009	7.994e-009
3.0 – 3.5	0.970	3.049e-008	8.912e-009	1.159e-008
3.0 – 3.5	1.015	1.423e-007	1.747e-008	5.406e-008
3.0 – 3.5	1.050	2.981e-008	1.033e-008	1.133e-008
3.0 – 3.5	1.370	5.597e-009	2.078e-009	2.127e-009
3.0 – 3.5	2.270	1.188e-009	9.273e-010	3.089e-010
3.0 – 3.5	2.945	1.268e-008	2.597e-009	3.297e-009
3.0 – 3.5	3.045	3.601e-008	7.095e-009	9.362e-009
3.0 – 3.5	3.100	5.052e-008	6.904e-009	1.313e-008
3.0 – 3.5	3.155	9.138e-009	4.539e-009	2.376e-009
3.0 – 3.5	3.365	1.723e-009	7.110e-010	4.481e-010
3.0 – 3.5	3.700	4.170e-010	4.597e-010	1.084e-010
3.0 – 3.5	6.275	1.130e-010	3.766e-011	2.939e-011
3.0 – 3.5	9.850	2.668e-011	3.380e-011	7.204e-012
3.0 – 3.5	12.500	2.935e-011	1.384e-011	7.924e-012
3.5 – 8.0	0.005	2.123e-005	2.882e-007	5.944e-006
3.5 – 8.0	0.015	1.489e-005	2.410e-007	4.170e-006
3.5 – 8.0	0.025	7.043e-006	1.657e-007	1.972e-006
3.5 – 8.0	0.035	4.498e-006	1.330e-007	1.260e-006
3.5 – 8.0	0.045	2.467e-006	9.837e-008	6.907e-007
3.5 – 8.0	0.055	1.840e-006	8.528e-008	5.151e-007
3.5 – 8.0	0.065	1.322e-006	7.284e-008	3.701e-007
3.5 – 8.0	0.075	8.995e-007	6.143e-008	2.518e-007
3.5 – 8.0	0.085	8.397e-007	5.926e-008	2.351e-007
3.5 – 8.0	0.095	6.147e-007	5.110e-008	1.721e-007
3.5 – 8.0	0.105	4.778e-007	4.736e-008	1.338e-007
3.5 – 8.0	0.115	3.657e-007	4.214e-008	1.024e-007
3.5 – 8.0	0.125	2.584e-007	3.448e-008	7.234e-008
3.5 – 8.0	0.135	2.797e-007	3.620e-008	7.832e-008
3.5 – 8.0	0.150	1.827e-007	2.244e-008	5.115e-008
3.5 – 8.0	0.170	1.876e-007	2.215e-008	5.254e-008
3.5 – 8.0	0.190	1.486e-007	2.011e-008	4.161e-008
3.5 – 8.0	0.220	1.495e-007	1.523e-008	4.486e-008
3.5 – 8.0	0.260	1.076e-007	1.307e-008	3.229e-008
3.5 – 8.0	0.330	9.757e-008	7.951e-009	2.927e-008

3.5 – 8.0	0.430	3.851e-008	6.948e-009	1.155e-008
3.5 – 8.0	0.530	3.932e-008	6.717e-009	1.494e-008
3.5 – 8.0	0.630	3.835e-008	6.717e-009	1.457e-008
3.5 – 8.0	0.705	4.088e-008	1.021e-008	1.553e-008
3.5 – 8.0	0.740	5.587e-008	1.724e-008	2.123e-008
3.5 – 8.0	0.760	1.380e-007	2.089e-008	5.242e-008
3.5 – 8.0	0.775	1.649e-007	3.079e-008	6.265e-008
3.5 – 8.0	0.785	2.049e-007	3.500e-008	7.785e-008
3.5 – 8.0	0.805	9.722e-008	1.517e-008	3.694e-008
3.5 – 8.0	0.880	1.834e-008	5.412e-009	6.969e-009
3.5 – 8.0	0.970	3.659e-008	8.624e-009	1.390e-008
3.5 – 8.0	1.015	1.276e-007	1.660e-008	4.848e-008
3.5 – 8.0	1.050	4.338e-008	9.739e-009	1.649e-008
3.5 – 8.0	1.195	6.616e-009	2.890e-009	2.514e-009
3.5 – 8.0	1.695	4.634e-009	1.402e-009	1.205e-009
3.5 – 8.0	2.320	2.656e-009	1.372e-009	6.906e-010
3.5 – 8.0	2.695	5.417e-009	1.959e-009	1.409e-009
3.5 – 8.0	2.870	2.399e-009	2.570e-009	6.237e-010
3.5 – 8.0	2.970	3.182e-008	4.372e-009	8.273e-009
3.5 – 8.0	3.040	4.287e-008	7.564e-009	1.115e-008
3.5 – 8.0	3.080	7.309e-008	9.860e-009	1.900e-008
3.5 – 8.0	3.120	7.326e-008	9.814e-009	1.905e-008
3.5 – 8.0	3.160	2.016e-008	7.077e-009	5.241e-009
3.5 – 8.0	3.365	2.057e-009	8.190e-010	5.348e-010
3.5 – 8.0	3.700	6.069e-010	6.080e-010	1.578e-010
3.5 – 8.0	6.275	8.448e-011	7.031e-011	2.196e-011
3.5 – 8.0	9.850	5.057e-011	4.130e-011	1.365e-011
3.5 – 8.0	12.500	-8.671e-012	1.567e-011	2.341e-012

Table B.3: Data points for Figure 9.5 with statistical and systematic uncertainties in various p_T slices.

Table B.4 gives the data points of the mass spectra in centrality slices from Figure 9.7.

Cent (%)	mass (GeV/c^2)	$\frac{1}{N_{evt}}\frac{dN}{dm_{ee}}$ (c^2/GeV)	Stat Uncert	Syst Uncert
0.0 – 20.0	0.005	7.313e-003	6.974e-005	2.048e-003
0.0 – 20.0	0.015	3.117e-003	4.720e-005	8.727e-004
0.0 – 20.0	0.025	1.462e-003	3.447e-005	4.094e-004
0.0 – 20.0	0.035	1.063e-003	3.143e-005	2.976e-004
0.0 – 20.0	0.045	6.515e-004	2.248e-005	1.824e-004
0.0 – 20.0	0.055	5.012e-004	2.064e-005	1.403e-004
0.0 – 20.0	0.065	3.854e-004	1.960e-005	1.079e-004
0.0 – 20.0	0.075	2.814e-004	1.746e-005	7.880e-005
0.0 – 20.0	0.085	2.140e-004	1.605e-005	5.993e-005
0.0 – 20.0	0.095	1.588e-004	1.470e-005	4.445e-005
0.0 – 20.0	0.105	9.131e-005	1.289e-005	2.557e-005
0.0 – 20.0	0.115	6.591e-005	1.296e-005	1.845e-005
0.0 – 20.0	0.125	5.527e-005	1.199e-005	1.548e-005
0.0 – 20.0	0.145	3.197e-005	6.816e-006	8.953e-006
0.0 – 20.0	0.180	3.347e-005	7.075e-006	9.373e-006
0.0 – 20.0	0.240	1.764e-005	6.832e-006	5.291e-006
0.0 – 20.0	0.330	1.309e-005	9.585e-006	3.927e-006
0.0 – 20.0	0.480	1.797e-006	6.796e-006	5.391e-007
0.0 – 20.0	0.630	7.359e-006	6.824e-006	2.796e-006
0.0 – 20.0	0.720	7.745e-006	5.570e-006	2.943e-006
0.0 – 20.0	0.765	2.053e-005	1.457e-005	7.802e-006
0.0 – 20.0	0.775	4.654e-005	1.439e-005	1.768e-005
0.0 – 20.0	0.785	1.916e-005	1.155e-005	7.280e-006
0.0 – 20.0	0.805	9.720e-006	6.436e-006	3.694e-006
0.0 – 20.0	0.860	6.921e-006	3.284e-006	2.630e-006
0.0 – 20.0	0.930	1.884e-006	2.857e-006	7.161e-007
0.0 – 20.0	0.970	8.968e-006	4.774e-006	3.408e-006
0.0 – 20.0	0.990	9.067e-006	3.817e-006	3.445e-006
0.0 – 20.0	1.005	1.686e-005	5.598e-006	6.407e-006
0.0 – 20.0	1.015	1.814e-005	6.055e-006	6.892e-006
0.0 – 20.0	1.025	1.014e-005	5.168e-006	3.855e-006
0.0 – 20.0	1.170	8.573e-007	6.168e-007	3.258e-007
0.0 – 20.0	1.360	9.338e-007	3.730e-007	2.428e-007
0.0 – 20.0	1.460	6.532e-007	2.858e-007	1.698e-007
0.0 – 20.0	1.560	3.454e-007	2.308e-007	8.981e-008
0.0 – 20.0	1.660	2.407e-007	1.828e-007	6.259e-008

0.0 – 20.0	1.760	4.487e-007	1.550e-007	1.167e-007
0.0 – 20.0	1.860	5.228e-008	1.212e-007	1.359e-008
0.0 – 20.0	1.960	1.949e-007	1.020e-007	5.068e-008
0.0 – 20.0	2.060	1.764e-007	8.195e-008	4.587e-008
0.0 – 20.0	2.160	1.724e-007	7.355e-008	4.481e-008
0.0 – 20.0	2.260	3.018e-007	6.198e-008	7.846e-008
0.0 – 20.0	2.360	9.979e-008	5.489e-008	2.595e-008
0.0 – 20.0	2.460	1.551e-007	5.128e-008	4.032e-008
0.0 – 20.0	2.560	1.260e-007	4.873e-008	3.277e-008
0.0 – 20.0	2.660	1.242e-007	3.865e-008	3.230e-008
0.0 – 20.0	2.730	4.431e-008	5.245e-008	1.152e-008
0.0 – 20.0	2.790	1.386e-007	3.773e-008	3.603e-008
0.0 – 20.0	2.850	1.372e-007	4.854e-008	3.568e-008
0.0 – 20.0	2.890	2.750e-007	5.034e-008	7.150e-008
0.0 – 20.0	2.920	3.748e-007	8.157e-008	9.744e-008
0.0 – 20.0	2.940	3.509e-007	7.620e-008	9.122e-008
0.0 – 20.0	2.960	3.178e-007	8.660e-008	8.264e-008
0.0 – 20.0	2.980	3.903e-007	8.746e-008	1.015e-007
0.0 – 20.0	3.000	7.423e-007	1.015e-007	1.930e-007
0.0 – 20.0	3.020	9.209e-007	1.052e-007	2.394e-007
0.0 – 20.0	3.040	1.011e-006	1.170e-007	2.629e-007
0.0 – 20.0	3.060	1.371e-006	1.392e-007	3.565e-007
0.0 – 20.0	3.080	1.853e-006	1.480e-007	4.818e-007
0.0 – 20.0	3.100	2.131e-006	1.540e-007	5.539e-007
0.0 – 20.0	3.120	1.821e-006	1.469e-007	4.736e-007
0.0 – 20.0	3.140	9.362e-007	1.198e-007	2.434e-007
0.0 – 20.0	3.160	7.055e-007	1.063e-007	1.834e-007
0.0 – 20.0	3.180	3.091e-007	7.831e-008	8.037e-008
0.0 – 20.0	3.200	1.079e-007	5.808e-008	2.805e-008
0.0 – 20.0	3.220	1.057e-007	3.804e-008	2.748e-008
0.0 – 20.0	3.240	1.715e-008	3.805e-008	4.459e-009
0.0 – 20.0	3.270	2.397e-008	2.326e-008	6.233e-009
0.0 – 20.0	3.310	3.783e-008	2.267e-008	9.837e-009
0.0 – 20.0	3.420	1.437e-008	9.750e-009	3.737e-009
0.0 – 20.0	3.585	2.010e-008	9.047e-009	5.227e-009
0.0 – 20.0	3.685	3.150e-008	1.661e-008	8.191e-009
0.0 – 20.0	3.785	4.474e-009	7.549e-009	1.163e-009
0.0 – 20.0	4.160	7.339e-009	2.641e-009	1.908e-009
0.0 – 20.0	5.010	4.014e-009	1.067e-009	7.626e-010
0.0 – 20.0	6.160	1.129e-009	5.433e-010	3.050e-010

0.0 – 20.0	7.635	3.288e-010	2.542e-010	8.877e-011
0.0 – 20.0	8.855	5.256e-010	3.378e-010	1.419e-010
0.0 – 20.0	9.400	1.440e-009	6.457e-010	3.887e-010
0.0 – 20.0	9.800	2.799e-010	4.995e-010	7.557e-011
0.0 – 20.0	10.200	2.656e-010	2.656e-010	7.170e-011
0.0 – 20.0	11.300	7.275e-011	1.284e-010	1.964e-011
0.0 – 20.0	13.100	1.250e-010	8.936e-011	3.375e-011
20.0 – 40.0	0.005	4.992e-003	5.841e-005	1.398e-003
20.0 – 40.0	0.015	2.121e-003	3.967e-005	5.940e-004
20.0 – 40.0	0.025	1.006e-003	2.847e-005	2.816e-004
20.0 – 40.0	0.035	7.082e-004	2.533e-005	1.983e-004
20.0 – 40.0	0.045	4.578e-004	1.905e-005	1.282e-004
20.0 – 40.0	0.055	3.520e-004	1.672e-005	9.855e-005
20.0 – 40.0	0.065	2.457e-004	1.464e-005	6.879e-005
20.0 – 40.0	0.075	1.844e-004	1.406e-005	5.164e-005
20.0 – 40.0	0.085	1.546e-004	1.310e-005	4.329e-005
20.0 – 40.0	0.095	1.099e-004	1.221e-005	3.078e-005
20.0 – 40.0	0.105	7.264e-005	1.123e-005	2.034e-005
20.0 – 40.0	0.120	3.843e-005	6.934e-006	1.076e-005
20.0 – 40.0	0.150	3.152e-005	4.907e-006	8.826e-006
20.0 – 40.0	0.205	1.873e-005	4.391e-006	5.244e-006
20.0 – 40.0	0.260	2.434e-005	6.458e-006	7.302e-006
20.0 – 40.0	0.330	7.328e-006	6.674e-006	2.198e-006
20.0 – 40.0	0.455	2.187e-006	5.868e-006	6.560e-007
20.0 – 40.0	0.610	5.711e-006	3.903e-006	2.170e-006
20.0 – 40.0	0.730	1.284e-005	3.662e-006	4.879e-006
20.0 – 40.0	0.775	3.192e-005	9.986e-006	1.213e-005
20.0 – 40.0	0.785	2.283e-005	7.690e-006	8.676e-006
20.0 – 40.0	0.830	1.896e-006	2.495e-006	7.205e-007
20.0 – 40.0	0.935	2.368e-006	1.411e-006	8.998e-007
20.0 – 40.0	1.005	6.873e-006	4.396e-006	2.612e-006
20.0 – 40.0	1.015	4.414e-006	3.341e-006	1.677e-006
20.0 – 40.0	1.025	8.348e-006	3.881e-006	3.172e-006
20.0 – 40.0	1.170	7.173e-007	4.170e-007	2.726e-007
20.0 – 40.0	1.410	7.311e-007	1.605e-007	1.901e-007
20.0 – 40.0	1.610	5.992e-007	1.064e-007	1.558e-007
20.0 – 40.0	1.810	2.445e-007	6.954e-008	6.358e-008
20.0 – 40.0	2.010	1.626e-007	4.646e-008	4.227e-008
20.0 – 40.0	2.210	1.005e-007	3.421e-008	2.613e-008
20.0 – 40.0	2.410	5.501e-008	2.858e-008	1.430e-008

20.0 – 40.0	2.610	7.794e-008	2.177e-008	2.027e-008
20.0 – 40.0	2.770	5.357e-008	2.189e-008	1.393e-008
20.0 – 40.0	2.870	1.380e-007	2.929e-008	3.588e-008
20.0 – 40.0	2.940	1.735e-007	3.454e-008	4.510e-008
20.0 – 40.0	2.990	3.663e-007	5.326e-008	9.524e-008
20.0 – 40.0	3.020	5.925e-007	8.713e-008	1.541e-007
20.0 – 40.0	3.040	9.708e-007	1.114e-007	2.524e-007
20.0 – 40.0	3.060	1.345e-006	1.232e-007	3.497e-007
20.0 – 40.0	3.080	1.427e-006	1.304e-007	3.709e-007
20.0 – 40.0	3.100	1.385e-006	1.272e-007	3.601e-007
20.0 – 40.0	3.120	1.119e-006	1.181e-007	2.909e-007
20.0 – 40.0	3.140	5.774e-007	8.292e-008	1.501e-007
20.0 – 40.0	3.160	4.528e-007	7.861e-008	1.177e-007
20.0 – 40.0	3.190	1.775e-007	3.699e-008	4.615e-008
20.0 – 40.0	3.410	1.966e-008	4.850e-009	5.111e-009
20.0 – 40.0	3.685	1.320e-008	6.794e-009	3.432e-009
20.0 – 40.0	4.335	4.556e-009	1.347e-009	1.184e-009
20.0 – 40.0	5.410	5.762e-010	6.374e-010	1.095e-010
20.0 – 40.0	7.410	2.756e-010	1.927e-010	7.442e-011
20.0 – 40.0	9.285	6.214e-010	4.409e-010	1.678e-010
20.0 – 40.0	11.830	3.789e-011	6.956e-011	1.023e-011
40.0 – 60.0	0.005	3.237e-003	4.722e-005	9.065e-004
40.0 – 60.0	0.015	1.356e-003	3.170e-005	3.798e-004
40.0 – 60.0	0.025	6.454e-004	2.338e-005	1.807e-004
40.0 – 60.0	0.035	5.216e-004	2.247e-005	1.460e-004
40.0 – 60.0	0.045	2.868e-004	1.449e-005	8.031e-005
40.0 – 60.0	0.055	2.138e-004	1.358e-005	5.987e-005
40.0 – 60.0	0.065	1.414e-004	1.128e-005	3.960e-005
40.0 – 60.0	0.075	1.111e-004	1.061e-005	3.111e-005
40.0 – 60.0	0.085	8.573e-005	9.806e-006	2.400e-005
40.0 – 60.0	0.095	8.516e-005	1.021e-005	2.384e-005
40.0 – 60.0	0.185	2.070e-005	2.062e-006	5.796e-006
40.0 – 60.0	0.345	3.952e-006	4.481e-006	1.186e-006
40.0 – 60.0	0.520	4.497e-006	3.054e-006	1.709e-006
40.0 – 60.0	0.690	8.471e-007	2.445e-006	3.219e-007
40.0 – 60.0	0.780	1.334e-005	2.944e-006	5.071e-006
40.0 – 60.0	0.890	1.144e-006	9.832e-007	4.347e-007
40.0 – 60.0	1.020	2.727e-006	9.467e-007	1.036e-006
40.0 – 60.0	1.285	4.040e-007	1.815e-007	1.535e-007
40.0 – 60.0	1.610	1.393e-007	7.167e-008	3.622e-008

40.0 – 60.0	1.810	1.258e-007	4.923e-008	3.272e-008
40.0 – 60.0	2.010	1.244e-007	3.437e-008	3.235e-008
40.0 – 60.0	2.210	3.976e-008	2.314e-008	1.034e-008
40.0 – 60.0	2.410	5.187e-008	2.040e-008	1.349e-008
40.0 – 60.0	2.610	6.832e-008	1.627e-008	1.776e-008
40.0 – 60.0	2.770	6.984e-008	1.711e-008	1.816e-008
40.0 – 60.0	2.870	9.153e-008	2.018e-008	2.380e-008
40.0 – 60.0	2.940	1.351e-007	2.501e-008	3.512e-008
40.0 – 60.0	2.990	2.549e-007	3.932e-008	6.628e-008
40.0 – 60.0	3.020	4.545e-007	7.211e-008	1.182e-007
40.0 – 60.0	3.040	3.967e-007	6.813e-008	1.031e-007
40.0 – 60.0	3.060	6.941e-007	9.502e-008	1.805e-007
40.0 – 60.0	3.080	8.083e-007	9.898e-008	2.102e-007
40.0 – 60.0	3.100	8.890e-007	9.912e-008	2.311e-007
40.0 – 60.0	3.120	7.164e-007	8.999e-008	1.863e-007
40.0 – 60.0	3.140	6.124e-007	8.440e-008	1.592e-007
40.0 – 60.0	3.160	2.358e-007	5.577e-008	6.130e-008
40.0 – 60.0	3.190	1.156e-007	2.901e-008	3.006e-008
40.0 – 60.0	3.410	9.490e-009	3.709e-009	2.467e-009
40.0 – 60.0	3.685	1.522e-008	4.618e-009	3.957e-009
40.0 – 60.0	4.410	1.321e-011	1.014e-009	3.436e-012
40.0 – 60.0	6.830	3.990e-011	1.800e-010	1.077e-011
40.0 – 60.0	9.500	4.019e-010	1.849e-010	1.085e-010
40.0 – 60.0	12.200	7.068e-011	4.999e-011	1.908e-011
60.0 – 88.0	0.005	1.479e-003	2.778e-005	4.142e-004
60.0 – 88.0	0.015	6.100e-004	1.792e-005	1.708e-004
60.0 – 88.0	0.025	2.940e-004	1.306e-005	8.231e-005
60.0 – 88.0	0.035	2.371e-004	1.351e-005	6.639e-005
60.0 – 88.0	0.045	1.435e-004	9.116e-006	4.019e-005
60.0 – 88.0	0.055	9.382e-005	7.340e-006	2.627e-005
60.0 – 88.0	0.065	8.338e-005	7.609e-006	2.335e-005
60.0 – 88.0	0.075	6.299e-005	6.708e-006	1.764e-005
60.0 – 88.0	0.085	4.030e-005	5.541e-006	1.128e-005
60.0 – 88.0	0.095	2.851e-005	4.881e-006	7.982e-006
60.0 – 88.0	0.185	7.417e-006	1.038e-006	2.077e-006
60.0 – 88.0	0.345	2.649e-006	1.808e-006	7.947e-007
60.0 – 88.0	0.520	1.671e-006	1.525e-006	6.350e-007
60.0 – 88.0	0.690	2.557e-006	1.172e-006	9.718e-007
60.0 – 88.0	0.780	3.512e-006	1.710e-006	1.335e-006
60.0 – 88.0	0.890	1.118e-006	4.654e-007	4.249e-007

60.0 – 88.0	1.020	1.583e-006	4.279e-007	6.015e-007
60.0 – 88.0	1.285	2.327e-007	8.695e-008	8.841e-008
60.0 – 88.0	1.610	8.450e-008	3.397e-008	2.197e-008
60.0 – 88.0	1.810	8.026e-008	2.290e-008	2.087e-008
60.0 – 88.0	2.010	5.923e-008	1.648e-008	1.540e-008
60.0 – 88.0	2.210	2.709e-008	1.128e-008	7.043e-009
60.0 – 88.0	2.410	3.435e-008	1.013e-008	8.932e-009
60.0 – 88.0	2.610	1.484e-008	7.522e-009	3.858e-009
60.0 – 88.0	2.770	3.853e-008	8.505e-009	1.002e-008
60.0 – 88.0	2.870	2.814e-008	1.038e-008	7.317e-009
60.0 – 88.0	2.940	6.150e-008	1.377e-008	1.599e-008
60.0 – 88.0	2.990	1.324e-007	2.421e-008	3.442e-008
60.0 – 88.0	3.020	2.139e-007	4.149e-008	5.562e-008
60.0 – 88.0	3.040	2.797e-007	4.718e-008	7.271e-008
60.0 – 88.0	3.060	3.626e-007	5.253e-008	9.427e-008
60.0 – 88.0	3.080	4.292e-007	6.084e-008	1.116e-007
60.0 – 88.0	3.100	5.348e-007	6.413e-008	1.391e-007
60.0 – 88.0	3.120	3.333e-007	5.250e-008	8.665e-008
60.0 – 88.0	3.140	1.810e-007	4.162e-008	4.707e-008
60.0 – 88.0	3.160	1.319e-007	3.561e-008	3.428e-008
60.0 – 88.0	3.190	9.779e-008	2.081e-008	2.543e-008
60.0 – 88.0	3.410	7.144e-009	2.023e-009	1.857e-009
60.0 – 88.0	3.685	8.614e-009	2.621e-009	2.240e-009
60.0 – 88.0	4.410	6.997e-010	3.870e-010	1.819e-010
60.0 – 88.0	6.830	-2.999e-012	8.116e-011	8.098e-013
60.0 – 88.0	9.500	4.550e-011	8.019e-011	1.229e-011
60.0 – 88.0	12.200	-5.398e-012	3.044e-011	1.457e-012

Table B.4: Data points for Figure 9.7 with statistical and systematic uncertainties in centrality slices.